Induction Welding of 3D-printed Core to Composite Facesheets with New Electromagnetic Susceptor

by

Romain Georges MARTIN

MANUSCRIPT-BASED THESIS PRESENTED TO ÉCOLE DE TECHNOLOGIE SUPÉRIEURE IN PARTIAL FULFILLMENT FOR THE DEGREE OF DOCTOR OF PHILOSOPHY
Ph. D.

MONTRÉAL, JULY 17TH, 2024

ÉCOLE DE TECHNOLOGIE SUPÉRIEURE
UNIVERSITÉ DU QUÉBEC

BOARD OF EXAMINERS

THIS THESIS HAS BEEN EVALUATED

BY THE FOLLOWING BOARD OF EXAMINERS

Ms. Martine Dubé, Thesis Supervisor
Department of Mechanical Engineering, École de technologie supérieure

Mr. Jason Robert Tavares, Thesis Co-supervisor
Department of Chemical Engineering, Polytechnique Montréal

Mr. Christer Johansson, Thesis Co-supervisor
RISE Research Institutes of Sweden

Ms. Claudiane Ouellet-Plamondon, President of the Board of Examiners
Department of Construction Engineering, École de technologie supérieure

Mr. Éric David, Member of the jury
Department of Mechanical Engineering, École de technologie supérieure

Ms. Yasmine Abdin, External Evaluator
Department of Mechanical Engineering, University of British Columbia

THIS THESIS WAS PRESENTED AND DEFENDED

IN PRESENCE OF A BOARD OF EXAMINERS AND PUBLIC

ON JULY 5TH, 2024

AT ÉCOLE DE TECHNOLOGIE SUPÉRIEURE

ACKNOWLEDGEMENTS

First, I would like to express my gratitude to Prof. Martine Dubé, Prof. Jason R. Tavares and Prof. Christer Johansson for your constant support and guidance during the past four years. This project gave me the chance to learn a lot by your side, and your advice will continue to serve me in the future steps of my career. I am also grateful that you decided to believe in me and keep me on the project even though the COVID-19 pandemic delayed my arrival in Montréal by 8 months in 2020.

Many thanks to Prof. Eric David, Prof. Yasmine Abdin for accepting to be jury members, and Prof. Claudiane Ouellet-Plamondon for accepting to be the president of the jury for the defence of my PhD.

I would like to extend my sincere thanks to all the industrial partners of the PEEKbot project (ArianeGroup, Mëkanic, NanoXplore and Dyze Design) for supporting and funding this project. Special thanks to Dr. Marie-Josée Potvin from the Canadian Space Agency, for all the support and feedback you gave me throughout my thesis, this was always appreciated and will be extremely useful in the future.

This journey would not have been the same without my friends and colleagues in the LIPEC research group at ÉTS. Many thanks to Maryam, Saré, Atefe, Carl-Olivier, Mélanie, Daria, Manon, and all the others that are not mentioned here. The time we spent together in the office, in the lab and during our various group meetings made this journey very special. A special thanks to Dr. Adam Smith, for your continued support from my Master Project in McGill to my PhD at ÉTS, I am grateful that you were around for all this time.

I would also like to acknowledge the support of all the technical staff at ÉTS, especially to Mr. Serge Plamondon for your availability and support for my mechanical tests, and to Mr. Nabil Mazeghrane, for all your help, for all the orders and deliveries, and for all our

conversations. I also want to thank Mr. Matthieu Gauthier for his support with the extruder at Polytechnique.

I would also like to thank the PEEKbot students, Olivier, Arthur, Aleksey, Behnam, Mohammad, Olivier, it was great to see our projects evolve and progress in parallel, and to share some great times during events and conferences. I'd also like to recognize the support of all the professors involved in the PEEKbot project for their comments during the follow-up meetings and for contributing to make this project dynamic and motivating.

I am grateful to all my friends and colleagues across Montréal, especially the McGill composites group, Sid, Farnaz, Nathan, Leo, Henri and all the others, as well as the PhotoSEL lab in Polytechnique, Wendell, David, Adya, and the rest of the team.

Lastly, the past four years would not have been the same without the support of my partner Julieta. Thank you for being there, for supporting and understanding me, in the good and in the bad moments. I am also extremely grateful to my parents, Corinne and Nicolas, for supporting me in this adventure from Day one, even tough it meant for me to go live 6000 km away from home. Despite the distance, you were always there for me, and I could not have done it without you.

Soudage par induction d’un cœur imprimé en 3D à des peaux en composites à l’aide d’un suscepteur électro-magnétique innovant

Romain Georges MARTIN

RÉSUMÉ

La survie d’un astromobile – ou rover – sur la Lune dépend de nombreux facteurs, en particulier de sa capacité à résister à la froide nuit lunaire, durant laquelle la température chute à -200°C pendant 14 jours. Afin de garantir une température suffisante à l’intérieure du rover, ce dernier doit être composé d’une structure offrant une grande isolation thermique. Pour cela, le projet PEEKbot propose d’utiliser des panneaux sandwich à base de matériaux composites thermoplastiques qui offrent une grande intégrité structurelle ainsi que les propriétés thermiques recherchées. Les structures suggérées sont composées de cœurs en nid d’abeilles produits par impression 3D et de deux peaux en composites thermoplastiques haute performance, assemblés par soudage thermoplastique.

Dans le présent projet, le soudage par induction est choisi, lequel utilise l’application d’un champ magnétique pour générer de la chaleur directement à l’interface de soudage grâce à un suscepteur. Les suscepteurs magnétiques, dans lesquels la dissipation de chaleur se produit grâce au phénomène des pertes par hystérèse, sont sélectionnés pour l’assemblage des panneaux sandwich. Ils sont composés des particules ferromagnétiques dispersées dans un polymère thermoplastique. La première étape consiste à déterminer les propriétés essentielles du matériau et établir une méthodologie de sélection des particules ferromagnétiques en fonction du polymère choisi et du dispositif de soudage par induction utilisé. Ensuite, grâce à cette méthodologie, les particules de Nickel sont choisies pour fabriquer des suscepteurs à base de poly-ether-ether-imide, un thermoplastique haute-performance. La caractérisation des ces suscepteurs révèle leurs bonnes propriétés de chauffe et confirme qu’ils peuvent être utilisé pour le soudage par induction.

Le montage expérimental de soudage par induction est adapté aux panneaux sandwich, et l’ajout d’un sac sous vide dans lequel sont placés les échantillons permet une application constante et uniforme de la pression durant le procédé. Grâce à cela, des échantillons sont ensuite assemblés par soudage par induction à l'aide de films de suscepteurs magnétiques précédemment développés. Les soudures réalisées avec les paramètres de procédé optimaux révèlent une résistance supérieure à celle du cœur imprimé en 3D. Par la suite, les films de suscepteur sont remplacés par une couche de suscepteur imprimé en 3D directement sur le cœur en nid d'abeilles, localisant ainsi la chauffe. Une caractérisation complète, du filament de suscepteur jusqu'au panneaux sandwich soudés à l'aide de ce matériau conclut que cette méthode de soudage fonctionne, ce qui est prometteur pour de futures utilisations.

Finalement, la méthode d'assemblage par induction sous vide est transférée à des panneaux sandwich à peaux en fibres de carbones, pour lesquels l'utilisation d'une suscepteur n'est pas nécessaire. La modélisation de la chauffe par induction des laminés est confirmée par des mesures expérimentale, et des panneaux sandwich sont soudés par induction. Une nouvelle fois, la résistance maximale des soudures se révèle supérieure à celle du cœur imprimé, confirmant le bon fonctionnement de la méthode de soudage par induction sous vide et sa capacité à être adaptée à différents matériaux et mécanismes de chauffe.

Mots-clés : composites thermoplastiques, soudage par induction, structures sandwich

Induction welding of 3D-printed core to composite facesheets with new electromagnetic susceptor

Romain Georges MARTIN

ABSTRACT

The survival of a rover on the Moon depends on various factors, especially its ability to resist the cold lunar night, during which the surface temperature drops to -200°C for 14 days. To ensure a sufficient temperature inside the rover, it must be made of a structure offering high thermal insulation. For that purpose, the PEEKbot project proposes to use thermoplastic composites sandwich panels, which provides high structural integrity and the required thermal properties. These suggested structures are composed of a 3D-printed honeycomb core and two high-performance thermoplastic composite facesheets, which are assembled using thermoplastic welding techniques.

In the present work, induction welding is selected. This method relies on the application of a magnetic field to generate directly at the joining interface thanks to a susceptor material. Magnetic susceptors, in which heat is dissipated by hysteresis losses, are selected for the assembly of the sandwich panels. They are made of dispersed ferromagnetic particles in a thermoplastic polymer. The first step is to determine the crucial properties of the material and define a material selection methodology to select ferromagnetic particles based on the thermoplastic polymer and the available induction welding setup. Then, using the proposed methodology, Nickel particles are selected to prepare susceptor with poly-ether-ether-imide, a high-performance thermoplastic polymer. Characterization of the susceptors shows their satisfying heating properties and confirms that they can be used for induction welding.

The induction welding experimental setup is then adapted to the assembly of sandwich panels. The addition of a vacuum bag in which the sample is placed allows for the application of a constant and homogeneous pressure throughout the process. Samples are welded with this updated method, using the previously developed magnetic susceptor films. The welds conducted with optimal process parameters exhibit a skin/core strength larger than the tensile strength of the 3D-printed core. Then, susceptor films are replaced with a layer of susceptor directly printed on the honeycomb core, localizing the heat dissipation on the top of the cell walls. A complete characterization, from the 3D-printing filament of susceptor to the sandwich panels welded using this material concludes that this induction welding method is feasible, which is promising for future applications.

Finally, the vacuum induction welding method is transferred to the assembly of sandwich panels made of carbon fibres reinforced sandwich facesheets, which do not require the use of a susceptor as heat can be generated directly in the material. Modelling of the induction heating of the laminates is confirmed by experimental measurements, and sandwich panels are welded by induction. Once again, maximum skin/core strength is higher than the 3D-printed core strength, which confirms that the vacuum induction welding method works correctly, and that it can be adapted to different materials and heating mechanisms.

Keywords: thermoplastic composites, induction welding, sandwich structures

TABLE OF CONTENT

Page

INTRODUCTION 1
Background 1
Structure of the thesis...3

CHAPTER 1 LITERATURE REVIEW 5
1.1 Thermoplastic Welding...5
    1.1.1 Composites joining techniques 5
    1.1.2 Thermoplastic welding methods 7
    1.1.3 Thermoplastic welding theory 10
        1.1.3.1 Degree of intimate contact 11
        1.1.3.2 Degree of healing 16
    1.1.4 Coupled model 19
    1.1.5 Amorphous bonding – Thermabond process 21
1.2 Induction Welding 23
    1.2.1 Induction welding process parameters 23
1.3 Susceptors 26
    1.3.1 Electrically-conductive susceptors – Eddy currents 26
        1.3.1.1 Heat dissipation mechanism 26
        1.3.1.2 Skin effect 27
        1.3.1.3 Edge effects... 28
        1.3.1.4 Eddy currents induction welding susceptors......................... 30
    1.3.2 Susceptor-less induction welding 31
    1.3.3 Magnetic susceptors – Hysteresis losses... 33
        1.3.3.1 Magnetic hysteresis in multi-domain materials 34
        1.3.3.2 Minor hysteresis loop.. 38
        1.3.3.3 Heat dissipation equation 39
        1.3.3.4 Curie Temperature 41
        1.3.3.5 Hysteresis losses susceptors.. 42
1.4 Composite sandwich structures..44
    1.4.1 Geometries and materials.. 44
    1.4.2 Skin-to-core joining 46
    1.4.3 Thermoplastic sandwich structures.. 48
    1.4.4 Skin/core welding 51
    1.4.5 Skin/core strength characterization methods 52

CHAPTER 2 RESEARCH OBJECTIVES 55
2.1 Current gaps in the literature...55
2.2 Objectives 56
2.3 Content of chapters 3 to 7 57

CHAPTER 3 MATERIAL SELECTION METHODOLOGY FOR AN INDUCTION WELDING MAGNETIC SUSCEPTOR BASED ON HYSTERSIS LOSSES 59
3.1 Abstract 59
3.2 Introduction 60
3.3 Methodology for susceptor materials selection and heating rate prediction 62
  3.3.1 Heating rate equation 62
  3.3.2 Magnetic field generation 63
  3.3.3 Thermoplastic matrix 64
  3.3.4 Ferromagnetic particles 64
  3.3.5 Curie temperature 66
  3.3.6 Methodology summary 67
3.4 Case Study 67
  3.4.1 Heating rate prediction 68
    3.4.1.1 Induction heating equipment 68
    3.4.1.2 Materials 69
    3.4.1.3 Hysteresis curves 71
    3.4.1.4 Predicted heating rate 73
  3.4.2 Experimental validation 74
    3.4.2.1 Samples preparation 74
    3.4.2.2 Experimentally measured heating rates 76
  3.4.3 Discussion 79
3.5 Conclusion 80
3.6 Acknowledgements 81

CHAPTER 4 DEVELOPMENT OF A PEI/NI SUSCEPTOR 83
4.1 Context 83
4.2 Methodology 84
4.3 Results 87

CHAPTER 5 MANUFACTURING OF THERMOPLASTIC COMPOSITE SANDWICH PANELS USING INDUCTION WELDING UNDER VACUUM 93
5.1 Abstract 93
5.2 Introduction 94
  5.2.1 Sandwich structures 94
  5.2.2 Skin-core assembly by thermoplastic welding 96
5.3 Theoretical background 97
  5.3.1 Thermoplastic welding 97
  5.3.2 Induction welding 98
  5.3.3 Dual-polymer bonding on sandwich skins 99
  5.3.4 Vacuum induction welding technique 100
5.4 Materials and Methodology 101
  5.4.1 Parts preparation 101
  5.4.2 Induction welding setup 102

5.4.3 Optical microscopy ... 105
5.4.4 Mechanical testing ... 105
5.5 Results and Discussion ... 107
5.5.1 Optical microscopy ... 107
5.5.2 Skin-core interfacial strength ... 110
5.5.3 Effective skin-core strength ... 113
5.6 Conclusion ... 115
5.7 Acknowledgements ... 116

CHAPTER 6 DEVELOPMENT OF A 3D-PRINTING MAGNETIC SUSCEPTOR FILAMENT ... 117
6.1 Context ... 117
6.2 Preliminary study on the susceptor filaments production ... 117
6.3 Methodology ... 120
6.4 Results ... 124
6.4.1 Susceptor filament characterization ... 124
6.4.2 Printed susceptor characterization ... 129
6.4.3 Susceptor deposition on honeycomb cores ... 134
6.4.4 Induction welding of honeycomb cores with printed susceptor ... 136

CHAPTER 7 CF/PEEK SKINS ASSEMBLY BY INDUCTION WELDING FOR THERMOPLASTIC COMPOSITE SANDWICH PANELS ... 143
7.1 Abstract ... 143
7.2 Introduction ... 143
7.2.1 Induction welding ... 144
7.2.2 Modelling of laminate heating by induction ... 145
7.2.3 Sandwich structures ... 148
7.3 Methodology ... 150
7.3.1 Samples manufacturing ... 150
7.3.2 Static induction heating ... 152
7.3.3 Induction heating finite element model ... 154
7.3.4 Continuous induction welding setup ... 157
7.3.5 Sandwich structures characterization ... 158
7.4 Results ... 159
7.4.1 Experiment-derived electrical conductivity ... 159
7.4.2 Current amplitude influence on induction heating ... 160
7.4.3 Impact of the sample width on the temperature profile ... 163
7.4.4 Optical microscopy on welded sandwich structures ... 167
7.4.5 Skin-core strength ... 169
7.5 Conclusion ... 172
7.6 Acknowledgements ... 172

CONCLUSION ... 175
Synthesis of the results ... 175
Original contributions ... 178

RECOMMANDATIONS 181

ANNEX I SUPPORTING INFORMATION – MATERIAL SELECTION METHODOLOGY FOR AN INDUCTION WELDING MAGNETIC SUSCEPTOR BASED ON HYSTERSIS LOSSES 185

ANNEX II HYSTERESIS LOSSES MAGNETIC SUSCEPTOR HEATING RATE CHARACTERIZATION 187

ANNEX III POLISHING PROCEDURE..207

ANNEX IV FWT SAMPLES PREPARATION 213

REFERENCES 217

LIST OF TABLES

Page

Table 3.1 Susceptor material selection methodology summary 67

Table 3.2 PP and PEEK specific heat capacity, melting point and recrystallisation temperature, as measured by DSC 70

Table 3.3 Magnetic particles suppliers, mean diameters and densities (from materials technical data sheets), and specific heat capacities and Curie temperatures (from literature) 71

Table 3.4 Predicted initial heating rates for PP- and PEEK-based susceptors, mixed with Fe, Ni and Fe_3O_4 particles, at 5%vol and 10%vol under a 32 kA m^{-1} magnetic field amplitude and a frequency of 269 kHz 74

Table 3.5 Predicted and measured initial heating rate for PP- and PEEK-based susceptors, mixed with Fe, Ni, and Fe_3O_4 particles, at 5%vol and 10%vol under a 32 kA m^{-1} magnetic field amplitude and a frequency of 269 kHz 77

Table 4.1 PEI/Ni susceptor samples density at 10%vol and 20%vol. Standard deviation based on the eight measurements is reported. Theoretical value of the density at each concentration is presented for comparison 91

Table 6.1 Summary of the welding of honeycomb cores incorporating a printed susceptor layer 137

Table 7.1 Electrical conductivity values for carbon fibres and laminates from the literature 147

Table 7.2 Materials properties used in the COMSOL Multiphysics induction heating simulations 157

LIST OF FIGURES

Page

Figure 1.1 Summary of the main techniques for joining thermoplastic composites 6

Figure 1.2 Fusion bonding techniques summary..8

Figure 1.3 Scheme of the various steps occurring at the welding interface during a fusion bonding process 11

Figure 1.4 Surface asperities representation based on Mantell and Springer model ..12

Figure 1.5 LSS results for resistance welding coupons with varying consolidation pressure. Optimal point is located between 0.4 and 0.8 MPa in this study..15

Figure 1.6 Disengagement of a chain from its initial tube-like region (dotted line). The minor chain spherical envelope is increasing with time.....................17

Figure 1.7 Joining interface before mobility started and after reptation time 17

Figure 1.8 Picture (top) and scheme (bottom) of the experimental TACOMA setup, developed by Avenet et al. to weld composites samples with controlled temperature and pressure 19

Figure 1.9 Schematic of the coupled model, showing the deformation of the rectangles with the evolution of the degree of healing on the surfaces that have reached a complete degree of intimate contact...........................21

Figure 1.10 PEEK and PEI modulus evolution with temperature. The highlighted process window of the “Thermabond” process is located between 260 and 315°C..23

Figure 1.11 Schematic representation of heat dissipation in induction welding: (a) eddy currents induced in an electrically-conductive susceptor, (b) eddy currents induced directly in an electrically-conductive adherend, and (c) heat dissipated by hysteresis losses in a magnetic susceptor.....................25

Figure 1.12 Scheme of the penetration depth with varying parameters.......................28

Figure 1.13 Induced edge effects caused by a pancake coil in an electrically-conductive material (top), and resulting temperature profile in the part (bottom)...29

Figure 1.14 Idealized loop at a [0,90] interface in a laminate. Current is induced in presence of a time-varying magnetic field B oriented perpendicularly to the fibre's plane 31

Figure 1.15 Heating mechanisms: (a) Fibre heating by Joule effect, (b) dielectric hysteresis and (c) contact resistance 32

Figure 1.16 Schematic of the typical M-H hysteresis loop of a ferromagnetic material. The initial magnetization curve corresponds to the magnetization of a material initially in an unmagnetized state 36

Figure 1.17 Scheme of a B-H hysteresis loop of a ferromagnetic material. When the applied field amplitude is smaller than saturation, the magnetization is interrupted (at point a) and a minor hysteresis loop is formed. The minor loop is enclosed in the major loop 39

Figure 1.18 Spontaneous magnetization of nickel. The Curie temperature of nickel is 628K, marked as Tc 42

Figure 1.19 Main sandwich structures core geometries. (a) corrugated (b) foam (c) honeycomb 45

Figure 1.20 Scheme of the sandwich skins to core assembly using adhesive film 47

Figure 1.21 Summary of the different assembly techniques for thermoplastic sandwich structures 50

Figure 1.22 Scheme of the skin-to-core fusion bonding process proposed by Grünewald et al. The intermediate steps of heating up the skin in the oven and quickly transferring them to the compression mould are not shown here 51

Figure 1.23 Flatwise tensile testing setup after DIN53292 52

Figure 1.24 DCB testing setup. The stiffening plates are visible along the two skins 53

Figure 1.25 Climbing drum testing method scheme. Nettles proposed an alternative clamping method (on the right side) to avoid the extreme bending of the skin that could break under those conditions 54

Figure 3.1 Schematic representation of heat dissipation in induction welding. (a) eddy currents induced directly in an electrically-conductive adherend. (b) eddy currents induced in an electrically-conductive susceptor. (c) heat dissipated by hysteresis losses in a magnetic susceptor 61

Figure 3.2 Hysteresis curve of a ferromagnetic material (magnetic induction B as a function of applied field H). The enclosed surface area (in grey) corresponds to the absorbed energy density E_h..65

Figure 3.3 Magnetic field density simulation around a hairpin water-cooled copper coil equipped with a Ferrotron 559H field concentrator, with a 700 A current at 269 kHz. (a) Field amplitude in a profile perpendicular to the coil axis. Black arrow corresponds to the sample location, 5 mm away from the coil. The color code scales from light blue (<2kA/m) to purple (>40kA/m) with increments of 2kA/m. (b) Field amplitude along the black arrow. Center of the coil is located at 30 mm on the x-axis............69

Figure 3.4 Heating and cooling DSC curves for PP (solid line) and PEEK (dashed line). The bottom peaks correspond to the melting of the polymer and the top peaks to the recrystallisation. The melting and recrystallisation temperatures are shown next to each peak...70

Figure 3.5 Absorbed energy density versus the applied field amplitude for Fe, Ni and Fe_3O_4 particles..72

Figure 3.6 Hysteresis curves (B versus μ_0H) of Fe, Ni and Fe_3O_4 particles. The applied field amplitude H_m is 32 kA m^{-1} ($\mu_0H_m = 0.04$ T).........................73

Figure 3.7 Typical induction heating curve (PP/Ni-5% specimen). The straight-line slope represents the initial heating rate, and the dashed line corresponds to the thermoplastic melting point. The flattening of the curve when approaching the melting temperature is due to the endothermic phase change. Induction heating is turned off after 60 seconds (dotted line) 75

Figure 3.8 Induction heating setup scheme 76

Figure 3.9 Induction heating of PP-based susceptors (applied magnetic field amplitude of 0.04 T, frequency of 269 kHz). Induction was turned off when reaching 250 °C to avoid sample degradation. Dashed lines correspond to particles concentration of 5%vol and solid lines to 10%vol 78

Figure 3.10 Induction heating of PEEK-based susceptors (applied magnetic field amplitude of 0.04 T, frequency of 269 kHz). Only the PEEK/Fe_3O_4-10%vol sample reached the melting point (solid green curve), for which induction was turned off after 45 seconds. Dashed lines correspond to particles concentration of 5%vol and solid lines to 10%vol.....................79

Figure 4.1 Picture (left) and schematic (right) of the induction heating characterization setup. The sample is supported by a Kapton film held by two supports, which allows to tune the coupling distance. The red point is the location where the temperature evolution is recorded by a thermal camera located above the sample 86

Figure 4.2 PEI/Ni susceptor films observed by optical microscopy with volume fraction of 10% of Ni particles. The grey area corresponds to the PEI matrix, and the white spots are the Ni particles. White scalebar is 300 microns..87

Figure 4.3 PEI/Ni susceptor films observed by optical microscopy with volume fraction of 15% of Ni particles. The grey area corresponds to the PEI matrix, and the white spots are the Ni particles. White scalebar is 300 microns..87

Figure 4.4 PEI/Ni susceptor films observed by optical microscopy with volume fraction of 20% of Ni particles. The grey area corresponds to the PEI matrix, and the white spots are the Ni particles. White scalebar is 300 microns..88

Figure 4.5 Experimental density of PEI/Ni-10%vol susceptor samples compared to the theoretical density obtained by the rule of mixture.............................89

Figure 4.6 Experimental density of PEI/Ni-15%vol susceptor samples compared to the theoretical density obtained by the rule of mixture.............................89

Figure 4.7 Experimental density of PEI/Ni-20%vol susceptor samples compared to the theoretical density obtained by the rule of mixture.............................90

Figure 4.8 PEI/Ni samples induction heating results. Enclosed scheme of the induction heating setup, with the red dot representing the position of the temperature measurement 92

Figure 5.1 Heating mechanisms in induction welding: (a) Susceptor-less welding, (b) electrically-conductive susceptor, (c) hysteresis-losses susceptor (adapted from (Martin et al., 2022)) 99

Figure 5.2 (a) Schematic of the honeycomb core with the single hexagonal cell dimensions and (b) the general sample dimensions................................101

Figure 5.3 (a) Schematic and (b) picture of the Vac-IW setup. The black horizontal arrow on the schematic represents the relative movement between the coil and the sample. The speed of the coil displacement corresponds to the welding speed..104

Figure 5.4 Schematic of the cutting pattern to extract four optical microscopy samples from a welded sandwich panel...105

Figure 5.5 (a) FWT testing jig installed on the tensile test machine, with a sample mounted to be tested and (b) schematic of the FWT test........................106

Figure 5.6 Cross section profile of a sandwich structure welded at 0.3 mm/s. Left side of the sample corresponds to the outer wall of the sandwich structure (black arrow). Visible deformation is seen on the top skin (solid white arrow). Top of honeycomb cell walls is deformed (dashed white arrows) 107

Figure 5.7 Welding profile on top of a core cell wall for a sandwich panel welded at (a) 0.5 mm/s, (b) 0.7 mm/s and (c) 0.9 mm/s. Dashed black lines correspond to the contact width. White vertical lines correspond to the susceptor thickness. The deformation of the top of the honeycomb cell walls is highlighted by the black arrows, The white scalebar represents 0.7 mm in the three pictures...109

Figure 5.8 Susceptor contact width and thickness after welding at different welding speeds 109

Figure 5.9 FWT skin-core strength of welded sandwich samples as a function of the welding speed. Three valid measurements were obtained at each speed. One supplementary sample welded at 0.5 mm/s that broke in the bonding adhesive used to bond the sample to the steel blocks. This value is reported and marked with an arrow pointing up........................111

Figure 5.10 Fractured FWT sandwich samples welded at (a) 0.5 mm/s, (b) 0.7 mm/s, (c) 0.9 mm/s)...112

Figure 5.11 Effective contact surface area of a honeycomb core as a function of the cell wall thickness. The two dashed lines highlight the original 0.8 mm and the 2.4 mm wall thicknesses...114

Figure 5.12 Effective skin-core interfacial strength as a function of the welding speed. Three valid measurements were obtained at each speed. One supplementary sample welded at 0.5 mm/s that broke in the bonding adhesive used to bond the sample to the steel blocks. This value is reported and marked with an arrow pointing up. The dominant failure mode is indicated 115

Figure 6.1 Scheme of the extrusion of PEI and Ni, resulting in a PEI/Ni 3D-printing filament. This corresponds to the one-step process where compounding and shaping of the filament occur simultaneously...........118

Figure 6.2 Picture of the micro-extruder used in the preliminary study. It can be used in (a) cycle mode or (b) flush mode. The green arrows indicate the path of the material in the extruder in both modes 119

Figure 6.3 Cross-section optical microscopy images of susceptor filament produced by Baptiste Renault during his Master's project using a micro-extruder 120

Figure 6.4 Leistritz extruder screws profile, extruding material from right to left. Mixing sections are highlighted in blue and transport sections in black. The initial transport section located below the main feeding point is highlighted in yellow 122

Figure 6.5 Honeycomb core (in blue) including susceptor layer (in green) printing configurations: (a) constant susceptor width and (b) variable susceptor width. For both (a) and (b), an enclosed picture shows the detailed geometry of the susceptor layer. A priming pillar is produced prior to honeycomb printing 124

Figure 6.6 Optical microscopy images of PEI/Ni-10%vol filament cross-sections. The diameter of each filament is reported on the figure 126

Figure 6.7 VSM results for (a) Ni particles and (b) PEI/Ni-10%vol susceptor at 25°C. Enclosed is zoom-in on the center of the magnetic hysteresis curves highlighted by the dashed black rectangle 127

Figure 6.8 VSM results for Ni particles and PEI/Ni-10%vol susceptor at room temperature, with magnetization reported (a) per unit of mass of the sample and (b) per unit of mass of Ni, assuming 10%vol of particles in the susceptor 128

Figure 6.9 Absorbed energy density of PEI/Ni-10%vol susceptor samples and Ni particles at different field amplitudes and temperatures, presented as a function of (a) the applied field amplitude, and (b) the temperature. Hysteresis curves of the PEI/Ni-10%vol susceptor samples tested at various temperatures under a field amplitude of 32 kA/m are presented in (c) 129

Figure 6.10 Optical microscopy images of printed susceptor films (a) in cross-section view and (b) in in-plane view 130

Figure 6.11 Comparison of cross-section views of 3D-printed (a) PEI/Ni-10%vol susceptor and (b) commercial CF/PEI composite. Binary pictures used for image analysis representing the porosities in (c) PEI/Ni-10%vol printed susceptor and (d) commercial CF/PEI printed composite 131

Figure 6.12 Induction heating curves of pressed and printed susceptor samples. Enclosed is a scheme of the induction heating setup, with the red point indicating where the temperature evolution is recorded by the thermal camera 132

Figure 6.13 Maximum temperature reached by pressed and printed susceptor samples during induction heating tests (a) as a function of the sample's density, and (b) as a function of the sample's weight.............................133

Figure 6.14 Pictures of the susceptor layer printed on top of the honeycomb wall (a) with constant susceptor width and (b) with variable susceptor width. Close-up view of (a) and (b) in (c) and (d), respectively........................134

Figure 6.15 Optical microscopy images of printed susceptor layer with (a) constant susceptor width and (b) variable susceptor width. Pictures in (c) and (d) overlays the expected print geometry in dashed white lines on the pictures (a) and (b). Picture (e) in a close-up view of the interface between the PEI honeycomb and the PEI/Ni susceptor layer.................136

Figure 6.16 Welding profile of printed susceptor layers with (a) constant susceptor width and (b) variable susceptor width. The white scalebar represents 1 mm in each picture..138

Figure 6.17 Skin/core strength versus welding speed, obtained by FWT tests on sandwich samples welded with printed susceptor layer. The solid black diamond represents the sample that failed in the core 139

Figure 6.18 Fractured FWT samples welded with (a) and (b) constant susceptor width and welding speed of 0.1 and 0.15 mm/s, respectively (no welding was obtained at 0.2 mm/s), and (c), (d) and (e) variable susceptor width welding speed of 0.1, 0.15 and 0.2 mm/s, respectively .140

Figure 7.1 Scheme of eddy currents distribution in an electrically-conductive material (a) without and (b) with edge effects due to induced eddy current loops concentration..145

Figure 7.2 Scheme of a sandwich sample, with close-up view on (a) the composite facesheet made of CF/PEEK laminate with a co-consolidated PEI layer, and (b) the 3D-printed PEI honeycomb core cells dimensions...............152

Figure 7.3 Scheme of the static induction heating setup. (a) General view of the setup, with the thermal camera located above the sample to record temperature evolution. (b) Side view showing the induction coil profile. The distance between the sample and the coil is defined as the coupling distance. (c) Top view of the setup as seen by the thermal camera, with the three lines of interest highlighted in green (center profile), red and blue (center and 5 mm width profiles)..153

Figure 7.4 3D geometry of the static induction heating setup model in COMSOL Multiphysics..155

Figure 7.5 Induction heating of a 10 cm by 5 cm laminate under a 50 A current amplitude. The measured temperature along the center profile of the sample is reported every 10 seconds for 90 seconds and compared to the model's results 160

Figure 7.6 Induction heating of 10 cm by 5 cm laminates under varying current amplitudes. The measured temperature along the center profile of the sample is reported every 10 seconds for 90 seconds 161

Figure 7.7 Pictures of samples heated by induction under a current of (a) 75 A and (b) 100 A after 90 s. The green line highlights the location of the temperature profile reported in Figure 7.6. The areas where the CF/PEEK laminate deconsolidated are clearly visible 162

Figure 7.8 Induction heating of 10 cm x 5 cm laminates under varying current amplitudes. The temperature distribution along the center profile line is reported. Only the temperature after 90 s is shown for clarity. Experimental measurements (dashed lines) are compared to simulations (solid lines)...163

Figure 7.9 Temperature distribution on the CF/PEEK samples surface under a 50 A current for varying samples widths. Experimental results as recorded by the thermal camera are compared to simulations. Edge effects are highlighted by the blue circles. The induction coil is located behind the samples and is orientated vertically 164

Figure 7.10 Induction heating of laminates under 50 A current amplitude for varying sample widths. The temperature distribution along the center profile is reported. Only the temperature after 90 seconds is shown for clarity. Experimental measurements (dashed lines) are compared to simulations (solid lines) 165

Figure 7.11 Induction heating of laminates under 50 A current amplitude for varying sample widths. The temperature distribution along both width profiles is reported. Only the temperature after 90 seconds is shown for clarity. Experimental measurements (dashed lines) are compared to simulations (solid lines) 166

Figure 7.12 Optical microscopy images for sandwich samples welded by induction. The welding profile is shown for samples with varying skin width: (a) 5 cm, (b) 6.25 cm, (c) 7.5 cm and (d) 10 cm. The cell walls that faced overheated and crushing are highlighted by the dashed red circles.........168

Figure 7.13 Skin-core FWT strength of induction welded sandwich structures as a function of the welding speed. Each point represents one measurement.

Dashed/dotted trend lines are guides to identify more clearly each dataset. Core failure is indicated by filled black data points 171

Figure 7.14 Fractured induction welded sandwich samples. The samples were welded using a skin’s width of (a) 5 cm, (b) 6.25 cm, (c) 7.5 cm, (d) 10 cm...171

LIST OF ABREVIATIONS

ASTM	American Society for Testing and Materials
CD	Climbing drum
CF	Carbon fibre
CFRP	Carbon fibre reinforced polymer
CREPEC	Centre de Recherche sur les Polymères et Composites
CSA	Canadian Space Agency
CTE	Coefficient of thermal expansion
DCB	Double cantilever beam
DIN	Deutches Institut für Normung
DSC	Differential Scanning Calorimetry
ETS	École de technologie supérieure
FWT	Flatwise tensile
GF	Glass fibre
GFRP	Glass fibre reinforced polymer
HDPE	High density polyethylene
JAXA	Japan Aerospace Exploration Agency
LEAP	Lunar Exploration Accelerator Program
MFC	Magnetic flux concentrator
NASA	National Aeronautics and Space Administration
NSERC	Natural Sciences and Engineering Research Council of Canada
PEEK	Poly-ether-ether-ketone
PEEKbot	Lunar rover project name

PEI	Poly-ether-imide
PEKK	Poly-ether-ketone-ketone
PP	Polypropylene
PPS	Poly-phenylene sulfide
PRIMA	Pôle de recherche et d'innovation en matériaux avancés
PSU	Poly-sulfone
RISE	Research Institutes of Sweden
TACOMA	Thermo-Adhesion by Conductive heating of composite Materials (test bench)
TDS	Technical datasheet
TPU	Thermoplastic polyurethane
Vac-IW	Vacuum Induction Welding

LIST OF SYMBOLS

Symbol	**Definition [unit]**
D_{ic}	Degree of intimate contact [-]
D_h	Degree of healing [-]
D_b	Degree of bonding [-]
D_{ic0}	Initial degree of intimate contact [-]
a_0	Initial rectangular asperities height [m]
b_0	Initial rectangular asperities width [m]
w_0	Initial distance between two rectangular asperities [m]
μ_{mf}	Matrix-fibre viscosity [Pa·s]
P	Pressure [Pa]
a*	Surface roughness geometric coefficient [-]
f	Frequency [Hz]
T_g	Glass transition temperature [°C]
T_m	Melting temperature [°C]
T_c	Curie temperature [°C]
t_r	Reptation time [s]
σ	Strength [Pa]
σ_∞	Ultimate strength [Pa]
B	Magnetic induction [T]
H	Magnetic field [A/m]
M	Magnetization [A/m]
μ_0	Magnetic permeability of vacuum [H/m]

μ_r	Relative magnetic permeability [-]
σ_{el}	Electrical conductivity [S/m]
ρ_{el}	Electrical resistivity [Ωm]
H_c	Coercivity [A/m]
H_s	Saturation magnetic field [A/m]
H_m	Applied magnetic field [A/m]
M_r	Remanent magnetization [A/m]
M_s	Saturation magnetization [A/m]
E_h	Absorbed energy density [J/m^3]
ρ	Density [kg/m^3]
c_p	Specific heat capacity [J/kg·°C]
v_f	Volume fraction [-]
σ_0	Electical conductivity in the direction of fibres [S/m]
σ_f	Fibre electrical conductivity [S/m]
σ_m	Matrix electrical conductivity [S/m]
f_x	Volume fraction of fibres in x-direction [-]

INTRODUCTION

Background

With the Artemis program, humanity is set to get back on the surface of the Moon. The Canadian Space Agency (CSA) is participating in an international collaboration with the National Aeronautics and Space Administration (NASA), the European Space Agency (ESA) and the Japan Aerospace Exploration Agency (JAXA) to plan and prepare the program, which includes the establishment of the first space station in orbit around the Moon (Lunar Gateway) and a ground base on the surface of Earth's satellite. Following the heritage of the collaboration with NASA, CSA will contribute to the Lunar Gateway with the Canadarm-3, the new generation of the robotic arm previously used on the Space Shuttles and on the International Space Station (ISS) (Canadian Space Agency, 2020).

In parallel, CSA has launched the Lunar Exploration Accelerator Program (LEAP), aiming to position the Canadian space sector at the forefront of the lunar science and technologies activities. One of the elements of the LEAP program is "the development, launch and operation of a Canadian rover, set to perform technology demonstration" (Canadian Space Agency, 2019). The development and construction of the 30 kg-rover have been attributed to the Canadian company Canadensys, with the objective to send it to the south pole of the Moon in 2026-2027. The principal scientific missions of the rover will be to search the Moon's surface for the presence of ice and to better understand the geology of the Moon. From a technological point of view, the major objective of the mission will be to demonstrate the rover's ability to survive the long and cold Lunar night.

As it can be observed from Earth, the Moon experiences a 28-day cycle during which the surface is facing the Sun for 14 days and then stays in the shade for another 14 days. During the Lunar day, the temperature at the surface is around 100 °C, and the rover can collect energy from the Sun by using its solar panels (Williams et al., 2017). This is the active phase of the rover's life when it can perform its tasks. Once it goes into the shade, the temperature at the surface of the Moon drops quickly to -200 °C (Williams et al., 2017). During the Lunar night, the rover goes into sleep mode, to minimize its energy consumption. It can only count on the energy stored in its batteries to survive the cold. As of today, no Lunar rover has been able to accomplish this task, mostly because of the lack of thermal insulation in the rover's structure. When the heat generated inside the rover is conducted through the structure and lost in the environment, the temperature inside the rover drops below 0 °C. When this happens, electronic equipment gets damaged by the subzero temperature and is unable to restart when the Sun returns at the end of the Lunar night.

To tackle this challenge, the PEEKbot project was launched in 2018 with the objective of developing a rover with a structure made of high-performance thermoplastic polymers and thermoplastic composites. These materials are exhibiting lower thermal conductivity, which should allow the structures to maintain a positive internal temperature during the Lunar night. They are also lighter than their metallic counterparts, which can reduce the weight of the rover and save costs at launch or allow more mass for the scientific equipment. The project regroups three academic institutions (École de technologie supérieure, Polytechnique Montréal and Université Laval), CSA and four industrial partners (ArianeGroup, NanoXplore, Mëkanic and Dyze Design). It is divided into five major axes (PRIMA Québec, 2020):

- Development of high-performance thermoplastic composites meeting space requirements.
- Manufacturing of rover composite components via additive manufacturing and pultrusion.
- Assembly of components by induction welding
- Modelling and optimization of the structure's mechanical performance.
- Integration of the sub-systems to build a prototype of the rover.

The work presented in this thesis is part of the third axis focusing on induction welding. It will be applied to the assembly of the sandwich panels that constitute the faces of the rover's structure. The use of thermoplastic composites sandwich panels is new to the aerospace industry. The joining methods must be adapted to these materials to produce sandwich panels fulfilling the requirements of the project.

Structure of the thesis

Following this introduction, Chapter 1 presents the current state of the art related to the topic of induction welding of sandwich structures. First, the theory of thermoplastic polymers welding is reviewed, followed by the different existing methods of welding and a presentation of the Thermabond process. Then, induction welding is presented in more details, followed by a description of the different heating mechanisms and susceptor materials available for this welding method. Finally, sandwich structures are described, including the different parts and materials currently used, the skin/core joining techniques and the main mechanical tests used to characterize the assembly of these structures.

Then, Chapter 2 summarizes the main gaps and points of interest identified in the literature review, helping to define the research objectives of this thesis.

Chapter 3 to 7 present the work conducted in this project, related to the objectives defined in Chapter 2. Chapter 3 was published as a journal paper in 2022 and Chapter 5 in 2024. Chapter 7 has been submitted as a journal paper and is currently undergoing the peer-review process. In Chapter 4, Martin Figueiredo worked on the preparation of the samples and the induction heating characterization during his internship project under the supervision of Prof. Martine Dubé and the mentorship of Romain G. Martin. In Chapter 6, Baptiste Renault, during his master project under the supervision of Prof. Martine Dubé and the mentorship of Romain G. Martin, worked on a preliminary study about the comparison between the one-step and the two-steps mixing processes. The Vibrating Sample Magnetometer measurements presented in this chapter were performed at Polytechnique Montréal by Prof. David Ménard and Djamel Seddaoui. The hysteresis loops were analyzed by Prof. Christer Johansson at RISE Research Institutes of Sweden in Göteborg, Sweden.

Finally, Chapter 8 concludes the thesis by proposing a synthesis of the results and the original contributions brought by this project. Some limitations of the current methods and recommendations for future work are also suggested in this chapter.

CHAPTER 1

LITERATURE REVIEW

1.1 Thermoplastic Welding

In the last decades, the use of thermoplastic composites has increased thanks to their favorable mechanical properties (high strength-to-weight ratio, stiffness-to-weight ratio, impact resistance, fracture toughness) as well as their ease of use (unlimited shelf life, faster processing than thermoset curing, low toxicity due to the absence of solvent, limited moisture absorption, potential for recycling) (Campbell, 2004a; Pegoretti, 2021). The main drawbacks of thermoplastic polymers are their high melt viscosity, caused by their high molecular weight, and their higher required processing temperature, as the thermoplastic matrix must melt to allow for processing (Campbell, 2004a). However, a growing potential to use thermoplastic composites to replace metallic parts as well as thermoset composites is observed in various fields, including aeronautics and space (Slayton & Spinardi, 2016; Vodicka, 1996). Their use in large structures requires to develop reliable joining methods to assemble complex structures.

1.1.1 Composites joining techniques

Three main techniques are used to join composite parts, as summarized in Figure 1.1: adhesive bonding, mechanical fastening and thermoplastic welding (Ageorges & Ye, 2002; Costa et al., 2012; Yousefpour et al., 2004).

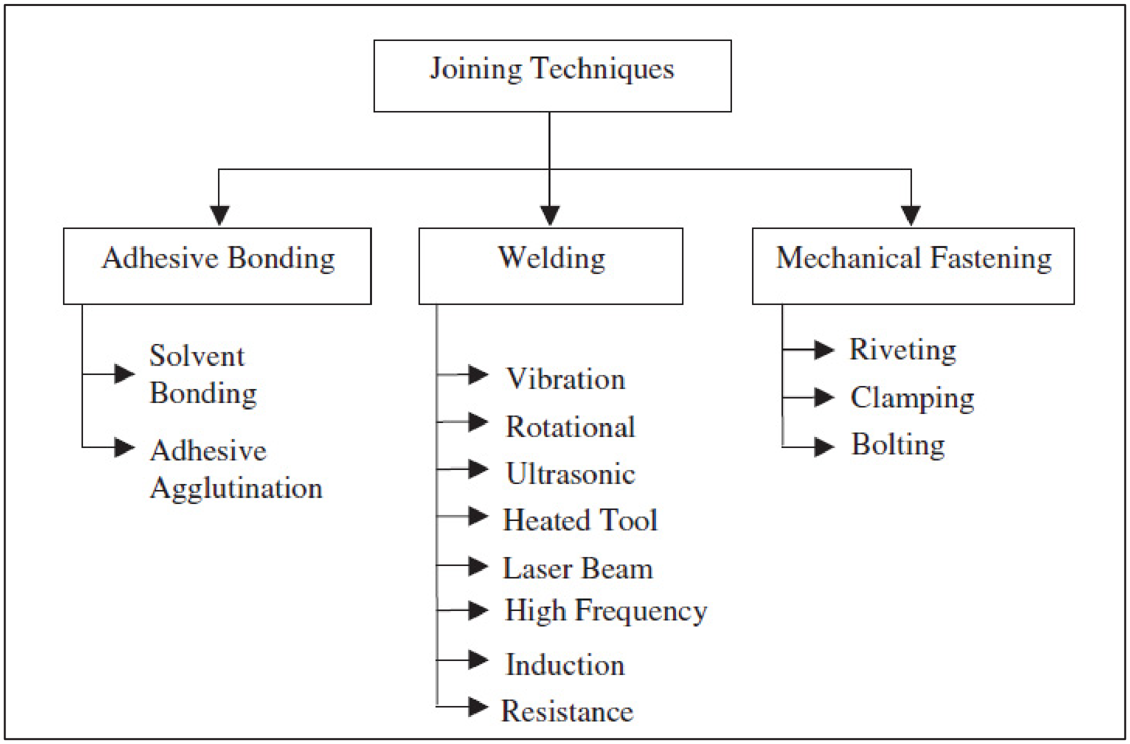

Figure 1.1 Summary of the main techniques for joining thermoplastic composites
Taken from Yousefpour et al. (2004, p. 305)

Mechanical fasteners are widely used to assemble metal components. Some fasteners like bolts can be removed without causing damage to the assembled parts, which allows for maintenance or repair to occur. On the other hand, others like rivets are permanent fasteners, so removing them can be more challenging or impossible (Troughton, 2009b). The main drawback of fasteners is the mass they are adding to the structure (which in turn increases the cost of launch when used in space applications), and the risk of galvanic corrosion caused by the metal insert (Cole, 1982). To reduce these issues, metallic fasteners are typically insulated from the rest of the structure using glass fibres. An alternative currently in development is to replace them by polymeric or composite fasteners like carbon fibres reinforced thermoplastics (Absi et al., 2022). In any case, the application of mechanical fasteners typically requires drilling holes in the parts to be assembled. These holes are undesirable in composite materials as their creation can induce delamination and cracks in the laminates (Cole, 1982). Also, these holes represent points of stress concentration, especially in the case of over-tightened bolts (Troughton, 2009b).

Adhesives are an alternative option to join composite components. The mass penalty caused using adhesives is smaller than with mechanical fasteners, and they do not require the presence of holes in the parts. However, adhesives typically create a permanent bond, which cannot be modified or removed without causing damage to the structure, making repairs and recycling of bonded structures challenging and sometimes impossible. Adhesives can be applied to both thermoset- and thermoplastic-based composites. However, thermoplastic polymers and thermoset adhesives typically exhibit low chemical compatibility, because of the low surface tension of thermoplastic polymers. Extensive surface preparation – such as plasma treatment, acid etching or grit blasting – of the thermoplastic adherend is therefore required (Campbell, 2004b; Silverman & Griese, 1989), but these processes are labour-intensive and time-consuming (Ageorges et al., 2001).

1.1.2 Thermoplastic welding methods

Thermoplastic welding offers an opportunity to efficiently join thermoplastic parts. It retains the presented advantages of adhesives (small weight penalty and the absence of drilled holes in the laminates) and mechanical fasteners (possibility of joint reopening). The working principle of thermoplastic welding is to heat up the interface to be joined, then apply pressure on the assembly to form a weld while the material cools down. There are different ways to heat up the interface to perform thermoplastic welding. Review studies (Ageorges et al., 2001; Villegas et al., 2013; Yousefpour et al., 2004) report three main methods to weld thermoplastic composites: thermal welding, in which the interface is heated using a external heat source, like autoclave assembly or laser heating in automated fibre (or tape) placement (Sonmez & Hahn, 1997); friction welding, where heat is dissipated mainly through friction caused by a relative movement of the parts to be joined, and electromagnetic welding, in which the heat is dissipated by various electromagnetic mechanisms, such as Joule heating or magnetic hysteresis heat dissipation (Figure 1.2). These techniques are complementary to each other, allowing welding of a wide range of structures, including those with complex geometries. As for other thermoplastic welding methods, they are favorable because they only heat up the welding interface to the melting temperature, reducing the heat transfer to the rest of the part and hence minimizing its impact on the integrity of the structure (Ageorges et al., 2001). There are three main welding techniques currently used in the composites industry: ultrasonic welding, resistance welding and induction welding (Villegas et al., 2013; Yousefpour et al., 2004).

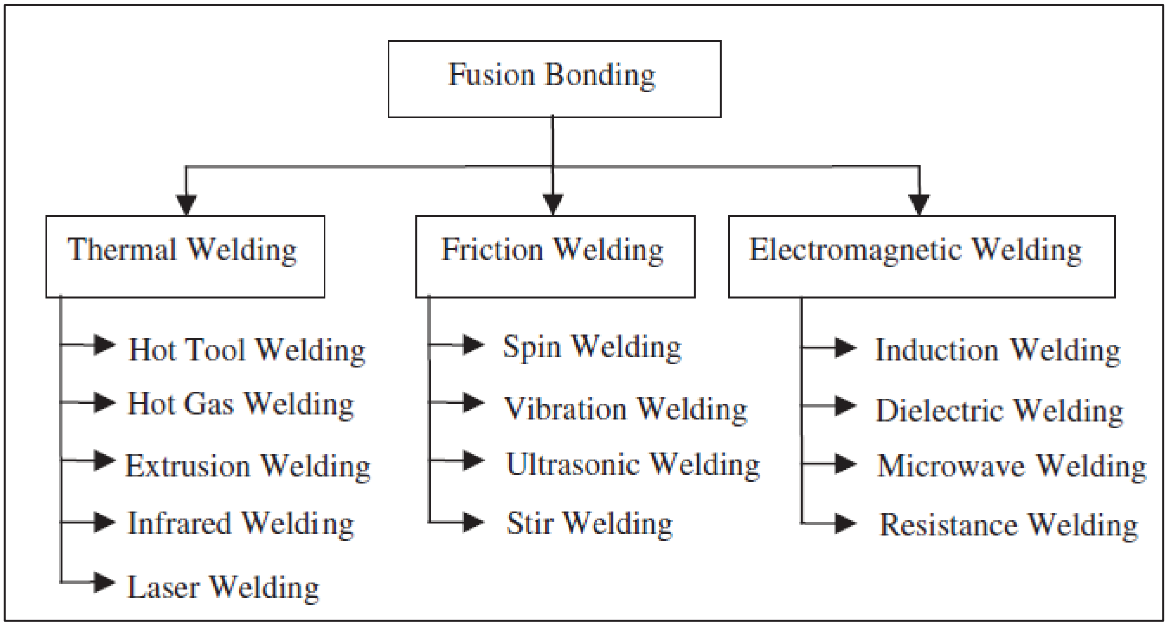

Figure 1.2 Fusion bonding techniques summary
Taken from Yousefpour et al. (2004, p. 306)

Ultrasonic welding consists in applying a low amplitude mechanical vibration at high frequency (20-40kHz) to generate heat by Coulomb friction and weld thermoplastic components (Yousefpour et al., 2004). The welding time is very fast, lasting approximately one second (Troughton, 2009a). The main difference with respect to other friction welding techniques is that the vibration direction is perpendicular to the joining interface, while in spin, stir and vibration welding, the relative movement of the parts is parallel to the interface. In ultrasonic welding, one part is fixed on the base and the other one is vibrating under a horn. To ensure efficient energy dissipation, triangular or rectangular asperities, called energy directors, are pre-moulded at the interface. They are designed to melt and flow at the interface under the applied pressure (Yousefpour et al., 2004). Recent research shows the possibility to replace these moulded energy directors by a neat thermoplastic film (Tsiangou et al., 2019). This welding technique is widely used in the plastics industry because of its high speed (a few seconds (Villegas et al., 2013)) and repeatability. In the composites industry, this method is usually used to hold plies in place before applying another process step, such as consolidation of another welding technique. However, the geometry is often limited to flat and almost flat surfaces, and the weld cannot be modified or reopen without damaging the part, inherently removing one of the key advantages of welding.

Resistance welding is classified as an electromagnetic welding technique. It consists of placing a resistive element located between the thermoplastic parts to be welded, in which current circulates thanks to copper connectors clamped at each end of the heating element. The heat is then dissipated at the interface by the Joule effect (Troughton, 2009a; Villegas et al., 2013; Yousefpour et al., 2004). The resistive element is often a metallic mesh or a carbon fibre weave. Recent development are also proposing nanocomposite heating elements (Brassard et al., 2019, 2021). This method is not restricted to flat surfaces, it is fast (around 90 s (Villegas et al., 2013)), and the welded structures can be repaired as the heating element typically remains in the weld (it must still be possible to connect it to the power source). However, the presence of the mesh can also be a source of failure in case of poor adhesion or in the presence of voids. There can also be a risk of uneven heating as the current flows unequally through different parts of the heating element (Troughton, 2009a).

The principle of induction welding relies on the application of an alternating electromagnetic field (instead of a current as in resistance welding) in which a heating element material called a susceptor reacts to the applied field (Ahmed et al., 2006; Bayerl et al., 2014; Rudolf et al., 2000). The susceptor is a material that can absorb electromagnetic energy and dissipate it into heat through various mechanisms (presented in more details in 1.3). Consequently, the surrounding thermoplastic polymer is melted, allowing for a weld to occur. Induction welding is already implemented in the aerospace industry. For example, Fokker developed in the late 2000’s fully thermoplastic composite elevators and rudders for the Gulfstream G650 (Van Ingen et al., 2010). These structures are assembled by induction welding, which relies on an electromagnetic mechanism to dissipate heat at the bonding interface; therefore, it is classified in the same category as resistance welding (Figure 1.2). Induction welding is a fast process (similar to resistance welding (Villegas et al., 2013)) than can be automated. Its main advantage is the absence of required physical contact with the parts to be welded. The induction coil, generating the applied magnetic field, must be placed in the vicinity of the welding line to properly heat up the susceptor. Induction welding process parameters are presented in more details in 1.2.

1.1.3 Thermoplastic welding theory

As presented, thermoplastic welding is performed by heating up the thermoplastic polymer matrix at the interface of the parts to be welded. As the temperature is increased and pressure is applied, a weld between the two parts can be formed. The interface eventually disappears, and the two parts are welded into one. Different mechanisms governing the weld formation are presented in this section. This theory is applicable to all the welding methods.

The general process of welding is summarized in Figure 1.3. If the parts are heated up before entering into contact, interface softening occurs first, reducing the viscosity of the polymer at the surface of the parts to be joined (Yang & Pitchumani, 2002). Then, two main mechanisms govern welding: intimate contact and interface healing (Ageorges & Ye, 2002; Butler et al., 1998). The evolution of those two parameters can be expressed as the degree of intimate contact and the degree of healing, respectively. These two mechanisms are presented in more detail in 1.1.3.1 and 1.1.3.2.

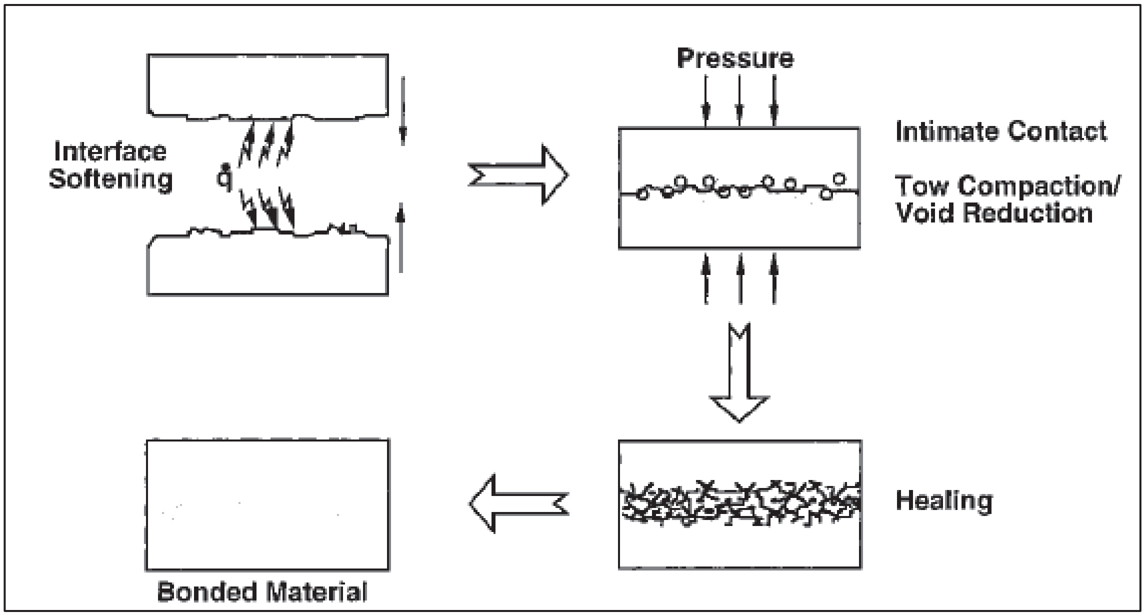

Figure 1.3 Scheme of the various steps occurring at the welding interface during a fusion bonding process
Taken from Yand and Pitchumani (2002, p. 3213)

1.1.3.1 Degree of intimate contact

The first mechanism that allows thermoplastic welding is the development of intimate contact between the parts. It corresponds to the establishment of physical contact at the interface to be welded. This is essential for the welding process, as healing can only happen on surfaces that are in intimate contact (Butler et al., 1998; Pitchumani et al., 1996). When two parts are brought together, asperities located at their interface enter in contact with each other. At that stage, only a fraction of the nominal surface is in physical contact, which is defined as the initial degree of intimate contact. Temperature and pressure are required to deform the asperities and eventually reach a 100% effective intimate contact, which can also be seen as the absence of voids between the parts. The degree of intimate contact, D_{ic}, is defined as the fraction of the total surface that is in actual physical contact. Multiple models have been developed to characterize the deformation of the asperities and the evolution D_{ic}. Dara and Loos first made the assumption that the surface can be approximated as a series of rectangles of variable dimensions, deformed at constant pressure and temperature (Dara &

Loos, 1985). Lee and Springer, followed by Mantell and Springer, simplified the surface with uniform rectangles, eventually extending the approach to account for varying pressure and temperature (W. I. Lee & Springer, 1987; Mantell & Springer, 1992). The Lee and Springer approach is the most commonly used model, in which the rough surface is represented by rectangular elements of initial height a_0 and width b_0, separated by a distance w_0, as represented in Figure 1.4 (Mantell & Springer, 1992).

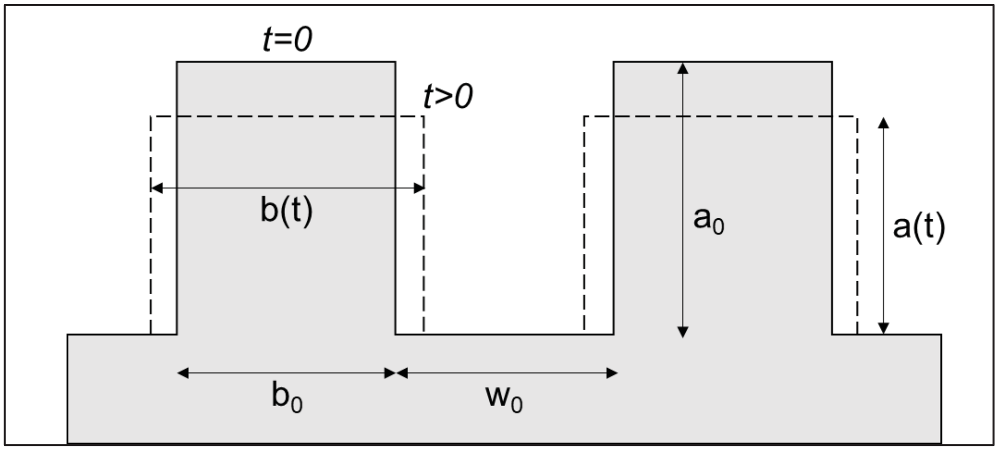

Figure 1.4 Surface asperities representation based on Mantell and Springer model

Upon application of pressure, these elements are deformed but conserve their total area (through conservation of mass), which results in an increase of their width and a reduction of their height, leading to a global increase of the intimate contact (Avenet et al., 2021; Levy et al., 2013). The evolution of the degree of intimate contact can be expressed with the following expression:

$$D_{ic} = \frac{b(t)}{b_0 + w_0} = D_{ic0}\left[1 + C_1 \int_0^{t_p} \frac{P}{\mu_{mf}} dt\right]^{\frac{1}{5}} \tag{1.1}$$

with D_{ic0} being the initial degree of intimate contact, C_1 a constant based on the initial geometry of the asperities, P the applied pressure, t_p the pressure time and μ_{mf} the fibre-matrix viscosity (Butler et al., 1998; Byron Pipes et al., 1991). The initial degree of intimate contact D_{ic0} can be expressed as:

$$D_{ic0} = \frac{b_0}{b_0 + w_0} \tag{1.2}$$

And the constant C_1, based on the representative rectangles' dimensions, is defined as:

$$C_1 = 5\left(\frac{b_0}{b_0 + w_0}\right)\left(\frac{a_0}{b_0}\right)^2 \tag{1.3}$$

Equation (1.1) can be simplified to:

$$D_{ic} = a^* \left[\int_0^{t_p} \frac{P}{\mu_{mf}} dt\right]^{\frac{1}{5}} \tag{1.4}$$

where, a^* is a single geometric factor accounting for the initial roughness of the interface. Values of 0.147 (Ageorges et al., 1998b; Colak et al., 2002) and 0.29 (Mantell et al., 1992; Sonmez & Hahn, 1997) are used in different papers for predicting the evolution of the degree of intimate contact. Like D_{ic0} and C_1, it can also be obtained experimentally, as done in the work of Grünewald et al. (Grünewald et al., 2017a). Values of a_0, b_0, and w_0 are determined to fit surface roughness measurements obtained with a stylus profiler. As the roughness depends on the material and the processing method (injection, infusion, consolidation), it varies from one case to another.

The viscosity term μ_{mf} corresponds to the fibre-matrix viscosity. It considers the impact of the presence of fibres on the local viscosity of the composite. Pipes et al. proposed models expressing μ_{mf} relative to the polymer matrix viscosity in different directions, due to the anisotropy of the composite material (Byron Pipes et al., 1991). At low fibre fraction, the fibre-matrix viscosity tends towards the polymer matrix viscosity. The fibre-matrix viscosity is also reported as an Arrhenius relationship in different papers for a given material, with a given volume fraction. For example, Mantell et al. report the fibre-matrix viscosity presented in Equation (1.5) for an APC-2/AS4 composite tape, with the temperature expressed in K (Mantell & Springer, 1992).

$$\mu_{mf} = 132.95 \cdot \exp\left(\frac{2969}{T\ [K]}\right) \tag{1.5}$$

The fibre-matrix viscosity is also experimentally calculated by Khan et al. for a CF/PEEK tape, based on the laminate thickness reduction under pressure at various temperatures. The relationship is determined to follow the Arrhenius function reported in Equation (1.6).

$$\mu_{mf} = 643 \cdot \exp\left(\frac{4367}{T\,[K]}\right) \tag{1.6}$$

Both these expressions are only valid for the material used in their respective studies, with the same volume fraction. Although it is hard to transfer them to other materials or grades of polymers, they give an order of magnitude of the fibre-matrix viscosity parameter.

As a periodic set of regular rectangles usually is not representative of a physical roughness at the surface of a composite part, other models have been developed to try to better approximate the shape of asperities. One interesting model is the fractal-based model proposed by Yang et al. (Yang & Pitchumani, 2001). This model approximates the surface as a series of rectangles of varying dimensions, with regular size decrease and repetitions like a fractal geometry. These rectangles are then compared to experimental roughness measurements, and the fractal parameters are adjusted to fit the curves. The model surface is then deformed in a similar way as for other models, with the rectangles flowing under pressure until reaching a completely flat plane. The evolution of the degree of intimate contact during these processes is expressed as (Yang & Pitchumani, 2001):

$$D_{ic}^{(n)}(t) = \frac{1}{f^n}\left[\frac{5}{4}\left(\frac{h_0}{L_0}\right)^2 \frac{f^{\frac{2nD}{2-D}+n+4}}{(f+1)^2}\int_{t_{n+1}}^{t}\frac{P_{app}}{\mu}\,dt + 1\right]^{\frac{1}{5}}, t_{n+1} \leq t \leq t_n \tag{1.7}$$

with D the fractal dimension, f the scaling ratio between two generations of asperities, h_0 the depth of the first generation of asperities, L_0 the horizontal length of the fractal block, and n the number of fractal generations.

As it appears in Equations (1.1), (1.4) and (1.7), the application of pressure is essential to increase the degree of intimate contact; it is the driving force for the deformation of the asperities. To weld thermoplastic composites, pressures ranging from 0.2 to 1.6 MPa have been reported (Ageorges et al., 1998b, 2000; V. Stokes, 2003; Xiao et al., 1994). Ageorges et al. reported an ideal pressure of 0.5 MPa for CF/PEI lap-shear coupons welded by resistance under the applied process parameters (69 kW/m^2 of power level and 90 s of welding time), as presented in Figure 1.5 (Ageorges et al., 2000). They also showed that pressure below 0.2 MPa cannot prevent laminate deconsolidation, while high pressure (from 1.6 MPa and above) causes excessive squeeze flow and fibre motion, leading to poor weld quality (Ageorges et al., 2000). Avenet et al. used pressure ranging from 0.15 to 0.5 MPa to weld CF/PEKK samples and showed that a minimum of 0.25 MPa was required to obtain a complete weld (Avenet et al., 2021). Shi et al. concluded that a pressure of at least 0.4 MPa but ideally 0.8 MPa was required to avoid deconsolidation-induced voids (Shi et al., 2017). However, they also showed that a much higher pressure (1.5 MPa) was needed to prevent the formation of residual volatile induced voids. As high pressure would create a low-quality weld as previously mentioned, it is essential to properly dry materials before processing to avoid creating porosities. Welding pressure must be applied on the joining interface also during cooldown, to avoid deconsolidation and voids formation. Beehag et al. showed that at least 0.2 MPa of cooling pressure is required to avoid deconsolidation during that phase (Beehag & Ye, 1996).

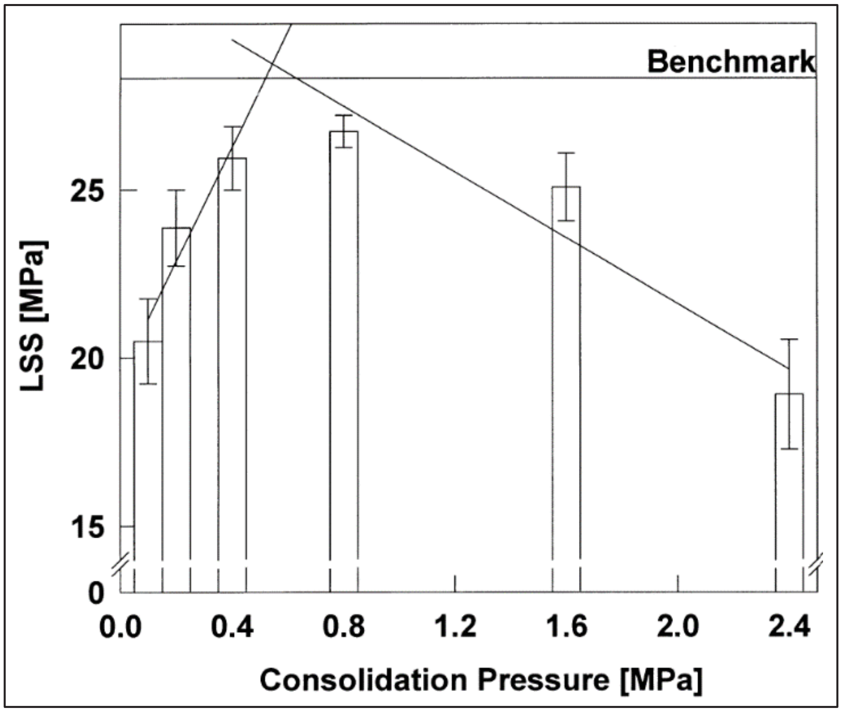

Figure 1.5 LSS results for resistance welding coupons with varying consolidation pressure. Optimal point is located between 0.4 and 0.8 MPa in this study
Taken from Ageorges et al. (2000, p. 1195)

1.1.3.2 Degree of healing

In the areas where intimate contact is established, polymer chains can move through the interface and entangle with the chains from the other side. This mechanism, referred to as healing or autohesion, provides the strength to the weld (Y. H. Kim & Wool, 1983; Wool et al., 1989; Yang & Pitchumani, 2002). At temperatures higher than the melting point T_m (for semi-crystalline thermoplastic polymers) or the glass transition temperature T_g (for amorphous polymers), the molecular chains that compose the polymer gain mobility and can slowly move from their initial position (Y. H. Kim & Wool, 1983; Wool et al., 1989). Their movement is modelled by the well-established reptation theory (de Gennes, 1971). This model assumes that at the initial time $t = 0$, the chain is contained in a tube-like region. The chains are entangled with each other, and they are unable to get out of this tubular region. When the temperature surpasses the T_m or the T_g of the polymer, these chains start to move from their initial position, starting from one or both extremities. The portion of the chain that is then out of the initial tube is called a minor chain. With time, the minor chain grows until the whole chain has eventually moved from its initial position. The minor chains can also be represented encapsulated in a circle (spherical envelope) that is increasing with time, as the minor chains grow. The growth of the minor chain as well as its respective spherical envelope are represented on Figure 1.6. The time required for the complete movement of the chain is defined as the reptation time t_R. After this time, this polymer chain has crossed the interface and is able to entangle with chains from the other side, thus forming a weld as shown in Figure 1.7.

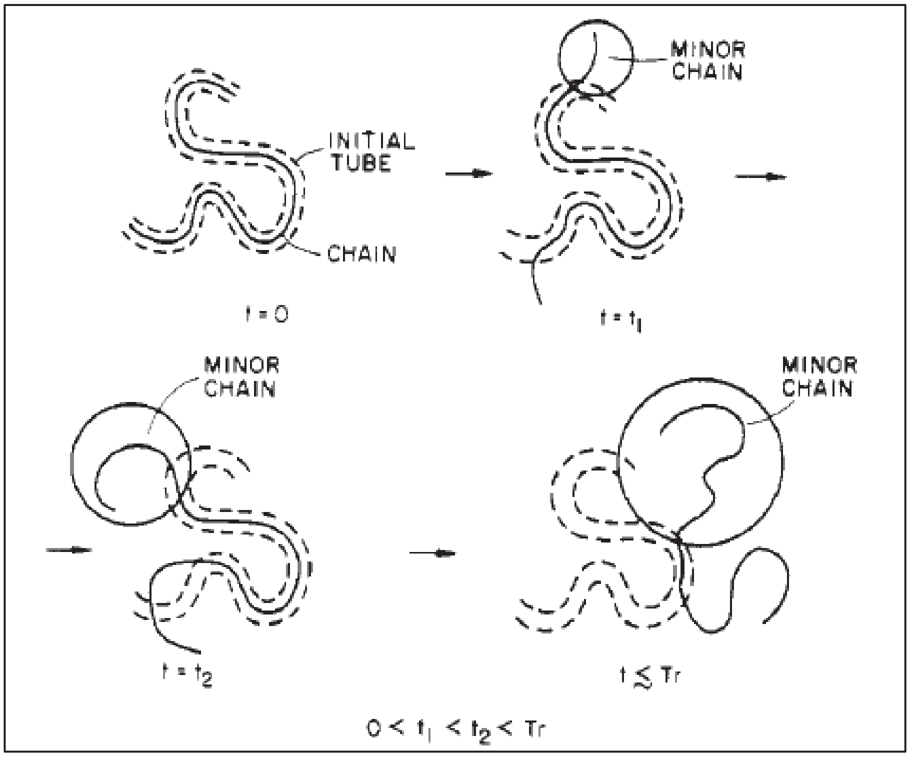

Figure 1.6 Disengagement of a chain from its initial tube-like region (dotted line). The minor chain spherical envelope is increasing with time
Taken from Kim and Wool (1983, p. 1116)

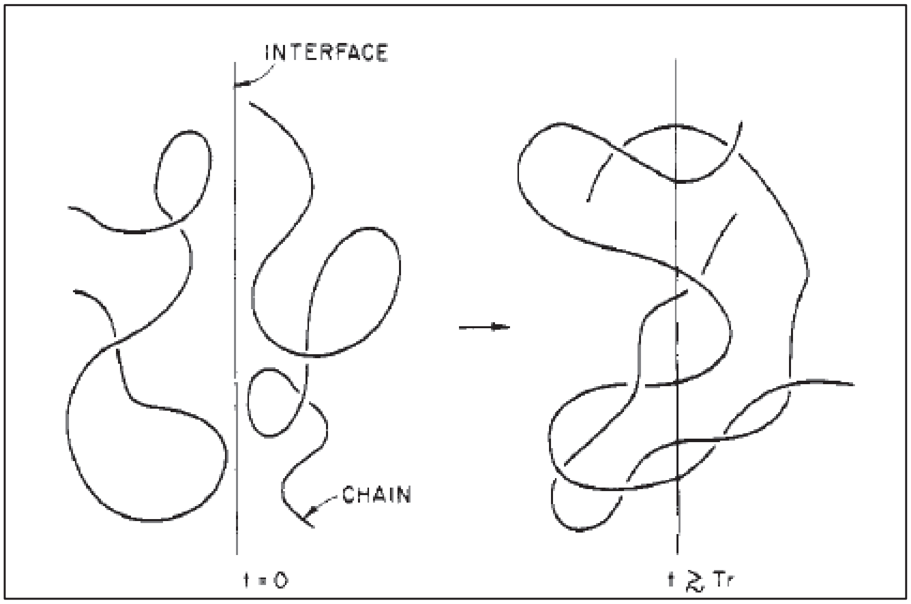

Figure 1.7 Joining interface before mobility started and after reptation time
Taken from Kim and Wool (1983, p. 1116)

The progression of the chain entanglement at the welding interface is defined as the degree of healing D_h and corresponds to the increase of strength of the interface. D_h at a given time t is expressed as a ratio between the current strength σ and the maximum strength σ_∞ corresponding to the bulk polymer strength, as shown in Equation:

$$D_h = \frac{\sigma}{\sigma_\infty} = \left(\frac{t}{t_R}\right)^{\frac{1}{4}} \tag{1.8}$$

The reptation time t_r can be expressed with an Arrhenius law (Bastien & Gillespie, 1991):

$$t_r = B_{rep} \exp\left(\frac{A_{rep}}{T}\right) \tag{1.9}$$

where A_{rep} and B_{rep} are material-dependent constants, which are usually calculated experimentally. For example, Bastien and Gillespie obtained values for PEI of -105.6 $s^{1/4}$ for $\ln(B_{rep})$ and 59 728 K^{-1} for A_{rep}. These results are based on the evolution of the lap-shear strength of samples welded in a hot press (Bastien & Gillespie, 1991). Barroeta et al. used a parallel plate rheometer to obtain experimental values of -129.8 $s^{1/4}$ for $\ln(B_{rep})$ and 77 201 K^{-1} for A_{rep} for PEI, and -105.2 $s^{1/4}$ for $\ln(B_{rep})$ and 72 597 K^{-1} for A_{rep} for PEEK (Barroeta Robles et al., 2023).

To experimentally measure the evolution of the degree of healing, a good control of the thermal history at the weld line, as well as the applied pressure, is necessary. Avenet et al. have developed a testing bench called TACOMA aiming to perform controlled welding tests (Avenet et al., 2020). This setup is equipped with heating cartridges to heat up the parts to be welded, control thermocouple and a pneumatic piston to apply the pressure, as presented in Figure 1.8. By varying the temperature, the pressure, and the processing time, they were able to measure the evolution of the degree of healing of CF/PEKK samples by performing double cantilever beam (DCB) tests on welded samples.

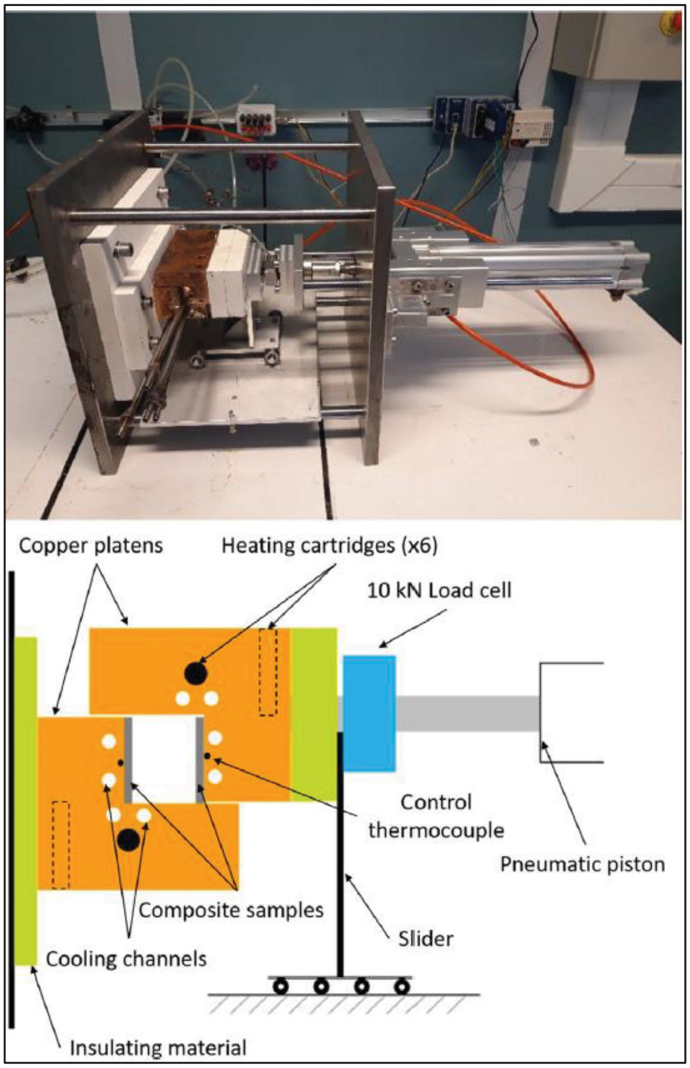

Figure 1.8 Picture (top) and scheme (bottom) of the experimental TACOMA setup, developed by Avenet et al. to weld composites samples with controlled temperature and pressure
Taken from Avenet et al. (2020, p.3)

1.1.4 Coupled model

Depending on the materials used and processing conditions, intimate contact and healing can occur at very different rates, making the development of mechanical properties limited by only one of the two mechanisms. In that case, only the rate-controlling step should be modelled to predict the evolution of properties, considering the faster step as instantaneous.

However, as pointed out by Butler et al., intimate contact and healing can occur in times on the same order of magnitude (Butler et al., 1998). While the degree of intimate contact keeps evolving, healing starts in the regions that are in contact. To correctly predict the evolution of the two mechanisms simultaneously, a coupled model is proposed (Ageorges & Ye, 2002; Butler et al., 1998; W. I. Lee & Springer, 1987). The degree of bonding D_b – or more precisely the degree of welding – can be expressed as:

$$D_b(t) = D_{ic}(t) \cdot D_h(t) \tag{1.10}$$

When the degree of welding reaches a value of 1, the weld is complete, and the maximum joint properties are reached. The weld should therefore exhibit similar mechanical properties to the bulk material.

Equation (1.11) is proposed to model the evolution of the degree of bonding using the coupled model, taking into account the evolution of both the degree of intimate contact and the degree of healing (Butler et al., 1998):

$$D_b(t) = D_{ic}(0) \cdot D_h(t) + \int_0^t D_h(t - t') \cdot \dot{D}_{ic}(t') dt' \tag{1.11}$$

With $\dot{D}_{ic}(t')$ being the rate of evolution of the local degree of intimate contact since the corresponding surface reached intimate contact, defined as:

$$\dot{D}_{ic}(t') = \left(\frac{dD_{ic}(y)}{dy} \right)_{y=t\prime} \tag{1.12}$$

This equation expresses that the healing starts on every part of the interface as soon as it reaches intimate contact. A few boundaries are added to the model, such as $D_h(t)$ and $D_{ic}(t)$ cannot be larger than 1 on any location at any time, and $D_h(t)$ and $\dot{D}_{ic}(t)$ are equal to zero when the temperature is below the transition temperature (T_g for amorphous and T_m for semi-crystalline polymers) or when no pressure is applied. An accurate visual explanation for the evolution of the coupled model proposed by Ageorges and Ye is reported in Figure 1.9 (Ageorges et al., 1998b).

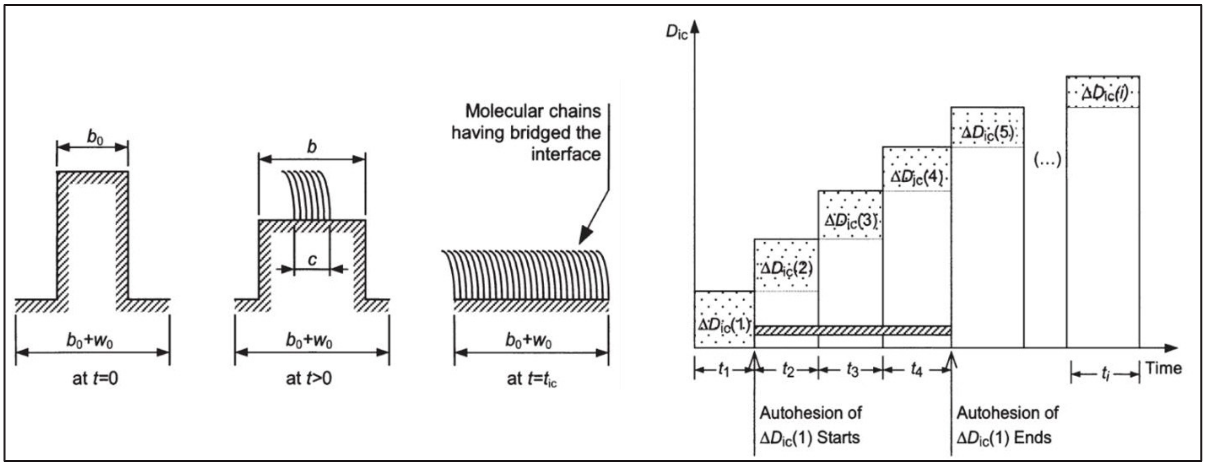

Figure 1.9 Schematic of the coupled model, showing the deformation of the rectangles with the evolution of the degree of healing on the surfaces that have reached a complete degree of intimate contact
Taken from Ageorges et al. (1998, p.912-913)

1.1.5 Amorphous bonding – Thermabond process

Welding must be conducted at temperatures higher than the melting point (or glass transition temperature) of the thermoplastic polymer to give the polymer chains move through the joining interface and create a weld when consolidated. When using fibre reinforced thermoplastic laminates, reaching this high temperature can be problematic as it may cause inter-ply deconsolidation inside of the laminate, distortion of the fibres under pressure and part dimension changes. To avoid this issue, the Thermabond process was proposed (Cogswell et al., 1989; Meakin et al., 1991; Smiley et al., 1991). An interlayer of amorphous thermoplastic, which exhibits a welding temperature lower than the melting point of the parent laminate, is attached to the composite adherend before joining. The adhesion between this interlayer and the adherend occurs during the consolidation phase of the composite part. The resulting laminate maintains the properties of the parent composite but presents an amorphous polymer-rich surface. During the welding process, welding can occur at a temperature higher than the T_g of the amorphous interlayer, but lower than the T_m of the adherend. That way, the mechanical and physical properties of the parent laminate are not compromised, as the matrix is not molten during the process. The amorphous interlayer can be heated up using thermal heating in oven, or through any other thermoplastic welding process. The Thermabond process can be used to perform patch repair on thermoplastic composites, as demonstrated by Heimerdinger et al. (Heimerdinger, 1994) In terms of recycling, the co-consolidation of the amorphous layer on the parent laminate prevents the further separation of the two materials, potentially reducing the recyclability of the structure.

Smiley et al. demonstrated this welding strategy by welding carbon fibres reinforced PEEK laminates using a PEI layer as the amorphous polymer surface layer (Smiley et al., 1991). PEEK and PEI are miscible, which is an essential criterion to create a strong bond between the surface layer and the parent composite laminate (Hsiao & Sauer, 1993). A 75 µm-thick PEI film is placed on the CF/PEEK laminate in the areas to be joined and the complete lay-up is consolidated at the required processing temperature for PEEK (around 400°C). PEI is not degraded during that process as its degradation temperature starts around 450°C (Carroccio et al., 1999). The resulting dual polymer plate is used as adherend for welding. The welding process must occur at a temperature higher than PEI's $T_{g,}$ (210°C in Figure 1.10, typically 215-217°C in commercially available PEI) but lower than PEEK's T_m (334°C in Figure 1.10, typically 343°C in commercially available PEEK). This gives a process window fixed between 260°C and 315°C, as highlighted in Figure 1.10.

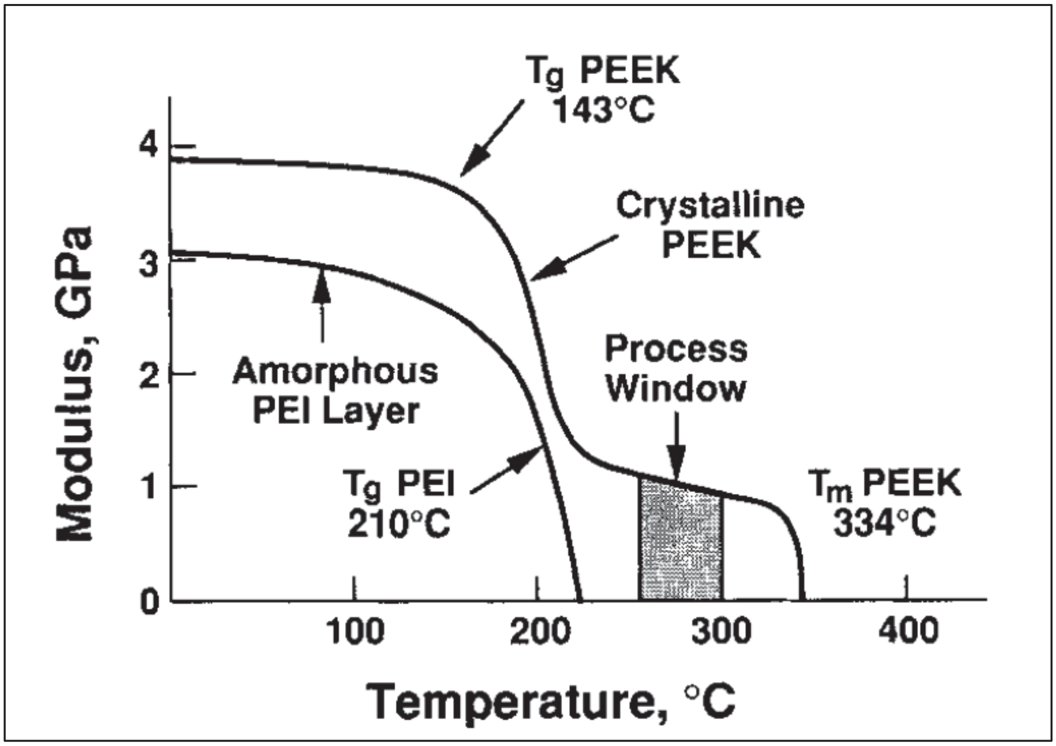

Figure 1.10 PEEK and PEI modulus evolution with temperature. The highlighted process window of the "Thermabond" process is located between 260 and 315°C
Taken from Smiley et al. (1991, p. 527)

1.2 Induction Welding

1.2.1 Induction welding process parameters

As previously introduced, induction welding relies on an alternating magnetic field to generate heat at the welding interface. The available electromagnetic energy depends on different parameters: the amplitude and frequency of the alternating current travelling through the induction coil, the geometry of the coil (shape and dimensions), and the distance between the coil and the weld line (i.e., the coupling distance). The current frequency typically varies from 200 kHz to 1000 kHz (Bayerl et al., 2014; Yousefpour et al., 2004). When higher frequencies are used, the welding method is not considered induction welding and becomes dielectric welding for frequencies in the MHz region, and microwave heating in the GHz region (Yousefpour et al., 2004). The applied current amplitude varies depending on the active heat dissipation mechanism (as presented hereafter), but is typically in the range of a few hundred amperes (Dermanaki Farahani et al., 2018; Mitschang et al., 2002; Pappadà et al., 2015; Seneviratnae et al., 2021).

The coil geometry can vary a lot, from pancake to helical shapes, from single to multiple turns coils (Bayerl et al., 2014; Sanders, 1987). This has a direct impact on the magnetic field intensity, orientation and distribution along the welding surface (Barazanchy et al., 2022; Lin et al., 1992; Rudolf et al., 2000). A homogeneous field distribution is desired to induce homogeneous heating at the welding line. It is therefore essential to adapt the coil geometry to the parts to be welded. The induction coil can be equipped with a magnetic flux (or field) concentrator (MFC) to concentrate the magnetic field amplitude on the side of the coil where welding is taking place by redirecting the field lines (Ahmed et al., 2006; O'Shaughnessey et al., 2016; Seneviratnae et al., 2021). This is useful to increase the available magnetic energy without increasing the current or the frequency of the current.

Rudolf et al. showed that the coupling distance greatly impacts heating by induction (Rudolf et al., 2000). The shorter the coupling distance, the higher the field amplitude, and therefore the higher the heating rate. They measured that the time required to reach 300°C in a part varied from a few seconds when located at 2 mm to more than a minute when located at 8 mm. The coupling distance is typically kept under 10 mm in the different papers available in the literature, depending on the other welding parameters (Bayerl et al., 2012, 2014; Dermanaki Farahani et al., 2018; Pappadà et al., 2015; Rudolf et al., 2000; Suwanwatana et al., 2006a).

The generated magnetic field can then interact with the parts to be welded and the susceptor (heating element). Two major heat dissipation mechanisms are available for induction welding:

- Eddy currents in electrically-conductive materials, which can be induced in an electrically-conductive susceptor at the interface (Figure 1.11a). This mechanism is presented in section 1.3.1. Eddy currents can also be induced directly in the adherend itself (Figure 1.11b). This is called susceptor-less welding and is described in section 1.3.2.

- Hysteresis losses in magnetic materials, which occur in the magnetic susceptor located at the joining interface (Figure 1.11c). This type of susceptor is presented in section 1.3.3.

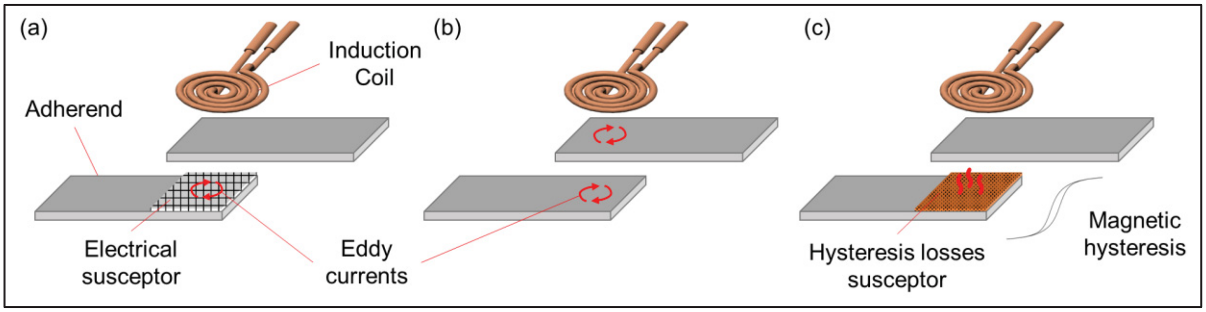

Figure 1.11 Schematic representation of heat dissipation in induction welding: (a) eddy currents induced in an electrically-conductive susceptor, (b) eddy currents induced directly in an electrically-conductive adherend, and (c) heat dissipated by hysteresis losses in a magnetic susceptor

The susceptor material, when one is used, is usually placed between two layers of – or embedded into – a thermoplastic matrix (chemically compatible with the adherends) to fill voids and ensure a more intimate contact between the surfaces to be welded (V. K. Stokes, 1989).

The main challenge during induction welding, as in other fusion bonding processes, is to sufficiently heat up the welding line to allow polymer chain migration through the joining interface and hence the weld formation, but at the same time avoid overheating the polymer, to prevent thermal degradation and laminate deconsolidation.

Induction welding is a reliable (Troughton, 2009a) and fast process (Yousefpour et al., 2004) which can be automated and adapted to complex geometries (V. K. Stokes, 1989). As for other methods, the presence of the heating element adds some polymer at the interface. This extra material can help fill in the voids resulting from surface roughness of the welded parts, hence resulting in better mechanical properties (V. K. Stokes, 1989). However, in continuous induction welding, the pressure is not applied where the temperature is at its maximum (just below the induction coil), but a few centimeters farther, where the pressure roller is located (Bayerl et al., 2014; Mitschang et al., 2002; O'Shaughnessey et al., 2016; Pappadà et al., 2015). The parts must then be overheated below the coil to have a sufficiently high temperature when pressure is applied on the welding line. The alternative method consists in applying pressure on the parts by placing them in a vacuum bag (Mahdi et al., 2003). This ensure a continuous and homogeneous pressure on the welding surface area but is limited as the maximum applicable pressure is 0.1 MPa, which is inferior to the required pressure for welding discussed in 1.1.3.1.

1.3 Susceptors

1.3.1 Electrically-conductive susceptors – Eddy currents

1.3.1.1 Heat dissipation mechanism

When an alternating magnetic field $\vec{B}$ is applied to an electrically-conductive material, an electric field $\vec{E}$ is induced in it, according to the Maxwell-Faraday's law:

$$\nabla \times \vec{E} = -\frac{\partial \vec{B}}{\partial t} \tag{1.13}$$

This electric field creates loops of current in the material, known as eddy or Foucault currents. The movement of the electrons in the conductive material dissipates heat through the Joule effect. These eddy current loops themselves induce a magnetic field in the opposite direction to the applied field. Nagel proposed an expression (Equation (1.14)) to link these two opposed fields (Nagel, n.d.):

$$\nabla^2 \overrightarrow{B_e} + k^2 \overrightarrow{B_e} = -k^2 \overrightarrow{B_\iota} \tag{1.14}$$

with $\overrightarrow{B_\iota}$ being the applied magnetic field, $\overrightarrow{B_e}$ the induced magnetic field and k defined as:

$$k = \sqrt{-j\omega\mu_0\sigma_{el}} \tag{1.15}$$

with ω being the radial frequency ($\omega = 2\pi f$), μ_0 the vacuum magnetic permeability and σ_{el} the electrical conductivity of the material.

The power dissipated by these induced currents can be derived from Equation (1.14) by expressing the related current density with the Ampere law (Equation (1.16)) and the corresponding power losses (Equation (1.17)):

$$\nabla \times \overrightarrow{B_e} = \mu_0 \vec{J} \tag{1.16}$$

$$P_{loss} = \int \frac{1}{\sigma_{el}} \vec{J} \cdot \vec{J}^* dV = \int \frac{1}{\sigma_{el}} \left| \vec{J} \right|^2 dV \tag{1.17}$$

with $\vec{J}^*$ being the complex conjugate of the current density vector $\vec{J}$. The product of $\vec{J}$ and $\vec{J}^*$ gives the square of the amplitude of the current density $\left|\vec{J}\right|^2$. This is a real number representing power density per unit volume in the conductor.

Equation (1.17) is a general expression valid for various geometries and magnetic field. In the case of induction welding, the heat is dissipated in a thin layer and the applied field is sinusoidal. The power P_{el} dissipated by the eddy currents is expressed by Equation (1.18) (Bertotti, 2001):

$$P_{el} = \frac{\pi^2 \sigma_{el}}{6} d^2 B^2 f^2 \tag{1.18}$$

with d being the thickness of the conducting element, B the amplitude of the applied magnetic field and f its frequency.

1.3.1.2 Skin effect

The presence of an alternating current in a conductive material causes a phenomenon called the skin effect. Experiments show that the current density is higher near the surface of a conducting part (e.g., a wire). There is a radial current density profile, which corresponds to an exponential decrease of current density and is usually characterized by a parameter called penetration depth. This corresponds to the depth where the current density has fallen to about 37% of the surface value (Figure 1.12). This is defined as the following equation (Bayerl et al., 2014; Nagel, n.d.):

$$\delta = \sqrt{\frac{2}{\omega \mu_r \mu_0 \sigma_{el}}} = \sqrt{\frac{\rho_{el}}{\pi f \mu_r \mu_0}} \tag{1.19}$$

It should be noted that this equation is valid in the wave regime (high frequency of the alternating current), such as $\omega\epsilon_r\epsilon_0 \gg \sigma_{el}$.

In induction welding, the penetration depth must be greater than the adherend's thickness when using an electrically-conductive adherend. If not, only a small amount of heat is dissipated at the joining interface, which will not be sufficient to melt the polymer and create a weld. If the adherends are not electrically-conductive, it is the thickness of the susceptor film that must be smaller than the penetration depth, to ensure that heat is dissipated on both sides during welding.

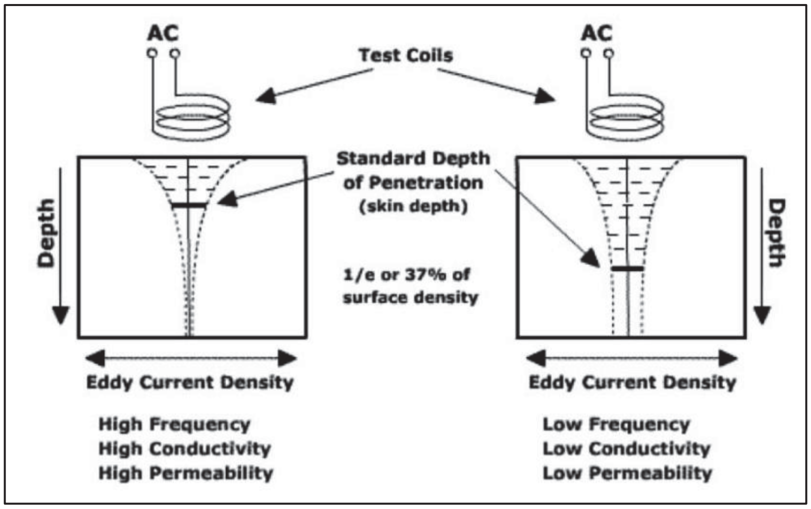

Figure 1.12 Scheme of the penetration depth with varying parameters
Taken from Ahmed et al. (2006, p. 1646)

1.3.1.3 Edge effects

When the induction coil gets close to an edge of a part welded by induction, induced eddy currents cannot circulate freely in the material and concentrate at the edge. Similar behaviour is observed when the part to be welded is smaller than the induction coil, as depicted in Figure 1.13 (Ahmed et al., 2006). The resulting temperature increase caused by induction heating is altered, with higher recorded temperatures towards the edges where the currents loops are concentrated. This phenomenon is known as edge effects and is a major issue in induction welding as is prevents homogeneous heating across the welded surface area.

To minimize this local increase in temperature, different options are suggested. Lin et al. proposed to modify the coil geometry to adjust it to the welded parts geometry (Lin et al., 1992). They showed that having an elongated coil rather than a pancake coil resulted in a more homogeneous heating in the part, minimizing edge effects and avoiding problems in corners caused by the circular shape of the currents induced by pancake coils. Barazanchy et al. proposed to take advantage of the anisotropy of a carbon fibre laminate (relying on direct heating in the laminate, as presented hereafter in 1.3.2 to concentrate heating towards the center of the part (Barazanchy, Pandher, et al., 2021). By comparing results with heating in an isotropic copper plate, they showed that the heating behaviour was modified when the coil was located close to the edge of the part. Finally, Hagenbeek et al. suggested adding an electrically-conductive material at the edge, in which currents would more favorably circulate (Hagenbeek et al., 2018). The proposed copper bypass allowed to reduce the edge effect by avoiding the increased current density at the edge of the laminate.

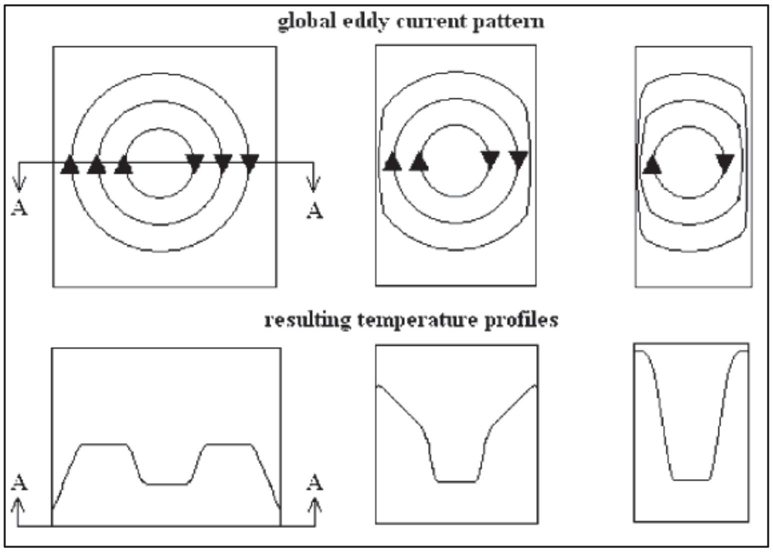

Figure 1.13 Induced edge effects caused by a pancake coil in an electrically-conductive material (top), and resulting temperature profile in the part (bottom)
Taken from Ahmed et al. (2006, p. 1645)

1.3.1.4 Eddy currents induction welding susceptors

When using electrically-insulating adherends or architectures in which eddy current loops cannot be induced, a heating element is located at the joining interface to dissipate heat. This susceptor material must be electrically conductive to allow for the creation of eddy current loops and dissipate heat by the Joule effect. An electrical susceptor is similar to resistance welding heating elements, as it takes the form of a metallic mesh, a carbon fibre fabric, or a conductive film (Dermanaki Farahani & Dubé, 2017; Yarlagadda et al., 2016). The main difference with resistance welding is the absence of copper connectors on both sides of the mesh, which are needed in resistance welding to apply current in the heating element.

As explained in 1.3.1.2, the skin effect creates a current density distribution through the thickness – or along the radius for a wire or a sphere – of a conductive part. The penetration depth shows how deep the current density, and hence the power dissipation by Joule effect, is occurring in the piece. In the case of an electrical susceptor film located at the welding interface, the skin effect can reduce the volume in which energy is dissipated. If the adherends are not electrically conductive, there is no magnetic shielding caused by induced eddy currents. However, there is some in the susceptor, therefore its thickness should be smaller than the penetration depth to ensure a homogeneous heat dissipation inside the susceptor (Bayerl et al., 2014).

One limitation of heating by Joule effect from eddy currents is that there must be electrical continuity to allow a highly conductive path inside the susceptor material, which ensures the creation of current loops in the conductive material. Metallic meshes and carbon fibres fabric satisfy this need for continuity. For particles dispersed in a polymeric film, the percolation threshold must be reached to guarantee the presence of a continuous conductive path (Bayerl et al., 2014; Dermanaki Farahani et al., 2018; Dermanaki Farahani & Dubé, 2017). This can induce a higher weight penalty, but it can also limit the available welding geometries. The coefficient of thermal expansion (CTE) of the continuous film or the mesh can also create residual stresses at the welding interface, as it is usually different than the one of the adherends. This CTE mismatch can also be a source of failure during thermal cycling, especially in space applications where parts can experience large temperature variations. Finally, the presence of foreign material at the joining interface can reduce the mechanical properties of the weld and be a source of failure of the joint.

1.3.2 Susceptor-less induction welding

Eddy currents can be induced in the composite material itself when electrically-conductive fibres are used as reinforcement, such as carbon fibres (Ahmed et al., 2006; Bayerl et al., 2014; Bengtsson, 2006; Mitschang et al., 2002; Moser, 2012; Pappadà et al., 2015; Rudolf et al., 2000). Closed loops of eddy currents can be generated in plain weaves and non-unidirectional laminates, as shown in Figure 1.14.

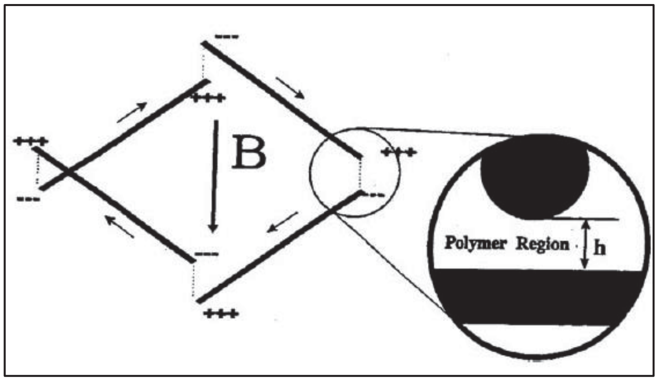

Figure 1.14 Idealized loop at a [0,90] interface in a laminate. Current is induced in presence of a time-varying magnetic field B oriented perpendicularly to the fibre's plane
Taken from Ahmed et al. (2006, p. 1648)

Three main mechanisms contribute to heat dissipation (Ahmed et al., 2006; Barazanchy & van Tooren, 2023; Bayerl et al., 2014; Fink et al., 1992; Yarlagadda et al., 2016), as summarized in Figure 1.15: Joule effect in the fibres, dielectric heating in the polymer region between fibres, and contact resistance at the junctions of fibres. As presented in Figure 1.15b, dielectric heating is typically modelled as a capacitor and a resistance in a parallel circuit.

Heating of the laminate is typically caused by a combination of two or all three mechanisms, although there is no clear agreement in the literature on the dominant mechanism. Some papers indicate that contact resistance between fibres is a significant heating mechanism (Ahmed et al., 2006; Mitschang et al., 2002; Yarlagadda et al., 2002), while others indicate that it can be neglected compared to fibre resistivity and polymer dielectric heating (Barazanchy & van Tooren, 2023; Bensaid et al., 2005; Duhovic, Hümbert, et al., 2014; Fink et al., 1992).

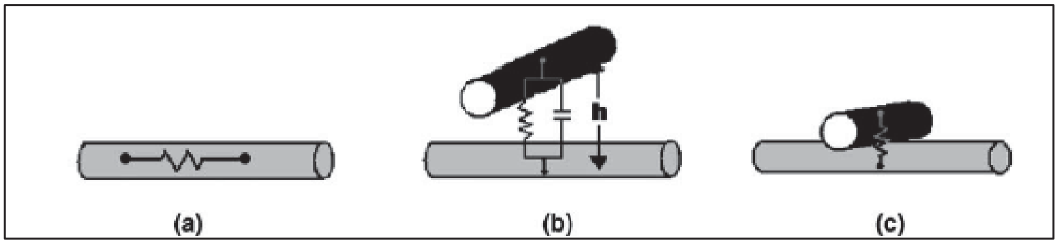

Figure 1.15 Heating mechanisms: (a) Fibre heating by Joule effect, (b) dielectric hysteresis and (c) contact resistance
Taken from Ahmed et al. (2006, p. 1642)

To reduce the complexity of the calculation related to this micro-scale model, considering the fibres and the matrix separately and their interactions, some researchers proposed to use a macro-scale model in which the laminate is approximated as an anisotropic homogeneous electrically-conductive material (Duhovic, L'Eplattenier, et al., 2014; Grouve et al., 2020; Hoffman et al., 2023; Lionetto et al., 2017; Moser, 2012; O'Shaughnessey et al., 2016). The electrical conductivity of the laminate is therefore expressed as a matrix with three non-zero values on its diagonal representing the conductivity both in-plane directions and through the thickness of the laminate.

The main advantage of susceptor-less welding is that no foreign material is added at the welding interface. This reduces the impact on the mechanical properties and the risk of failure during thermal cycling due to CTE mismatch. It also removes the weight penalty of the susceptor. But there are some important drawbacks. First, as presented, this strategy is only available when using electrically-conductive fibres in an architecture that allows the creation of conductive closed loops. Aramid, natural or glass fibres composites cannot be joined in this manner, as well as fully unidirectional lay-ups of carbon fibres. It is also difficult to localize the heat dissipation at the welding interface. The heat will be dissipated through the whole thickness of the part, which can induce delamination, crack creation or crack propagation. Because of magnetic shielding due to induced eddy currents, more heat will be dissipated on the outer adherend surface facing the induction coil than at the joining interface (Moser, 2012).

To minimize this effect and localize heat dissipation at the welding interface, different methods are used. First, an air jet nozzle can be added to the setup, blowing air on the outer surface of the composite adherend to cool it down. The effect of this air jet is to change the thermal gradient through the thickness of the laminate by reducing the temperature at its surface, while keeping the same temperature at the joining line (Duhovic, L'Eplattenier, et al., 2014; Moser, 2012). Another approach is to modify the laminate architecture to control the heating through the thickness. Worrall and Wise proposed to place insulating layers (like glass fibres for examples) between non-parallel unidirectional CF plies, which limits the generation of eddy currents and reduces the heat dissipation (Wise & Worrall, 2014; Worrall & Wise, 2014). This is done only in the top adherend, which is experiencing the unfavorable heating gradient, to minimize overheating of its outer surface. Alternatively, Becker and Mitschang suggested varying the architecture of the laminate through the thickness, placing layers generating more heat closer to the welding line (Becker & Mitschang, 2022). The optimized laminate structure resulted in a more localized heating at the joining interface, eventually exhibiting a higher temperature in the weld than on the outer surface of the adherend.

1.3.3 Magnetic susceptors – Hysteresis losses

As presented in Figure 1.11, susceptors can also rely on a magnetic mechanism, called hysteresis losses, to dissipate heat at the welding interface. Ferromagnetic materials, such as iron (Fe), cobalt (Co) or nickel (Ni), are composed of microscopic zones called magnetic domains. In a magnetic domain the magnetization is oriented in the same direction, as if the ferromagnetic material were made of thousands of microscopic atomic magnets oriented in the same direction. Typically, for several numbers of magnetic domains their magnetization directions are randomly oriented, so the overall magnetization of a sample can be equal to zero. In the case of magnetic nanoparticles, they can be single-domain particles if their diameter is close to or smaller than the average magnetic domain size (typically between 50 and 100 nm (Krishnan et al., 2006)). These particles can absorb the energy and release it due to the magnetization reversal in the single domain (Dutz et al., 2007; Dutz & Hergt, 2013; Kneller & Luborsky, 1963; Krishnan et al., 2006; J. S. Lee et al., 2015; Mørup et al., 2011). In this work, multi-domain particles in the μm range are used.

1.3.3.1 Magnetic hysteresis in multi-domain materials

Between every magnetic domain, there is a frontier region, called the domain wall, in which the orientation of the magnetization changes gradually from one domain to the neighbouring one. Under an applied magnetic field $\vec{H}$, which is pointing to one direction, the overall magnetization of the part will increase in a similar direction. To do so, the magnetic domains with a similar orientation as the orientation of the field will grow at the expense of the others. This is done through a displacement of the domain walls. During displacement, the walls encounter impurities or crystal imperfections, which block the progression and require extra energy to pass them (Chikazumi, 2009; Spaldin, 2003). Hence, the applied field needs to be increased to overcome the impurity and to continue the growth of favorably oriented domains. This growth of magnetic domains at the microscopic level can be measured at the macroscopic level by recording the change in magnetization of the ferromagnetic material when a magnetic field is applied.

In a ferromagnetic material the magnetization $\vec{M}$ is non-linear and irreversible (Coey, 2010), as it can be visualized in the hysteresis curve in Figure 1.16. As the field $\vec{H}$ applied to an initially unmagnetized ferromagnetic material increases, its magnetization $\vec{M}$ increases too, following the initial magnetization curve (Bertotti, 1998). After reaching a maximum value of magnetization, called saturation (or spontaneous) magnetization M_s, that occurs at the saturation field value H_s, the magnetization ceases to progress. This means that all the magnetic domains are aligned with field $\vec{H}$. When the applied field is decreased back to 0, the magnetization $\vec{M}$ remains at a positive value, called the remanence M_r, located between 0 and M_s , as visible in Figure 1.16. At this point, all the domains that were similarly oriented at the saturation need to start turning, which requires energy and a field of opposite direction. To bring the magnetization $\vec{M}$ to 0, a negative magnetic field must be applied (a negative value means that the field is in the opposite direction). This is completed when the applied field $\vec{H}$ reaches the value of $-H_c$. This value H_c of the field $\vec{H}$ is called the coercivity. If the field $\vec{H}$ goes to larger negative values, the spontaneous magnetization can be reached in the opposite direction, taking then a value of $-M_s$. At that point, every single magnetic domain is oriented in the opposite direction as previously. As it appears clearly in Figure 1.16, this delay in the magnetization response happens both when the field $\vec{H}$ is increasing and decreasing, creating the major hysteresis loop.

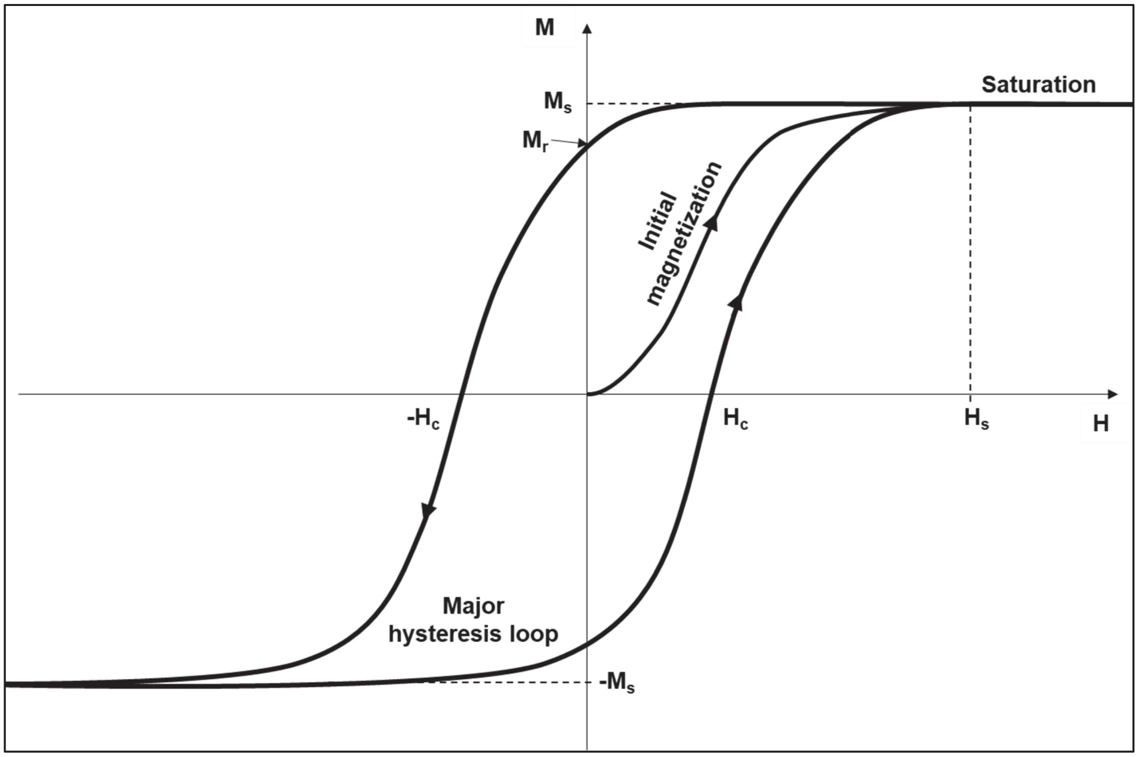

Figure 1.16 Schematic of the typical M-H hysteresis loop of a ferromagnetic material. The initial magnetization curve corresponds to the magnetization of a material initially in an unmagnetized state

There are two main types of magnetic materials which exhibit different hysteresis loops. Soft magnets do not require a lot of energy to be magnetized and demagnetized, because of their low coercivity H_c, typically lower than 1000A/m. Their hysteresis loops are narrow, which leads to minimal heat losses, while their magnetic susceptibility and permeability are high. They are used to make temporary magnets, as they cannot retain their magnetism when the applied magnetic field H is removed. On the other hand, hard magnets possess a high coercivity value (>50000A/m) and exhibit large hysteresis loops. Hence, a larger magnetic field amplitude is required to magnetize them. However, they retain their magnetization well to make permanent magnets. In addition, due to their large hysteresis, the magnetic energy and heat losses (through eddy current and hysteresis losses) are higher than in a soft magnet (Coey, 2010).

The magnetic field $\vec{B}$ is linked to $\vec{H}$ and $\vec{M}$ by the following expression (Spaldin, 2003):

$$\vec{B} = \mu_0(\vec{H} + \vec{M}) \tag{1.20}$$

This expression is valid using SI units. The magnetic permeability of vacuum μ_0 is a constant and is equal to $4\pi \cdot 10^{-7}$ H/m. Following Equation (1.20), the hysteresis curve can be plotted as $\vec{M}$ versus $\vec{H}$ or $\vec{B}$ versus $\vec{H}$. The remanence M_r corresponds to a zero H-field, so it can be stated that $M_r = \mu_0 B_r$.

When undergoing a complete hysteresis loop, a magnetic material absorbs a fraction of the electromagnetic energy and releases it into heat. This energy is defined as the absorbed energy density E_h and is equal to the enclosed surface area of the hysteresis loop, as presented in Equation (1.21). Under a time-varying magnetic field, the magnetic material experiences hysteresis loops at a high rate – a frequency 1 kHz meaning 1000 times per second – and is locally dissipating a small amount of heat during the completion of every hysteresis loop. In the case of a magnetic susceptor made of dispersed magnetic particles, this dissipated energy will heat up the surrounding thermoplastic polymer matrix through heat conduction. Using magnetic materials as susceptor is therefore interesting as it can promote heat dissipation for induction welding.

The absorbed energy density E_h for one complete hysteresis loop and per volume unit of material is defined as:

$$E_h = \int \vec{H} d\vec{B} = \mu_0 \int \vec{H} d\vec{M} \tag{1.21}$$

This is the basic equation behind the phenomenon of magnetic heating by hysteresis losses. It is important to note that the value of E_h depends on the applied field amplitude, as discussed in 1.3.3.2. The dissipated power per unit volume corresponds to the absorbed energy density E_h multiplied by the frequency f:

$$P_h = f \cdot E_h \tag{1.22}$$

The complete hysteresis curve is usually not available in the literature or in material technical datasheets. Instead, only the second quadrant (top left in Figure 1.16, where $\vec{H} < 0$, $\vec{M}$ or $\vec{B} > 0$) may be provided. This curve is often sufficient to obtain relevant information such as the remanence and the coercivity of a given material. It is also in this quadrant where the maximum energy product BH_{max} is calculated, corresponding to the highest value of the product of $\vec{B}$ and $\vec{H}$ along the hysteresis curve. This property is used to define the maximum amount of magnetic energy that a magnet can store (the "magnetic strength"). With this value, it is possible to evaluate the magnitude of the full hysteresis of different materials. However, this is not sufficient to obtain the value of E_h under various applied field amplitudes. Therefore, characterization of the magnetic hysteresis of the material is required to access to this information.

1.3.3.2 Minor hysteresis loop

A hysteresis loop is completed when applying an alternating magnetic field with an amplitude H_m large enough to reach the saturation magnetization ($H_m \geq H_s$). This is also called the major loop. If the amplitude of the applied field is smaller ($H_m \leq H_s$), saturation is not reached but the material is still experiencing a smaller hysteresis, which is called a minor loop (Figure 1.17). Such minor loops are enclosed within the major loop, and they usually exhibit a similar shape (oval with tipped extremities). The line connecting the tips of the successive minor loops represents the initial magnetization curve (Figure 1.16 and Figure 1.17).

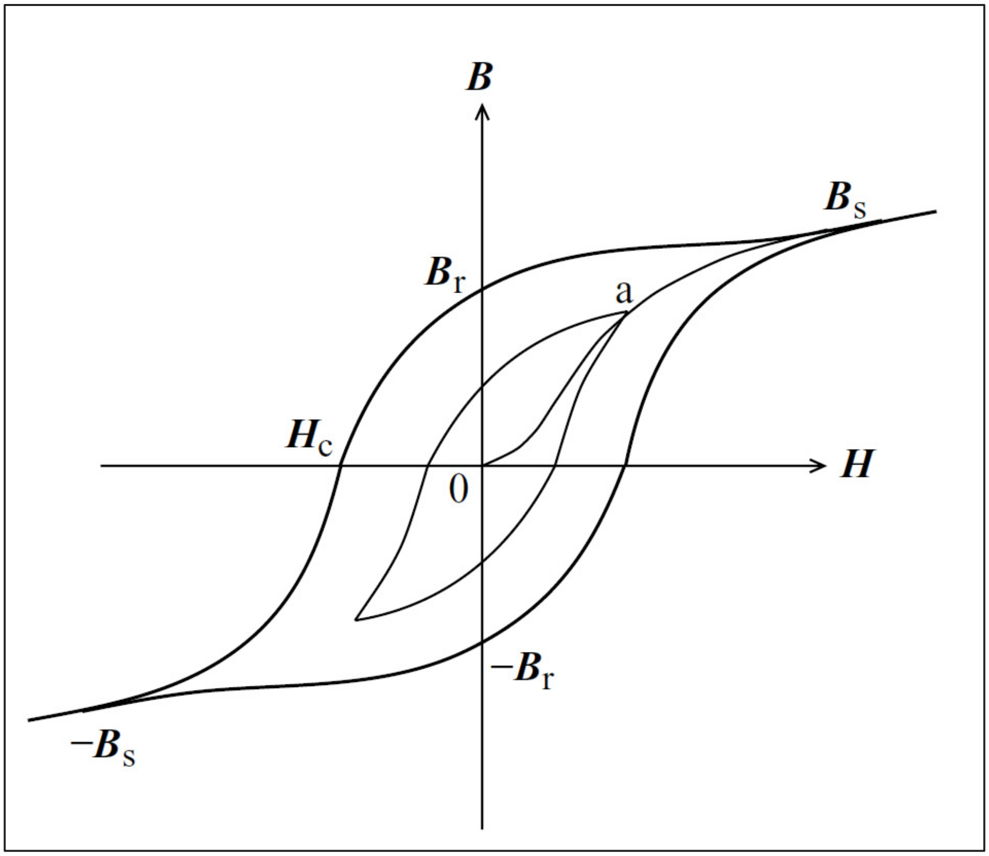

Figure 1.17 Scheme of a B-H hysteresis loop of a ferromagnetic material. When the applied field amplitude is smaller than saturation, the magnetization is interrupted (at point a) and a minor hysteresis loop is formed. The minor loop is enclosed in the major loop
Taken from Spalin (2003, p. 18)

1.3.3.3 Heat dissipation equation

The power dissipated through hysteresis losses per unit volume of material can be expressed following the Steinmetz law (Landgraf et al., 2008; Steinmetz, 1984), presented in Equation (1.23). It is only valid in the narrow field range, which means at fields significantly lower than the saturation field ($H_m \ll H_s$).

$$P_h = f \cdot E_h = k \cdot f \cdot {B_{max}}^{1.6} \tag{1.23}$$

This expression is correct for certain materials but must be generalized to fit more materials. The following expression was proposed to be adapted to different materials (Muhlethaler et al., 2012):

$$P_h = f \cdot E_h = k \cdot f^{\alpha} \cdot {B_{max}}^{\beta} \tag{1.24}$$

with f being the time-varying applied magnetic field frequency, B_{max} the peak value of magnetic field – or flux density – reached by the susceptor material, and k, α and β factors related to the magnetic properties of the susceptor material. This expression is only valid for sinusoidal flux density B.

Equation (1.24) is applicable in induction welding as the current generated by the power source and circulating through the coil is sinusoidal, as well as the applied magnetic field. In the case of a non-sinusoidal excitation, the improved generalized Steinmetz equation (iGSE) must be used (Muhlethaler et al., 2012). This equation is valid only in iso-thermal process, because as the magnetization is not linear with temperature, B_{max} might also not be linear as the temperature increases. Therefore, minor loops can be measured experimentally at different temperatures to determine the value of E_h and estimate the heating power of the material.

Another approach proposed by Wetzel and Fink is to observe the major hysteresis loop corresponding to the full magnetization of the magnetic material (Wetzel & Fink, n.d.). The area of this loop corresponds to the maximum energy that can be dissipated by the material, if a sufficiently high magnetic field is applied to it. The paper defines these values as E_{hs} for the saturation absorbed energy density of the complete hysteresis and H_s for the saturation field applied to reach the saturation magnetization. They also assume that minor loops obtained by applying a smaller field H_m smaller than the saturation field ($H_m < H_s$) keep the same shape as the major loop, but only with a proportionally smaller surface area. They hence dissipate less energy into heat.

It is possible to link the absorbed energy density E_h for a minor loop under an applied field H_m to the major loop E_{hs} reached with a saturation field H_s by using the following expression proposed by Wetzel and Fink:

$$P_h = f \cdot E_h = f \cdot E_{hs} \left(\frac{H_m}{H_s}\right)^2 \tag{1.25}$$

This is valid if the applied field is smaller than the saturation field ($H_m < H_s$). When $H_m > H_s$, the absorbed energy density cannot exceed that of complete hysteresis, regardless of the magnitude of the applied field. In this case, Equation (1.25) simply becomes $E_h = E_{hs}$. It is also important to note that this is an approximation used to predict the absorbed energy density at a given field H_m while knowing the saturation hysteresis parameters E_{hs} and H_s. Like for the Steinmetz approximation, it is only valid at low fields ($H_m \ll H_s$), far from H_s. Experimental curves do not follow a quadratic behaviour up to the saturation, requiring more detailed characterization when applying a magnetic field amplitude located in that range. It appears that there is no model to predict the E_h versus H_m curve when the applied field approaches H_s. This curve must then be obtained experimentally by repeating hysteresis measurements at various field amplitudes.

1.3.3.4 Curie Temperature

When magnetic materials heat up, their magnetic properties and their efficiency are reduced. This reduction in the magnetic properties is related to the Curie temperature, T_c. Above this temperature, a ferromagnetic material loses its ordered magnetic state and becomes paramagnetic. The intrinsic saturation magnetization does not drop suddenly when reaching T_c, instead it decreases when approaching that temperature, as presented in Figure 1.18. This is reversible, as the material recovers its magnetic properties when cooled below T_c. Typically, when reaching 90% of T_c (in Kelvin), the remaining maximum magnetization is about 50% (Coey, 2010; Vinum et al., 2018). The Curie temperatures of magnetic materials are well-documented in the literature (Chikazumi, 2009; Coey, 2010). Consequently, the absorbed energy density of the magnetic material also decreases with increasing temperature, which will impact the heat generation as explained in 1.3.3.5.

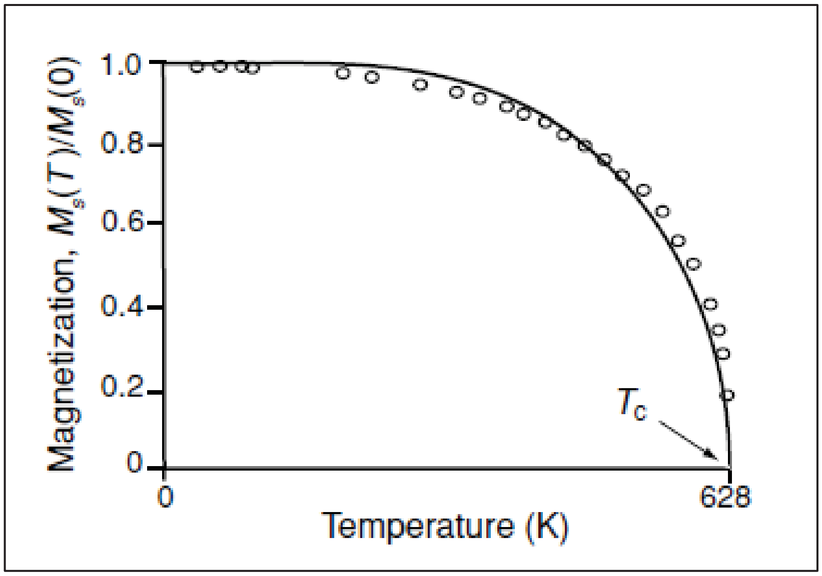

Figure 1.18 Spontaneous magnetization of nickel. The Curie temperature of nickel is 628K, marked as T_c
Taken from Coey (2010, p. 9)

1.3.3.5 Hysteresis losses susceptors

Hysteresis losses susceptors take advantage of the heat dissipated when ferromagnetic materials are subjected to a time-varying magnetic field. Typically, a susceptor material takes the form of ferromagnetic particles dispersed in a thermoplastic matrix (Bayerl et al., 2012; Sanders, 1987; Suwanwatana et al., 2006a). The thermoplastic polymer is chosen to be similar or compatible with the two interfaces to be welded.

Wetzel and Fink determined the equation for the heating rate of a susceptor relying on hysteresis losses (Wetzel & Fink, n.d.):

$$\frac{dT}{dt} \cong f E_h \left(\rho c_p + \left(\frac{1}{v_f} - 1 \right) \tilde{\rho} \tilde{c}_p \right)^{-1} \tag{1.26}$$

with ρ and c_p being the density and the specific heat capacity of the particles, respectively, E_h the energy dissipated, v_f the volume fraction of particles in the polymeric matrix, $\tilde{\rho}$ and $\tilde{c}_p$ the density and the specific heat capacity of the matrix, respectively, and f the frequency of the time-varying field applied to the particles. As discussed, E_h depends on the applied field amplitude H_m.

The heating power of various ferromagnetic particles susceptors was investigated by Wetzel and Fink (Wetzel & Fink, n.d., 2001), who defined Equation (1.26). They explored the theoretical heating capability of Ni, a hard ferrite (Strontium-ferrite) and a soft ferrite (Nickel-zinc-ferrite). Based on this work, Suwanwatana et al. used Ni particles ranging from 79 nm to 22 μm in size into polysulfone (PSU) to demonstrate the feasibility of hysteresis heating and its application to weld polyphenylene sulfide (PPS) based composites (Suwanwatana et al., 2006a, 2006b). Bae et al. conducted a similar study and measured the heating capability of Fe particles (8 to 74 μm) dispersed in thermoplastic polyurethane (TPU) adhesives (Bae et al., 2015). These two materials were also present among the different particulate materials (carbon black, magnetite (Fe_3O_4), Ni and Fe) that Bayerl et al. explored when mixed with high-density polyethylene (HDPE) (Bayerl et al., 2012). Finally, Stokes used Emaweld products without disclosing the nature of the ferromagnetic particles dispersed in various thermoplastic matrices (V. K. Stokes, 1989). They all concluded on the susceptor material efficiency based on experimental results. In summary, the reported results are valid for a given thermoplastic matrix and a specific induction heating setup.

The Curie temperature of the magnetic susceptor can be used advantageously to implement a temperature-control feature in the material (McGaffigan, 1994; Suwanwatana et al., 2006b; Wetzel & Fink, n.d.). If the T_c is larger than the melting point or glass transition temperature of the polymer, but below its degradation temperature, the susceptor will inherently be unable to overheat and burn the material. Due to the loss of magnetic properties when approaching T_c, the susceptor will stop heating before reaching degradation, and will instead maintain its temperature. If this temperature falls into the welding temperature range, this can improve the control and quality of the weld (Wetzel & Fink, n.d.). Unfortunately, the Curie temperature of ferromagnetic materials varies from a few dozen to over 1000 K. Finding a susceptor material exhibiting a T_c within the desired temperature range, while also offering large heating capability, i.e. a large magnetic hysteresis, can result in a very limited choice of materials, or even be impossible. However, the Curie temperature of materials can be adjusted by tuning alloy composition. By varying the composition of Ni, Fe or Cr for example, the Curie temperature can be shifted by hundreds of degrees (Goncharov et al., 2024; Milone et al., 1982; Wei et al., 2014). But one must ensure not to lose heating capability by adjusting the Curie temperature to match the desired welding temperature.

1.4 Composite sandwich structures

Sandwich structures are widely used in applications where the demand for lightweight structures is critical, like in the aerospace industry, because of their high bending stiffness and low weight (Herrmann et al., 2005). They are made of two main elements: a low-density part called the core, surrounded by high-stiffness plates called skins or facesheets (Castanie et al., 2020; Hoff & Mautner, 1998). The skins are assembled with the core to transfer the loads and ensure the structure's integrity (Zenkert, 1997). The core is typically subjected to transverse shear stresses while normal stresses will occur in the facesheets (Butukuri et al., 2012). These structures may also provide other advantages like acoustic and vibration dampening, as well as low thermal conductivity (Butukuri et al., 2012; Grünewald et al., 2017a; Kindinger, 2001).

1.4.1 Geometries and materials

Sandwich structure cores can be classified into three main categories: foams, honeycomb cores and corrugated cores, as presented in Figure 1.19. There are also hybrid structures, such as foams reinforced by a corrugated structure (Birman & Kardomateas, 2018), and more exotic geometries, based on meshes (Birman & Kardomateas, 2018; Johnson, 2008; Yixiong et al., 2020).

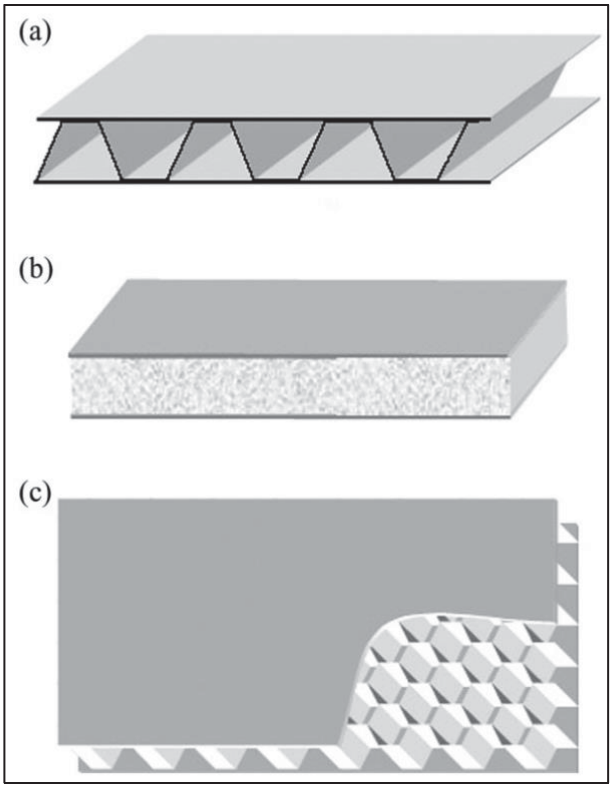

Figure 1.19 Main sandwich structures core geometries. (a) corrugated (b) foam (c) honeycomb
Taken from Grünewald et al. (2017b, p. 441)

Foam cores are generally made of polymer. Honeycomb cores can be made of kraft paper, metal, thermoplastics or fibres reinforced composites (Kindinger, 2001). The material choice impacts the mechanical properties of the sandwich structure, as well as the final cost of the panel. The performance of the core depends on several parameters (strength, stiffness, energy absorption, impact, fatigue, abrasion resistance, etc.). Aluminium honeycomb cores are widely used in the aerospace industry for their excellent price-to-performance ratio. Plastic honeycomb cores, though they exhibit lower relative performance, are also interesting because they offer better thermal insulation properties (Kindinger, 2001).

Recently, honeycombs manufactured by additive manufacturing – or 3D-printing – have been reported (Pollard et al., 2017). This process allows to build thermoplastic honeycomb cores with geometries ranging from classical hexagonal cells to complex shape such as re-entrant cells or origami-based structures. Sugiyama et al. reported using continuous carbon fibre-reinforced thermoplastic filaments to print various cell geometries, from hexagonal to rectangular and circular (Kindinger, 2001; Sugiyama et al., 2018). They used the fused filament fabrication (FFF) method, in which a filament of polymer is molten and extruded to be deposited at its final position, allowing to build 3D structures layer-by-layer. Lu et al. presented different types of grid structures (Lu et al., 2018), and Hou et al. proposed a spline corrugated-core using FFF to increase the compression strength while keeping the weight of structure low (Hou et al., 2018). 3D-printing also allows varying the profile of cellular cells through the thickness of the structure, as shown by Townsend et al. with their origami honeycomb cores (Townsend et al., 2020). This structure presents higher impact absorption properties due to its specific buckling behaviour. Duchesne et al. proposed to optimize the cells distribution based on Voronoi patterns in a 3D-printed honeycomb core to reduce the sandwich panel's mass while increasing its stiffness (Duchesne et al., 2023). Alshear et al. have used the selective laser sintering (SLS) method, in which fine layers of powder are progressively added to the structure and polymerized with a laser in selected areas, to produce complex core geometries in polymer materials, such as re-entrant cells, pyramids or gyroid structures (Alshaer & Harland, 2021; Harland et al., 2019).

Sandwich skins are plates of variable thickness, depending on the overall sandwich thickness and the desired mechanical properties. They generally are made of aluminium or fibre reinforced polymer composites (usually with thermoset matrix). Fibres can be glass, aramid or carbon for high-performance parts.

1.4.2 Skin-to-core joining

The bond between the core and the two skins is a critical parameter in the manufacturing of sandwich structures. Its quality is decisive to ensure good mechanical properties of the sandwich structure. The bond is usually done by adding an adhesive layer at the interface between the two components, as presented in Figure 1.20 (Banea & da Silva, 2009; Butukuri et al., 2012; Castanie et al., 2020; Kratz, 2010; Nettles, 2006; Park et al., 2014; Widagdo et al., 2020). By heating up the panel, the adhesive cures and joins the core and the skins. This method presents the advantage of being simple and relatively cheap. The drawback is that it is labour-intensive and time-consuming due to the required surface preparation and the curing time. Another technique is to stack the composites prepreg layers and the adhesive film directly on the core structure and to cure everything together in a vacuum bag in the oven (Butukuri et al., 2012; Kratz, 2010; Zenkert, 1997).

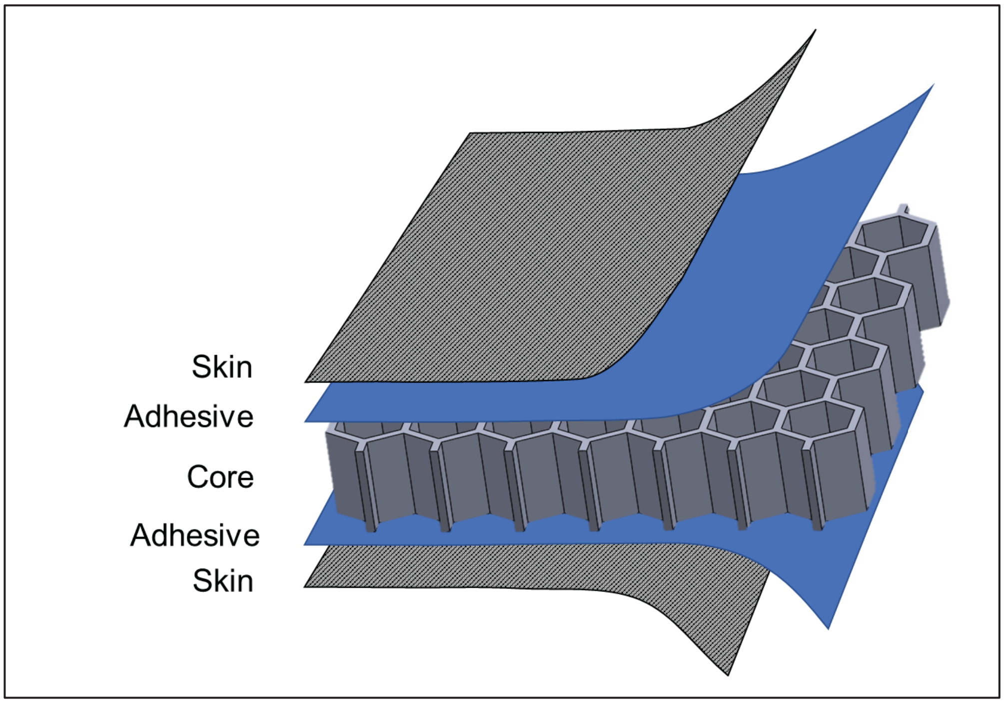

Figure 1.20 Scheme of the sandwich skins to core assembly using adhesive film

When it comes to the space industry, major drawbacks appear when using adhesives. The materials used often outgas, which must be avoided as the evaporated molecules can condensate on critical equipment such as lenses or electronics. In the case of honeycomb structures, vacuum could lead to an excessive pressure inside the cells and consequently a risk of explosion and damage of the structure. The CTE of an adhesive film is generally larger than that of the skins and the cores, which can induce residual stresses in the structure during large thermal cycle characteristic of space operations.

1.4.3 Thermoplastic sandwich structures

Thermoplastic composite sandwich panels were recently proposed to replace metallic and thermoset composite sandwich parts (Åström et al., 1998; Ma & Elkin, 2021; Skawinski et al., 2004). These all-thermoplastic sandwich structures, like other thermoplastic composite parts, present high fracture toughness and impact resistance, short processing time, and offer the potential to be repaired or recycled (Barroeta Robles et al., 2022; Pegoretti, 2021). 3D-printed thermoplastic honeycombs, as mentioned in 1.4.1, are good candidates for sandwich cores. For the sandwich facesheets, fibre reinforced thermoplastic composite laminates can be used. Assembly of thermoplastic composites parts using thermoset adhesives offers poor mechanical properties (Grünewald et al., 2017b). Extensive surface preparation procedures and long curing cycles are needed to reach optimal performances, as mentioned in 1.1.1 (Ageorges et al., 2001; Park et al., 2014). The resulting strength is usually still limited because of the chemical incompatibility between thermoplastic and thermoset polymers. Therefore, it is necessary to explore other joining techniques to assemble thermoplastic composites skins efficiently and safely with thermoplastic core structures. As mechanical fastening is clearly not adapted to the sandwich structure geometry, thermoplastic welding techniques are interesting to be investigated as a solution.

To manufacture sandwich structures by thermoplastic welding, it is required to melt the thermoplastic polymer at the skin-core interface to weld it. This process can by conducted in two ways: isothermally, where the pressure is applied during heating of the parts, and non-isothermally, where the parts are first heated, then transferred to a secondary device in which pressure is applied to consolidate the parts together (Skawinski et al., 2004). The control of the temperature and the applied pressure can be done in various ways, depending on the selected assembly method.

Different techniques have been reported to assemble skins and cores by thermoplastic welding, as reported in Figure 1.21. The first one is vacuum moulding, where the parts are placed in a vacuum bag. The consolidation pressure is applied on the parts by pulling the vacuum. The assembly can be done in an oven (isothermal process) or the parts can be heated in an oven, then transferred in a vacuum bag for consolidation (non-isothermal process). Isothermal heating of the sandwich structure is almost impossible because the core loses its mechanical properties at elevated temperatures, making it prone to collapse under the applied pressure (Grünewald et al., 2018). In non-isothermal vacuum moulding, the critical parameters are the skins' preheat temperature and the speed at which the parts are transferred to the vacuum bag and the pressure is applied (Brooks et al., 2008). The temperature lost during transfer implies overheating the skins to maintain enough heat when reaching the welding step. This can lead to deconsolidation of the laminates, therefore limiting the use of this method.

Compression moulding of sandwich structures is similar to vacuum moulding, but instead of applying pressure with vacuum, a hot press is used (Grünewald et al., 2017a; Latsuzbaya et al., 2023; Rozant et al., 2001). The advantage is that the press can reach much higher pressures and can also heat up the parts. This method showed good results but faces the same challenges and limitations as vacuum moulding, not counting the fact that higher pressure increases the risk of core crushing. The main advantage is that the transfer from the oven to the press can be more easily automated, faster, and therefore reduce the heat losses.

Double-belt lamination is a continuous process in which parts are assembled, then guided through heating elements by two belts (Pflug et al., 2001; Trende et al., 1999; Xinyu et al., 2009). The heat is brought to the welding interface by conduction through the skins. The parts temperature must be continuously monitored to avoid core crushing.

Another technique only adapted to foam cores is *in situ* foaming, which consists in developing the foam core from a film directly between two facesheets during the assembly process (Beukers, 1992). .Finally, hot-melt adhesives can also be used (Cabrera et al., 2008). Their process is somewhat similar to welding, except that they can be bonded at lower temperatures, if surface compatibility is acceptable (Pappadà et al., n.d.). These adhesives are also used to join dissimilar materials (Ageorges et al., 2001).

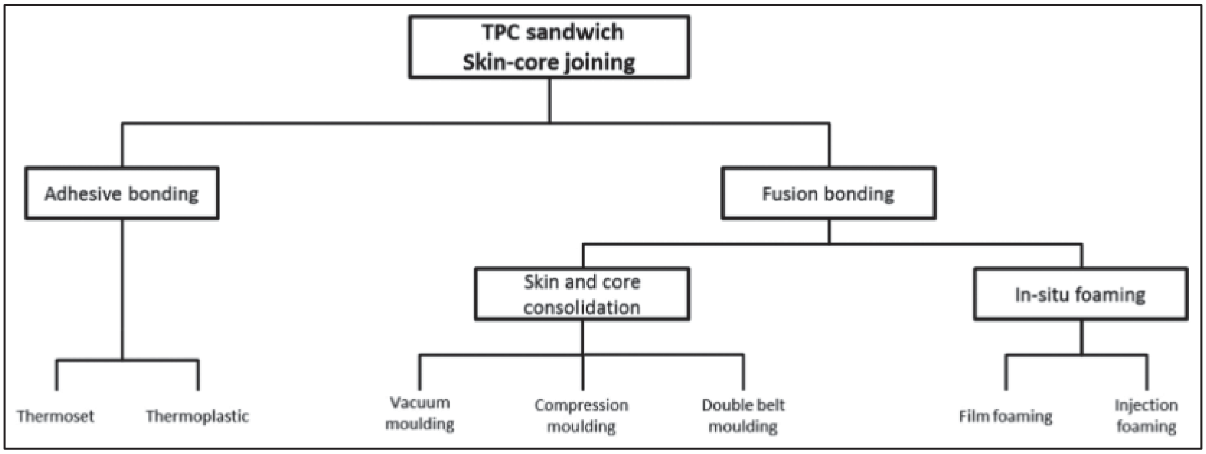

Figure 1.21 Summary of the different assembly techniques for thermoplastic sandwich structures
Taken from Grünewald et al. (2017b, p. 443)

In all these techniques, the main challenge is to reach the required skin/core interface welding temperature. It must be high enough to allow for chain mobility to weld the thermoplastic polymer. This corresponds to the thermoplastic processing temperature and is higher than the temperature required for thermoset adhesive curing. But at that temperature, the core is also softened if it is also made of similar polymer material, making It unable to sustain the applied pressure without crushing. Composite laminates can also experience deconsolidation if they exceed their melting point without sufficient pressure applied on them.

When the heat source is located outside of the sandwich structure, the skins or the core are heated through their thickness, which makes them face these critical issues. Localising heat dissipation at the joining interface, instead of across the totality of the structure, could solve the problem. It is therefore interesting to explore more localised thermoplastic welding techniques.

1.4.4 Skin/core welding

Grünewald et al. proposed a solution to the issue. They presented a method to join CF/PEEK skins to a PEI foam core using a non-isothermal (two-step) compression moulding process (Grünewald et al., 2017a, 2018). In order to perform the weld at a lower temperature, reducing the risk of core crushing and laminate deconsolidation, a PEI layer is co-consolidated on the CF/PEEK skins, following the Thermabond process presented in 1.1.5. Then, the skins are heated up in an oven, quickly transferred to a press to minimize the heat losses (evaluated at 1°C/s [19]) and placed on the core. Pressure is applied to consolidate the bond during the cooling, which makes it a non-isothermal process. The steps are schematized in Figure 1.22. This process requires additional preparation steps but presents the interest that the temperature is lower during the second step when the pressure is applied on the core. This is critical to achieve good properties of the structure when using thermoplastic welding. The limitation of this work is that, to obtain the best skin/core strength, the core must be heated up before being welded to the skins, increasing therefore the risk of core crushing during the process.

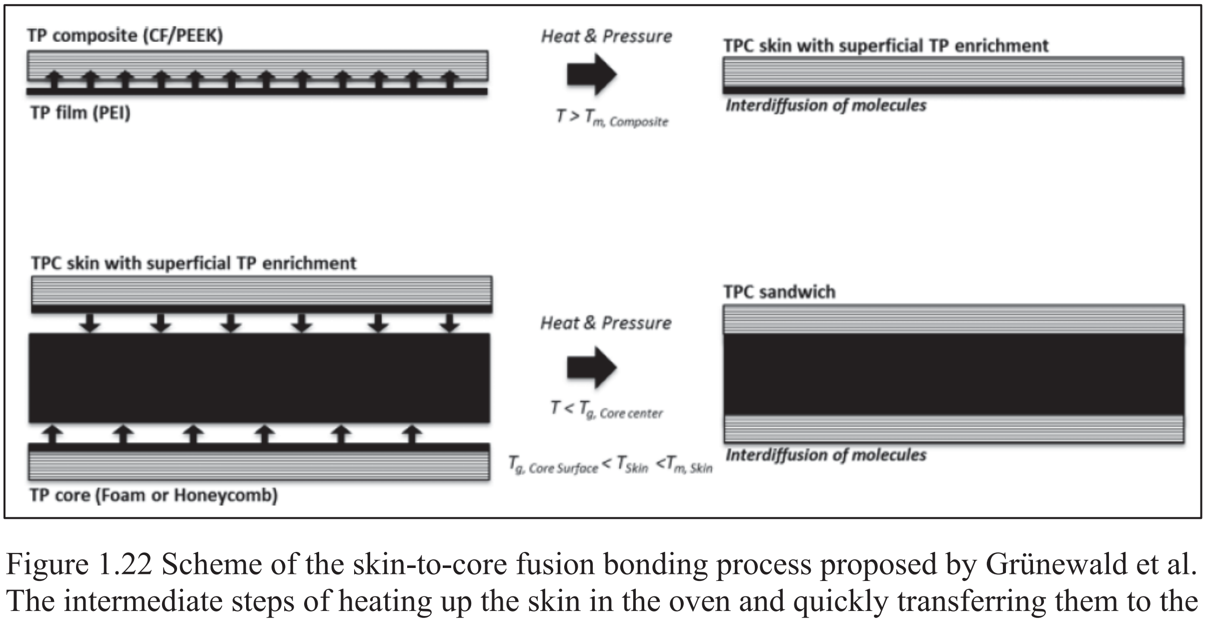

Figure 1.22 Scheme of the skin-to-core fusion bonding process proposed by Grünewald et al. The intermediate steps of heating up the skin in the oven and quickly transferring them to the compression mould are not shown here
Taken from Grünewald et al. (2017a, p. 3)

1.4.5 Skin/core strength characterization methods

Three major testing methods for the skin/core strength are reported in the literature. These methods are typically applied to adhesively bonded sandwich panels but can also be used to characterize welded sandwich samples. Flatwise tensile (FWT) tests are widely used and are reported in various studies (Butukuri et al., 2012; Park et al., 2014; Widagdo et al., 2020; Grünewald et al., 2018; Hegde & Hojjati, 2019). They consist in testing the interface strength in traction, by pulling on the skins perpendicularly to their surface. To do so, metal blocks are adhesively bonded to both sides of the 50 mm-wide square sandwich sample. These blocks act as connectors to the tensile machine through a system of bolts and pivots (Figure 1.23). The preparation is easy, and requires small specimens compared to other methods. The standards for this test are the ASTM C297 or the DIN53292.

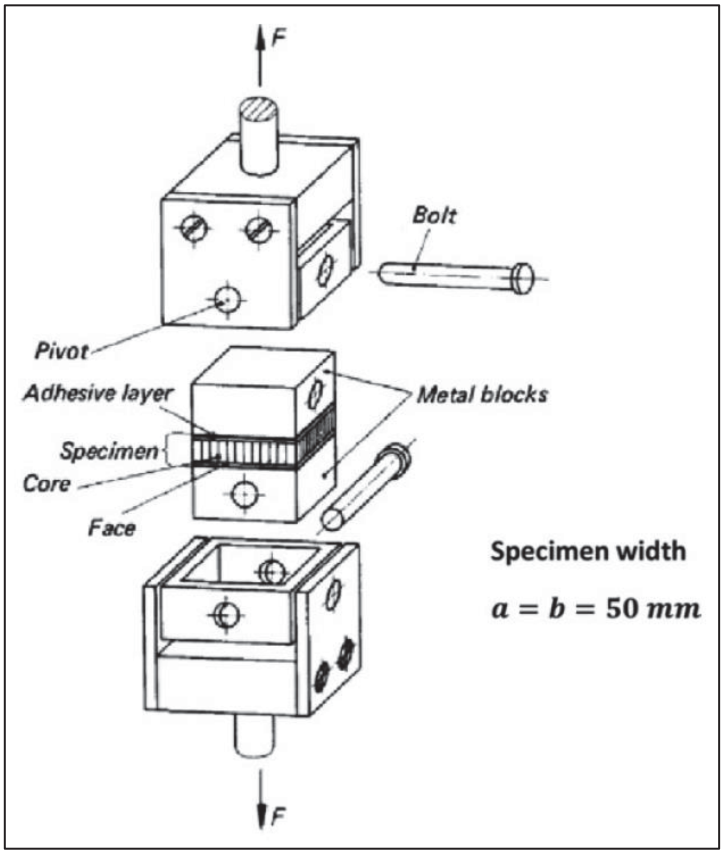

Figure 1.23 Flatwise tensile testing setup after DIN53292
Taken from Grünewald et al. (2018, p. 807)

The second method is called the double cantilever beam (DCB). Different variations exist in the literature, with traction being applied by hinges or wires, with or without stiffening plates on the skins to avoid early cracking of the peeled skin (Nettles, 2006; Weidmann et al., 2023). A version with stiffening plates is presented on Figure 1.24. This method requires bigger samples (three to four times longer than for FWT). Results are also more difficult to analyze as they depend on more factors like the pre-crack length, the stiffening plates properties, and the ability to accurately track the crack's progression. The standard corresponding to DCB testing is the ASTM D5528.

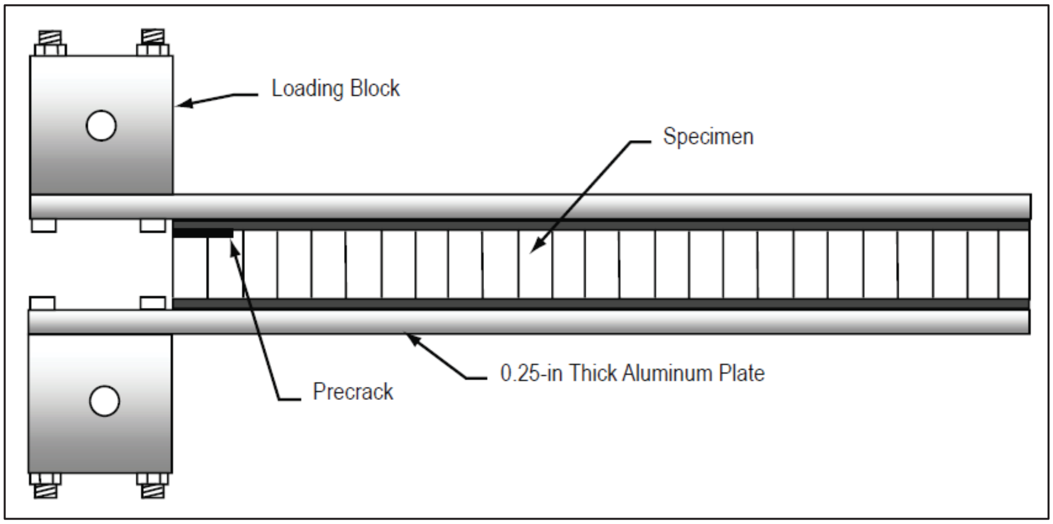

Figure 1.24 DCB testing setup. The stiffening plates are visible along the two skins
Taken from Nettles (2006, p. 16)

One last pertinent method also in use to test the adhesion between the skins and the core of a sandwich panel is the climbing drum (CD), presented in standard ASTM D1781. (Weidmann et al., 2023). It measures the force required to peel the skin away from the core. One advantage of this method compared to DCB is that the crack propagation is not influence by the rigidity of stiffening plates, and the core experiences less bending. However, the sample preparation is complex, and it requires a specific test setup (including the drum and the connectors to the tensile test machine to be applied (Figure 1.25). This method requires the largest samples among the three presented testing methods (30cm long by 7.5cm wide) (Nettles, 2006; Park et al., 2014).

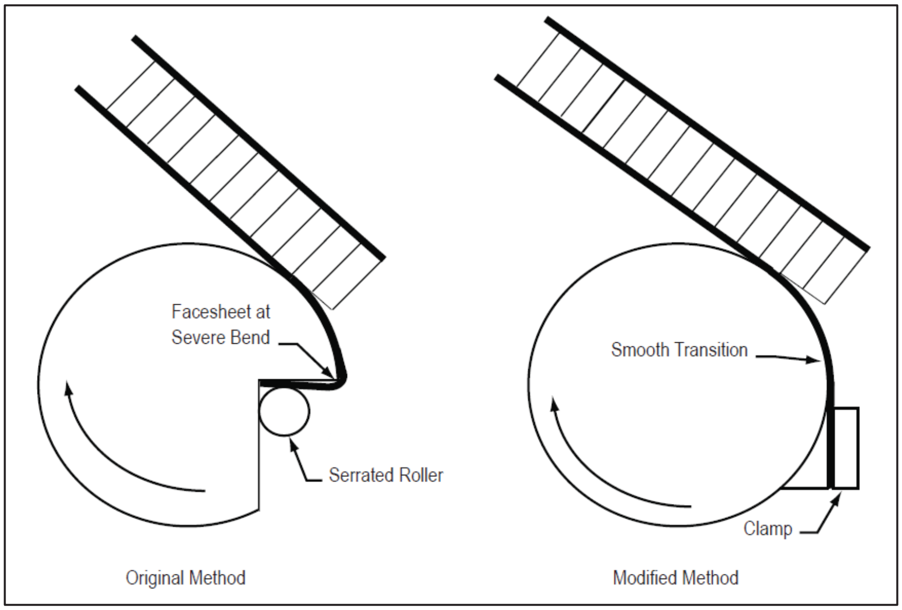

Figure 1.25 Climbing drum testing method scheme. Nettles proposed an alternative clamping method (on the right side) to avoid the extreme bending of the skin that could break under those conditions
Taken from Nettles (2006, p. 16)

CHAPTER 2

RESEARCH OBJECTIVES

2.1 Current gaps in the literature

In the prior works presented in Chapter 1 concerning hysteresis losses susceptors, it is apparent that the selection of the magnetic particles is never clearly explained nor motivated. The authors present which material they use for their experiments, but no explanation is provided about why it was selected. The definition of a clear methodology of material selection depicting how to select optimal magnetic particles depending on the induction heating equipment and the thermoplastic polymer to be welded is required. This would provide engineers with guidelines on the material's selection that can be adapted to their needs.

Another aspect of hysteresis losses susceptors that needs to be further investigated is the evolution of the susceptor properties with increasing temperatures. Typically, the density of materials is reduced, and specific heat is increased at higher temperature. The absorbed energy density E_h will also be significantly reduced when approaching the Curie temperature T_c. The behaviour at high temperature must be known to predict the heating rate throughout the whole process and ensure high-quality welding.

More specifically on materials, induction welding of PEEK and PEI high-performance thermoplastic composites using hysteresis losses susceptors has not been demonstrated. These polymers exhibit high mechanical properties and high processing temperatures, making them difficult to join by welding. Hysteresis losses susceptors should be investigated to determine if they can generate enough heat at the interface to weld parts made of these materials. Also, the Thermabond process was never used on parts welded by induction. This approach could help achieve high weld strength without risking part deconsolidation.

The assembly of all-thermoplastic sandwich structures by thermoplastic welding with the methods proposed so far present limitations, mostly due to the use of thermal welding methods, in which the whole parts are heated up to perform welding. The temperature processing window to obtain high welding strength while avoiding overheating issues (facesheet deconsolidation and core crushing) is very small. The opportunity to use other welding techniques, such as induction welding, to generate heat directly at the joining interface and limit the increase in temperature in the rest of the parts is promising.

Temperature and pressure control during the welding process is critical and needs to be studied to obtain a high skin/core strength. Using induction welding to join skins to a honeycomb core in an all-thermoplastic sandwich panels is unexplored and could be a new and innovative way to perform that joining step. Depending on the nature of the reinforcements of the composite facesheets (electrically conductive or not), the heating mechanism can be adapted, as presented in Chapter 1. Magnetic hysteresis losses susceptor films placed at the skin/core interface could be used as the heating element to join sandwich panels, which has never been investigated.

As discussed, sandwich cores can be produced using 3D-printing to satisfy the need for complex geometries. The deposition of a heating element using the same method has never been explored. The discontinuity of the filler in hysteresis losses susceptors, compared to other continuous heating elements such as meshes, offers the possibility to produce susceptor in a printable filament form, and deposit it by 3D-printing to adapt to the core geometry. This takes advantage of the versatility of both the additive manufacturing method and the magnetic hysteresis losses susceptors made of distributed, properly selected magnetic particles.

2.2 Objectives

Based on the gaps observed in the current state of the art and the requirements of the project, the general objective of developing and testing a novel method to assemble composite facesheets to a honeycomb core using induction welding, to produce all-thermoplastic, adhesive free sandwich panels, is defined. To reach that general objective, the following sub-objectives are defined:

1. Propose a material selection methodology for induction welding hysteresis losses susceptors, based on the thermoplastic polymer processing temperature and the magnetic properties of candidate ferromagnetic particles.
2. Develop a method to inductively weld sandwich panels made of GF/PEEK facesheets and a 3D-printed PEI honeycomb core using hysteresis losses susceptors.
3. Manufacture the hysteresis losses susceptors as 3D-printing filaments and validate their printability and weldability.
4. Apply the induction welding method developed for sandwich panels to samples made of CF/PEEK facesheets to validate the method's adaptability to other materials.

2.3 Content of chapters 3 to 7

The content of the following chapters is linked to the identified objectives. Chapter 3 is composed of a journal paper presenting a methodology for the material selection of magnetic particles in hysteresis losses susceptors. Chapter 4 focuses on applying this methodology to a specific thermoplastic polymer (PEI) and characterize the resulting susceptor. Chapter 5 presents a second journal paper introducing a method to assemble skins to core in thermoplastic sandwich structures by induction welding under vacuum, using the susceptors developed in Chapter 4. Then, Chapter 6 proposes to replace susceptor films by 3D-printed susceptor layers, directly added to the honeycomb core. The development, production, and characterization of the susceptor filament is presented, followed by its deposition on honeycomb cores. These cores are welded to sandwich skins and characterized to validate the welding capability of the printed susceptor. Finally, Chapter 7 includes a third journal paper exploring the use of the vacuum induction welding method introduced in Chapter 5 to weld CF-based skins to honeycomb cores. Instead of using susceptor materials, the heat is directly dissipated inside the conductive carbon fibres, following the susceptor-less welding technique.

CHAPTER 3

MATERIAL SELECTION METHODOLOGY FOR AN INDUCTION WELDING MAGNETIC SUSCEPTOR BASED ON HYSTERSIS LOSSES

Romain G. Martin[a], Christer Johansson[b], Jason R. Tavares[c] and Martine Dubé[a],

[a] CREPEC, Department of Mechanical Engineering, École de technologie supérieure, 1100 Notre-Dame West, Montreal, Quebec, Canada H3C 1K3
[b] RISE Research Institutes of Sweden, Arvid Hedvalls Backe 4, Göteborg, Sweden, SE-411-33
[c] CREPEC, Department of Chemical Engineering, Polytechnique Montréal, 2500 chemin de Polytechnique, Montréal, Québec, Canada, H3T 1J4

Paper published in *Avanced Engineering Materials*, March 2022

3.1 Abstract

Induction welding is a fusion bonding process relying on the application of an alternating magnetic field to generate heat at the joining interface. This study investigates magnetic hysteresis losses heating elements, called susceptors, which are made of magnetic particles dispersed in a thermoplastic polymer. We propose a methodology to identify the parameters influencing the heating rate of the susceptors and to select suitable magnetic particles for their fabrication. The applied magnetic field amplitude is modelled based on the induction coil geometry and the alternating electrical current introduced to it. Then, properties of the evaluated susceptor particles are obtained through measurements of their magnetic hysteresis. A case study is presented to validate the suitability of the proposed methodology. Particles of iron (Fe), nickel (Ni) and magnetite (Fe_3O_4) are evaluated as susceptor materials in polypropylene (PP) and polyetheretherketone (PEEK) matrices. Heating rates are predicted using the proposed method, and samples are produced and heated by induction to experimentally verify the results. Good agreement with the predictions is obtained. Ni is the most suitable susceptor material for a PP matrix, while Fe_3O_4 is preferable for PEEK.

3.2 Introduction

The growing demand for thermoplastic composites in different fields such as aerospace has highlighted the need for techniques allowing their reliable and efficient assembly. Fusion bonding (or welding) offers an alternative to mechanical fastening and adhesive bonding for joining thermoplastic composites. Welding relies on the capability of thermoplastics to melt and flow to create a bond under pressure and solidify after cooling (Ageorges et al., 2001; Brassard et al., 2019, 2021; V. K. Stokes, 1989; Yousefpour et al., 2004). A few processes – ultrasonic, resistance and induction welding – are of particular interest for the aerospace industry. Among them, induction welding relies on the conversion of an electromagnetic field into heat using an implant, or heating element, called a susceptor. It is a fast process (Yousefpour et al., 2004) which can be automated and adapted to complex geometries (V. K. Stokes, 1989).

There are two major heat dissipation mechanisms exploited by susceptor materials: eddy currents and magnetic hysteresis. Eddy currents are induced in electrically-conductive materials subjected to a time-variable magnetic field (Figure 3.1a). They consist in electrical current closed loops which dissipate heat by resistive heating, also defined as Joule losses (Ahmed et al., 2006; Dermanaki Farahani & Dubé, 2017; Moser, 2012). When electrically-conductive carbon fibre-based composites are to be welded, the eddy currents can be induced directly in the adherends, without the need for a susceptor. Direct heating of the carbon fibre works best for fabrics, which provide the closed loops required for the eddy currents generation. When direct heating of the carbon fibre is not possible or if another composite material is used (e.g. glass fibre-based composites), an electrically-conductive susceptor is required at the weld interface, as schematized on Figure 3.1b (Dermanaki Farahani et al., 2018; Dermanaki Farahani & Dubé, 2017; Yarlagadda et al., 2016). The two main limitations of this heating mechanism are the need for continuity in the susceptor to achieve the creation of current loops and, when directly heating the adherends' carbon fibre, the magnetic shielding, which concentrates the electrical currents, and thus heating, close to the outer adherend's surface (Moser, 2012).

Alternatively, magnetic hysteresis exploits the property of ferromagnetic materials to dissipate heat when subjected to an alternating magnetic field. Magnetic hysteresis is observed in a susceptor because of the change in the material magnetization; a small amount of energy is dissipated into heat during every single hysteresis loop through magnetic hysteresis losses (Bayerl et al., 2014). To exploit magnetic hysteresis in welding (Figure 3.1c), the susceptor is typically made of ferromagnetic micro- or nanoparticles dispersed into a thermoplastic polymer film (Bae et al., 2015; Bayerl et al., 2012; Suwanwatana et al., 2006a).

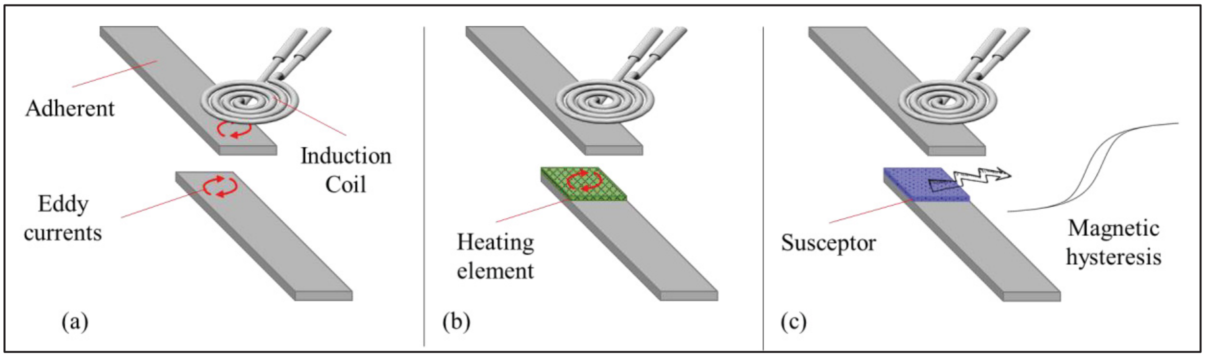

Figure 3.1 Schematic representation of heat dissipation in induction welding. (a) eddy currents induced directly in an electrically-conductive adherend. (b) eddy currents induced in an electrically-conductive susceptor. (c) heat dissipated by hysteresis losses in a magnetic susceptor

The heating power of various ferromagnetic particles was investigated by Wetzel and Fink, who defined the heating rate equation explored further in this article (Wetzel & Fink, n.d., 2001). They explored the theoretical heating capability of nickel (Ni), a hard ferrite (Strontium-ferrite) and a soft ferrite (Nickel-Zinc-ferrite). Based on this work, Suwanwatana et al. used Ni particles ranging from 79 nm to 22 μm into polysulfone (PSU) to demonstrate the feasibility of hysteresis heating and its application to weld polyphenylene sulfide (PPS) based composites (Suwanwatana et al., 2006a, 2006b). Bae et al. conducted a similar study and measured the heating capability of another magnetic material, iron (Fe) particles (8 to 74 μm), dispersed in thermoplastic polyurethane (TPU) adhesives (Bae et al., 2015). These two materials were also present among different particulate materials (carbon black, magnetite (Fe_3O_4), Ni and Fe) that Bayerl et al. explored when mixed with high-density polyethylene (HDPE) (Bayerl et al., 2012). Finally, Stokes used Emaweld products without disclosing the nature of the ferromagnetic particles dispersed in various thermoplastic matrices (V. K. Stokes, 1989). They all concluded on the susceptor material efficiency based on the experimental results. In these different studies, no proper justification is provided for selecting one susceptor material over another. In addition, the reported results are valid for a given thermoplastic matrix and a specific induction heating setup.

The goal of this work is to present a more general methodology to predict the heating capacity of ferromagnetic particles dispersed in a thermoplastic polymer, for a given induction heating equipment. To evaluate the heating capability of a susceptor, its initial heating rate, i.e. the heating rate at room temperature, is considered. A method is proposed to select a susceptor material with the highest initial heating rate and the ability to reach a pre-determined temperature corresponding to thermoplastic polymer processing temperature. This approach is applied to a case study in which three potential ferromagnetic materials (Fe, Ni and Fe_3O_4) are evaluated as susceptor candidates. Predicted heating rates are verified experimentally to assess the suitability of the material selection methodology.

3.3 Methodology for susceptor materials selection and heating rate prediction

3.3.1 Heating rate equation

Wetzel and Fink proposed a governing equation to express the heating rate of a magnetic susceptor under adiabatic conditions (Wetzel & Fink, n.d.):

$$\frac{dT}{dt} = f E_h \left(\rho c_p + \left(\frac{1}{v_f} - 1 \right) \tilde{\rho} \tilde{c}_p \right)^{-1} \tag{3.1}$$

with f being the frequency of the alternating magnetic field, E_h the hysteresis absorbed energy density for an applied magnetic field amplitude, v_f the volume fraction of ferromagnetic particles, ρ and $\tilde{\rho}$, the density of the magnetic particles and thermoplastic polymer, respectively, and c_p and $\tilde{c}_p$, their specific heat capacities. The terms ρc_p and $\tilde{\rho}\tilde{c}_p$ are the volumetric heat capacity of the magnetic particles and thermoplastic polymer, respectively. Equation (3.1) can be used to predict the heating rate of a given susceptor material, and hence identify the most efficient ferromagnetic material to use as a susceptor.

3.3.2 Magnetic field generation

The first parameters that must be known for the susceptor material selection are the frequency, amplitude and shape of the generated magnetic field. These parameters depend on the material and geometry of the coil and the intensity I and frequency f of the alternating electrical current circulating in it. The coil is generally a water-cooled copper tube, whose geometry has a significant impact on the magnetic induction field amplitude (V. K. Stokes, 1989). Various shapes and sizes of coil exist, and they must be chosen to comply with the application and weld geometry (Pappadà et al., 2015; Sanders, 1987; Troughton, 2009a).

The amplitude of the magnetic field applied on the susceptor is referred to as H_m. This amplitude depends strongly on the distance between the induction coil and the susceptor (i.e. the coupling distance). The shorter this coupling distance is and the higher the heating rate is. This distance is typically kept under 10 mm (Bayerl et al., 2012, 2014; Dermanaki Farahani et al., 2018; Pappadà et al., 2015; Rudolf et al., 2000; Suwanwatana et al., 2006a).

The coil material properties and its geometry as well as the electrical current intensity and frequency are used to calculate the magnetic field amplitude H_m at any point in space and especially at the joining interface. Finite elements modelling software such as FEMM 4.2 can be used to that end (Crozier & Mueller, 2016). The H_m value is then used to determine the absorbed energy density E_h.

3.3.3 Thermoplastic matrix

The susceptor material is composed of ferromagnetic particles dispersed in a thermoplastic matrix, which must be selected to be compatible with the composite adherends to be welded (Sanders, 1987). The glass transition temperature T_g and melting temperature T_m (for semi-crystalline polymers) of the thermoplastic matrix are obtained by Differential Scanning Calorimetry (DSC). The specific heat capacity of the polymer can also be extracted from DSC measurements following the ASTM E1269 standard.

3.3.4 Ferromagnetic particles

The main part of the susceptor material selection is the choice of the ferromagnetic particles. The density ρ and specific heat c_p of the material must be known. When subjected to an alternating magnetic field of frequency f, magnetic materials experience a magnetization whose direction will alternate at a similar frequency. The magnetization of ferromagnetic materials (e.g. cobalt (Co), Fe, Ni) lags behind the applied field, causing a magnetic hysteresis visible on the B-H curve (Figure 3.2), with H being the applied magnetic field and B the magnetic induction of the magnetic material.

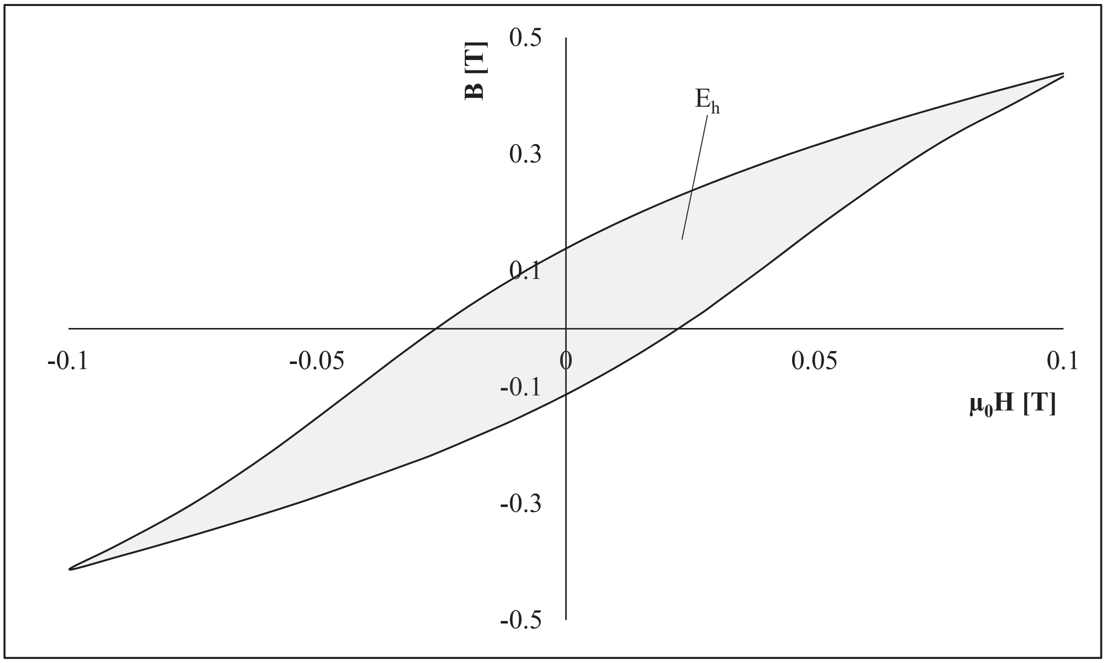

Figure 3.2 Hysteresis curve of a ferromagnetic material (magnetic induction B as a function of applied field H). The enclosed surface area (in grey) corresponds to the absorbed energy density E_h

The absorbed energy density per hysteresis loop and per unit volume E_h is determined as:

$$E_h = \oint HdB \tag{3.2}$$

and corresponds to the enclosed surface area (in grey in Figure 3.2) (Vinum et al., 2018). The magnetic permeability of vacuum μ_0 is equal to $4\pi \cdot 10^{-7}$ H m^{-1}. During every single loop of hysteresis, an amount of energy equal to the absorbed energy density E_h is dissipated into heat (Goodenough, 2002). The dissipated power per unit volume is thus obtained by multiplying the absorbed energy density E_h by the frequency f:

$$P_h = fE_h \tag{3.3}$$

Predicting E_h for given values of H_m is challenging. It can be done using the Steinmetz equation (classic and generalized (Goodenough, 2002; Landgraf et al., 2008; Muhlethaler et al., 2012; Steinmetz, 1984)), although its parameters are defined empirically and it is valid at low field amplitudes only (i.e. when the applied field amplitude H_m is largely smaller than the saturation field at which the material reaches its saturation magnetization). The best way to obtain E_h versus H_m is through Vibrating Sample Magnetometer (VSM) measurements for various field amplitudes and extrapolate the curve from the results (Vinum et al., 2018). If the experimentally applied field amplitude H_m is known, then only the hysteresis for that applied field is to be measured by VSM to extract the corresponding value of E_h for the magnetic material.

3.3.5 Curie temperature

Ferromagnetic materials exhibit temperature-dependent magnetic properties. As temperature increases, the material gradually loses its properties, until it reaches the Curie point (noted T_c) where they disappear (Chikazumi, 2009; Vinum et al., 2018). The Curie temperatures of magnetic materials are well-documented in the literature (Chikazumi, 2009; Coey, 2010).
Susceptor materials used in induction welding must have their T_c above the polymer processing temperature, as heating of the ferromagnetic particles is interrupted at T_c:

$$T_{c,particles}\ [K] > T_{process,thermoplastic}\ [K] + 10\% \tag{3.4}$$

A 10% margin is suggested as the magnetic properties of the ferromagnetic particles decrease when approaching T_c, leading to reduced heating capabilities. When $T = 0.9T_c$, the remaining magnetization is approximately 50% of its maximum value (Coey, 2010), corresponding to the lower limit ensuring efficient heating.

In some cases, susceptor materials can be selected so that T_c is above the polymer melting point but below the polymer degradation temperature. The susceptor is then used as a thermal control feature capable of melting the polymer and stop heating before degrading it. Unfortunately, T_c of ferromagnetic materials vary over a large range, from a few dozen degrees to over 1000 K. Finding a susceptor material exhibiting a T_c within the polymer's processing window is sometimes impossible.

3.3.6 Methodology summary

The presented methodology is summarized in Table 3.1. As explained, the three main steps are the characterization of the applied magnetic field using a finite element modelling software, the thermoplastic polymer thermal and physical properties using DSC and material technical datasheet (TDS), and the magnetic particles magnetic, thermal and physical properties using VSM measurements and material TDS. The Curie temperature of the evaluated magnetic particles must satisfy the criterion presented in Equation (3.4). Once all the required parameters are characterized, the heating rate can be predicted using Equation (3.1).

Table 3.1 Susceptor material selection methodology summary

	1. Magnetic field	**2.Thermoplastic polymer**	**3. Magnetic particles**
Parameters to define/characterize	H_m, f	T_m (or T_g), $T_{process}$, $\tilde{\rho}$, $\tilde{c}_p$	E_h, ρ, c_p, T_c, v_f
Method	Magnetic field modelling	DSC, TDS	VSM, TDS
T_c criterion	-	$T_{c,particles}\ [K] > T_{process,thermoplastic}\ [K] + 10\%$	
	↓	↓	↓
Heating rate prediction	$\frac{dT}{dt} = fE_h\left(\rho c_p + \left(\frac{1}{v_f} - 1\right)\tilde{\rho}\tilde{c}_p\right)^{-1}$		

3.4 Case Study

Three potential ferromagnetic materials for an induction welding susceptor film are evaluated as a case study, following the presented methodology (Table 3.1). The considered materials are Fe, Ni and Fe_3O_4. Two semi-crystalline thermoplastics are evaluated: a commodity polymer, polypropylene (PP), and a high-performance polymer, poly-ether-ether-ketone (PEEK). In the first part of the case study, the heating rates of the susceptors are predicted using the presented approach. In the second part, susceptor samples are prepared and the heating rate predictions are compared with experimental results to verify the method.

3.4.1 Heating rate prediction

3.4.1.1 Induction heating equipment

Induction heating is performed using an Ambrell EASYHEAT 10kW power supply (maximum current 750 A with a frequency range of 150-400 kHz). A hairpin coil is mounted on the induction working head. The intensity of the alternating current travelling through the induction coil is fixed at 700 A. The frequency is automatically calculated by the generator software to reach the LC resonance frequency of the induction coil, based on the following formula:

$$f = \frac{1}{2\pi\sqrt{LC}} \tag{3.5}$$

with L being the inductance of the coil and C the capacitance of the generator. For the present experiments, two 2 μF capacitors are mounted in series in the work head, providing a total capacitance C = 1 μF. Together with the inductance of the coil L = $0.35\ \mu H$, the resonance frequency is calculated by the generator to be 269 kHz. Induction experiments are conducted at that frequency.

The induction coil is equipped with a Ferrotron 559H magnetic field concentrator from Fluxtrol. The induction magnetic field around the hairpin coil and the field concentrator is calculated using the FEMM4.2 software (Crozier & Mueller, 2016), as presented in Figure 3.3a. Details about the finite element model are available in the supporting information (ANNEX I). The absolute value of the intensity of the induced magnetic field density H when located 5 mm away from the coil is shown in Figure 3.3b. The maximum intensity H_m is 32 kA m^{-1} (0.04 T) at 700 A and 269 kHz. An assumption is made that the presence of the magnetic susceptor does not impact the magnetic field lines.

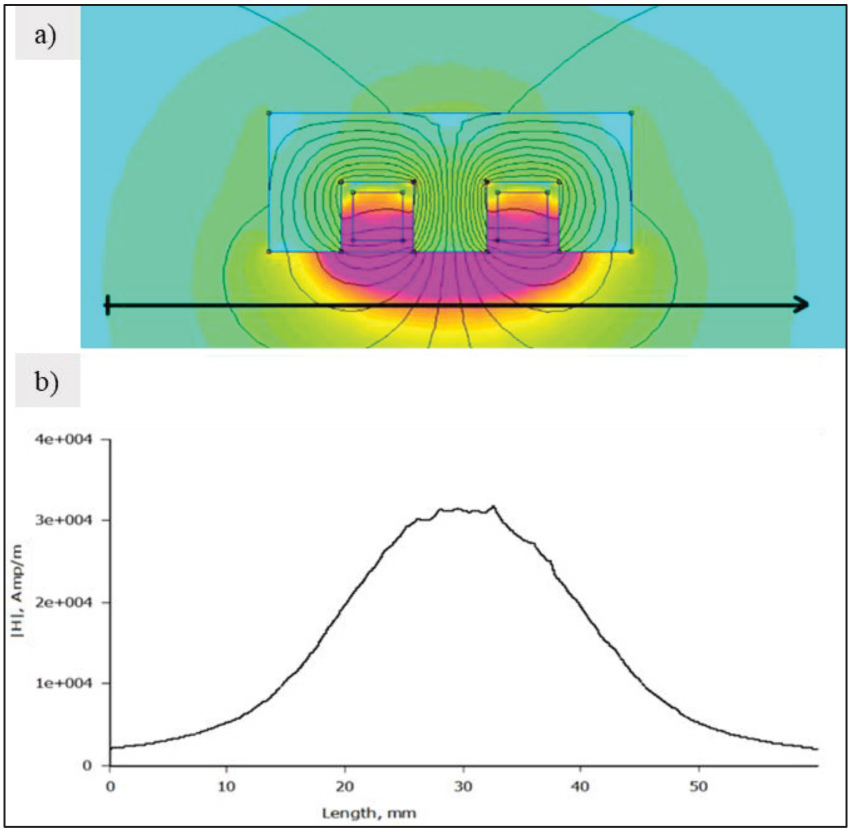

Figure 3.3 Magnetic field density simulation around a hairpin water-cooled copper coil equipped with a Ferrotron 559H field concentrator, with a 700 A current at 269 kHz. (a) Field amplitude in a profile perpendicular to the coil axis. Black arrow corresponds to the sample location, 5 mm away from the coil. The color code scales from light blue (<2kA/m) to purple (>40kA/m) with increments of 2kA/m. (b) Field amplitude along the black arrow. Center of the coil is located at 30 mm on the x-axis

3.4.1.2 Materials

PEEK (grade 90G from Victrex) and PP (grade 1104A from Pinnacle Polymers) densities are 1300 kg m^{-3} and 900 kg m^{-3}, respectively. Their melting points and recrystallisation temperatures are obtained by DSC with heating and cooling rates of 10 °C min^{-1}, as presented in Figure 3.4 and reported in Table 3.2. Their room temperature specific heat capacities are calculated from the DSC curves and are reported in Table 3.2.

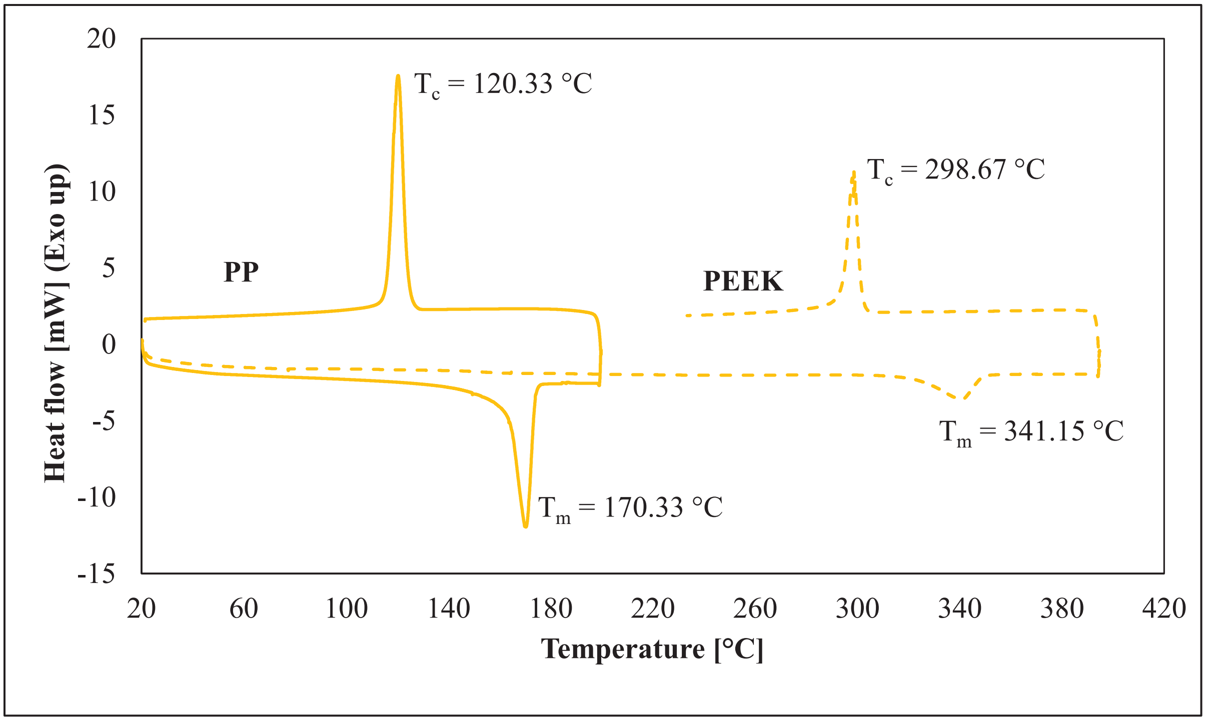

Figure 3.4 Heating and cooling DSC curves for PP (solid line) and PEEK (dashed line). The bottom peaks correspond to the melting of the polymer and the top peaks to the recrystallisation. The melting and recrystallisation temperatures are shown next to each peak

Table 3.2 PP and PEEK specific heat capacity, melting point and recrystallisation temperature, as measured by DSC

Material	**Specific heat capacity at 25 °C [J kg^{-1} K^{-1}]**	**Melting point [°C]**	**Recrystallisation temperature [°C]**
PP 1104A	1970	170	120
PEEK 90G	1140	341	299

Fe, Ni and Fe_3O_4 particles are well-known for their magnetic properties. Fe has a small coercivity and is typically classified as a soft magnet (Tumanski, 2011). Fe_3O_4 is classified as a hard ferrite and therefore exhibit a larger coercivity and hysteresis curve (Ahmadzadeh et al., 2017). Ni's magnetic properties are intermediate (Wetzel & Fink, n.d.). In general, materials with large coercivity exhibit large magnetic hysteresis. The goal of this methodology is to evaluate which of the three candidates can provide the highest heating rate when used as a susceptor under the described experimental conditions.

The particles diameter, density and specific heat capacity are summarized in Table 3.3, along with their T_c. All particles, including Fe_3O_4, have large enough diameters so that their magnetic properties fall in the multi-domain region. Fe_3O_4's critical diameter at which the material is in a single domain region and the coercivity is maximum is around 80 nm (Kneller & Luborsky, 1963; Krishnan et al., 2006; J. S. Lee et al., 2015; Mørup et al., 2011).

Table 3.3 Magnetic particles suppliers, mean diameters and densities (from materials technical data sheets), and specific heat capacities and Curie temperatures (from literature)

Material	**Supplier**	**Particles mean diameter [µm]**	**Density [kg m^{-3}]**	**Specific heat capacity [J kg^{-1} K^{-1}]**	**Curie temperature [°C]**
Fe	US Research Nanomaterials Inc.	45	7874	448 (Callister, 1997)	768 (Bayerl et al., 2014)
Ni	Sigma-Aldrich	50	8900	443 (Callister, 1997)	358 (Bayerl et al., 2014)
Fe_3O_4	Höganäs AB	0.8	5170	647 (Westrum & Grønvold, 1969)	575 (Bayerl et al., 2014)

3.4.1.3 Hysteresis curves

The magnetic hysteresis *B-H* curves of the three magnetic particles are measured, using a VSM model 7307 (Lakeshore Cryotronics). The maximum applied field H_m varies from 16 to 32, 40, 48, 64 and 80 kA m^{-1} (0.02, 0.04, 0.05, 0.06, 0.08 and 0.1 T). The absorbed energy density E_h of the three susceptor materials under these field amplitudes is calculated using equation (2) and reported in Figure 3.5. The corresponding hysteresis of Fe, Ni and Fe_3O_4 under H_m = 32 kA m^{-1}, the calculated field amplitude in the inductor, are presented in Figure 3.6. Ni presents the largest measured enclosed surface area (2200 J m^{-3}), with approximately 50% more absorbed energy than Fe_3O_4 (1500 J m^{-3}). Fe exhibits a small hysteresis and small coercivity and negligible enclosed surface area. These properties indicate that Fe particles cannot dissipate a large quantity of heat and thus are a poor magnetic susceptor.

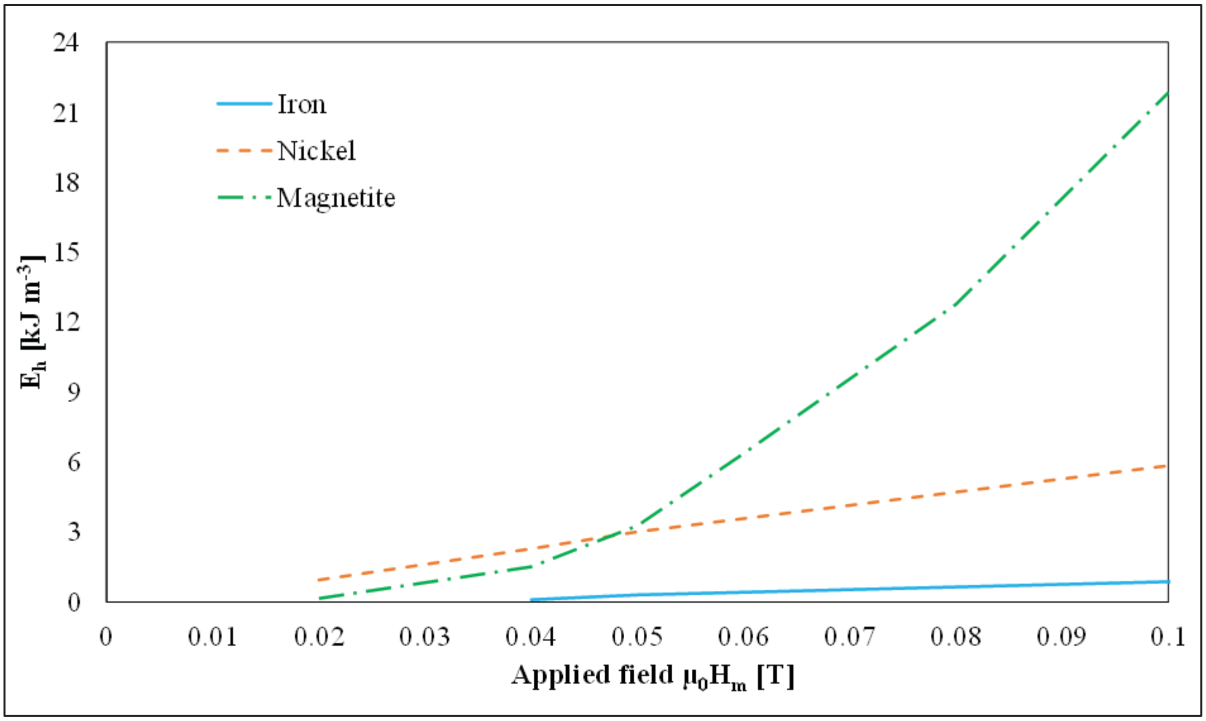

Figure 3.5 Absorbed energy density versus the applied field amplitude for Fe, Ni and Fe_3O_4 particles

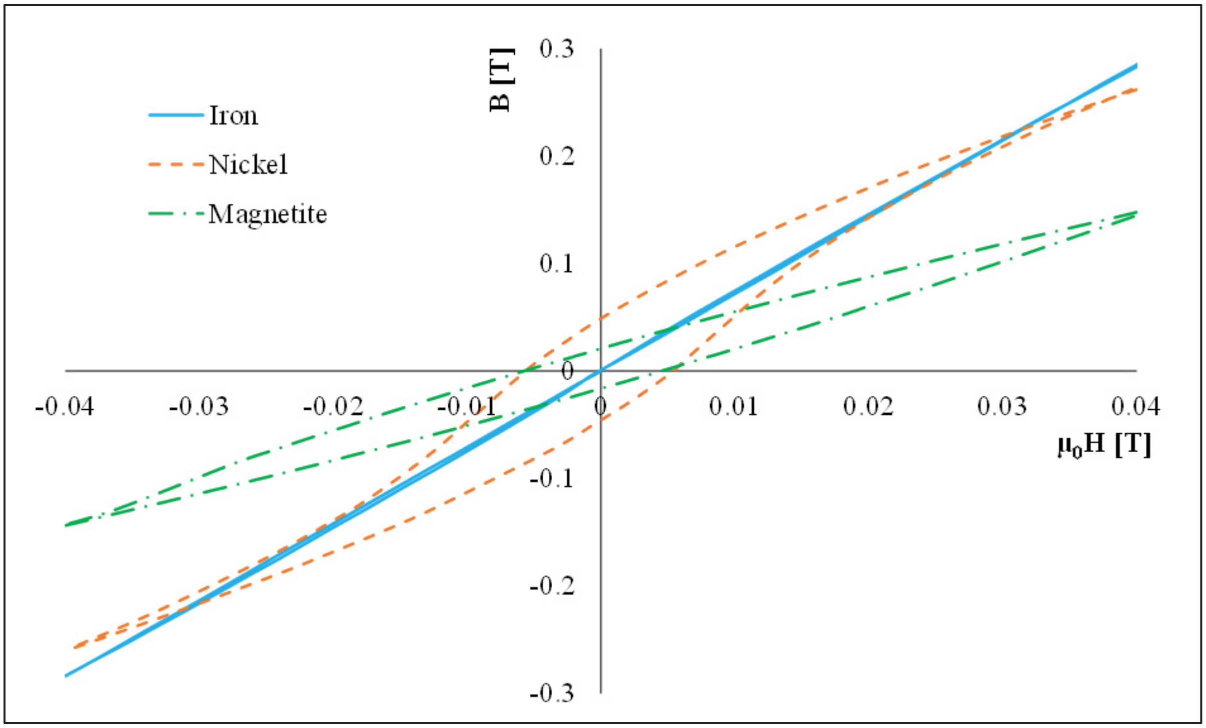

Figure 3.6 Hysteresis curves (B versus μ_0H) of Fe, Ni and Fe_3O_4 particles. The applied field amplitude H_m is 32 kA m^{-1} ($\mu_0H_m = 0.04$ T)

3.4.1.4 Predicted heating rate

Equation (3.1) is used to calculate the initial heating rate for Fe, Ni and Fe_3O_4, mixed with PP and PEEK (5%vol and 10%vol). It appears clearly in equation (3.1) that the predicted heating rate is proportional to the absorbed energy density, or the hysteresis enclosed surface area. On this basis, Ni-based susceptor films should exhibit the largest initial heating rate, due to Ni's largest magnetic hysteresis under the applied field density of 32 kA m^{-1}. Table 3.4 summarizes the predicted heating rates for PP and PEEK susceptors for the two considered magnetic particles and two volume fractions. The predicted initial heating rates of the PP and PEEK susceptors are similar, which is due to the close volumetric specific heat capacity of the two thermoplastic matrices. However, Ni does not satisfy equation (3.4) as its Curie temperature (631 K = 358 °C) is lower than the PEEK processing temperature of 380 °C to 400 °C. Therefore, although Ni offers a higher heating rate than Fe_3O_4, it cannot reach the PEEK processing temperature and is not a suitable susceptor for this polymer. We conclude that Ni is a good choice of susceptor for PP (offers higher heating rate than Fe_3O_4 and can reach the PP processing temperature) while Fe_3O_4 is better for PEEK (lower heating rate but can reach the PEEK processing temperature). Fe susceptors should present a negligible heating rate due to hysteresis losses because of the negligible enclosed surface area of Fe's magnetic hysteresis (Figure 3.6). Their predicted value of initial heating is then set at 0 in Table 3.4.

Table 3.4 Predicted initial heating rates for PP- and PEEK-based susceptors, mixed with Fe, Ni and Fe_3O_4 particles, at 5%vol and 10%vol under a 32 kA m^{-1} magnetic field amplitude and a frequency of 269 kHz

	Predicted initial heating rate [K s^{-1}]			
Polymer	**PP**		**PEEK**	
Volume fraction	5%	10%	5%	10%
Ni	15.7	29.7	18.4	34.3
Fe_3O_4	10.9	20.9	12.8	24.2
Fe	0	0	0	0

3.4.2 Experimental validation

3.4.2.1 Samples preparation

Susceptor samples are prepared by mixing magnetic particles with either PP or PEEK in a Thermo Scientific HAAKE Minilab II micro-extruder. The polymer is melted at 180 °C (PP) and 370 °C (PEEK) for 5 minutes. The Fe, Ni or Fe_3O_4 particles are then added and mixed with the polymer for 10 minutes, and the resulting mix is extruded. The remaining material inside the machine is also recovered. To ensure a more homogeneous distribution of the particles, the extruded material is melted and mixed again in the micro-extruder, following the same procedure. After this second mixing step, the obtained material is shredded into small pellets and pressed into a 1-mm thick film in a hot press. The polymers are pressed at 180 °C for PP and 370 °C for PEEK under a pressure of 5 MPa for 5 minutes. Two volume ratios, 5% and 10%, are considered for each combination of polymer and magnetic particles. Samples are cut into 4 cm x 4 cm specimens for characterization.

Temperature during induction heating is measured using a Jenoptik IR-TCM HD infrared thermal camera. The maximum temperature measured over the sample is recorded and used to produce the heating curves. To perform an accurate quantitative thermography analysis, the emissivity of the sample is first estimated (Testo SE & Co., 2017): the sample is placed on a heating plate, and temperature is monitored with a thermocouple and the thermal camera, set with a default emissivity of 1. The ratio between the two values is the actual emissivity of the sample: 0.9 for both PP-Ni and PEEK-Ni samples, and 0.94 for both the Fe- and Fe_3O_4-based samples. The emissivity value is considered as temperature-independent.

Temperature evolution during induction heating is extracted from the thermal camera using the IRT Analyzer 7 software. The initial heating rate is the largest slope of the curve (i.e. the largest temperature increase over an elapsed time of 1 s), which typically occurs at the beginning of the heating, as shown in Figure 3.7.

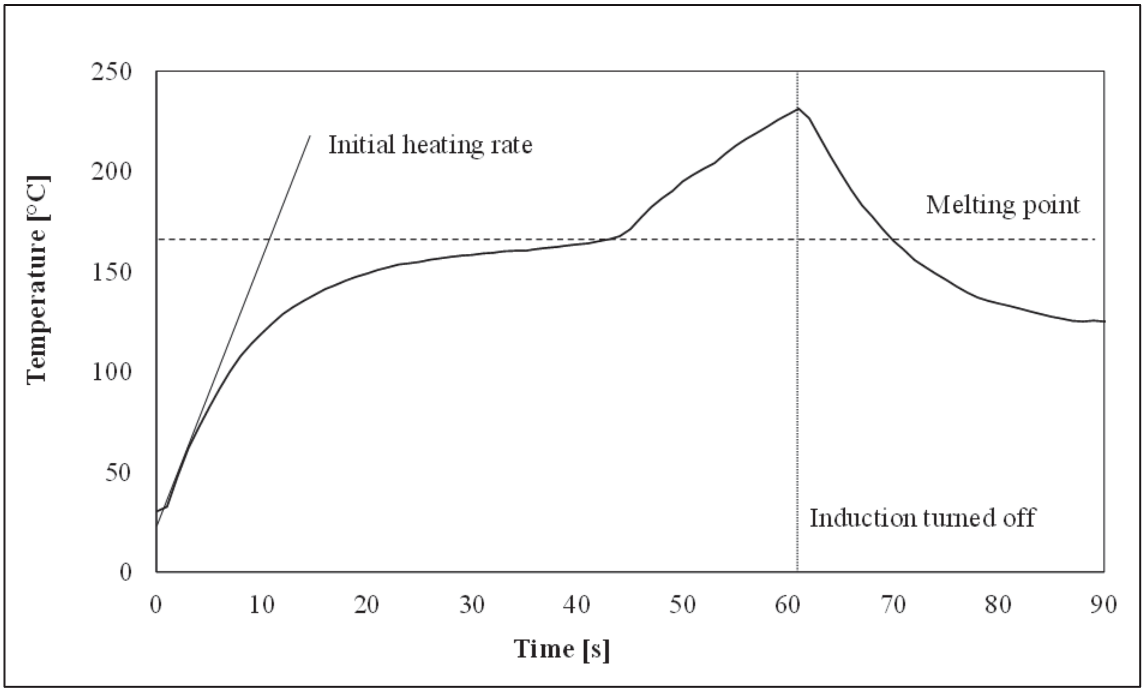

Figure 3.7 Typical induction heating curve (PP/Ni-5% specimen). The straight-line slope represents the initial heating rate, and the dashed line corresponds to the thermoplastic melting point. The flattening of the curve when approaching the melting temperature is due to the endothermic phase change. Induction heating is turned off after 60 seconds (dotted line)

3.4.2.2 Experimentally measured heating rates

The temperature evolution of the sample during induction heating is measured using the setup presented in Figure 3.8. The distance between the coil and the sample is fixed at 5 mm. The hairpin coil is equipped with a magnetic field concentrator, as previously explained. The IR camera records the temperature evolution.

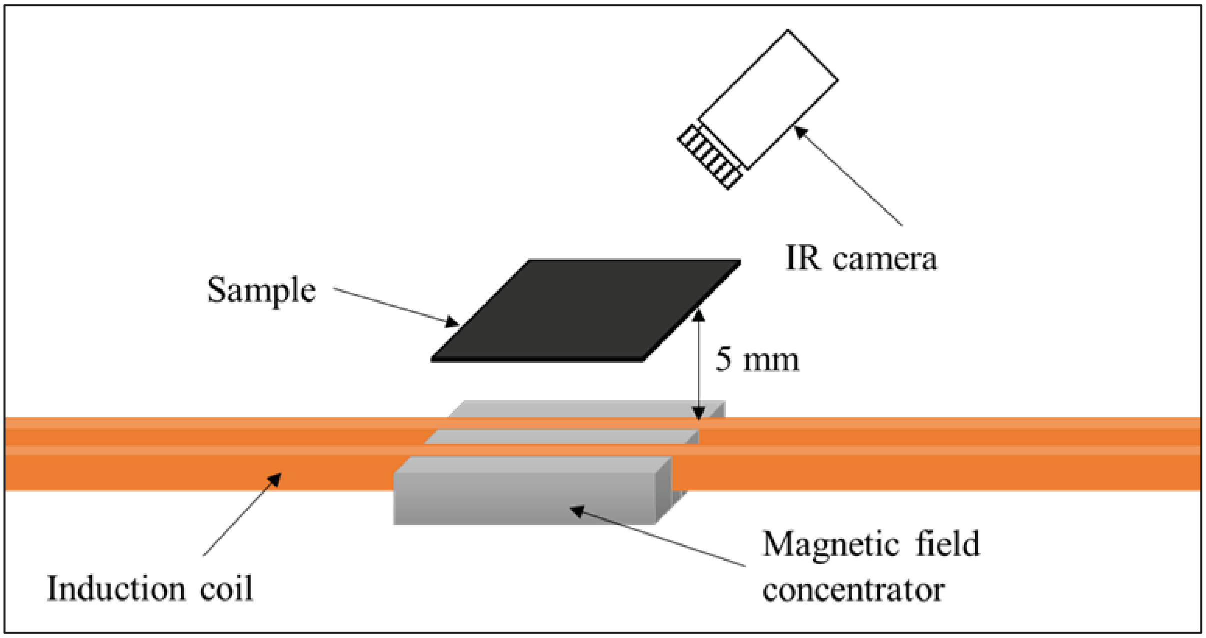

Figure 3.8 Induction heating setup scheme

Initial heating rates of PP-based susceptors are presented in Table 3.5. Samples made of Fe, Ni and Fe_3O_4 at volume fractions of 5% and 10% are prepared and four specimens per sample are used. Figure 3.9 presents the full heating curves for one representative specimen from each sample. Ni-based susceptors exhibit a larger initial heating rate at both volume fractions, as predicted by the model equation. Experimental values are lower than the model predictions because the model does not consider thermal losses by conduction into the support plate or by convection into the surrounding ambient air. Fe_3O_4-based samples show lower heating rates than Ni-based ones, but they are higher than the predicted values. This is explained by the presence of small hot spots observed during heating, attributed to locally higher volume fraction of Fe_3O_4 than in the rest of the sample. An improved distribution would reduce such occurrences and produce more consistent results. Fe-based samples present the lowest initial heating rates, as expected from the model. The observed heating rates most probably come from the heat dissipated by induced eddy currents in the Fe particles. However, such heating is too small to reach the melting point of PP. In general, as predicted from the model (equation (3.1)), susceptors made of Ni particles heat faster than Fe_3O_4-based ones.

Table 3.5 Predicted and measured initial heating rate for PP- and PEEK-based susceptors, mixed with Fe, Ni, and Fe_3O_4 particles, at 5%vol and 10%vol under a 32 kA m^{-1} magnetic field amplitude and a frequency of 269 kHz

Initial heating rate (Predicted / Measured) [K s^{-1}]				
Polymer	**PP**		**PEEK**	
Volume fraction	5%	10%	5%	10%
Ni	15.7 / 13.6	29.7 / 25.7	18.4 / 16.5	34.3 / 28.7
Fe_3O_4	10.9 / 10.6	20.9 / 22.3	12.8 / 9.8	24.2 / 25.1
Fe	0 / 3.0	0 / 3.9	-	-

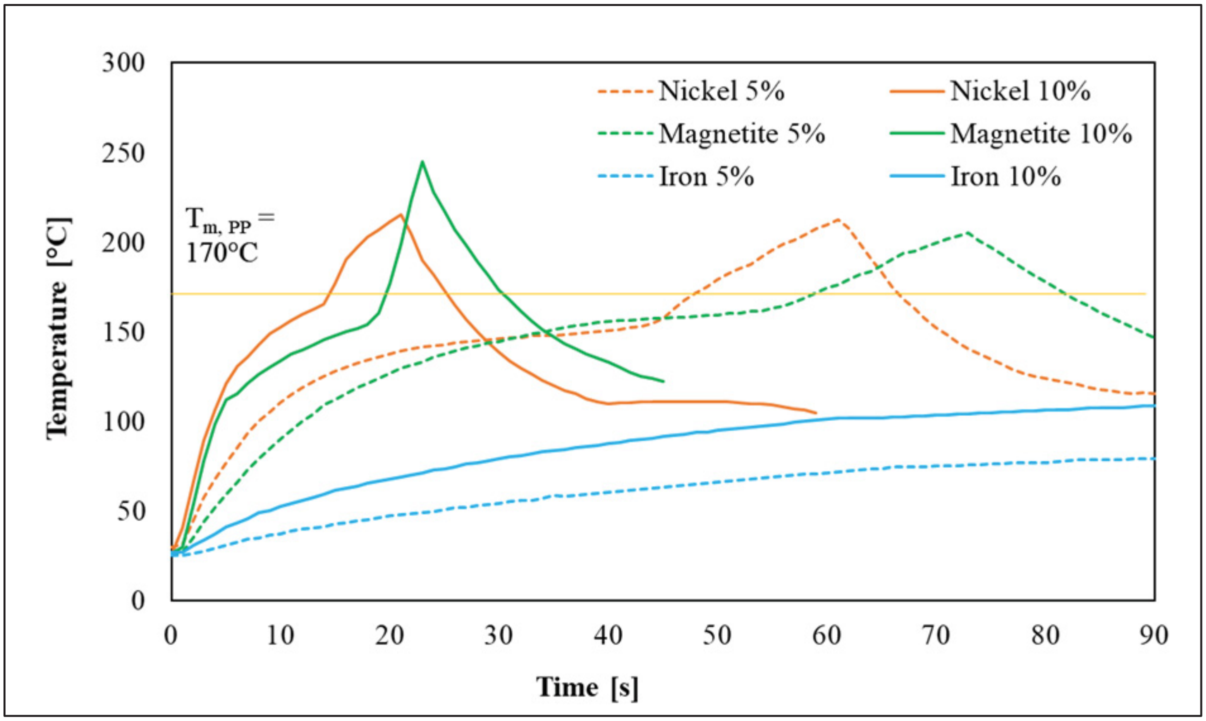

Figure 3.9 Induction heating of PP-based susceptors (applied magnetic field amplitude of 0.04 T, frequency of 269 kHz). Induction was turned off when reaching 250 °C to avoid sample degradation. Dashed lines correspond to particles concentration of 5%vol and solid lines to 10%vol

Due to the poor results of the PP/Fe susceptors, Fe is not evaluated with PEEK. The model predicts a larger initial heating rate for PEEK/Ni susceptors, but the T_c of Ni should prevent it from reaching the melting point of PEEK (343 °C). Experimental results confirm this hypothesis; the 5%vol Ni sample only reached 202 °C and the 10%vol sample reached 264 °C. Figure 3.10 shows a representative heating curve for each sample. The 5%vol PEEK/Fe_3O_4 sample do not reach the melting point either, showing a maximum measured temperature of 283 °C, likely due to thermal losses in the surrounding air and in the supporting plate. However, the 10%vol PEEK/Fe_3O_4 sample was able to melt PEEK. During this test, induction heating was turned off after 45 seconds to avoid burning the thermoplastic. The results for PEEK-based susceptors also agree with the model prediction, which correctly determined that the favorable magnetic particle material to use is Fe_3O_4.

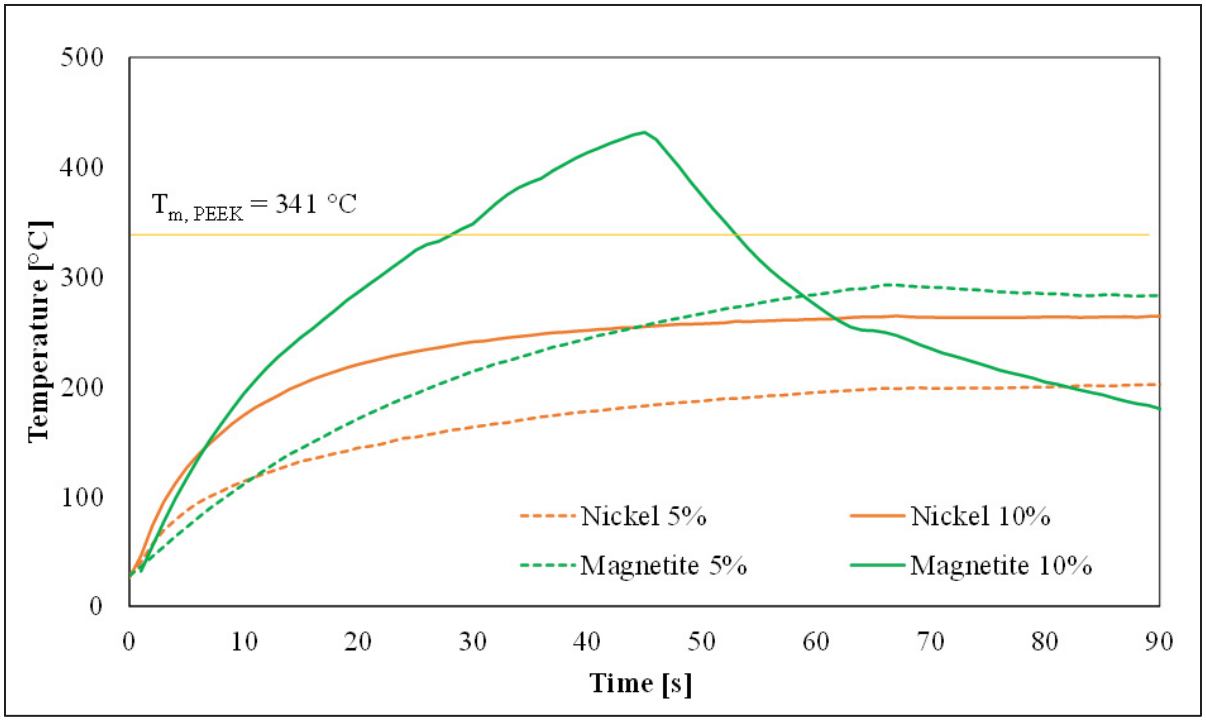

Figure 3.10 Induction heating of PEEK-based susceptors (applied magnetic field amplitude of 0.04 T, frequency of 269 kHz). Only the PEEK/Fe_3O_4-10%vol sample reached the melting point (solid green curve), for which induction was turned off after 45 seconds. Dashed lines correspond to particles concentration of 5%vol and solid lines to 10%vol

3.4.3 Discussion

Experimental results generally show lower heating rates than the model predictions. This can be explained by equation (3.1) being valid for thermally insulated susceptors, without consideration for any heat transfer by convection with the surrounding air or by conduction in the samples support. The presented methodology nonetheless provides the correct ranking of the three susceptors heating efficiency, offering engineers a tool to determine which susceptor material is the most suitable for a given thermoplastic matrix and the generator used for induction heating. On a practical note, however, the hardness of Fe_3O_4 presents a processing drawback for the mixing with the thermoplastic matrix. On the Mohs scale, Fe_3O_4 has a hardness ranging from 6 to 6.5 (Wilson, 1992), whereas Ni and Fe typically have a hardness of 4 (*The Hardness of Metals: A Visual Representation of the Mohs Scale for Mettalic Elements and Alloys*, n.d.). Mixers are typically made of steel (hardness between 4 and 4.5), meaning that Ni and Fe cannot scratch it, but Fe_3O_4 can. Abrasion was observed on the micro-extruder used during the mixing procedure. Special mixers made of harder materials (e.g. ceramics or hardened steels), should be used to avoid damaging the equipment while mixing Fe_3O_4 with thermoplastic polymers.

Another observation made during the experiments is the apparent phase change that Fe_3O_4 underwent during mixing with PEEK at 380 °C. The dark grey/black color of the Fe_3O_4 particles before mixing became a brown color, similar to rust. This reveals the possible presence of maghemite (γ-Fe_3O_2), which is an intermediate state in the transformation from Fe_3O_4 to hematite (Fe_3O_2) that appears at temperatures around 300-400 °C (Wahyuningsih et al., 2019). The complete transformation into Fe_3O_2 occurs at higher temperature (around 600 °C). γ-Fe_3O_2 has the same atomic structure as Fe_3O_2 but remains in the same crystalline structure as Fe_3O_4, which gives somewhat similar magnetic properties (Shokrollahi, 2017). Its absorbed energy density is considered as equal to the one measured for Fe_3O_4.

3.5 Conclusion

A methodology was presented to select susceptor materials for the induction welding of thermoplastic composites, with minimal material characterization effort. The proposed methodology can be applied to any combination of magnetic particles and thermoplastic matrices, being a reliable screening tool for material selection of induction welding susceptor films relying on hysteresis losses for heat generation. The methodology requires knowledge of the magnetic field amplitude that the welding setup can produce, the thermal properties of the matrix and particles used for the susceptor and the magnetic hysteresis of the magnetic particles as measured by VSM.

A case study was presented in which three magnetic particles and two thermoplastic polymers were considered for susceptor manufacturing. The heating rate was predicted based on Wetzel and Fink equation and compared with experimental data. A good agreement was obtained, although the prediction does not consider thermal losses in the environment. Fe presented poor heating rates with PP and therefore was not investigated with PEEK. Ni was shown to be the most appropriate susceptor material to melt PP while Fe_3O_4 was more appropriate for PEEK, due to the low Curie temperature of Ni.

3.6 Acknowledgements

The authors acknowledge financial support from NSERC (Natural Sciences and Engineering Research Council of Canada) (grant number ALLRP 556497 - 20), the Canadian Space Agency (CSA), Ariane Group, Nanoexplore, Mëkanic and CREPEC (Centre for Applied Research on Polymers and Composites).

CHAPTER 4

DEVELOPMENT OF A PEI/NI SUSCEPTOR

This chapter presents the work conducted on the preparation of magnetic hysteresis losses susceptors that will be used in Chapter 5. Part of the work presented here was published in the SAMPE Journal in 2023 (Martin, Figueiredo, et al., 2023a). The paper is presented in ANNEX II.

4.1 Context

As presented in Chapter 3, magnetic hysteresis losses susceptors are promising heating elements for induction welding of thermoplastic composites structures. Here, it is desired to apply the method for the assembly of PEEK-based composites. The typical thermoplastic welding method for those materials is to weld directly PEEK on PEEK, which requires the interface to reach the PEEK welding temperatures, which are typically around 380-400°C (Li et al., 2021; Silverman & Griese, 1989). The problem with this strategy is that, at these elevated temperatures, the PEEK matrix is molten and the composite laminates that must be assembled face a high risk of deconsolidation. This would result in porosities between the fibre layers and dramatically reduce the mechanical performance of the parts. To mitigate this effect, the heat must be generated at the welding interface and not be conducted to the rest of the parts, or the parts must remain under consolidation pressure all the time they are subjected to high temperatures to avoid deconsolidation.

Another strategy is to apply the Thermabond process (presented in 1.1.5), which relies on an intermediate layer of PEI located at the welding interface to perform the weld at a temperature below the PEEK melting point, typically in the 280-300°C range. When applying this strategy for induction welding, hysteresis losses susceptors must be based on PEI to properly weld the parts to be joined. Based on the materials selection methodology presented in Chapter 3, Ni particles are a good candidate for PEI-based susceptor, as their

Curie temperature (358°C) is higher than the target welding temperature range, but lower than the degradation temperature of the polymer (450 °C (Carroccio et al., 1999)). It is therefore interesting to investigate the manufacturing and characterization of PEI/Ni susceptors for induction welding magnetic susceptors.

4.2 Methodology

PEI pellets (ULTEM 1010 grade from SABIC) and Ni particles (5 µm of average diameter particles from Sigma-Aldrich) are dried beforehand for 4 to 6 hours at 150°C to ensure that no moisture is present during processing, as this would result in porosity formation and potential material degradation. Compounding is conducted in a Haake^{TM} Rheomix OS 1010 internal mixer at 320°C and 50rpm. This machine is equipped with two co-rotating rollers and allows to prepare batches of up to 45cm^3 of material. The PEI pellets are first added to the mixer and soften for 5 min before adding the Ni particles. The two materials are mixed for 5 more minutes before recovering the compounded material. Three volume fractions of Ni are evaluated: 10%vol, 15%vol and 20%vol. The resulting material is then shredded into pellets (using an industrial shredder) to be subsequently formed into films using a hydraulic hot press for 10 minutes under 1 MPa of pressure at 320°C. Two types of samples are cut from the films for characterization: 1 cm x 1 cm squares for optical microscopy observations, and 4 cm x 2 cm samples for density and induction heating measurements.

The optical microscopy samples are mounted in acrylic resin and polished using the procedure described in ANNEX III and analyzed using an Olympus GX-51 optical microscope. A visual qualitative analysis is conducted on the images to determine the porosity level and the homogeneity of the particles’ distribution in the polymer matrix.

Induction heating samples are then used, first for density measurements to define the Ni volume fraction and verify that it matches the expected concentration. Two methods are applied for this measurement. First, the thickness of the sample is obtained by taking the average of three points of measure along the length of the sample. The volume is then obtained by multiplying this thickness by the surface of the sample, which is assumed to be similar for all samples and equal to 8 cm^2. The sample is then weighted, and the result is divided by the previously obtained volume to get the experimental density. This first method – later reported as "Volume method" – is very fast, simple, and only requires a scale. The second method is the water displacement method, also known as the Archimedes method, which is explained in ASTM D792 standard. This method requires to weigh the sample in air, and then repeat the same measurement in water, typically by hanging the sample below a scale and immerging it into water. The density with this method is calculated per Equation (4.1):

$$\rho \left[\frac{kg}{m^3}\right] = \frac{m_{air}}{m_{air} + m_{wire} - m_{water}} \cdot 997.5 \left[\frac{kg}{m^3}\right] \tag{4.1}$$

With m_{air} the mass of the sample in air (directly on the scale), m_{water} the mass of the sample completely immersed in water, and m_{wire} the mass of the partially immersed wire used to hold the immersed sample. The 997.5 kg/m^3 corresponds to the density of water at 23°C. It must be adjusted in the temperature is different. This method is expected to be more precise as it does not require to measure or calculate the volume. It is therefore most efficient for samples of complex geometry. Eight samples of each Ni volume fraction are tested with both methods to obtain a representative measurement of the density at the different Ni contents. The experimental results are compared with theoretical densities obtained by applying the rule of mixture, per Equation (4.2):

$$\rho = v_{f,Ni} \cdot \rho_{Ni} + \left(1 - v_{f,Ni}\right) \cdot \rho_{PEI} \tag{4.2}$$

With $v_{f,Ni}$ the volume fraction of Ni particles, and ρ_{Ni} and ρ_{PEI} the densities of Ni particles and PEI pellets, respectively.

Due to thickness variability of the density samples, only those with thicknesses as close to 0.6 mm as possible are retained, to avoid inducing variability in the induction heating measurements. Therefore, five samples out of the eight used for density measurements are selected for induction heating tests. A similar setup to the one described in Chapter 3 is used for these measurements. It consists of an induction coil which generates an alternating magnetic field in the surrounding air. It is equipped with a Ferrotron 559H (Fluxtrol) magnetic field concentrator (MFC) to concentrate the magnetic field at the sample and increase locally the field amplitude. The current is supplied to the coil by an Ambrell EASYHEAT 10 kW generator. The frequency of the magnetic field, adjusted by the setup to match the resonance frequency of the system, is automatically fixed at 388 kHz. The sample is placed on a Kapton film held by two supports to minimize cooling due to thermal conductivity in the support. The supports also allow to control the coupling distance, which is the distance between the coil and the sample. This distance is fixed at 4 mm. Finally, the thermal evolution of the sample during the test is recorded by a FLIR A700 thermal camera fixed above the sample. The testing setup is presented in Figure 4.1. For all the tests, the emissivity of the PEI/Ni samples is fixed at 0.9, as in Chapter 3. The testing procedure is to turn on the induction heating for 60 s, then turn it off and keep recording the temperature evolution for an extra 60 s.

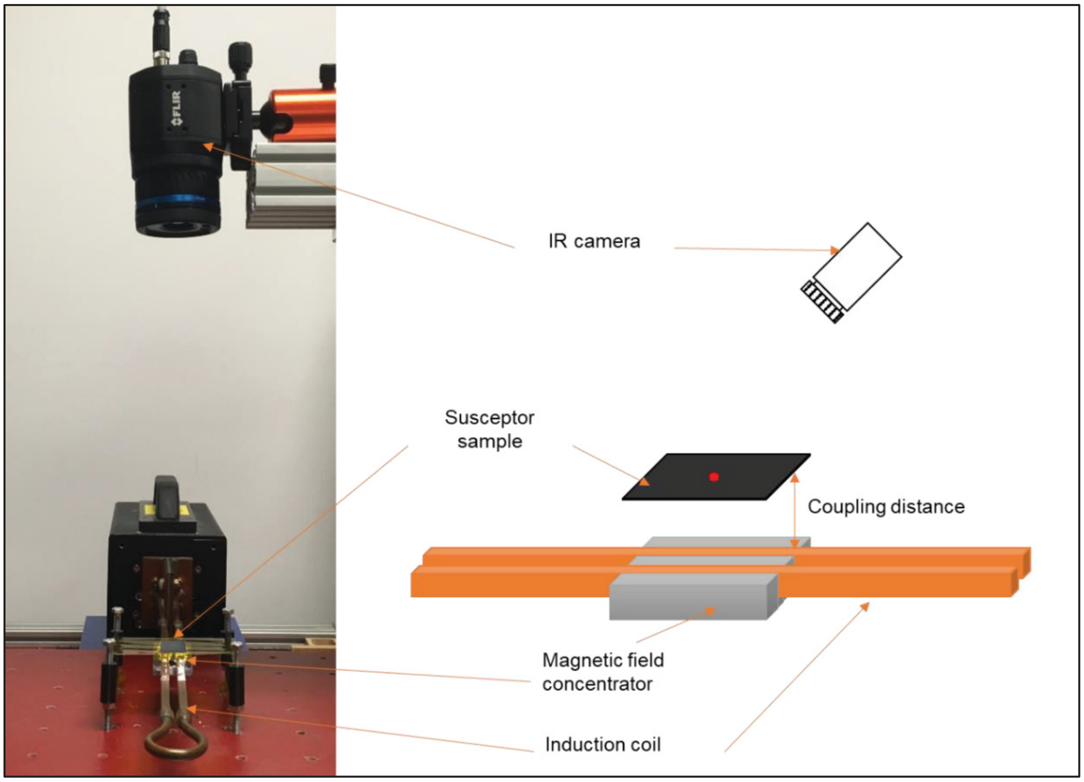

Figure 4.1 Picture (left) and schematic (right) of the induction heating characterization setup. The sample is supported by a Kapton film held by two supports, which allows to tune the coupling distance. The red point is the location where the temperature evolution is recorded by a thermal camera located above the sample

4.3 Results

Two representative optical micrographs for each 10%vol, 15%vol and 20%vol Ni concentrations are presented in Figure-A II., Figure 4.3 and Figure 4.4. It appears that there are no visible porosities at these three concentrations, and no visible agglomerates of Ni particles. It is therefore assumed that the porosity level is zero and the particles distribution is homogeneous, highlighting the good quality of the production process.

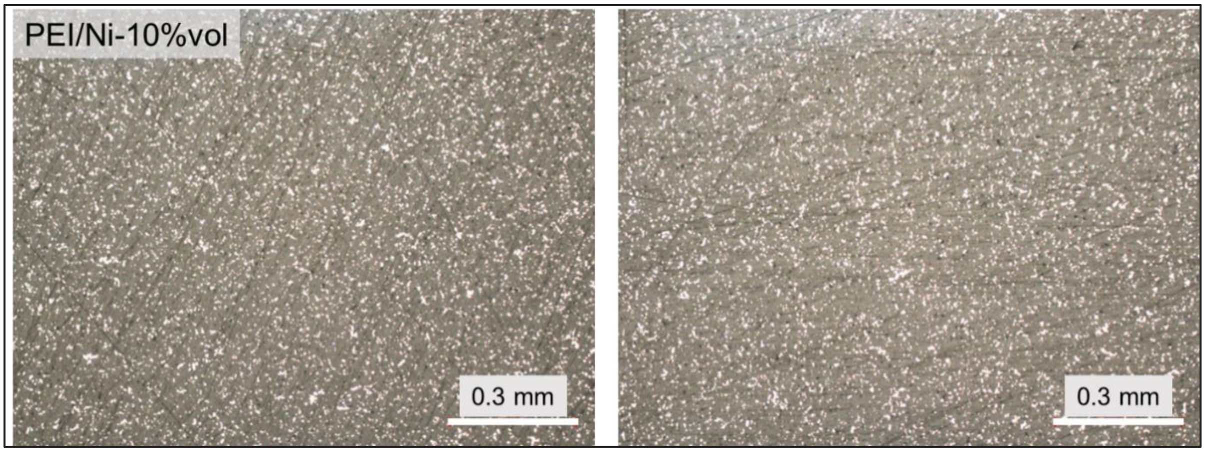

Figure 4.2 PEI/Ni susceptor films observed by optical microscopy with volume fraction of 10% of Ni particles. The grey area corresponds to the PEI matrix, and the white spots are the Ni particles. White scalebar is 300 microns

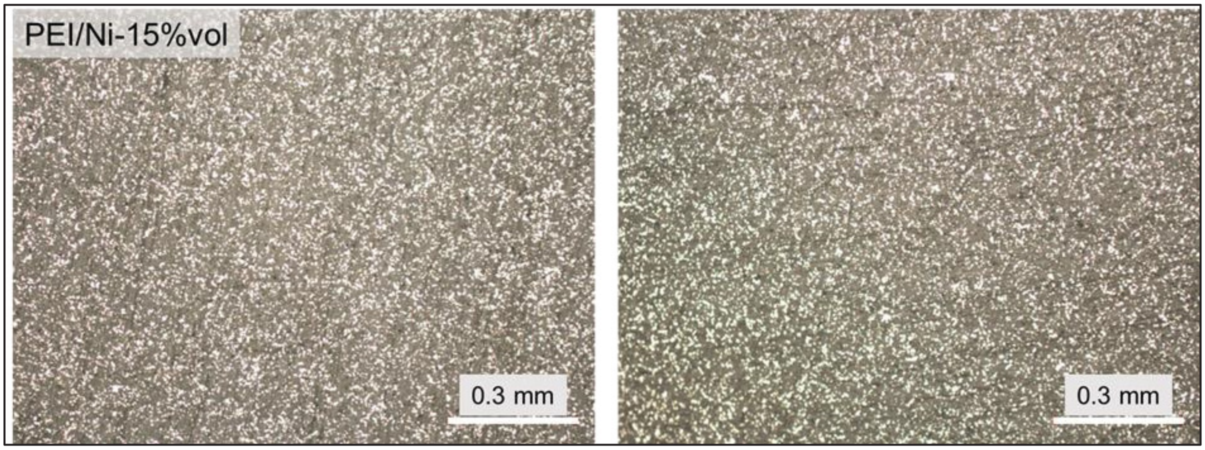

Figure 4.3 PEI/Ni susceptor films observed by optical microscopy with volume fraction of 15% of Ni particles. The grey area corresponds to the PEI matrix, and the white spots are the Ni particles. White scalebar is 300 microns

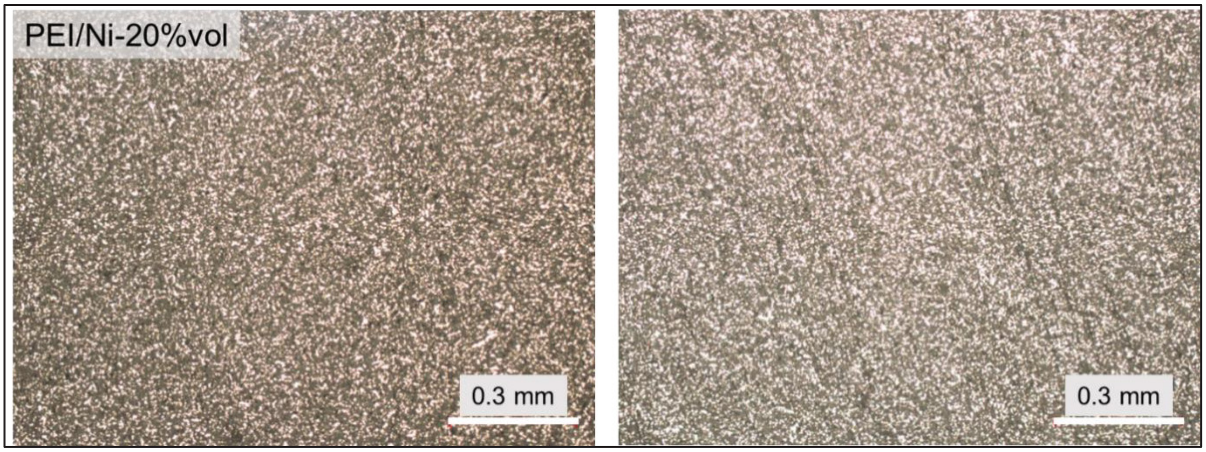

Figure 4.4 PEI/Ni susceptor films observed by optical microscopy with volume fraction of 20% of Ni particles. The grey area corresponds to the PEI matrix, and the white spots are the Ni particles. White scalebar is 300 microns

Eight samples for each concentration are tested and their densities are compared with the theoretical value obtained by the rule of mixture. For each sample, both methods are applied and compared to the theoretical density. The difference between experimental and theoretical values is presented in Figure 4.5 for 10%vol, in Figure 4.6 for 15%vol and in Figure 4.7 for 20%vol. The measurements generally do not deviate by more than 5% from the theoretical density. Based on the eight measurements for each concentration, average density and standard deviation are calculated.

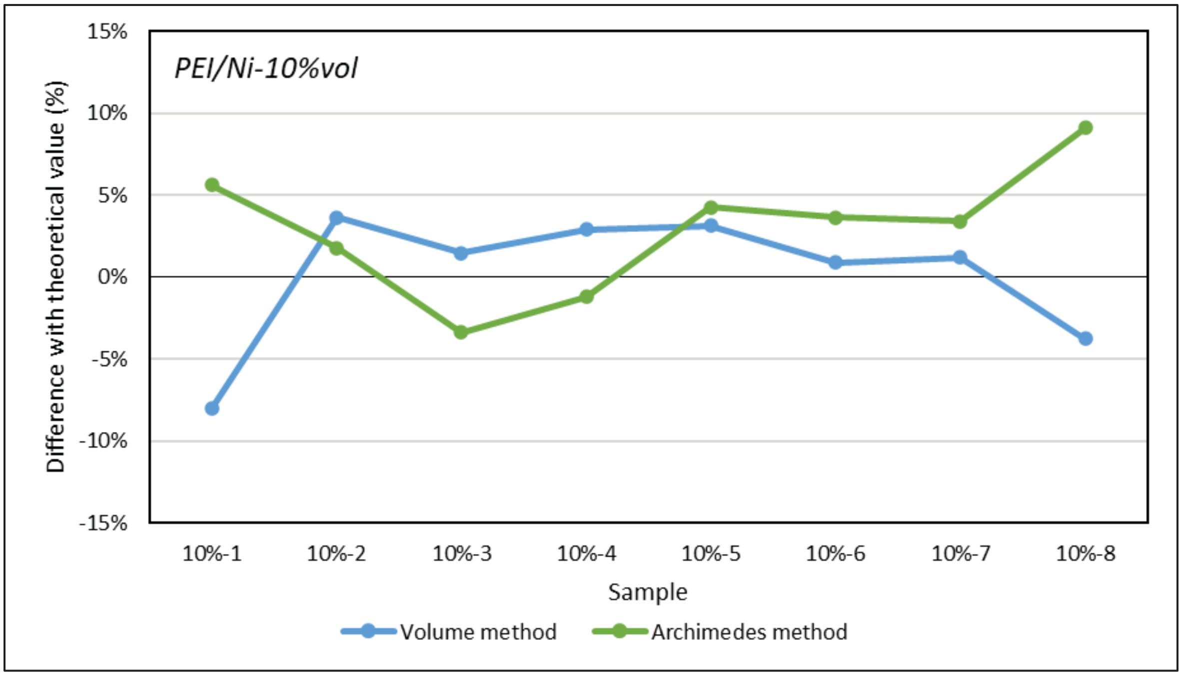

Figure 4.5 Experimental density of PEI/Ni-10%vol susceptor samples compared to the theoretical density obtained by the rule of mixture

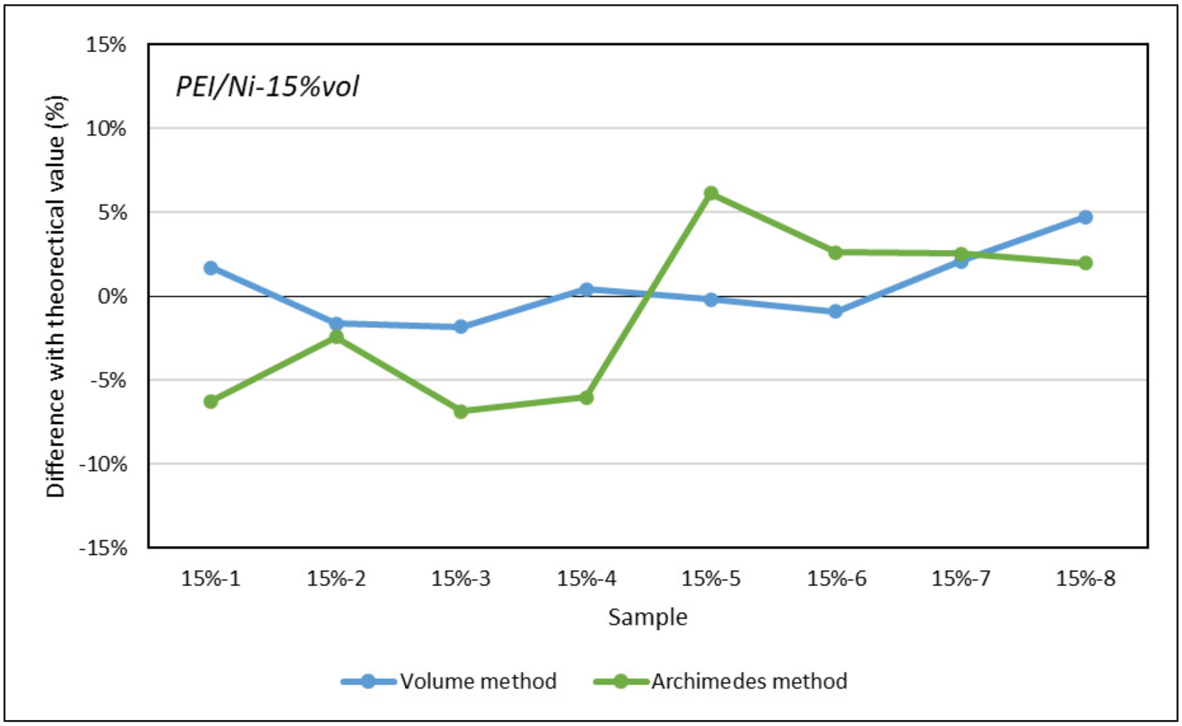

Figure 4.6 Experimental density of PEI/Ni-15%vol susceptor samples compared to the theoretical density obtained by the rule of mixture

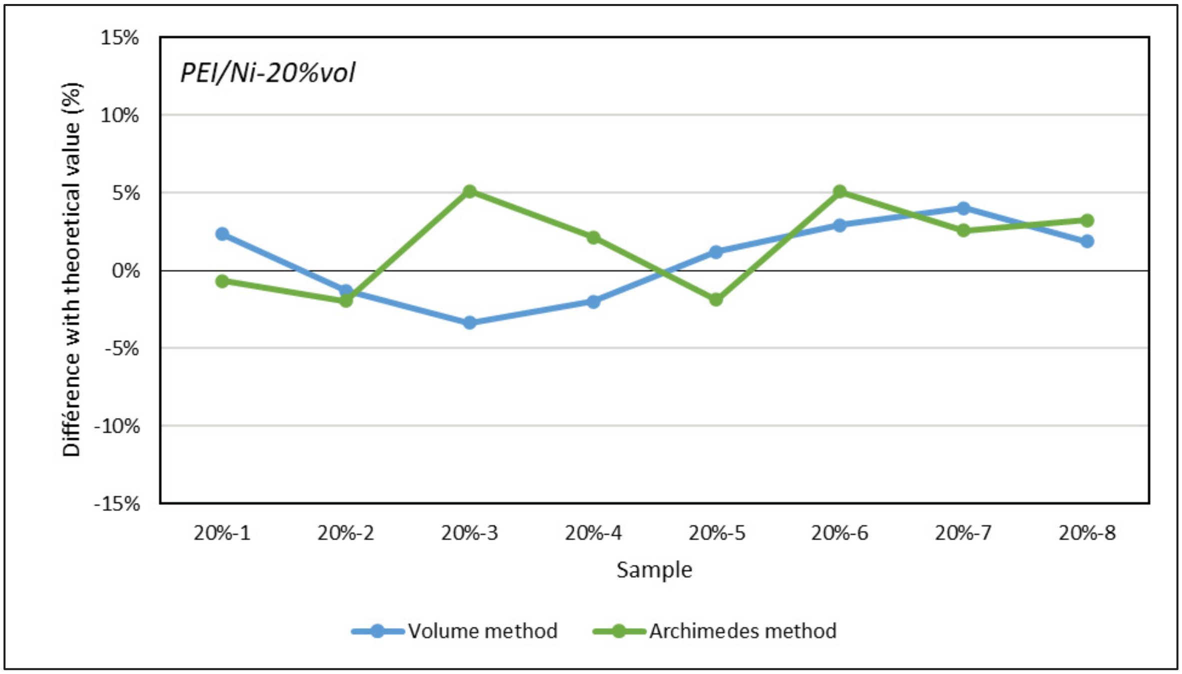

Figure 4.7 Experimental density of PEI/Ni-20%vol susceptor samples compared to the theoretical density obtained by the rule of mixture

Both experimental and theoretical densities are reported in Table 4.1. The experimental densities match the theoretical values, indicating that the Ni volume fraction present in the samples is the one expected. It is interesting to note that the "Volume" method, based the volume calculation from the thickness measurement, gives similar results to the Archimedes method with slightly smaller variability. This method, which is faster to apply, can therefore be used with confidence to quickly evaluate the density of a sample. One should note that this is true because of the simple geometry of the samples. For more complex or irregular samples, the standardized Archimedes method remains the most efficient technique. Overall, the density measurements and the optical microscopy observations confirm that the produced susceptors exhibit the desired fraction of well-distributed particles and without porosities.

Table 4.1 PEI/Ni susceptor samples density at 10%vol and 20%vol. Standard deviation based on the eight measurements is reported. Theoretical value of the density at each concentration is presented for comparison

PEI/Ni susceptor samples density [g/cm^3]			
Ni particles volume fraction	Theoretical – Rule of mixture	Experimental – Volume method	Experimental – Archimedes method
20%	2.796	2.816 ± 0.073	2.844 ± 0.081
15%	2.415	2.428 ± 0.054	2.389 ± 0.121
10%	2.033	2.037 ± 0.082	2.092 ± 0.079

Induction heating tests of five samples with thickness around 0.6mm are conducted for each Ni volume fraction using the presented setup. The maximum temperature of each sample is extracted from their respective thermal camera induction heating measurements and the corresponding temperature-time curves are presented in Figure 4.8. As expected, 20%vol samples reach higher temperature (324°C) compared to the 15%vol (316°C) and the 10%vol ones (299°C). The initial heating rate (at $t = 0$) of the susceptor samples follows the same trend, an average initial heating rate of 114 °C/s at 20%vol, 76 °C/s at 15% vol and 54 °C/s at 10%vol. It is interesting to note the good repeatability of the tests, which indicates once again the quality of the manufacturing process of the susceptors. At the three different concentrations, a plateau is reached, indicating an equilibrium between the heat generated and the thermal losses in the surrounding environment. As expected, the plateau is lower than the Curie temperature of Ni (358°C). This highlights the inherent thermal control feature provided by magnetic hysteresis losses susceptors, which cannot overheat when a material with an adequate Curie temperature is selected. The slight variability observed in the cooling curves comes from the difference of thickness between the samples. Thin samples tend to cool down faster than thicker ones.

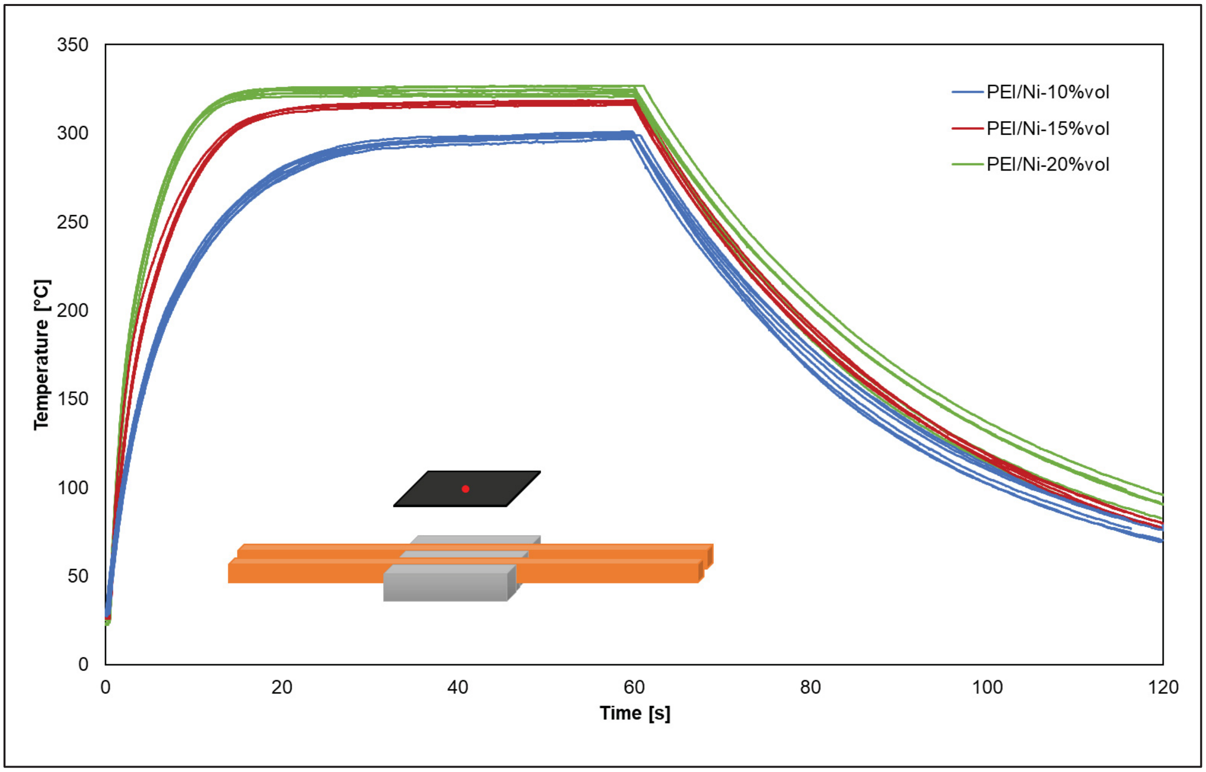

Figure 4.8 PEI/Ni samples induction heating results. Enclosed scheme of the induction heating setup, with the red dot representing the position of the temperature measurement

It appears that PEI/Ni-10%vol samples reach a temperature of approximately 300°C, which is the target temperature for induction welding of PEEK-based composites structures. The 20%vol samples reach a higher temperature but an increased content of metallic particles can decrease the mechanical properties, so it is favorable to minimize it. Therefore, PEI/Ni-10%vol is selected to be used as induction welding susceptor for the experiments presented in Chapter 5.

CHAPTER 5

MANUFACTURING OF THERMOPLASTIC COMPOSITE SANDWICH PANELS USING INDUCTION WELDING UNDER VACUUM

Romain G. Martin[a], Christer Johansson[b], Jason R. Tavares[c] and Martine Dubé[a],

[a] CREPEC, Department of Mechanical Engineering, École de technologie supérieure, 1100 Notre-Dame West, Montreal, Quebec, Canada H3C 1K3
[b] RISE Research Institutes of Sweden, Arvid Hedvalls Backe 4, Göteborg, Sweden, SE-411-33
[c] CREPEC, Department of Chemical Engineering, Polytechnique Montréal, 2500 chemin de Polytechnique, Montréal, Québec, Canada, H3T 1J4

Paper published in *Composites Part A: Applied Science and Manufacturing*, April 2024

5.1 Abstract

A new method to manufacture thermoplastic composite sandwich panels is presented, making use of the induction welding process in which a magnetic susceptor generates the heat at the core/facesheet interface. This technique proposes a fast way to assemble thermoplastic sandwich structures without risking the deconsolidation of the composites skin. The welding pressure is obtained by applying vacuum over the sandwich panel. This vacuum induction welding method (Vac-IW) allows joining thermoplastic composite facesheets to a thermoplastic polymer core in a clean and non-contact manner. The feasibility of the method is demonstrated by preparing sandwich samples made of glass fibre reinforced polyetheretherketone (PEEK) skins and a 3D-printed polyetherimide (PEI) honeycomb core. A susceptor made of PEI and µm-sized nickel (Ni) particles is used to generate heat by magnetic hysteresis losses. The strength of the sandwich samples assembled by the Vac-IW method is evaluated by flatwise tensile (FWT) tests.

5.2 Introduction

The demand for thermoplastic composites in various industries, such as the aerospace and automotive sectors, has been growing in the last decades. To reduce fuel consumption and CO_2 emissions, manufacturers try to reduce the structural weight by replacing traditional materials like metals for materials exhibiting similar mechanical properties with a lower density, such as fibre reinforced composites. In the space industry, the weight is even more critical because of the high impact it has on the launch cost. Space structures must also comply with other requirements such as vibration absorption and thermal insulation to survive launch and thermal cycles faced during the mission (Williamson, 1991). For these purposes, sandwich panels are often selected as the main parts of the space structures.

5.2.1 Sandwich structures

Sandwich structures consist of two thin high-strength, high in-plane stiffness outer layers – known as facesheets or skins – and a core material located between the two skins. The low-density core provides the compression strength, supports the through-the-thickness shear loads, and contributes to the high flexural stiffness of the sandwich panel (Daniel & Gdoutos, 2010; Gao et al., 2020; Neumeyer et al., 2017). These structures are lightweight and may offer shock and vibration absorption, as well as good impact resistance properties (Skawinski et al., 2004; Vieille et al., 2012).

Thermoset-based sandwich panels are well-established, but their production is labour and time-intensive, and they do not fulfill current growing requirements for sustainability (Grünewald et al., 2017b). High-performance thermoplastic polymers and composite materials present an alternative in sandwich structures, as they offer an ideal combination of light weight, thermal stability and high mechanical properties making them ideal candidates for aerospace and automotive structures (Grünewald et al., 2017b). Many thermoplastic polymers are also known for their high fracture toughness, good chemical stability and unlimited shelf life (Skawinski et al., 2004). They also offer a high potential of being recycled (Pegoretti, 2021).

There are different types of cores and skins commonly used in the aerospace industry. Foam cores made of materials such as polyethylene terephthalate (PET), polypropylene (PP), and polyvinyl chloride (PVC) are often retained, mostly for their compression strength, impact absorption properties and thermal insulation. Honeycomb cores made of aramid fibres or aluminium are also common due to their high strength-to-weight ratio and excellent energy absorption capability (Kodiyalam et al., 1996). Honeycomb cores can also be made out of thermoplastic polymers, typically by joining small tubes of polymer together (Gao et al., 2020). In recent years, additive manufacturing (or 3D-printing) has been used to produce thermoplastic honeycomb cores. This process allows to create honeycomb cells with exotic shapes, like for example reentrant cells (Özen et al., 2020), with variable geometry across the thickness (Townsend et al., 2020) or cores with variable in-plane density.

The skins are typically made of high-performance composite materials, such as carbon fibre reinforced polymers (CFRP) and glass fibre reinforced polymers (GFRP) (Grünewald et al., 2017b). The core and the skins are joined to ensure proper loads transfer through the structure. Adhesive bonding is the predominant technique used for that joining step. Although it is well-established in the aerospace industry, adhesive bonding presents limitations. Adhesives typically have a different coefficient of thermal expansion (CTE) than the bonded parts, which can lead to failure when experiencing large thermal cycles. Most of them also do not meet the space requirements with regards to outgassing, making them unusable for space applications (Walter & Scialdone, 1997).

Thermoplastic composite sandwich panels are not common. Only a few research groups have looked at the manufacturing of these structures, with an increasing interest in the recent years (Åkermo & Aström, 2000a; Åström et al., 1998; Breuer et al., 1998; Brown et al., 2007; Denkena et al., 2022; Grünewald, 2018; Skawinski et al., 2004). Two main methods for joining the skins to the core have been reported: adhesive bonding and welding, also known as fusion bonding. Adhesive bonding is typically achieved using epoxy polymers, which present compatibility challenges with thermoplastics, and requires extensive surface preparation. The curing of the epoxy adhesives also requires time and is labour-intensive (Wingfield, 1993). Thermoplastic welding, on the other hand, requires low to no surface preparation and is a fast process (Ageorges et al., 2001; Yousefpour et al., 2004).

5.2.2 Skin-core assembly by thermoplastic welding

The joining of thermoplastic composite sandwich panels is done in a one-step or two-step process in (Skawinski et al., 2004). The one-step process, referred to by the authors in (Skawinski et al., 2004) as “isothermal”, consists in placing the core and the two skins together in a hot press or oven and apply heat and pressure to join the skins to the core. The two-step process, referred to as “non-isothermal”, consists in heating up one face of each skin and then transferring the skins rapidly over the core and applying pressure. This second process has the advantage of not melting the core through its thickness, which may lead to collapse due to the core losing its mechanical properties past its melting temperature (Grünewald et al., 2018). The pressure can be applied on the parts by placing them in a vacuum bag. Once the vacuum is pulled inside the bag, a homogeneous atmospheric pressure is applied on the sample. In such a case, the important parameters controlling the skins to core joining quality are the skins pre-heat temperature and the transfer time in the vacuum bag (Brooks et al., 2008; Brown et al., 2007). The heat losses during transfer imply to overheat the skins in the pre-heat phase, which can lead to deconsolidation of the laminates or degradation of the polymer, therefore limiting the use of this method.

Pressure can also be applied using a hot press (Grünewald et al., 2017a; Latsuzbaya et al., 2023; Rozant et al., 2001) which can reach much higher pressures than the atmospheric pressure and can also heat up the parts. This method showed some good results but faces the same challenges and limitations as vacuum moulding when a one-step process is considered with the melting of the core and associated loss of stiffness and strength. The main advantage is a shorter transfer time when a two-step process is considered, due to the possible automatization of the process. Finally, double-belt lamination is a continuous process in which parts are assembled, then guided through heating elements by two belts (Trende et al., 1999; Xinyu et al., 2009). The heat is brought to the joining interface by conduction through the skins. The parts temperature must be continuously monitored to avoid core crushing.

In all of the described techniques, the heat source is located outside of the sandwich structure and the skins are heated through their thickness. Localising the heat dissipation at the joining interface, e.g., using a welding technique, is an interesting avenue to explore for the manufacturing of thermoplastic composite sandwich panels.

5.3 Theoretical background

5.3.1 Thermoplastic welding

In practice, thermoplastic welding techniques can be divided into three mains methods: thermal welding, friction welding and electromagnetic welding (Yousefpour et al., 2004). Thermal welding methods consist in preheating the parts directly before assembling them under pressure. Friction welding implies that heat at the joining interface is generated due to the relative movement of the parts against each other. Electromagnetic welding is more adapted to the geometry of sandwich panels. The working principle is to place at the joining interface a material able to react to an applied electromagnetic solicitation and dissipate heat in the surrounding parts (Ahmed et al., 2006; Bayerl et al., 2014; Brassard et al., 2019, 2021). When placed between the skin and the core, this material allows for welding to occur, without having to heat up the rest of the sandwich structures, preventing the risks of core crushing and skin delamination, as experienced in the previously mentioned methods. The most used electromagnetic welding techniques are resistance and induction welding. Resistance welding is limited in welding width due to current leakage issues and potentially non-uniform temperature distribution (Dubé et al., 2008). It also involves connecting a heating element to a power supply which may prove difficult to scale-up and apply to a sandwich panel. This study focuses on the induction welding method.

5.3.2 Induction welding

Induction welding is of particular interest to the aerospace industry due to its speed and adaptability to complex geometries. It relies on the transformation of a time-varying magnetic field into heat by a heating element called a susceptor (Ahmed et al., 2006; Bayerl et al., 2014; Mitschang et al., 2002; Rudolf et al., 2000). Direct heating (Joule heating) of carbon fibre-based composites is possible when eddy currents are induced directly in the adherents, which is known as susceptor-less welding, as shown in Figure 5.1a (Barazanchy & van Tooren, 2023; Fink et al., 1992; Pappadà et al., 2015; Worrall & Wise, 2014). However, a susceptor is required when direct heating is undesirable or if a non-electrically conductive composite material is used, such as glass fibre reinforced polymers. There are two main heat dissipation mechanisms happening in susceptor materials: Joule heating by eddy currents and magnetic hysteresis-losses. When subjected to a time-varying magnetic field, eddy currents are induced in electrically conductive materials, which generates heat through resistive heating, also known as Joule heating (Figure 5.1b). The heating element can be a conductive mesh – such as stainless steel – or a carbon fibre woven ply (Yarlagadda et al., 2016). It can also be a single layer of conductive polymer (Dermanaki Farahani et al., 2018; Dermanaki Farahani & Dubé, 2017). On the other hand, susceptors based on magnetic hysteresis exploit the capability of ferromagnetic materials to absorb energy from an applied alternating magnetic field and release it into heat, inducing an increase in temperature (Figure 5.1c). These susceptors are typically made of ferromagnetic micro- or nanoparticles dispersed in a thermoplastic polymer (typically the same as the parts to be welded) (Bae et al., 2015; Bayerl et al., 2012; Martin et al., 2022; Suwanwatana et al., 2006a; Wetzel & Fink, n.d.). Hysteresis losses susceptors present multiple advantages. First, as there is no need to reach a percolation threshold (unlike for electrically-conductive susceptors), the particles concentration is low and impacts the mechanical properties and the weight of the susceptor to a lesser degree. As magnetic materials lose their properties – and their ability to heat up during induction welding – when passing a certain temperature known as the Curie temperature (Coey, 2010), it is therefore possible to get a susceptor that will not overheat (Martin et al., 2022). This offers the opportunity to include an inherent temperature-control feature in the susceptor.

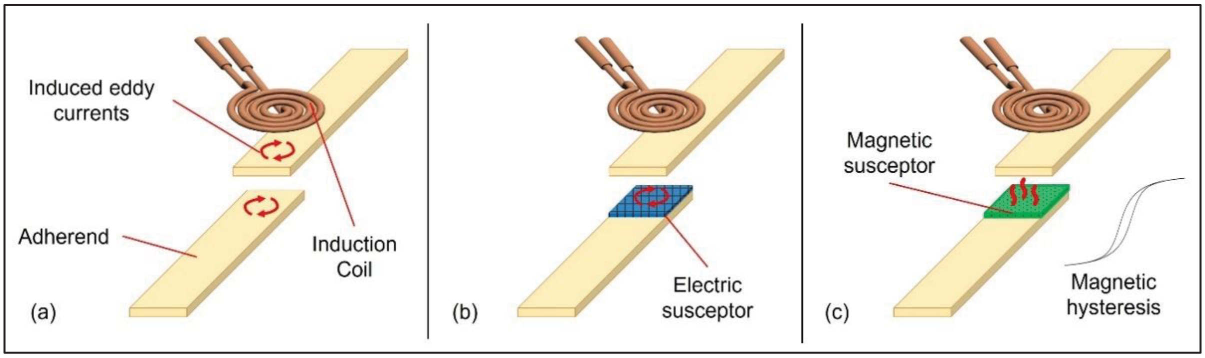

Figure 5.1 Heating mechanisms in induction welding: (a) Susceptor-less welding, (b) electrically-conductive susceptor, (c) hysteresis-losses susceptor (adapted from (Martin et al., 2022))

5.3.3 Dual-polymer bonding on sandwich skins

One major challenge when using thermoplastic welding to assemble sandwich structures is to generate enough heat at the interface to weld the parts together, while avoiding deconsolidating the skins. Grünewald et al. proposed to apply the dual-polymer bonding technique on sandwich skins to solve this issue (Grünewald et al., 2017a).

The dual-polymer bonding technique – or Thermabond process – consists in co-consolidating a secondary polymer on the surface of the parent laminate to be welded (Cogswell et al., 1989; Meakin et al., 1991; Smiley et al., 1991). The secondary polymer must have a processing temperature lower than that of the matrix of the parent adherend and be miscible in it. A film of the secondary polymer is added to the plies stack before consolidation. During compression moulding, the two polymers can diffuse into each other, ensuring a strong interface between them and leaving a polymer-rich layer at the surface composed of the secondary polymer. For example, it is possible to co-consolidate a polyetherimide (PEI) film on the surface of a polyetheretherketone (PEEK) adherend, as the two polymers are miscible. PEI is an amorphous thermoplastic exhibiting a glass transition temperature of 215-217°C (Martin, Figueiredo, et al., 2023b; SABIC, 2021). Welding can therefore occur at a lower temperature than the melting point of PEEK (341-344 °C (Martin, Figueiredo, et al., 2023b; Wetzel & Fink, n.d.)), as the joining interface is made of PEI. The authors of the original study determined a temperature range between 260°C and 315°C to weld PEEK adherends with co-consolidated PEI surface layers (Bastien & Gillespie, 1991; Smiley et al., 1991). By staying in that temperature range, the PEEK matrix of the skins does not melt, ensuring a better dimensional stability of the final part.

5.3.4 Vacuum induction welding technique

Herein, an innovative method to assemble skins to core in sandwich structures is introduced. This method uses a vacuum bag for pressure application and relies on induction to generate heat directly at the joining interface. A susceptor material based on magnetic hysteresis losses is located at the interface between the skin and the core to localize heat dissipation. As heat is generated at the same time as the pressure is applied, this method can be considered as a "one-step" process, but as the heat is generated locally and not throughout the whole structure, it is considered a welding process, contrarily to the original vacuum moulding method.

A secondary polymer with a lower welding temperature is added on the surface of the sandwich skins. This prevents the risk of laminate deconsolidation and the loss of mechanical properties of the skin. The honeycomb core exhibits low thermal conductivity, which means that the heat dissipated at the interface will not be rapidly transferred to the rest of the structure, lowering the risk of core crushing. During this process, the second skin, located on the other face of the sandwich panel, is far away from the coil. Typically, sandwich cores are half an inch to one inch thick, sometimes even more. Therefore, the opposite skin is subjected to a very low magnetic field amplitude which does not induce significant heating. This lack of direct heating and the poor heat transfer occurring by conduction through the core thickness ensure that the opposite skin is not affected by the ongoing welding process.

Therefore, the goal of this paper is to demonstrate the feasibility of the vacuum induction welding (Vac-IW) method using a hysteresis losses susceptor. First, a magnetic susceptor for the induction welding of thermoplastic composites sandwich panels is developed. Following the susceptor development, an experimental setup allowing induction welding under vacuum pressure is presented. Finally, sandwich samples are welded and characterized by optical microscopy and mechanical testing to verify the feasibility of the method.

5.4 Materials and Methodology

5.4.1 Parts preparation

Honeycomb core samples are produced by Fused Filament Fabrication (FFF) additive manufacturing using an AON3D M2 3D-printer. The core is composed of 4 mm wide hexagonal cells with wall thickness of 0.8 mm and a height of 10 mm, as presented in Figure 5.2. The cell dimension is selected to obtain an integral number of cells along the width of the sample (50 mm), ensuring the symmetry of the honeycomb core. The core is directly printed on the bottom sandwich skin, a 1 mm PEI layer, for a total thickness of 11 mm. A 0.8 mm thick frame wall surrounds the honeycomb core, ensuring the outer dimensions of 50 x 50 mm. ThermaX ULTEM 1010 (PEI) filament (3DxTech) is used as the feeding material and the printing parameters are the following: nozzle temperature of 390°C, bed temperature of 160°C and chamber temperature of 125°C.

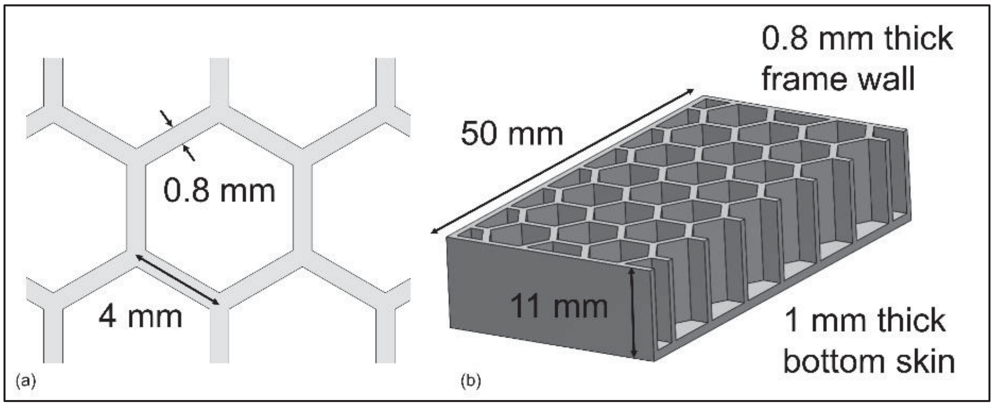

Figure 5.2 (a) Schematic of the honeycomb core with the single hexagonal cell dimensions and (b) the general sample dimensions

The top sandwich skin is made of glass fibre reinforced PEEK (GF/PEEK), with a co-consolidated 125 µm-thick PEI film (ULTEM 1000, Sabic). Glass fibre reinforcement was selected to avoid direct heating in the skin, which would happen in carbon fibres. This allows to perform the weld using a hysteresis losses susceptor and validate its use for induction welding of sandwich structures. The laminates are produced using a hot press (700 kN hot press from Pinette PEI) following a consolidation cycle of 20 min at 380°C under a pressure of 2 MPa. To guarantee the presence of a PEI-rich surface layer at the joining interface and to avoid polymer squeezing out of the tool, a 100 µm-thick polyimide film (Kapton) is placed around the PEI film. The resulting laminates are cut into 50 mm x 50 mm samples to be used as sandwich top skins.

To prepare the susceptor film, ULTEM 1010 pellets (Sabic) and Ni particles (Sigma-Aldrich, mean diameter 5 µm) are mixed in an internal mixer at 320°C for 5 min, with Ni particles (10%vol) Both materials are dried for 4 h at 150°C beforehand to remove moisture. After mixing, the material is processed into thin films in a hot press at 320°C. The resulting films are approximately 0.6 mm thick. Square 50 mm x 50 mm samples are cut to be used as induction welding susceptors in the sandwich panels.

The selection of Ni particles to produce a hysteresis losses susceptor for induction welding made of PEI is based on the heating properties of the particles. Compared to other magnetic materials such as magnetite or iron, Ni provides the largest heating rate at the magnetic field amplitude available with the experimental setup (Martin et al., 2022; Martin, Figueiredo, et al., 2023b). Also, due to its Curie temperature (358°C) close to the melting point of PEEK (343°C), Ni cannot overheat and locally degrade the polymer during the process. This thermal control feature makes Ni an ideal candidate for this study.

5.4.2 Induction welding setup

The samples are welded using a Vac-IW lab-scale setup. An Ambrell EASYHeat 10 kW generator (maximum current 750 A, frequency range 150-400 kHz) is used to produce the alternating current to the coil system. The current travels in a water-cooled copper induction coil, generating the alternating magnetic field required to perform induction welding. The frequency of the alternating current is automatically calculated by the generator, based on the coil geometry. In this case, it is fixed at 389 kHz. To increase the magnetic field amplitude in the region of the weld, a magnetic field concentrator (Ferrotron 559H from Fluxtrol) in placed around the induction coil. This low permeability magnetic material (relative magnetic permeability around 16) concentrates the magnetic field lines towards the side of the coil where the sample is located (Martin, Figueiredo, et al., 2023b).

The sandwich parts to be welded are placed on a plate and covered with a vacuum bag, fixed to the plate with sealing joint. The vacuum bag is made of Kapton to sustain the high welding temperature. Once the parts are in place, vacuum is pulled, and pressure is applied on the sample during the complete duration of the Vac-IW process. Figure 5.3 presents a schematic view of the Vac-IW setup used to weld the sandwich samples.

To allow for relative displacement between the sample and the induction coil, the setup is equipped with a linear displacement table enabling lateral displacement at controlled speed. The vacuum bag containing the sample to be welded is placed on this table and the distance between the sample and the induction coil is fixed. Typically, the pressure inside the bag reaches -0.9kPa and is maintained during the process.

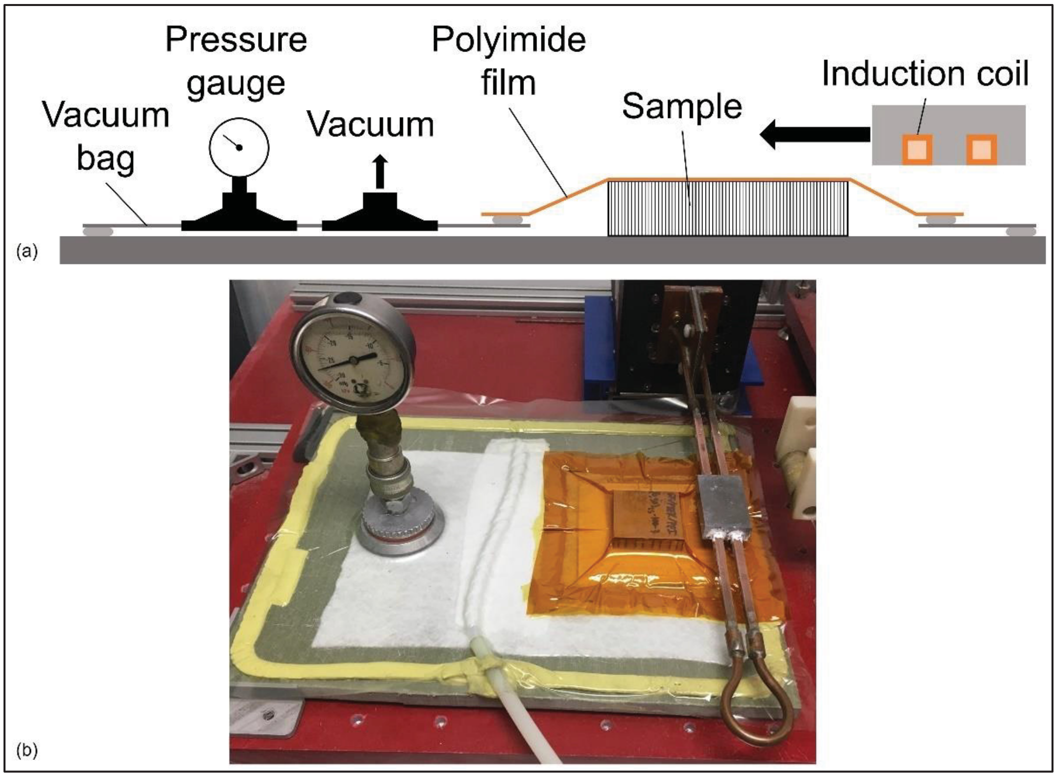

Figure 5.3 (a) Schematic and (b) picture of the Vac-IW setup. The black horizontal arrow on the schematic represents the relative movement between the coil and the sample. The speed of the coil displacement corresponds to the welding speed

A total of 17 samples are prepared to evaluate the welding interface and for mechanical characterization. The different parts of the sandwich panels are simply wiped with alcohol before assembly to remove dust. No other surface preparation is performed before welding.

The influence of the welding speed, or the relative speed between the induction coil and the sample, is evaluated in this study. It has been reported in the literature that changing the welding speed during continuous induction welding process affects the thermal history at the weld line (Lionetto et al., 2017). The alternating current amplitude is fixed at 600 A, the frequency at 389 kHz, and the coupling distance at 3 mm for all samples. Based on previous work, this configuration corresponds to a maximum magnetic field amplitude of 32kA/m on the welding line (Martin, Figueiredo, et al., 2023b). One sample is welded for six different welding speeds (0.3, 0.4, 0.5, 0.7, 0.9 and 1.0 mm/s) to be analyzed by optical microscopy, and five, three and three samples are welded for each of the three selected intermediate speeds (0.5, 0.7 and 0.9 mm/s), respectively, to evaluate the mechanical properties of the weld.

5.4.3 Optical microscopy

One sample from each welding speed is cut as shown on the schematic in Figure 5.4 for optical microscopy observation of the weld interface. The samples are mounted into an acrylic mounting compound to be polished and an Olympus GX51 optical microscope is used for the observation.

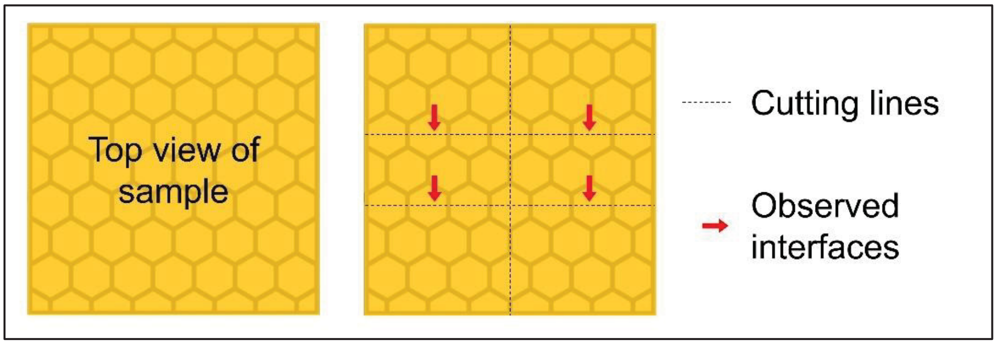

Figure 5.4 Schematic of the cutting pattern to extract four optical microscopy samples from a welded sandwich panel

5.4.4 Mechanical testing

The skin to core adhesion is characterized using the flatwise tensile (FWT) mechanical test, following the ASTM C297 standard (ASTM C297, 2021). A steel block is bonded to each side of the sandwich specimen to apply the tensile force evenly on, and normal to, the surface. Loctite® 415^{TM} Super Bonder® instant adhesive is used to bond the steel blocks on the specimens. The parts are stored at room temperature for 24 hours to fully cure the adhesive.

To execute the FWT mechanical test, an MTS Insight electromechanical tensile testing machine is equipped with the designated jig to hold the sample (manufactured by Wyoming Testing Fixture), as presented in Figure 5.5 (right). Specimens with bonded steel blocks are mounted and fixed using pins. The testing speed is 0.5 mm/min, as per the ASTM C297 standard, and a 50 kN load cell is used to record the load during the test.

The main types of possible failures are adhesive (glue) failure (not an acceptable failure mode, leading to an invalid test), facing failure, adhesive failure of the welded joint, cohesive failure of the welded joint or core failure (ASTM C297, 2021). Hybrid failure, combining at least two acceptable failure modes, can also be reported.

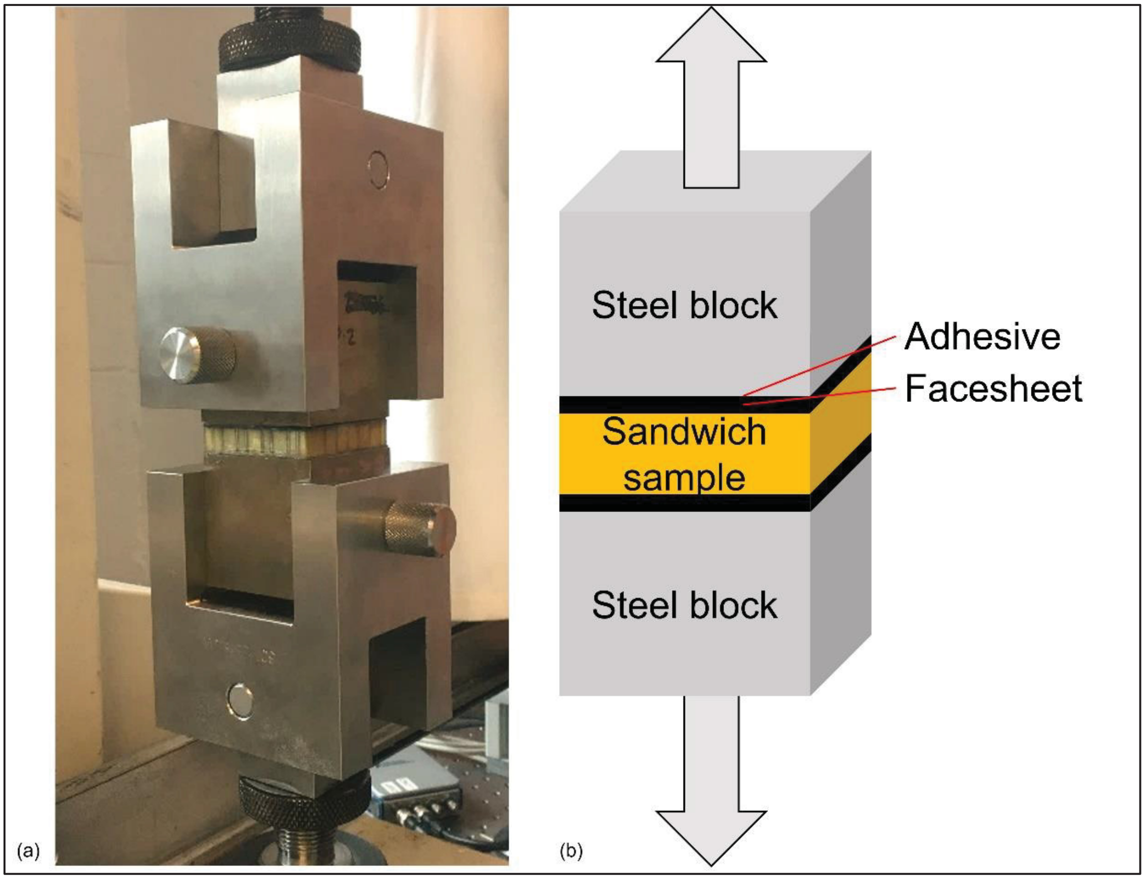

Figure 5.5 (a) FWT testing jig installed on the tensile test machine, with a sample mounted to be tested and (b) schematic of the FWT test

5.5 Results and Discussion

5.5.1 Optical microscopy

The analysis of the weld interface allows to observe the impact of the process on the contact between the skin and the core. The temperature evolution at the welding line is deduced by observing the deformation of the cell walls. The temperature is not directly monitored by thermocouples due to their inaccuracy in presence of a magnetic field. The first observation is made on samples welded at welding speeds of 0.3 and 0.4 mm/s. At these low speeds, with the applied magnetic field amplitude, too much heat is generated, thereby inducing deformation of the structure, especially towards the center of the structure, as visible in Figure 5.6. This sample was welded at 0.3 mm/s. The wall on the left corresponds to the external wall of the sandwich structure. The top of the honeycomb walls is largely deformed (dashed white arrows in Figure 5.6), confirming the high temperature experienced in that area. The difference of deformation observed between the edge (black arrow in Figure 5.6) and the center is most probably due to a difference in thermal history. There was less heating on the edge due to larger thermal losses on the side of the sandwich structure. The dimensional stability of the sample is not conserved at such low welding speeds. Finally, it also appears that overheating induced a large expansion of porosities in the 3D-printed honeycomb and in the susceptor close to the interface, which might reduce the mechanical properties.

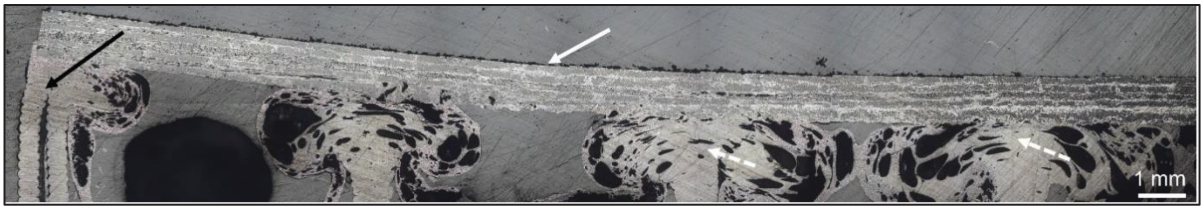

Figure 5.6 Cross section profile of a sandwich structure welded at 0.3 mm/s. Left side of the sample corresponds to the outer wall of the sandwich structure (black arrow). Visible deformation is seen on the top skin (solid white arrow). Top of honeycomb cell walls is deformed (dashed white arrows)

On the other hand, at a welding speed of 1.0 mm/s, the skin is not assembled to the core at all. The parts merely stuck together, and detached shortly after welding, probably due to the induced stress caused by the difference of thermal expansion and contraction of the core and the skin. This indicates that 1.0 mm/s is too fast a welding speed for this combination of materials and applied magnetic field amplitude. This observation on the impact of the welding speed corresponds to what has been reported in the literature (Lionetto et al., 2017). It can be explained by the fact that, at lower speeds, the susceptor is exposed to the magnetic field for a longer duration, which makes it reach higher temperatures, as it was reported by the authors in a previous study (Martin, Figueiredo, et al., 2023b).

Cross section profile of samples welded at intermediate welding speeds of 0.5, 0.7 and 0.9 mm/s do not exhibit evidence of core crushing, a sign that overheating was avoided (Figure 5.7). A good contact seems to have been reached between the skin and the core. The three pictures show an evolution of the contact between the susceptor and the skin. The susceptor final thickness also evolves with the welding speed. The core wall flow observed here is in agreement with reports from the literature, in the context of compression moulding (Åkermo & Aström, 2000a). Here, as the weld is conducted in the upper part of the sandwich structure, the softened core polymer is pulled down by gravity, creating a visible mushroom shape. It appears that welding the sandwich panel upside down could be an alternative, as it would keep the susceptor in contact with the skin. At lower speed (0.5 mm/s, Figure 5.7a), a larger susceptor deformation is seen, increasing the contact width with the skin (dashed black lines in Figure 5.7). Conversely, at 0.9 mm/s (Figure 5.7c), the contact width is smaller and the final susceptor thickness between the skin and the core is larger. These two parameters were measured for each welding speed based on the optical microscopy images; the results are presented in Figure 5.8.

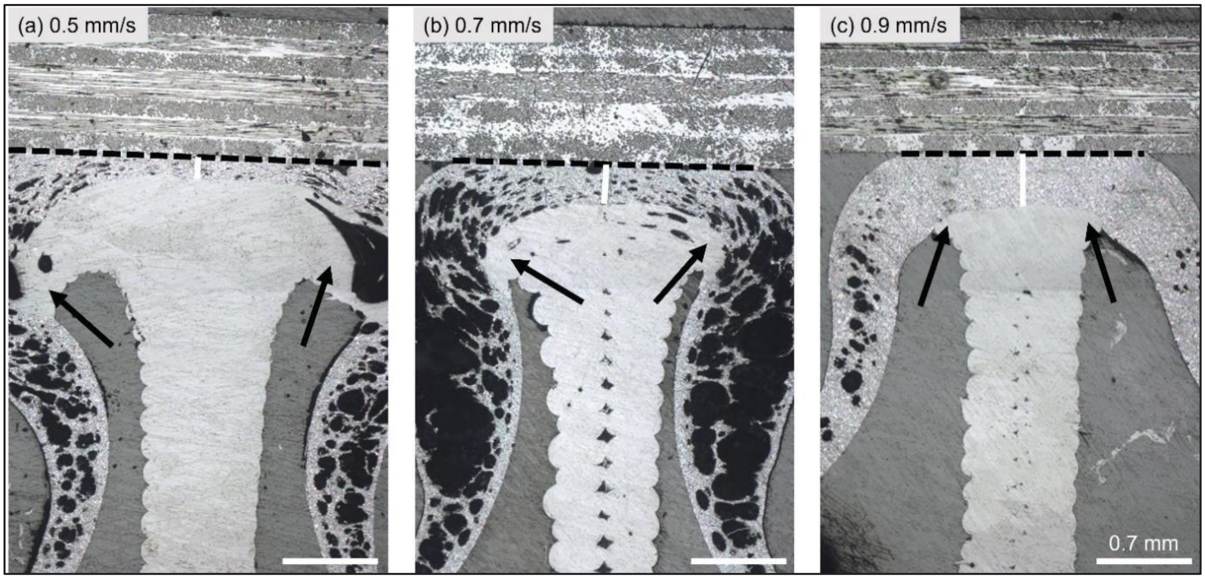

Figure 5.7 Welding profile on top of a core cell wall for a sandwich panel welded at (a) 0.5 mm/s, (b) 0.7 mm/s and (c) 0.9 mm/s. Dashed black lines correspond to the contact width. White vertical lines correspond to the susceptor thickness. The deformation of the top of the honeycomb cell walls is highlighted by the black arrows, The white scalebar represents 0.7 mm in the three pictures

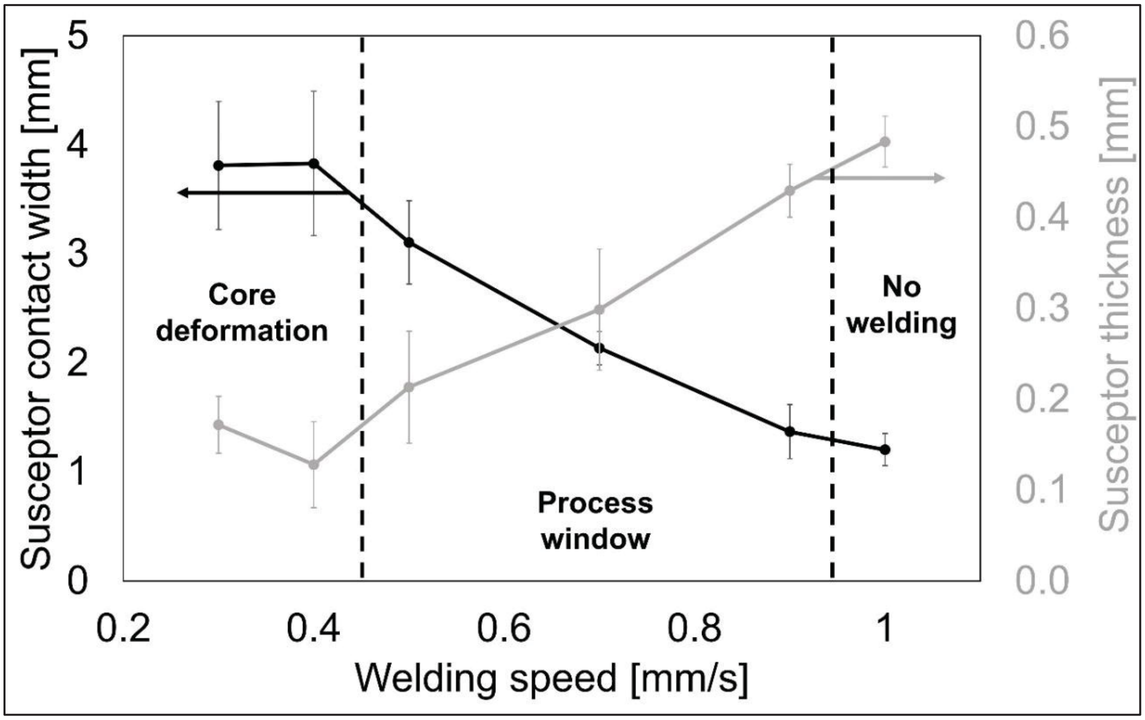

Figure 5.8 Susceptor contact width and thickness after welding at different welding speeds

5.5.2 Skin-core interfacial strength

It appears from the optical microscopy observations that the welding speeds of 0.5, 0.7 and 0.9 mm/s correspond to the optimal processing window for this combination of materials (thermoplastic polymer and magnetic particles, under the applied magnetic field amplitude) in this experimental setup. The mechanical properties of the sandwich panels welded at these three speeds are characterized by FWT and presented in Figure 5.9. As per the ASTM C297 standard, the strength is expressed as the load at failure divided by the total surface of the sample. For reference, a strength of 6 MPa corresponds to a force of 15 kN. One of the five samples welded at 0.5 mm/s failed inside the core at a lower stress, probably indicating a defect in the honeycomb core created during 3D-printing. This sample is not reported in Figure 5.9, as the value does not represent the skin-core strength. Another one failed in the bonding adhesive used to bond the sample to the steel blocks. The maximum load recorded is therefore slightly inferior to the other samples. This value is reported but it should be kept in mind that the actual joint strength is superior to that value. This point is shown in Figure 5.9 with a black arrow pointing up. As expected, samples welded at lower speeds exhibit higher strength, as they reached a higher temperature for a longer period of time during the induction welding process. The samples welded at 0.9 mm/s exhibit a lower strength, highlighting the lower quality of the weld at this welding speed. Results of flatwise tensile tests on polymer honeycomb sandwich panels are limited in the literature to compare with the presented values. Grünewald at al. tested PEI foam cores joined to CF/PEEK skins by thermoplastic thermal welding and reported maximum skin-core strength of 1.2 MPa (Grünewald et al., 2019). However, this value corresponds to the foam core failure, which does not indicate the skin-core strength. Another interesting study from Widagdo et al. presents carbon fibre epoxy skins joined to fibre glass honeycomb cores using an epoxy film adhesive (Widagdo et al., 2020). This is not directly comparable as the joining method is not thermoplastic welding but adhesive bonding, but the same mechanical test is used to characterize the samples. Skin-core strengths (cohesive failure inside the adhesive layer) between 5.1 and 5.6 MPa are reported. The results presented here for sandwich samples welded with the Vac-IW method reach up to 6 MPa, without any specific surface preparation. This highlights the good quality of the process.

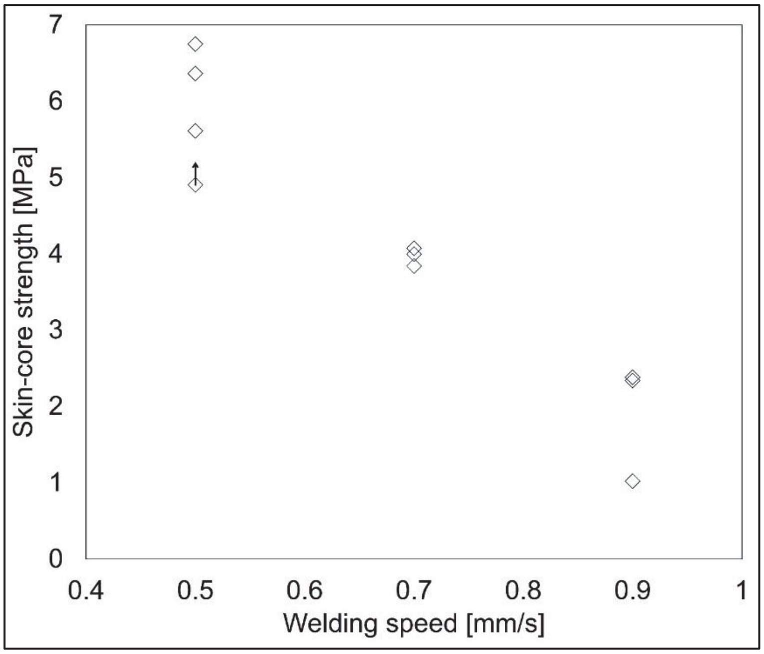

Figure 5.9 FWT skin-core strength of welded sandwich samples as a function of the welding speed. Three valid measurements were obtained at each speed. One supplementary sample welded at 0.5 mm/s that broke in the bonding adhesive used to bond the sample to the steel blocks. This value is reported and marked with an arrow pointing up

The samples failure mode is analyzed. One representative sample for each welding speed is presented in Figure 5.10. At a welding speed of 0.5 mm/s, the dominant failure mode is a cohesive failure of the susceptor layer, easily identified with its black color (Figure 5.10a). At 0.7 mm/s, an adhesive failure is observed either between the skin-susceptor interface or the susceptor/core interface (Figure 5.10b). Finally, at 0.9 mm/s, adhesive failure dominates on the whole surface, and is located at the susceptor/core interface (Figure 5.10c).

The change in failure mode indicates that the decrease in speed induces a higher degree of welding, caused by a higher temperature reached during the process. The increase of contact width between the core and the skins observed in the optical microscopy images is confirmed by the change of failure behaviour observed in the fractured samples. This has been previously reported in the literature (Åkermo & Aström, 2000b). The effective contact surface area is increased at a low welding speed, which contributes to the improvement of the mechanical strength. In the three specimens, welding was less advanced close to the edges of the skin. This is especially visible on the sample welded at 0.5 mm/s (Figure 5.10a). As discussed, the dominant failure mechanism in this case is cohesive failure, but on top of the outside wall, the failure is clearly adhesive, highlighting the lower degree of welding in that region.

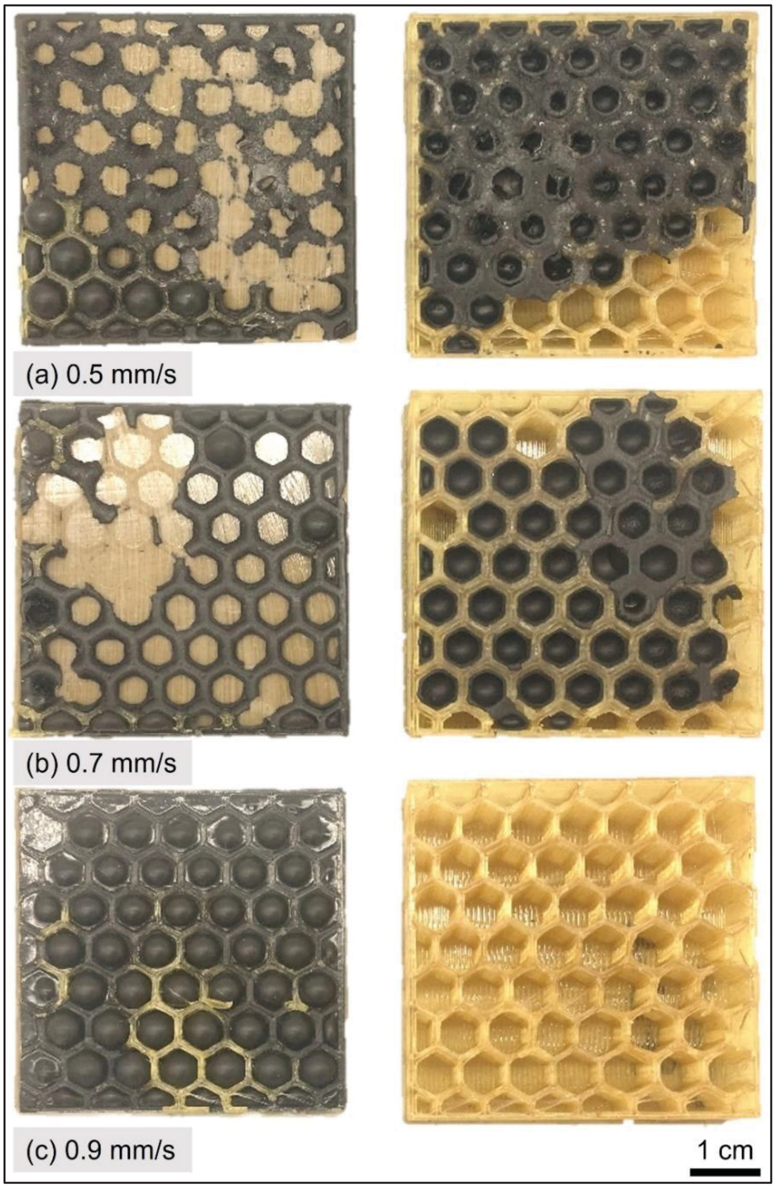

Figure 5.10 Fractured FWT sandwich samples welded at (a) 0.5 mm/s, (b) 0.7 mm/s, (c) 0.9 mm/s)

5.5.3 Effective skin-core strength

The fracture analysis shows a higher degree of welding in the samples welded at low speeds. Another way to verify this is to normalize the strength of the skin to core interface by the effective surface area of contact between the skin and the core. As mentioned above and reported in Figure 5.8, the susceptor contact width with the skin increases when the welding speed decreases, as observed in the optical microscopy images. By assuming that this effective contact width is constant throughout the structure, it is possible to calculate the effective contact surface area, as shown in Figure 5.11. For example, as highlighted by the dashed line in Figure 5.11, the effective contact surface area evolves from 25% with the original 0.8 mm wall thickness to 60% with 2.4 mm wall thickness. The effective contact surface area is more than doubled, which in turn impacts the skin-core strength of the sandwich panel. Based on this assumption, it is possible to calculate the effective interfacial strength by dividing the load at failure by the effective contact surface area instead of the skin surface area. These results are presented in Figure 5.12. If the increase in strength observed in Figure 5.9 was only caused by the larger contact surface area, then the data points in Figure 5.12 would all be aligned. As it appears, the normalized strength of the sandwich sample increases when the welding speed is reduced, which further confirms that a higher degree of welding is achieved at lower speeds, which can be related to the observations on the fractured samples (Figure 5.10).

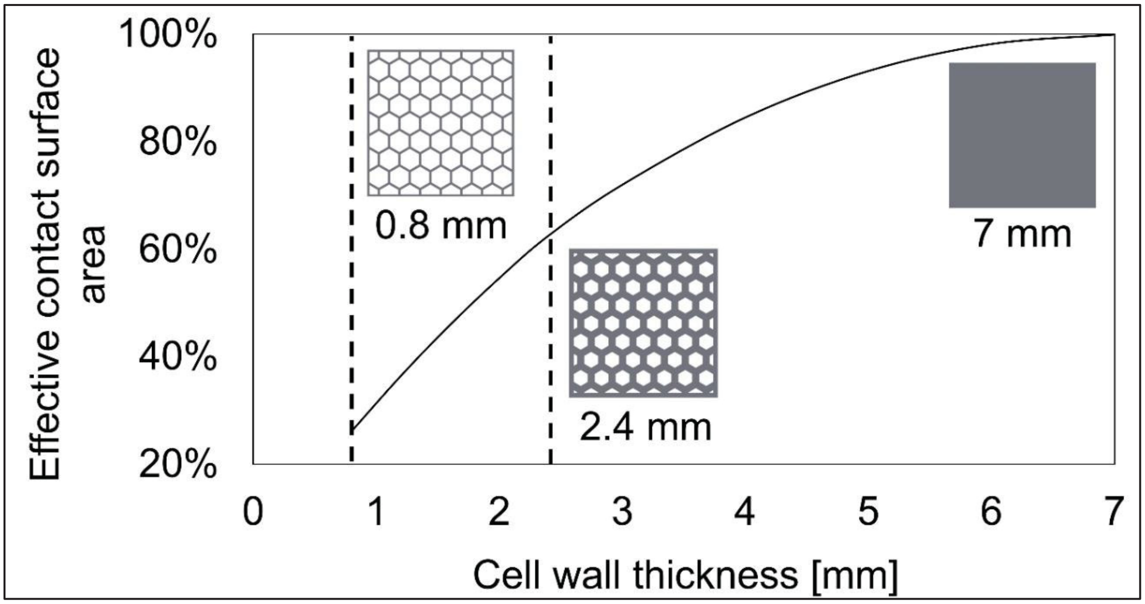

Figure 5.11 Effective contact surface area of a honeycomb core as a function of the cell wall thickness. The two dashed lines highlight the original 0.8 mm and the 2.4 mm wall thicknesses

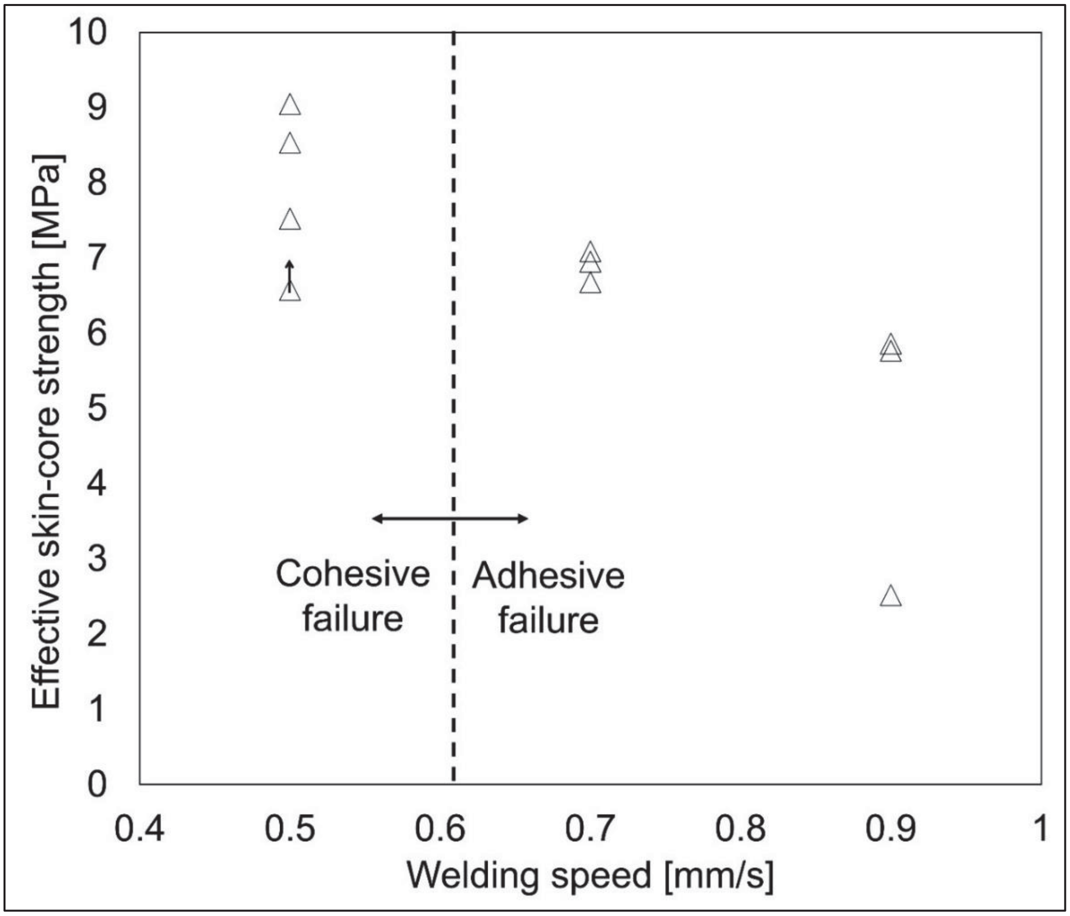

Figure 5.12 Effective skin-core interfacial strength as a function of the welding speed. Three valid measurements were obtained at each speed. One supplementary sample welded at 0.5 mm/s that broke in the bonding adhesive used to bond the sample to the steel blocks. This value is reported and marked with an arrow pointing up. The dominant failure mode is indicated

5.6 Conclusion

This paper presents a new method for joining thermoplastic composites sandwich structures under vacuum and using induction welding. The described Vac-IW method proposes a contactless induction welding method, allowing for heat localisation at the joining interface with a constant pressure application during the process. The atmospheric pressure applied during assembly, which is usually considered too low to weld or consolidate high performance thermoplastics, is shown to be high enough here, due to the effective higher pressure supported by the core cell walls. The optical microscopy observations allowed to define an appropriate processing window and the FWT mechanical tests validated that welding occurred between the skin and the core, proving the feasibility of the technique. The application of the dual-polymer bonding method on the sandwich skins allows for the weld to occur at a lower temperature than the skin thermoplastic matrix melting point, avoiding issues like deconsolidation. Although it is tested with a honeycomb core in this study, the Vac-IW method can also be applied to corrugated or foam cores made of thermoplastic polymers. This study demonstrates the feasibility of the method, which is promising for the assembly of thermoplastic composite sandwich structures, without having to heat non-electrically-conductive skins through their thickness. The contactless approach showed here may also open the door to the assembly of non-flat thermoplastic composite sandwich panels on which a coil could be moved using a robot with temperature control through the susceptor Curie temperature and thermabond process. In the future, thermoplastic sandwich panels assembled with the Vac-IW method should be tested in 3-points bending and double cantilever beam test, to assess the fracture toughness of the weld and compare with other experiments reported in the literature.

5.7 Acknowledgements

The authors acknowledge financial support from CREPEC (Research Center for High Performance Polymer and Composite Systems), NSERC (Natural Sciences and Engineering Research Council of Canada) (grant number ALLRP 556497-20), PRIMA Québec (Pôle de Recherche et d’Innovation en Matériaux Avancés) (grant number R20-13-004), the Canadian Space Agency (CSA), Ariane Group, NanoXplore inc, Mekanik and Dyze Design. They also want to thank Mr. Adrien Fage (Ariane Group) for his help with the optical microscopy images, as well as Mr. Kambiz Chizari and Mr. Olivier Duchesne (Polytechnique Montréal) for their help with the mechanical tests.

CHAPTER 6

DEVELOPMENT OF A 3D-PRINTING MAGNETIC SUSCEPTOR FILAMENT

6.1 Context

As previously discussed, hysteresis losses susceptors can be made of magnetic particles embedded inside a thermoplastic matrix. The particles are a non-continuous filler, inversely to other typical heating elements such as metallic meshes or carbon fibres. Also, as each particle can heat up when exposed to the magnetic field, there is no need to reach the percolation threshold. The composite susceptor can then be moulded in various shapes depending on the targeted induction welding application. The objective of this chapter is to demonstrate the possibility to fabricate magnetic susceptors in the form of 3D-printable filaments. Such filaments would be applicable to a large field of applications as they could be deposited by the fused filament fabrication (FFF) technique in various patterns on thermoplastic composites to be welded. They could also be used in various applications where heating is desired with a higher density of deposited susceptor filaments at locations where more heat is needed. In this chapter, we develop magnetic susceptor made of PEI/NI in 3D-printable filament form and use the filaments in the FFF technique to assemble thermoplastic composite sandwich samples, replacing the pressed susceptor films presented in Chapter 5.

6.2 Preliminary study on the susceptor filaments production

Printing a susceptor requires processing the material into the form of a filament of fixed diameter that can be subsequently deposited by a 3D-printing machine. This can be divided into two main steps: the compounding step, where the thermoplastic polymer is mixed with the magnetic particles at a given concentration, and the shaping step, where the susceptor material is extruded into the form of a filament. Those two steps can occur simultaneously (one-step process, as presented in Figure 6.1) or separately (two-step process).

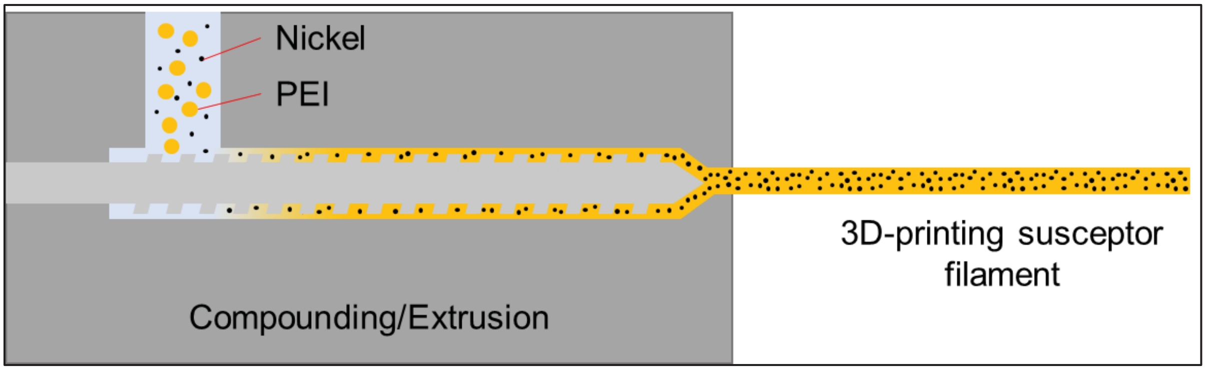

Figure 6.1 Scheme of the extrusion of PEI and Ni, resulting in a PEI/Ni 3D-printing filament. This corresponds to the one-step process where compounding and shaping of the filament occur simultaneously

A preliminary study on the manufacturing of PEI/Ni filament was conducted by Baptiste Renault during his Master project (Renault, 2023). The goal was to evaluate the need of a preliminary compounding step to mix PEI and Ni particles before the extrusion process dedicating to shaping the material into a 3D-printing filament, or if these two steps could occur concurrently during a single pass through the extruder. A Thermo Scientific HAAKE MiniLab II twin-screw micro-extruder was used in this study. This extruder possesses a single heating zone, covering the complete working area, which is fixed at 320°C. The rotation of the screws is fixed at 150 rpm. Two modes of mixing can be selected in the micro-extruder: a cycle mode and a flush mode. In the cycle mode, after passing through the screws, the material is recirculated via a side channel towards the beginning of the screws (Figure 6.2a). This allows the material to pass multiple times through the screws, increasing the mixing and the total residence time at high temperature. This can be used as a compounding step, alternatively to the internal mixer compounding used in Chapters 4 and 5. The drawback of the micro-extruder in cycle mode is that only a small amount of material can be mixed and produced at a time (5-7 g). The longer residence time can also start degrading the polymer, even if the temperature should be low enough to avoid it. On the other hand, the flush mode directly extrudes the material after it passes once through the screws (Figure 6.2b). This reduces the mixing time but allows for continuous extrusion by continuously feeding with material, as it is an open circuit. Extrusion of the material corresponds to the shaping step, to manufacture the 3D-printing filament. For this purpose, a

2 mm round die is mounted at the exit of the micro-extruder to impart a round shape to the filament.

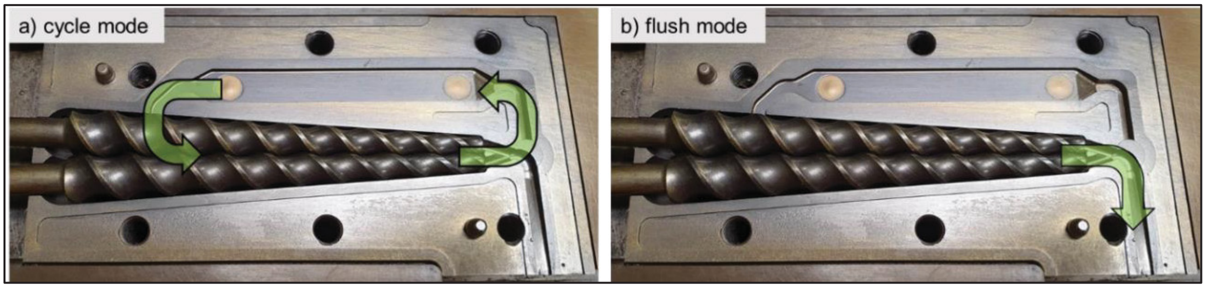

Figure 6.2 Picture of the micro-extruder used in the preliminary study. It can be used in (a) cycle mode or (b) flush mode. The green arrows indicate the path of the material in the extruder in both modes

The conclusion of this preliminary study was that a good distribution of Ni particles can be obtained after a single pass in flush mode. It is therefore unnecessary to perform a compounding step separately before the extrusion step. This is positive as it removes one cycle at high temperature for the material, preserving its properties. It was also noted that the use of PEI in powder instead than of pellets resulted in better particles distribution and lower porosity level. Therefore, the material form was changed for the experiments presented hereafter. Finally, the porosity level was minimal in the susceptor material after extrusion without the round die. The addition of the die induced some porosities in the center of the filament, as presented in Figure 6.3. Despite the presence of porosities in the final material, this study demonstrated that the production of susceptor filament is possible through a single extrusion process.

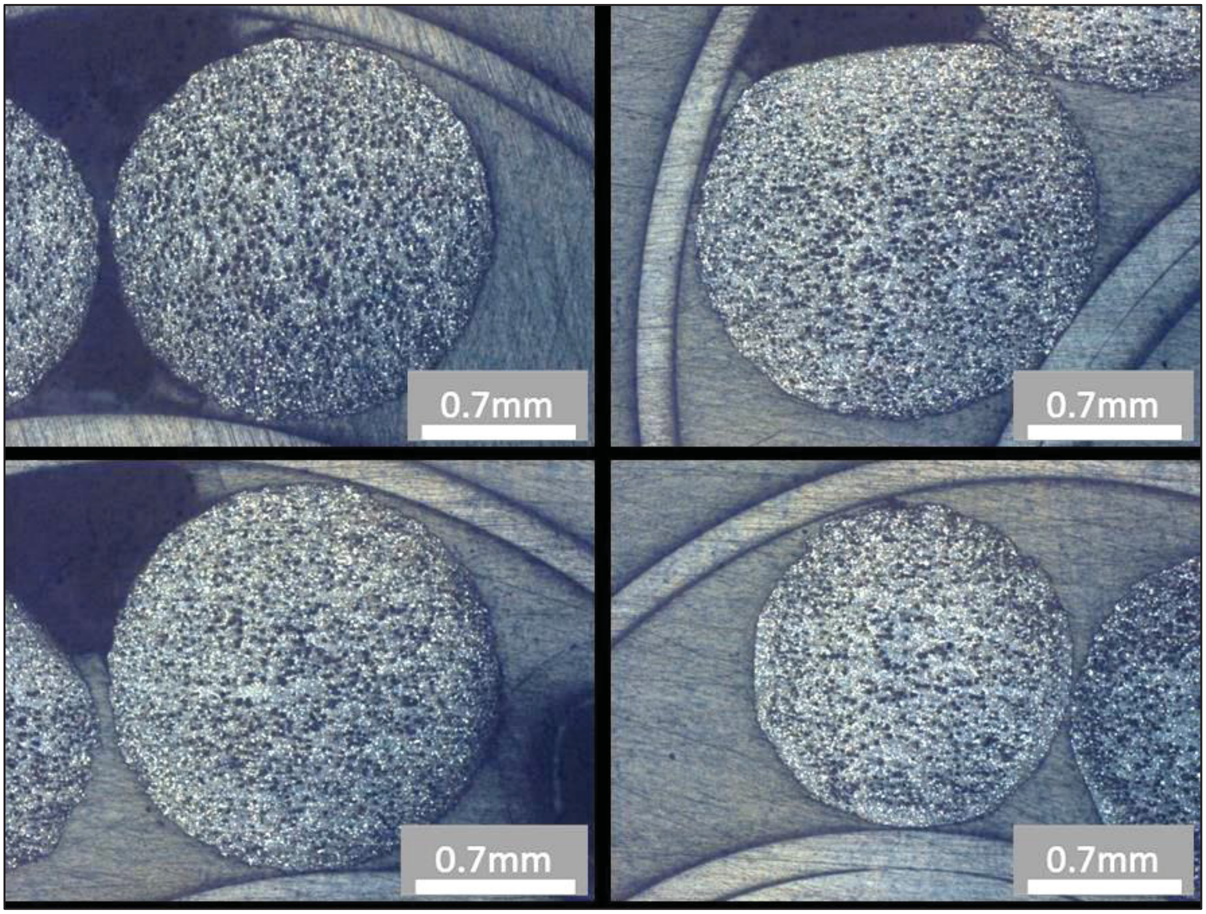

Figure 6.3 Cross-section optical microscopy images of susceptor filament produced by Baptiste Renault during his Master’s project using a micro-extruder
Taken from Renault (2023, p. 47)

6.3 Methodology

As the one-way process (compounding and shaping using a single pass in the micro-extruder) produces good quality susceptor filaments, the production is moved to a larger extruder to prepare larger quantities of filament. The selected materials are Ni particles (average diameter 5 microns) from Sigma-Aldrich and PEI ULTEM 1010 in powder form from SABIC. These are the same materials that were used in Chapter 4 and 5, except that the form of the PEI has changed from pellets to powder, based on the observations of the preliminary study. PEI powder and Ni particles are pre-mixed by hand to ensure good distribution, then the material is fed to the extruder. The Ni concentration is fixed at 10%vol because when increasing the concentration to 15%vol, the extruder started making metal-on-metal noises, which can indicate that the Ni particles were directly in contact with the screws and the barrel. As this presented a risk of excessive abrasion of the extruder parts, it was chosen not to continue the extrusion at that concentration, and remain at 10%vol.

A Leistritz ZSE18HP-400 twin-screw extruder is used to produce large quantities of PEI/Ni filament. The screws are equipped with different transport and mixing sections, as presented in details in Figure 6.4. A 1.75 mm nozzle is mounted at the extremity of the extruder. Eight heating zones are available:

- The first one (where the material is fed to the extruder) is set at 260°C to avoid melting the material too early and clog the feeding port.
- The following five at set at 320°C.
- The last two sections are set at 335°C, to improve the filament surface quality and reduce the instabilities at the extruder nozzle.

The diameter of the extruded filament is controlled by a two-axis laser measurement system (from Zumbach). The filament should be pulled by a spooling system, however the extrusion was too slow for the available spooling device, thus an operator was required to pull the filament by hand, while ensuring to stay in the desired diameter range by controlling the value on the diameter measurement device. This reduced the accuracy and consistency of the filament diameter. The target diameter is 1.75 mm; the limitations are to be larger than 1.6 mm to be correctly pushed by the printing head gears, and smaller than 1.9 mm to pass through cylinder of the printing head of reach the printing nozzle.

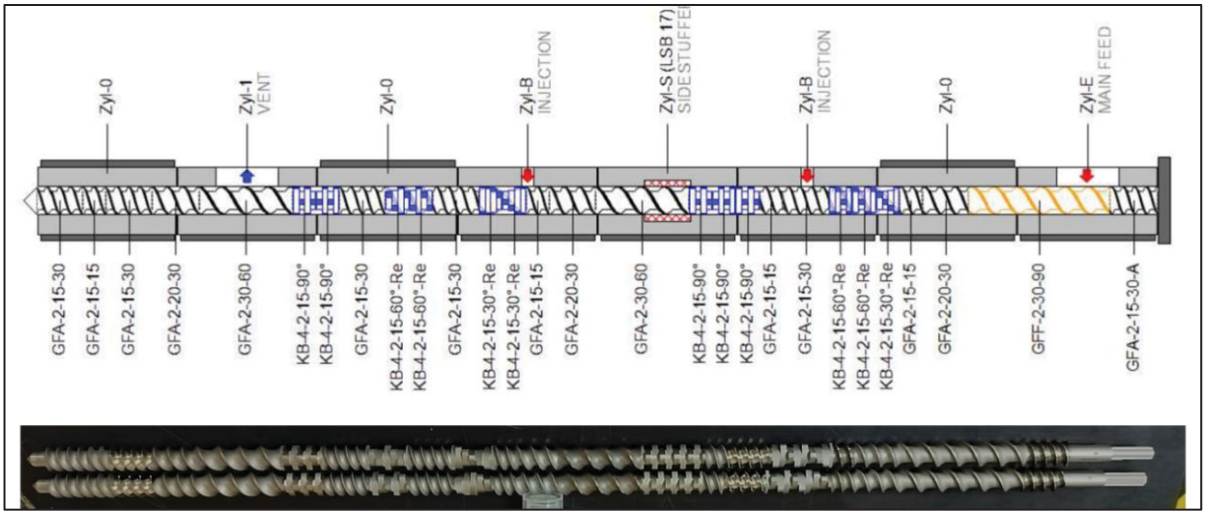

Figure 6.4 Leistritz extruder screws profile, extruding material from right to left. Mixing sections are highlighted in blue and transport sections in black. The initial transport section located below the main feeding point is highlighted in yellow

After extrusion, the filament is characterized first by observing its cross-section using an Olympus GX-51 optical microscope. The porosity level is a critical parameter that must then be controlled as it can lead to brittleness and inhomogeneous heating. To analyze the magnetic properties of the filament, vibrating sample magnetometry (VSM) measurements are also performed on the extruded filament at 25°C, 100°C and 200°C. Pure Ni particles are also analyzed with the same method at 25°C to be compared with the filament.

The produced filament is then printed using an AON3D M2 printer equipped with a 0.4 mm nozzle. The nozzle temperature is fixed at 410°C, the printing bed is fixed at 160°C and the printing chamber at 135°C. First, 1 mm-thick round samples (2 cm diameter) of printed susceptor are observed by optical microscopy to analyze the porosity level and the particle distribution after printing. Then, 0.6 mm-thick rectangles of 2 cm x 4 cm, similar to the pressed films tested in Chapter 4, are printed to be heated up by induction to measure their heating properties. A similar setup to the one presented in Chapter 3 and 4 is used for that purpose.

Finally, to evaluate the ability of the susceptor filament to be deposited on complex structures and to verify its welding capabilities, honeycomb cores incorporating a layer of susceptor are produced. Similar honeycomb samples as those presented in Chapter 5 are manufactured, but a few extra layers of susceptor are printed directly on top of it. To do so, the secondary printing head of the AON3D M2 printer is used. In the slicer software Simplify3D, the printing procedure is set up to switch printing heads when reaching the final layers. It is important to properly calibrate both printing heads and their relative position. If this step is not conducted accurately, the secondary material deposition will be shifted compared to the previous layer, preventing good adhesion between layers and, accordingly, good mechanical properties.

The susceptor layer thickness is fixed at 1 mm, which is equivalent to five printed layers of 0.2 mm. The printing temperature of PEI is set to 390°C, like in Chapter 5, and susceptor printing at 410°C, like for the printing of the characterization samples. The difference in temperature is caused by the difference of viscosity of the two materials. Two susceptor deposition configurations are evaluated: a constant susceptor width, made of five 0.8 mm-wide layers on top of the cell walls (Figure 6.5a), and an increasing susceptor width, varying from 0.8 to 2.4 mm by 0.4 mm increments. This corresponds to a width of two, three, four, five and six filaments in width per layer (Figure 6.5b). The goal of increasing the width is to increase the amount of susceptor material at the interface, and therefore the heating rate. It also increases the contact surface area between the susceptor and the skin, which can increase the interface strength. For both configurations, a priming pillar is printed next to the honeycomb core. This part is composed of PEI layer and one single susceptor layer, which is printed before the actual honeycomb susceptor layer. As this is the first part printed after switching nozzles, it provides some time and space for the print to correctly initiate and ensures that susceptor is properly printed when the nozzle moves to the honeycomb core.

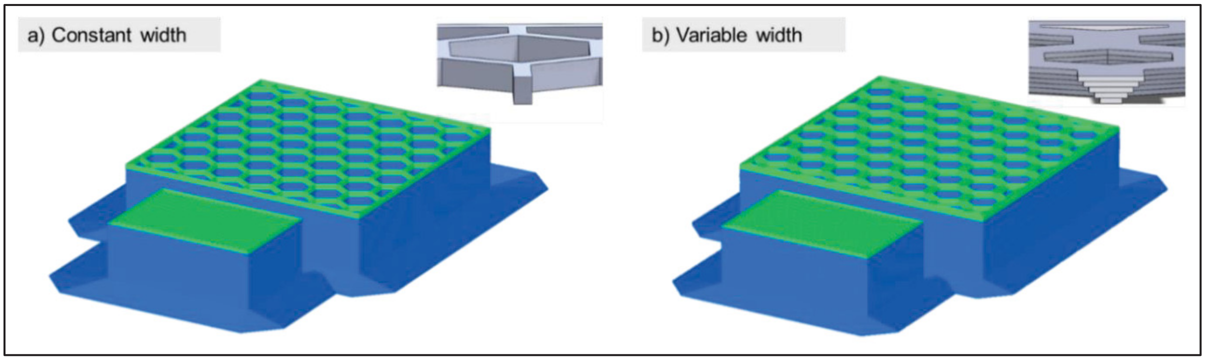

Figure 6.5 Honeycomb core (in blue) including susceptor layer (in green) printing configurations: (a) constant susceptor width and (b) variable susceptor width. For both (a) and (b), an enclosed picture shows the detailed geometry of the susceptor layer. A priming pillar is produced prior to honeycomb printing

The printed honeycomb incorporating the susceptor layer can be directly welded to their skin, without any additional material. GF/PEEK laminates are used as skins, with a co-consolidated PEI layer at the welding surface, like the ones used in Chapter 5. The vacuum-assisted induction welding technique presented in Chapter 5 is used to assemble skins and cores. Three welding speeds (relative displacement speed between the induction coil and the sample) are evaluated: 0.1, 0.15 and 0.2 mm/s. Welded sandwich samples are first characterized by observing the weld line profile by optical microscopy, then the skin/core strength is evaluated using FWT tests, as presented in Chapter 5. The preparation od the FWT samples is described in details in ANNEX IV. One sample is welded at each speed for each susceptor configuration to be tested in FWT, plus one extra sample of each configuration welded at 0.1 mm/s for optical microscopy observations, for a total of 8 welded sandwich samples.

6.4 Results

6.4.1 Susceptor filament characterization

The susceptor filaments produced with the Leistritz extruder exhibit a smooth surface finish, which is probably due to the higher temperature (350°C) in the final two heating zones of the extruder. The porosity level and Ni distribution are analyzed by observing the cross-section of the filament by optical microscopy. Four representative filament pictures are presented in Figure 6.6. The porosity level inside the filament varies significantly between samples, with a limited number of visible porosities in Figure 6.6d to a large amount in Figure 6.6b. It also seems that porosities are getting larger towards the center of the filament. Further experiments should be conducted on the extruding parameters of the large extruder to minimize the porosities in the filament. However, Ni particles appear to be well distributed in the PEI matrix, with no visible agglomerates. This confirms the previous results obtained with the micro-extruder that it is possible to perform a one-step process regrouping compounding and shaping. The porosity level looks higher than in the filament obtained with the micro-extruder (Figure 6.3), which indicates that improvement can be done on the process parameters with the large extruder.

The diameter of the filament is another important parameter that must be controlled during extrusion. As reported in Figure 6.6, it varies around the target value of 1.75 mm. This is mostly caused by the absence of a mechanical pulling/winding system able to constantly pull the filament at the exit of the extruder. To comply with the required 1.6 to 1.9 mm diameter range, sections of filaments that are out of this range are cut out. Remaining sections vary from 30 cm to more than 1 m, which is sufficient to print the different samples analyzed hereafter.

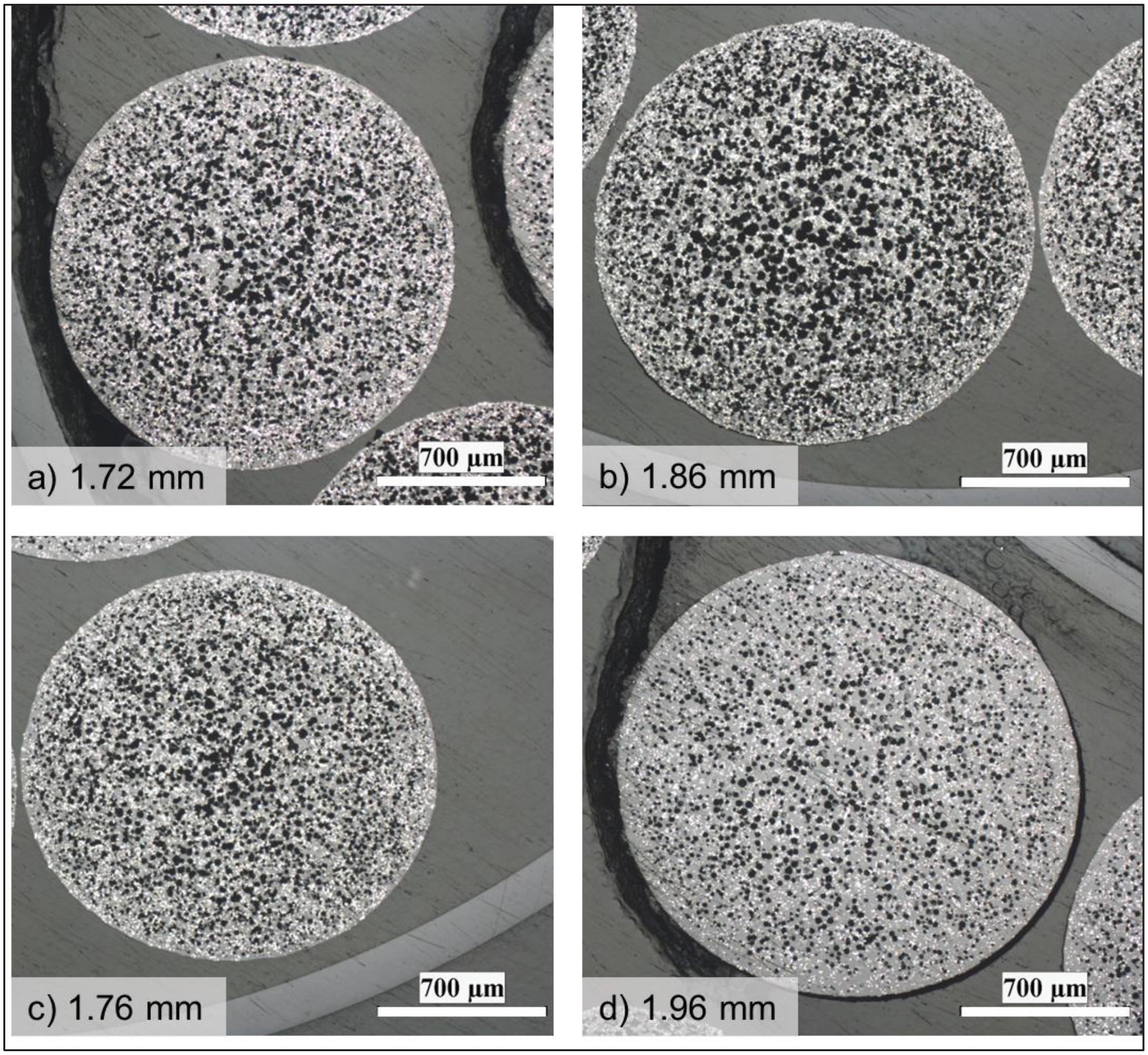

Figure 6.6 Optical microscopy images of PEI/Ni-10%vol filament cross-sections. The diameter of each filament is reported on the figure

The filament's magnetic properties, measured using VSM, are reported in Figure 6.7. First, the magnetic hysteresis of Ni particles and PEI/Ni-10%vol susceptor measured at 25°C are compared. The maximum applied amplitudes are 16, 32 and 48 kA/m, which is in the range of what is applied during the induction welding process (Martin, Figueiredo, et al., 2023b). In both Figure 6.7a and b, the minor loops at the different amplitudes are clearly visible. As expected, the hysteresis size increases with increasing applied field amplitude. The saturation magnetization is not reached, even at 48 kA/m. The magnetization of the susceptor sample

(Figure 6.7b) is smaller, because it is only composed of 10%vol of Ni particles, the rest of the sample – the PEI matrix – is not magnetic.

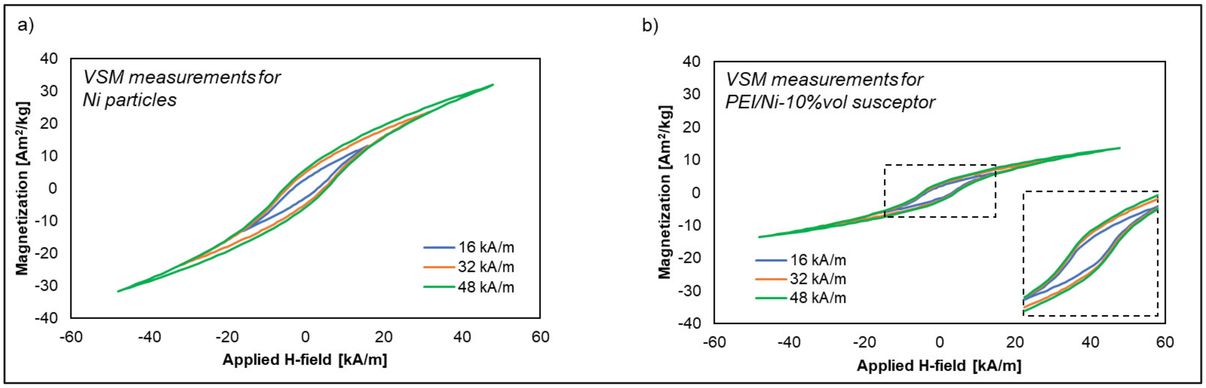

Figure 6.7 VSM results for (a) Ni particles and (b) PEI/Ni-10%vol susceptor at 25°C. Enclosed is zoom-in on the center of the magnetic hysteresis curves highlighted by the dashed black rectangle

To better compare both materials, the hysteresis curves at 32 kA/m are presented in Figure 6.8. The measured magnetic moment is normalized by the total mass of the sample to obtain the mass magnetization, which is presented in Figure 6.8a (similar curves as in Figure 6.7a and b), and by the mass of the Ni in Figure 6.8b, assuming a volume fraction of 10%. The curves overlap in Figure 6.8b, which is a good indicator that the actual Ni concentration is 10%vol as expected. The shape of the hysteresis loop differs a little in the center, with a slightly lower coercivity for the susceptor, which can be caused by the difference of magnetic interactions between the particles. Further measurements would be required to better understand the small difference of hysteresis shape between the two materials. The enclosed surface areas of both hysteresis curves presented in Figure 6.8b are calculated. Absorbed energy densities of 2244 J/m^3 and 2091 J/m^3 are obtained for the Ni particles and the PEI/Ni-10%vol susceptor, respectively, considering the volume of Ni particles.

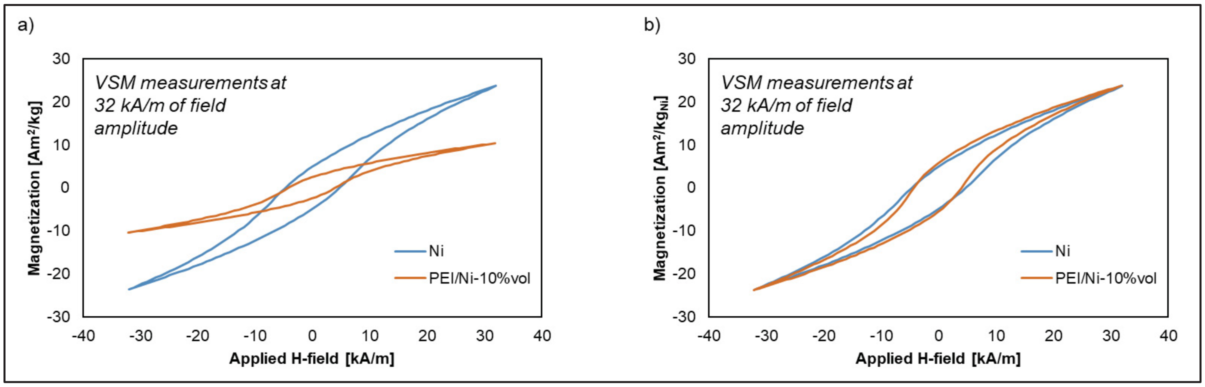

Figure 6.8 VSM results for Ni particles and PEI/Ni-10%vol susceptor at room temperature, with magnetization reported (a) per unit of mass of the sample and (b) per unit of mass of Ni, assuming 10%vol of particles in the susceptor

The evolution of the absorbed energy density of both Ni particles and susceptor is also measured as a function of temperature, to observe the expected decrease of magnetic properties. Measurements are conducted at 25°C, 100°C and 200°C on the PEI/Ni-10%vol susceptor and at 25°C on the Ni particles. The results are presented as a function of the maximum applied magnetic field in the hysteresis loop and are shown in Figure 6.9a. The measurements follow the typical Steimetz equation as presented in 1.3.3.3. The slope is different between the Ni particles and the PEI/Ni susceptor. This might be caused by the difference of magnetic interactions between Ni particles, as their packing is different in the two samples. In the susceptor, the distance between particles is larger, because of the PEI matrix. Ni particles alone are packed more densely, which can affect their magnetic response to the applied magnetic field during VSM measurements. In Figure 6.9b, the same results are presented as a function of the temperature. This allows to observe the decrease of the absorbed energy density with the increase of temperature. An extra data point at 358°C is added corresponding to the Curie temperature at which the material theoretically has lost all magnetic ordering. The decrease is almost linear, which corresponds to what has been reported in the literature for Ni (Harrison, 1904). Finally, a comparison of the magnetic hysteresis of the PEI/Ni-10%vol susceptor tested at 25°C, 100°C and 200°C under an applied field amplitude of 32 kA/m is presented in Figure 6.9c. The decrease of the enclosed surface area, which corresponds to the absorbed energy density, is visible in this figure.

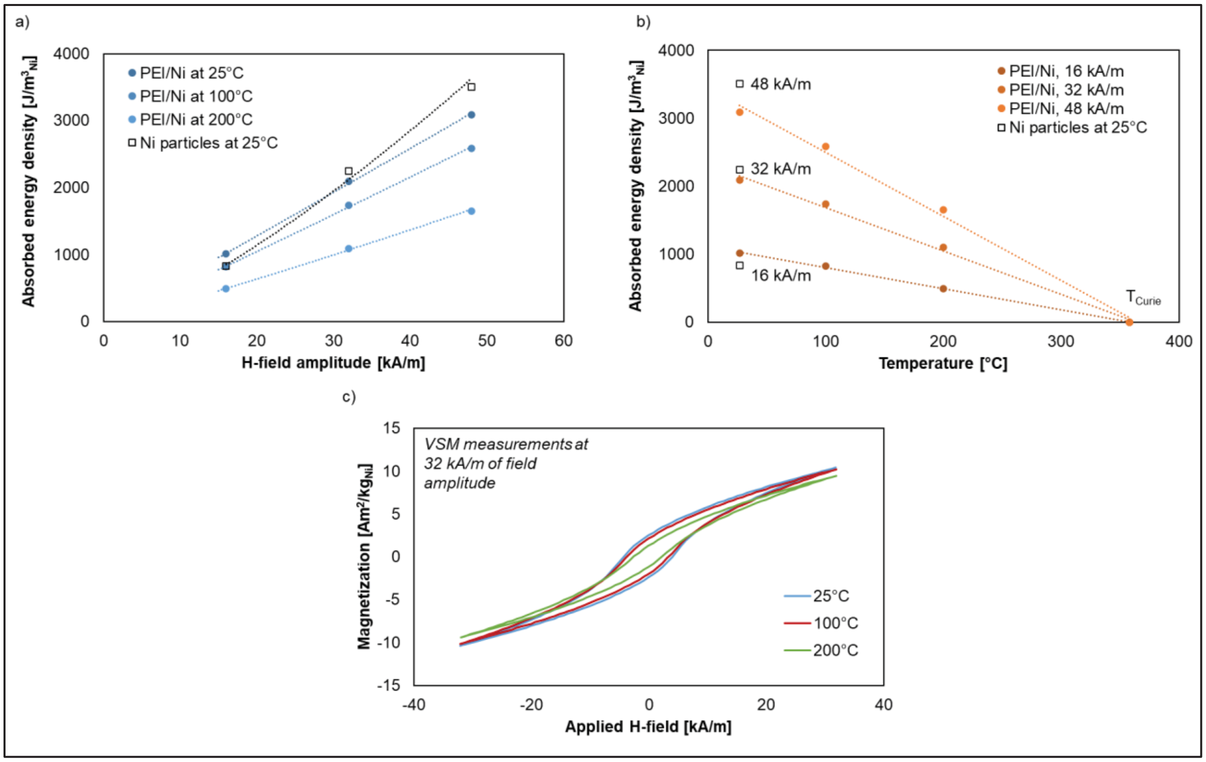

Figure 6.9 Absorbed energy density of PEI/Ni-10%vol susceptor samples and Ni particles at different field amplitudes and temperatures, presented as a function of (a) the applied field amplitude, and (b) the temperature. Hysteresis curves of the PEI/Ni-10%vol susceptor samples tested at various temperatures under a field amplitude of 32 kA/m are presented in (c)

6.4.2 Printed susceptor characterization

The susceptor is then observed and characterized after the printing step. Figure 6.10 shows cross-section and in-plane views of a printed film of susceptor. The porosities that were observed in the filament are still present in the printed part. Overall, the dimensions of the printed part are comparable to the expected values, with a total thickness close to 1 mm in Figure 6.10a. There is good continuity between printed filaments, as their interface is not visible, in both cross-section and in-plane views, which indicates a high degree of contact and welding between deposited layers. As observed in the filament before printing, the Ni distribution in the printed susceptor is homogeneous, with no signs of agglomeration. This indicates that the susceptor will be able to heat up evenly during induction welding.

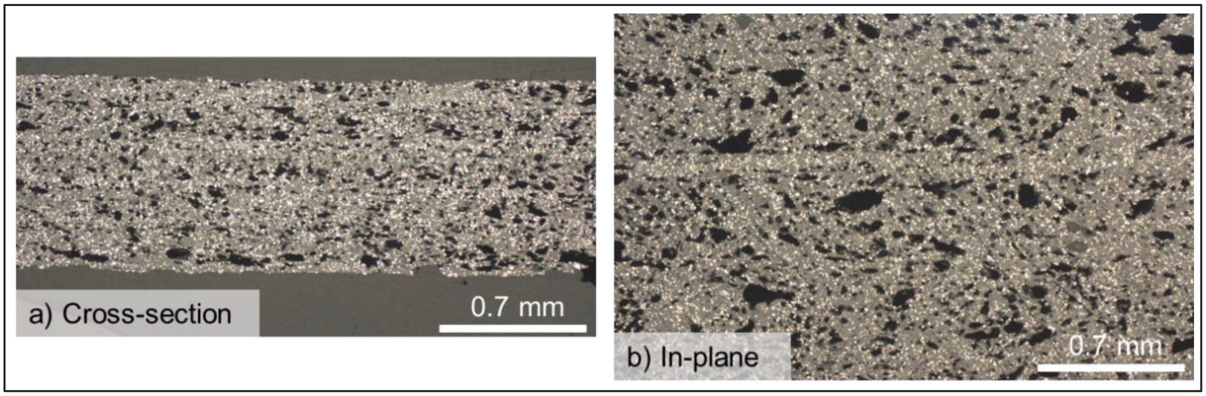

Figure 6.10 Optical microscopy images of printed susceptor films (a) in cross-section view and (b) in in-plane view

For the sake of comparison, a similar 1 mm-thick 3D-printed film of CF/PEI is prepared using commercial filament from 3DxTech. Cross section of this film is observed with optical microscope and compared to the printed PEI/Ni-10%vol susceptor film. The comparison of both materials is presented in Figure 6.11. The apparent surface fraction of porosities is quantified by performing image analysis with the ImageJ software. Binary images extracted from Figure 6.11a and b and used for the analysis are presented in Figure 6.11c and d. For the PEI/Ni film, a surface concentration of 15.9% of porosities is measured. It must be noted that the porosities with size close to the Ni particles diameter (approx. 5 mm) could be holes left by particles being pulled out during polishing and not actual porosities. But as it is impossible to distinguish which fraction of the measured porosities are caused by this mechanism, it is not considered in the calculation. For the CF/PEI sample, a porosity level of 8.0% is obtained. This is lower than in the printed susceptor, but large porosities appear to be the same size in both materials. This is a good indicator that the quality of the susceptor filament is already promising, although improvement can still be made to reduce the porosity level below 10% and reach similar level as in commercially available composites filaments. In Figure 6.11a and b, the concentration of filler is larger in the susceptor than in the commercial CF/PEI. This can also affect the porosity level and be responsible for the higher measured value. Reducing the Ni content, if the heating capability remains satisfying, could also help reducing the porosity level.

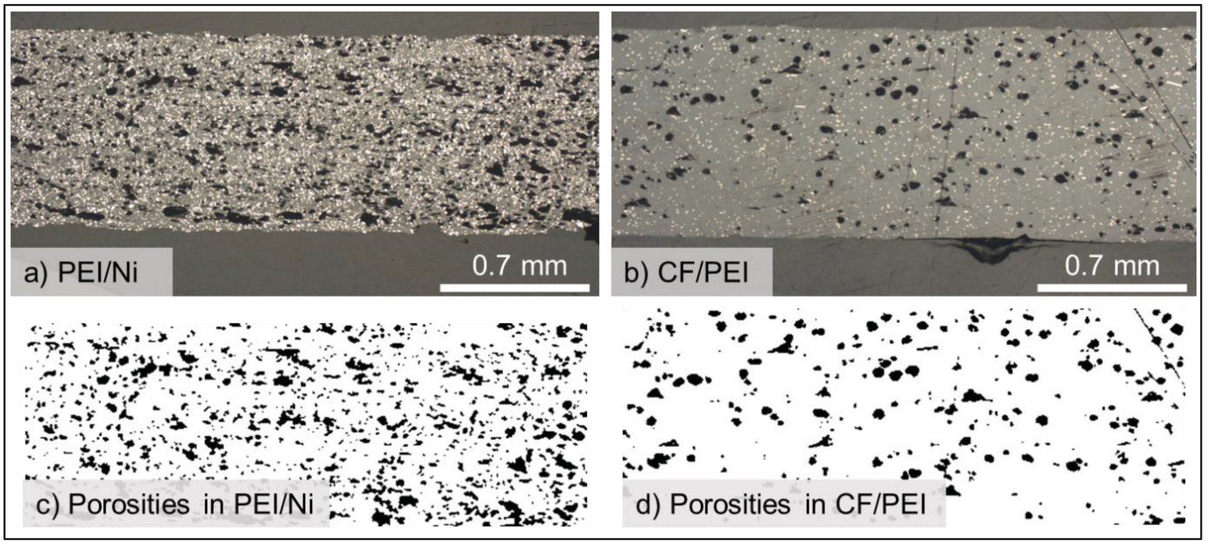

Figure 6.11 Comparison of cross-section views of 3D-printed (a) PEI/Ni-10%vol susceptor and (b) commercial CF/PEI composite. Binary pictures used for image analysis representing the porosities in (c) PEI/Ni-10%vol printed susceptor and (d) commercial CF/PEI printed composite

Finally, the induction heating capabilities of the printed susceptor are characterized. A total of eight printed samples are measured. Four pressed samples like those characterized in Chapter 4 are also tested to ensure a proper comparison can be conducted (same coupling distance, room temperature, etc.). First, the samples are weighted, and their thickness is measured to evaluate their density using the "Volume method" presented in Chapter 4. The average densities of pressed samples and printed samples are 2.128 g/cm^3 and 1.443 g/cm^3, respectively. The density of the printed samples is clearly lower than the pressed samples. This is probably mostly due to the presence of porosities in the printed samples. Based solely on this explanation, the difference of density between pressed and printed samples corresponds to a porosity level of 32%vol in the printed samples. This result confirms the need to reduce the porosity level inside the printed susceptor to obtain good quality material. One should note that this result differs from the value obtained by image analysis. This comes from the fact that in image analysis, a surface concentration is obtained, but a volume fraction is calculated when comparing densities.

Following this preliminary characterization step, samples are heated up for 60 s, then the induction heating system is turned off, while temperature is recorded for another 60 s. The temperature at the center point of the sample is extracted from the thermal camera data Figure 6.12). The printed susceptor samples reach lower temperature than the pressed ones. The lower heating can be attributed to the lower density of the samples, caused by porosities. As less Ni particles are present in the same volume, less heat is generated. This highlights once again the need to reduce the porosity level inside the susceptor filament to increase the heating properties. The printed samples also present a larger variability than the pressed samples. This needs to be addressed as it could lead to local differences in heating and in welding.

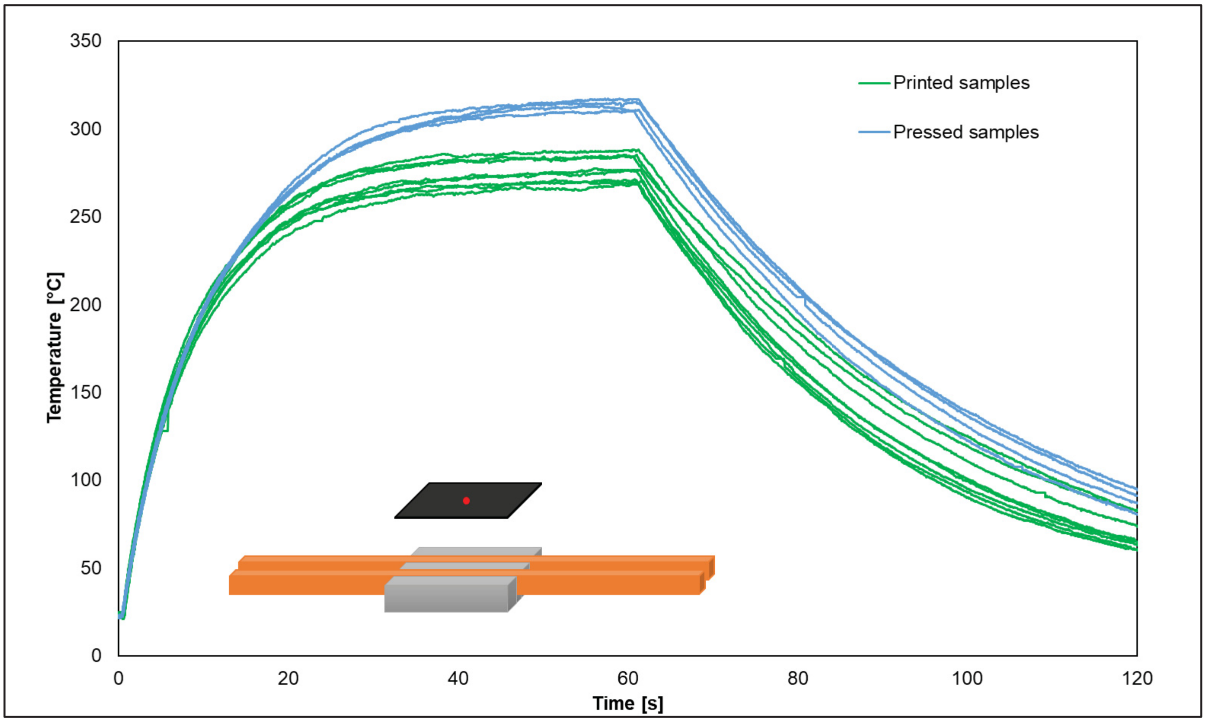

Figure 6.12 Induction heating curves of pressed and printed susceptor samples. Enclosed is a scheme of the induction heating setup, with the red point indicating where the temperature evolution is recorded by the thermal camera

Figure 6.13 presents the maximum temperature reached during induction heating tests as a function of the sample's density and the sample's weight, respectively. In Figure 6.13a, the printed samples have a lower density, as discussed, which is causing the lower average temperature, as already observed in Figure 6.12. However, Figure 6.13b shows that the variability of the measurements for both printed and pressed samples can be correlated to the mass of the sample. The mass variation is caused by the thickness variation of the samples. In the case of printed susceptor samples, this can be attributed to the variation of the filament's diameter. The slicing software, which prepares the instructions for the 3D-printer, assumes a constant diameter of 1.75 mm. However, if in reality the filament exhibits a different diameter, the printer cannot adjust and will extrude too much or too little material. Compared to a 1.75 mm filament, printing with a 1.6 mm filament represents a reduction of 16% of the deposited material, and an increase of 18% with a 1.9 mm filament. The tested printed samples exhibit thickness variability of the same range, indicating that the filament diameter variability is most probably responsible for the variations of thickness, which in turn impacts the heating variability.

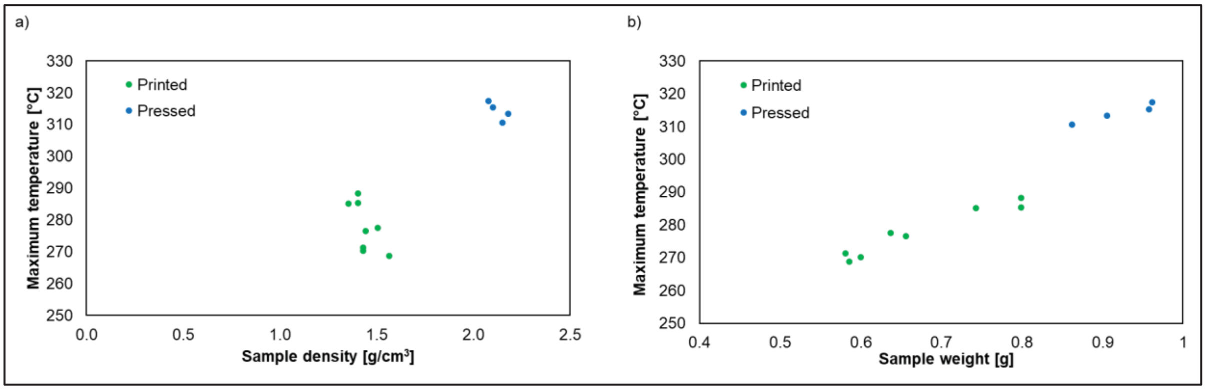

Figure 6.13 Maximum temperature reached by pressed and printed susceptor samples during induction heating tests (a) as a function of the sample's density, and (b) as a function of the sample's weight

6.4.3 Susceptor deposition on honeycomb cores

To verify the printability of the susceptor filament in complex geometry, a susceptor layer is printed directly on top of a honeycomb core. The process of printing PEI honeycomb with one printing head and then shifting to the second printing head to deposit the susceptor layers is conducted successfully. One sample for each susceptor printing configuration is presented in Figure 6.14; the complex geometry of the susceptor layer is correctly reproduced, and the deposition is clean and uniform across the surface of the sample. Close-up views of the printed susceptor layer indicate that there is no space between printed filaments inside the top layer.

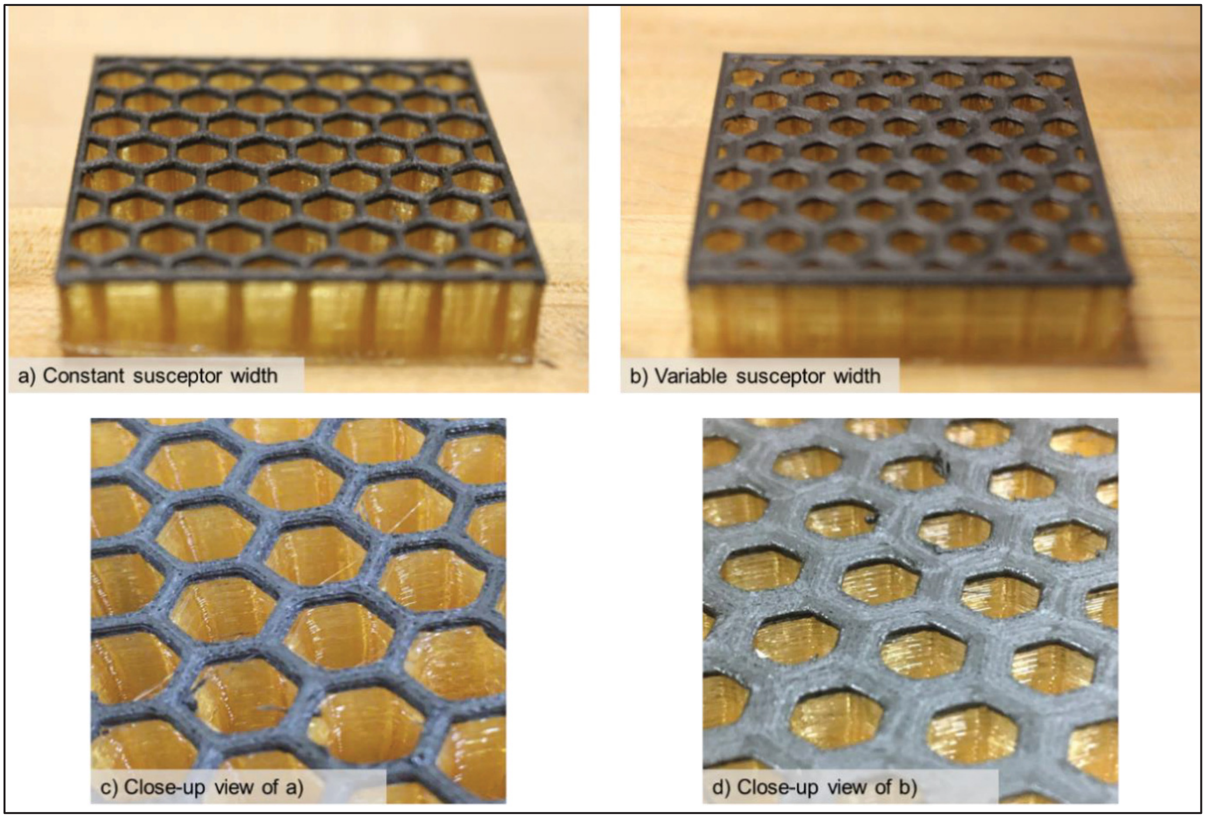

Figure 6.14 Pictures of the susceptor layer printed on top of the honeycomb wall (a) with constant susceptor width and (b) with variable susceptor width. Close-up view of (a) and (b) in (c) and (d), respectively

Optical microscopy images of the printed susceptor layer reveal similar results to the susceptor films presented in Figure 6.15. Porosities are still visible, especially towards the edges of the variable width layers (Figure 6.15b), where no counter-pressure is present during printing, allowing the porosities to remain in their initial round shape. The overall shape of the deposited susceptor layer corresponds well to the expected printing geometry, as highlighted by the overlayed white dashed lines in Figure 6.15c and d. This is an indication of the good printability of the susceptor and of the correct selection of the printing parameters. There is a bit too much printed materials, indicating that over-extrusion, currently set at 1.1, could be slightly reduced.

Careful observation at the inter-filament interface reveals that no interface is visible. It also seems that the porosities are larger and more concentrated in the center of each filament, as previously noted in Figure 6.6. This is beneficial for the inter-filament welding, as porosities in that area would prevent to reach complete degree of intimate contact. It can also be observed that the interface between pure PEI and PEI/Ni susceptor, presented in Figure 6.15e is also very clean, without remaining separation line. This indicates that the printing parameters, especially the printing temperatures, are set correctly, allowing a good contact and a good welding between these two layers.

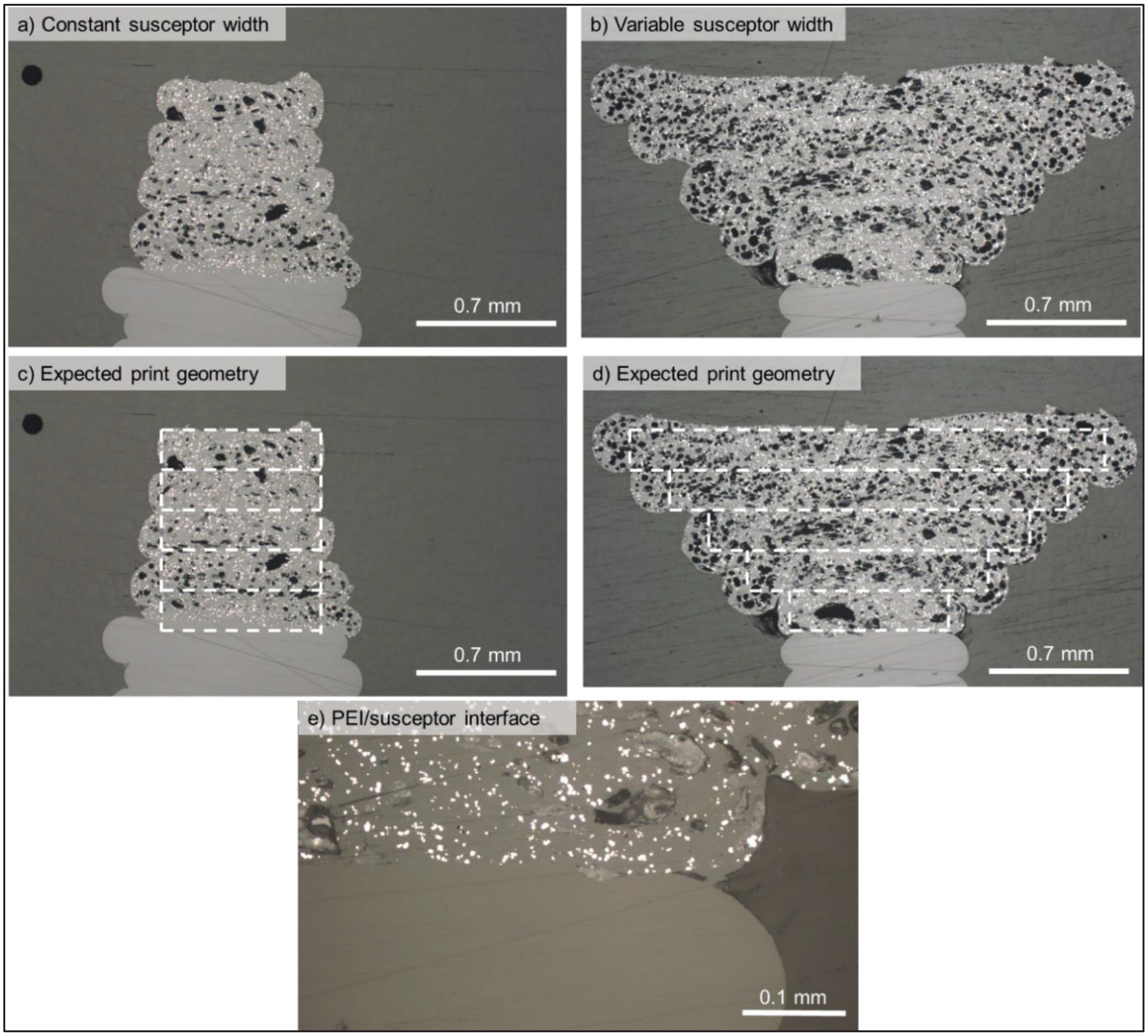

Figure 6.15 Optical microscopy images of printed susceptor layer with (a) constant susceptor width and (b) variable susceptor width. Pictures in (c) and (d) overlays the expected print geometry in dashed white lines on the pictures (a) and (b). Picture (e) in a close-up view of the interface between the PEI honeycomb and the PEI/Ni susceptor layer

6.4.4 Induction welding of honeycomb cores with printed susceptor

Printed cores including a susceptor layer with the two presented geometries are welded to GF/PEEK skins. Welding speeds of 0.1, 0.15 and 0.2 mm/s are used. This is lower than the welding speeds presented in Chapter 5: as less susceptor material is present at the welding interface with a printed susceptor compared to a film susceptor, there is proportionally less heat generation. Also, as previously observed with the induction heating results, the printed susceptor has a slightly lower heating rate due to its porosities.

The observations made on the 6 welded samples are summarized in Table 6.1. For the variable width susceptor layer, a good weld was obtained at 0.15 and 0.2 mm/s. At 0.1 mm/s, some core crushing is visible towards the back edge of the sample, indicating the presence of overheat in that zone. The location of the overheating zone towards the back edge can be explained: as the welding speed is very low, heat dissipated close to the front edge, at the beginning of the welding process, is conducted to the rest of the structure. Therefore, when the coil reaches the areas farther in direction of the back edge, the sample is already hot, which changes the initial temperature and allows the susceptor to reach higher temperatures after application of induction heating, therefore inducing core crushing.

On the other hand, the constant width susceptor layer presents good weld at 0.1 and 0.15 mm/s. When welded at 0.2 mm/s, the sample detached by itself when opening the vacuum bag after the process. In Table 6.1, the variable width susceptor layer presents a higher heating efficiency, allowing it to be welded faster. This is mostly caused by the larger volume of susceptor present at the weld line.

Table 6.1 Summary of the welding of honeycomb cores incorporating a printed susceptor layer

	Welding speed [mm/s]		
	0.1	0.15	0.2
Constant susceptor width	Good weld	Good weld	No weld
Variable susceptor width	Slight overheating/core crushing	Good weld	Good weld

Welded samples are characterized similarly as in Chapter 5, with optical microscopy observations of the welded profile and FWT mechanical tests. Optical microscopy images of samples welded at 0.1 mm/s with both susceptor layer configurations are presented in Figure 6.16. Deformation of the deposited susceptor layer and of the top of the cell walls is clearly visible. As expected from the observations in Table 6.1, more deformation occurred in the variable width susceptor layer (Figure 6.16b), indicating that more heat was dissipated there. A consequence of that are the larger porosities visible in that sample. The porosities are fairly limited in the constant width susceptor, which also seem to be leaning towards one side of the cell walls. This is probably caused by a slight misalignment between the printed honeycomb and the printed susceptor. This is a good representation of the importance of properly calibrating the two printing heads.

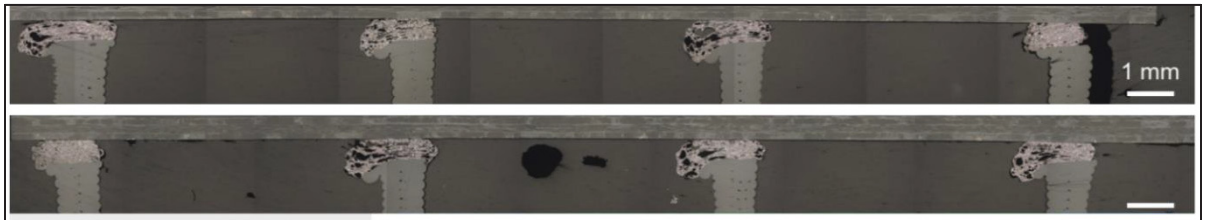

a) Constant susceptor width

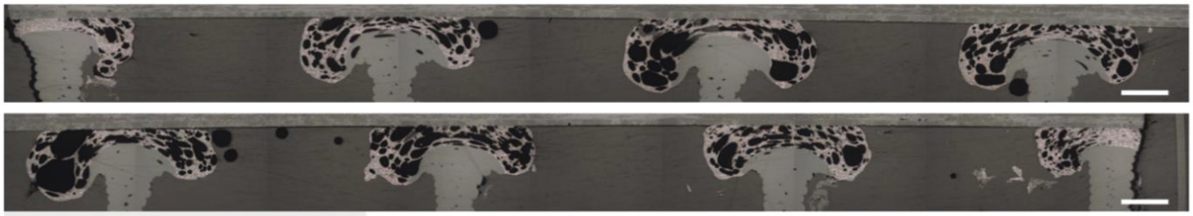

b) Variable susceptor width

Figure 6.16 Welding profile of printed susceptor layers with (a) constant susceptor width and (b) variable susceptor width. The white scalebar represents 1 mm in each picture

Skin/core strength is evaluated by performing FWT tests on the welded sandwich panels (Figure 6.17). The sample with a constant width of susceptor welded at 0.2 mm/s is not tested as it did not weld, but it is reported in the results as a zero strength to highlight that this speed is insufficient. Samples welded at 0.15 and 0.1 mm/s exhibit a similar strength (around 1.8 MPa). The failure mode in these two samples is cohesive in the susceptor layer (Figure 6.18a and b), indicating that welding was achieved but the susceptor layer broke. This might be caused by the porosities inside that layer, and thus might be the maximum available strength with that material. On the other hand, samples welded with a variable susceptor width exhibit higher strength. The sample welded at 0.2 mm/s reached equivalent strength as the two successful welds with the constant susceptor width, despite the higher speed. It also exhibits a similar cohesive failure (Figure 6.18e). Then, the sample welded at 0.15 mm/s broke at approximately 11.4 kN, which corresponds to a skin/core strength of 4.6 MPa. Plus, as visible in Figure 6.18d, the failure mode is mostly core failure, indicating the high strength of the weld compared to the printed core. Finally, the sample welded at 0.1 mm/s could not be evaluated as failure occurred in the adhesive layer between the sample in the steel block. This is mostly caused because an incomplete bonding was reached as the surface of the sample is not flat due to the crushed core. As visible in Figure 6.18c, the adhesive was only able to cover about two thirds of the surface, which reduced its resistance during FWT tests and lead to an early failure.

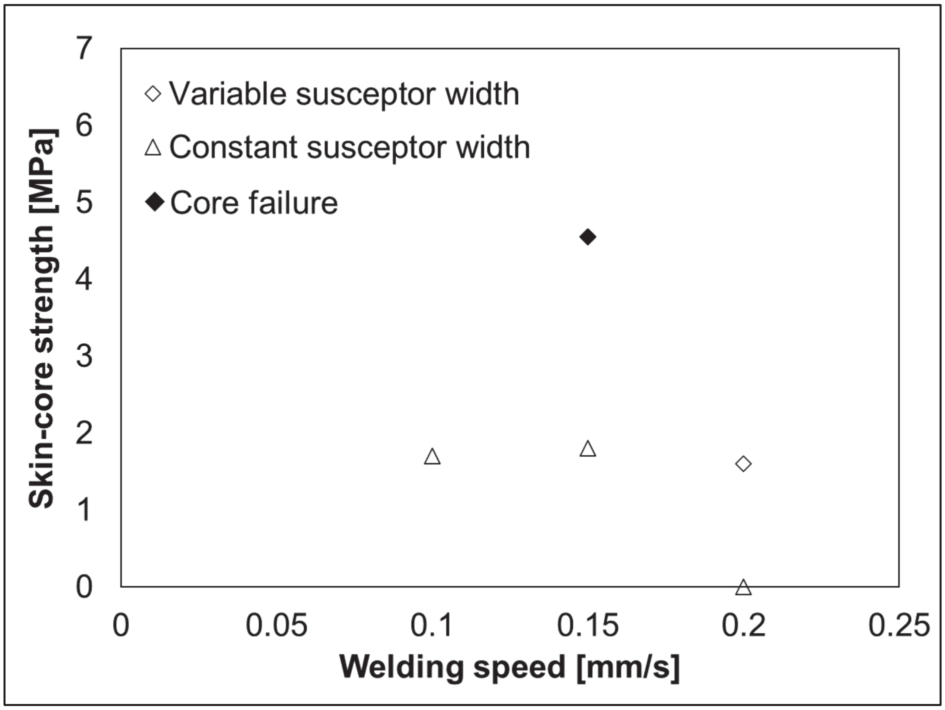

Figure 6.17 Skin/core strength versus welding speed, obtained by FWT tests on sandwich samples welded with printed susceptor layer. The solid black diamond represents the sample that failed in the core

a) Constant width & 0.1 mm/s

b) 0.15 mm/s

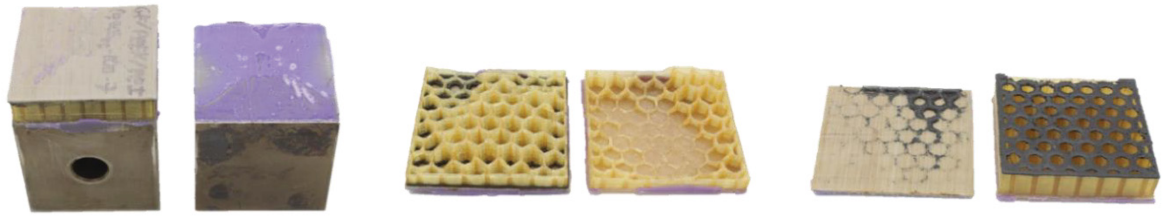

c) Variable width & 0.1 mm/s

d) 0.15 mm/s

e) 0.2 mm/s

Figure 6.18 Fractured FWT samples welded with (a) and (b) constant susceptor width and welding speed of 0.1 and 0.15 mm/s, respectively (no welding was obtained at 0.2 mm/s), and (c), (d) and (e) variable susceptor width welding speed of 0.1, 0.15 and 0.2 mm/s, respectively

These preliminary results provide valuable information, although they are based on only one sample per welding configuration (susceptor layer geometry and welding speed). First, the printed susceptor layer requires a slower welding speed to reach sufficient welding, between 0.1 and 0.2 mm/s compared to 0.5 to 1.0 mm/s for susceptor films. However, it is possible to obtain high strength and reach core failure with printed susceptor, showing that this material has the capability to weld the samples. This is a major milestone to prove the feasibility of using printed induction welding susceptors to weld high-performance thermoplastics. The geometry of the susceptor layer has a large impact on the skin/core strength. The variable width provides a larger contact surface area between the skin and the core, which explains the increase in strength observed for the sample welded at 0.15 mm/s. Additionally, as more material is deposited in the variable susceptor width layer, more heat is generated. As observed with the sample welded at 0.1 mm/s, too much heat was generated, which indicated that this geometry could be optimized (reduced overall layer thickness, Ni particles concentration, etc.). The combination of larger contact surface area and larger heat generation explains the higher strength reached with the variable susceptor width. Despite the large porosities observed in Figure 6.16b, the welded skin/core strength is still larger than the tensile strength of the core, where failure ultimately occurred.

When looking at the samples welded with a constant printed susceptor width, lower speed was required to reach welding. Once again, this is due to the minimal quantity of material that was added, leading to a lower amount of generated heat. However, this also means a smaller weight penalty due to the heating element, which can be favorable. It was still possible to reach almost 2 MPa of skin/core strength, which is a good result for a preliminary, proof-of-concept test. The cohesive failure observed for these samples indicated that the susceptor layer was partially welded, but it was mechanically weaker than the core. An improvement on the susceptor filament production leading to a reduction of the porosity level could be beneficial to increase the strength of the susceptor layer. Lower porosity level would also increase the heating rate, as discussed in 6.4.2. Interestingly, the fact that the strength did not increase when reducing the welding speed from 0.15 to 0.1 mm/s gives several indications: first, it is not possible to increase the degree of welding, meaning that 0.15 mm/s is the optimal speed. Also, no overheating is observed, as no core crushing is visible, even at lower speed. That indicated that the susceptor cannot overheat in that configuration, once again highlighting the temperature-control feature of the hysteresis losses susceptors thanks to the Curie temperature of Ni. Finally, sources of improvements are not in the welding parameters but mostly in the materials development, by reducing the porosity level, selecting the optimal susceptor layer geometry and thickness, and its Ni content.

CHAPTER 7

CF/PEEK SKINS ASSEMBLY BY INDUCTION WELDING FOR THERMOPLASTIC COMPOSITE SANDWICH PANELS

Romain G. Martin[a], Christer Johansson[b], Jason R. Tavares[c] and Martine Dubé[a],

[a] CREPEC, Department of Mechanical Engineering, École de technologie supérieure, 1100 Notre-Dame West, Montreal, Quebec, Canada H3C 1K3
[b] RISE Research Institutes of Sweden, Arvid Hedvalls Backe 4, Göteborg, Sweden, SE-411-33
[c] CREPEC, Department of Chemical Engineering, Polytechnique Montréal, 2500 chemin de Polytechnique, Montréal, Québec, Canada, H3T 1J4

Paper published in *Composites Part B: Engineering*, July 2024

7.1 Abstract

A method to assemble sandwich panels made of carbon fibre reinforced poly-ether-ether-ketone (CF/PEEK) facesheets and 3D-printed poly-ether-imide (PEI) honeycomb cores using induction welding is presented. Heating patterns inside CF/PEEK laminates of variable dimensions are first evaluated with a thermal camera and compared to a COMSOL Multiphysics model. The good agreement between the measurements and the simulations indicates that the model can be used to predict heat dissipation. Sandwich samples are then prepared by vacuum-assisted continuous induction welding under conditions recommended by the modelling efforts. Facesheets do not deconsolidate in the process and core crushing is avoided. Flatwise skin/core strength of the welded samples reaches up to 7 MPa, above reported performance for thermoset or thermoplastic composite sandwich panels.

7.2 Introduction

Thermoplastic composites are gaining traction in the aerospace and automotive fields due to their unlimited shelf life, their weldability, and their recyclability (Ageorges et al., 2001).

Welding in particular is increasingly used in various fields to assemble thermoplastic composite parts. Various welding methods exist, relying on thermal, friction or electromagnetic mechanisms to generate heat at the joining interface (Yousefpour et al., 2004). Amongst these, ultrasonic welding, resistance welding and induction welding are the most used methods and are already implemented in industry (Van Ingen et al., 2010). They all present advantages and limitations, which makes them complementary. In the present study, the focus is placed on induction welding as a joining technique to fabricate thermoplastic composite sandwich panels.

7.2.1 Induction welding

Induction welding relies on the application of an alternating magnetic field on the joining interface to melt or soften the surrounding thermoplastic polymer. Heat can be generated at the interface by two different mechanisms: induced eddy currents in electrically-conductive materials (Ahmed et al., 2006; Bayerl et al., 2014; Yousefpour et al., 2004), or hysteresis losses in magnetic materials (Martin et al., 2022; Suwanwatana et al., 2006a; Wetzel & Fink, n.d.). When needed, a heating element called a susceptor can be placed at the interface to localise the heat generation. This is required when welding non-conductive composites, such as those made of glass or natural fibres, which do not possess the ability to heat up by induction. Due to their good electrical conductivity, carbon fibre reinforced thermoplastic composites can be welded without using a susceptor, in a process known as susceptor-less welding (Bayerl et al., 2014; Kane et al., 2020; Mitschang et al., 2002; Rudolf et al., 2000). As an alternating magnetic field is applied to the laminate, eddy currents are induced in the carbon fibres, which heat up due to the Joule effect. Three main mechanisms are responsible for the heat dissipation inside the laminate (Ahmed et al., 2006; Barazanchy & van Tooren, 2023; Bayerl et al., 2014; Yarlagadda et al., 2016). First, the heat is generated by the Joule effect as current circulates in the fibres. Secondly, at the intersection of fibres – typically between two non-parallel plies in laminates composed of unidirectional layers, or at the junctions of fibres in woven fabrics – heat is generated by contact resistance or, thirdly, by dielectric heating when a thin layer of polymer stands in between the two fibre tows. Those mechanisms all contribute to the induction heating of laminates.

There is one important drawback to using the susceptor-less method: when eddy currents are induced in an electrically-conductive material, the formed current paths are loops. When the induction coil approaches the edges of the material, these loops are compressed, locally increasing the current density and inducing high heat generation at the edges (edge effect) (Ahmed et al., 2006; Barazanchy, Pandher, et al., 2021). This phenomenon, schematized in Figure 7.1, causes inhomogeneous heating at the joining interface and must be minimized. Different propositions have been made to reduce this effect, such as for example placing a conductive bypass material at the edges of the parts (Hagenbeek et al., 2018).

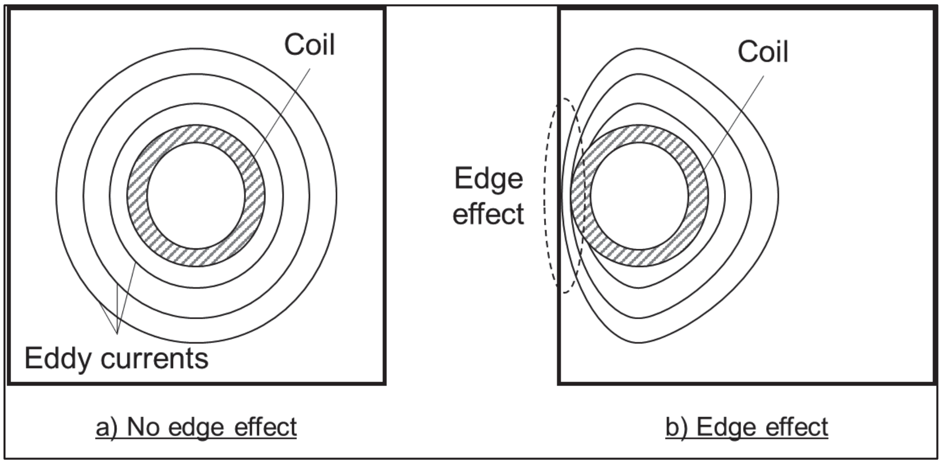

Figure 7.1 Scheme of eddy currents distribution in an electrically-conductive material (a) without and (b) with edge effects due to induced eddy current loops concentration

7.2.2 Modelling of laminate heating by induction

Understanding and predicting the temperature distribution in a laminate to be welded is critical to ensure the good quality of the weld. As explained, different mechanisms impact heat generation, and variation of local parameters such as the distance between fibres can affect the heating rate. To avoid modelling the matrix and the fibres individually, various studies apply the simplifying assumption that the laminate behaves as a macroscopic homogenous conductive material with equivalent anisotropic properties (Duhovic, L'Eplattenier, et al., 2014; Hoffman et al., 2023; Lionetto et al., 2017; Moser, 2012; O'Shaughnessey et al., 2016). This considerably reduces the calculation time of the models.

The in-plane electrical conductivity of a carbon fibre-based laminate is a critical parameter to simulate the induction heating as it controls the temperature distribution in the sample (Grouve et al., 2020). It can be estimated from the electrical conductivity of the carbon fibre itself, depending on the fibre volume fraction and the ply orientation sequence in the laminate. The rule of mixture (Equation (7.1)) can be used to calculate the longitudinal electrical conductivity of a ply σ_0 (in the direction of the fibres) (Grouve et al., 2020):

$$\sigma_0 = \sigma_f \cdot v_f + \sigma_m \cdot \left(1 - v_f\right) \approx \sigma_f \cdot v_f \qquad (7.1)$$

With σ_f and σ_m representing the fibre and matrix electrical conductivity, respectively, and v_f the fibre volume fraction. As $\sigma_m \ll \sigma_f$, the second term of the addition can be neglected. The transverse electrical conductivity σ_{90} is also very small compared to the longitudinal one and can be neglected. Then, the electrical conductivity of the laminate is calculated by considering the orientation of each ply. In a $[0,90]_{2S}$ laminate, half of the plies are in the x-direction and the other half in the y-direction, which means the equivalent electrical conductivity will be equal in both directions. The electrical conductivity in the x-direction can be calculated using Equation (7.2):

$$\sigma_0 = \sigma_f \cdot v_f + \sigma_m \cdot \left(1 - v_f\right) \approx \sigma_f \cdot v_f \qquad (7.2)$$

With f_x representing the fraction of plies in the x-direction. In the case of a $[0,90]_{2S}$ laminate ($f_x = 0.5$) with a fibre volume fraction of 60%, the electrical conductivity of the laminate equals 0.3 times the fibre electrical conductivity.

Recent work from Van den Berg et al. showed the 6-probe method to be an efficient and reliable way to measure the in-plane anisotropic electrical conductivity of a laminate (Van den Berg et al., 2023). Their work also concluded that the rule of mixture based on the carbon fibre conductivity provided a good approximation of the electrical conductivity of the composite laminate, which is why it is retained in this paper.

A wide range of values for the carbon fibre electrical conductivity have been reported in the literature, depending on the fibre type and the measurement method. This variability impacts the equivalent electrical conductivity of the laminate. The electrical conductivities of Tenax HTS45 and other commercially available carbon fibres are summarized in Table 7.1, also presenting the corresponding laminate electrical conductivities, based on Equation (7.2). It appears that there is variability in the reported values, but a range between 16000 and 22000 S/m seems to be reasonable.

Table 7.1 Electrical conductivity values for carbon fibres and laminates from the literature

Carbon fibre type	**Fibre electrical conductivity [S/m]**	**Equivalent $[0,90]_{2S}$ laminate electrical conductivity (v_f = 60%) [S/m]**	**References**
Tenax HTS45	66667	20000	(Teijin Carbon America, Inc., 2019)
IM7	67114	20134	(Ji et al., 2022)
AS4	64935	19481	(Ji et al., 2022)
AS4	59000	17700	(Grouve et al., 2020)
T1000G	71429	21429	(Toray Composites Materials America, Inc., 2024)
T700S	62500	18750	(Toray Composites Materials America, Inc., 2018b)
T300	58824	17647	(Toray Composites Materials America, Inc., 2018a)
T300	55556	16667	(Gaier et al., 2003)

The main limitation of this approach is that it does not consider the interactions between non-parallel carbon fibre plies. It has been demonstrated that the number of 0°/90° interfaces in the laminate affects the induction heating. For example, a $[0,90]_{2S}$ and a $[0_2,90_2]_S$ laminate have the same amount of fibres in each direction and the same equivalent electrical conductivity is obtained using the presented rule of mixture (Equation (7.1)), but they will not heat up the same way, since there are more 0°/90° interfaces in the $[0,90]_{2S}$ assemblies (Martin, Johansson, et al., 2023). To correctly predict the heat generation, it is therefore necessary to use a microscale model, which considers each ply separately and calculates their interactions (Barazanchy, Van tooren, et al., 2021; de Wit et al., 2023; Hoffman et al., 2023; H. J. Kim et al., 2003). These models are more precise but more complicated to implement and more calculation-intensive than those using the equivalent homogeneous material approximation.

7.2.3 Sandwich structures

Sandwich structures are used in some applications where a high bending stiffness and low weight are required. They are composed of two skins – or facesheets – at the top and bottom of a low-density core, which can be a cellular structure (honeycomb, corrugated, etc.) or a foam (Castanie et al., 2020). The skins are typically made of carbon fibre reinforced thermoset composites or aluminium. The cores can be made of a large variety of materials and geometries, from Nomex and aluminium honeycombs to polymeric foams. The skin-core assembly, which is required to transfer the loads across the structure, is usually accomplished through adhesive bonding. Recently, the interest for all-thermoplastic sandwich panels has been growing, as these materials present the advantages of being potentially repairable and recycled (Barroeta Robles et al., 2022; Pegoretti, 2021). However, the use of thermoplastic polymers requires adapting the skin-core joining method, as adhesive bonding usually requires extensive surface preparation and can lead to low mechanical properties (Ageorges & Ye, 2002).

The use of welding for this joining step is evaluated as an alternative. It is reported that the assembly of sandwich structures by thermoplastic welding can by done in two ways: isothermally, where the pressure is applied during heating of the parts, and non-isothermally, where the parts are first heated, then transferred to a secondary device in which pressure is applied to consolidate the parts together (Skawinski et al., 2004). The pressure is applied by placing parts in a vacuum bag (Brooks et al., 2008; Grünewald et al., 2018; Pappadà et al., 2010), by compression moulding in a hot press (Åkermo & Aström, 2000b; Latsuzbaya et al., 2023; Rozant et al., 2001) or by double-belt lamination (Trende et al., 1999; Xinyu et al., 2009). In these methods, either the whole part is heated up, making the core prone to collapse under the applied pressure and causing the facesheets to deconsolidate, or heat is lost during parts transfer when laminates skins are heated up separately, requiring them to be overheated.

In a previous work from the authors, glass fibre thermoplastic composite facesheets were joined to a thermoplastic polymer core by induction welding, using a hysteresis-losses susceptor placed at the interface between the skins and the (Martin et al., 2024). In that case, heat was generated directly at the joining interface instead of across the complete structure. This method demonstrated the advantages of welding as a joining technique to manufacture sandwich panels. The use of a susceptor was necessary to join glass fibre facesheets. In the case of carbon fibre facesheets, a susceptor located at the weld interface may not be necessary because it would be possible to heat up the carbon fibre directly. In such a case, the facesheets would likely be heated across their entire thickness, as opposed to a local heating at the joint interface when a susceptor is used.

The goal of the present study is to join skins made of carbon fibre reinforced poly-ether-ether-ketone (CF/PEEK) laminate to a honeycomb core made of poly-ether-imide (PEI). The induction heating behaviour of the laminate must first be analyzed to determine the induction welding parameters that can be used to weld the facesheets to the core, in order to produce sandwich panels. As edge effects, and therefore overheating that could lead to core crushing, are expected at the edges of the panels, it is proposed to increase the sandwich skin dimensions compared to the core of the sandwich structure to be welded. This will reduce edge effects – or localise them in the sacrificial skin length – and allow for a more homogeneous temperature distribution along the weld line with the core. As previously demonstrated, the use of the Thermabond process on the sandwich skins can be applied to sandwich structures (Grünewald et al., 2017a). This method consists in co-consolidating a layer of PEI at the surface of the CF/PEEK laminate (Cogswell et al., 1989; Smiley et al., 1991), which is possible due to the miscibility of PEEK and PEI (Hsiao & Sauer, 1993). This allows welding to occur at temperatures in the range of 280 to 300°C, i.e., lower than the melting point of PEEK (343°C). Remaining below the PEEK melting temperature reduces the risk of core crushing and skin deconsolidation while ensuring skin-core PEI-PEI joining by thermoplastic welding (Grünewald et al., 2017a).

The induction heating of CF/PEEK skins of various dimensions is first characterized experimentally and compared to a finite element model, to verify its accuracy and its capability to predict heat generation and the temperature distribution in the laminates. Then, 3D-printed PEI honeycomb cores are assembled to the CF/PEEK thermoplastic composite skins comprising a layer of PEI at their surface using the vacuum induction welding technique (Martin et al., 2024) without a susceptor, i.e., by direct heating of the skins' carbon fibre. Finally, the quality of the weld is assessed by testing the sandwich panels under the flatwise mechanical tensile test and the failure modes are reported.

7.3 Methodology

7.3.1 Samples manufacturing

PEEK is selected as the composite matrix due to its high mechanical properties and high service temperature, and because it was used in previous studies reported in the literature, alongside other poly-aryl-ether-ketone polymers such as poly-ether-ketone-ketone (PEKK). PEI was retained due to its compatibility and miscibility with PEEK (Hsiao & Sauer, 1993), and because it exhibits a processing temperature inferior to the melting point of PEEK.

Composite laminates are manufactured using CF/PEEK unidirectional prepreg (Tenax®-E TPUD PEEK-HTS45 from Teijin) in a $[0,90]_{2S}$ lay-up sequence (Teijin Carbon America, Inc., 2020). The consolidation is done by compression moulding in a hot press for 20 min at 380°C and 2 MPa. The resulting 8-ply laminates exhibit a thickness of 1.1 mm. They are cut into 5 cm-long samples of various widths. These samples are to be heated by induction to obtain their surface temperature distribution as a function of time.

Similar samples are produced to be induction-welded to thermoplastic polymeric cores. They are made of the same CF/PEEK lay-up with an additional 100 µm-thick layer of PEI at the surface, based on the Thermabond process (Cogswell et al., 1989; Smiley et al., 1991). Thus, the resulting laminate presents a co-consolidated surface layer of PEI in the area that is welded to the PEI core. The PEI layer is added at the surface of the laminate during the consolidation process, which would have to take place in all cases to produce the composite laminate sandwich skin. The addition of PEI does not add a process step, which would increase the manufacturing time and cost.

The honeycomb cores are manufactured by 3D-printing using an AON3D M2 printer equipped with a 0.4 mm nozzle. The samples have a surface of 5 cm by 5 cm and a height of 11 mm, including a 1 mm thick bottom skin, also 3D-printed from PEI. Hexagonal honeycomb cells have a side length of 4 mm. The cell wall thickness is 0.8 mm. The material used for 3D-printing is an ULTEM 1010 filament with a 1.75 mm diameter (3DxTech). The nozzle temperature is fixed at 390°C, the printing bed at 160°C and the printing chamber at 135°C. The layer height is 0.2 mm, and the printing speed 30 mm/s. Nano-polymer adhesive (Vision Miner) is applied onto the printing bed to improve part's adhesion and minimize warping. The complete sandwich structure to be welded is summarized in Figure 7.2.

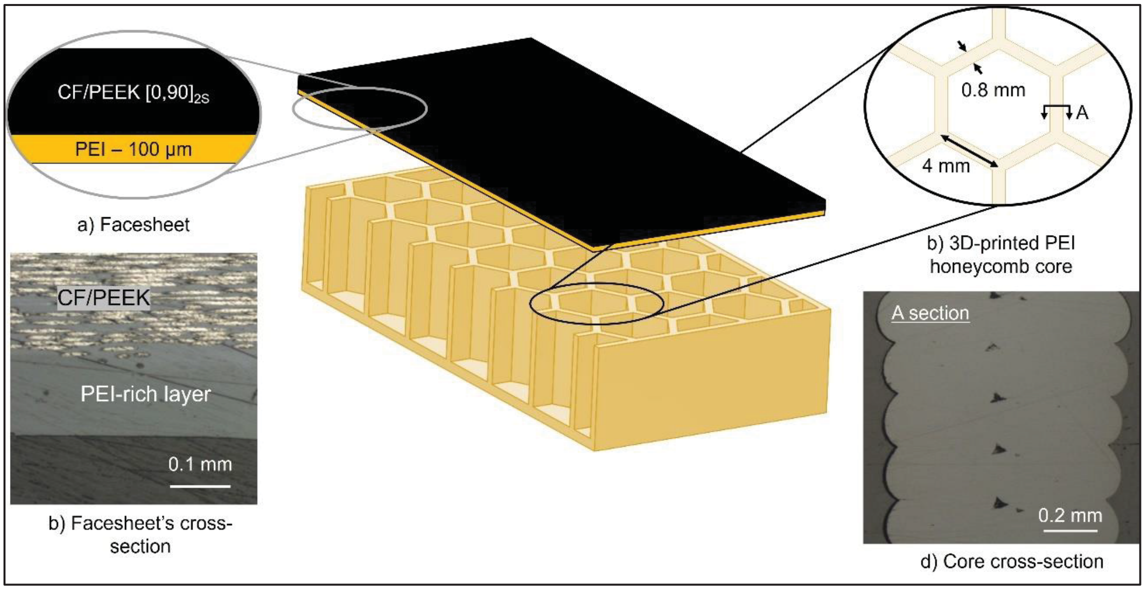

Figure 7.2 Scheme of a sandwich sample, with close-up view on (a) the composite facesheet made of CF/PEEK laminate with a co-consolidated PEI layer, (b) an optical microscopy cross-section image of the facesheet, with the co-consolidated PEI layer highlighted by the white line, (c) the 3D-printed PEI honeycomb core with the cells dimensions, and (d) an optical microscopy cross-section image of the printed core

7.3.2 Static induction heating

To characterize the induction heating of CF/PEEK skins, a tailored setup (Figure 7.3a/b) including a hairpin copper coil equipped with a magnetic field concentrator (MFC) is used (Martin, Figueiredo, et al., 2023b). The sample is placed on a Kapton film that keeps it suspended above the coil at coupling distance of 4 mm. A FLIR A700 thermal camera records the thermal evolution of the static sample during a heating period of 90 s. The alternating current amplitude is varied in the range of 50 A to 100 A, and the frequency is automatically adjusted by the generator to match the resonance frequency of the system. This frequency depends on the current, the size of the MFC, the coil geometry and the interaction with the sample.

The emissivity of the laminate is determined by heating up a sample on a heating plate, and by recording the temperature at the surface simultaneously with a thermocouple and the thermal camera, initially with an emissivity set at 1. The emissivity is then reduced until the reading of the thermocouple and the thermal camera are matching, which happens with an emissivity of 0.95 in this case, which corresponds to what was reported in the literature (Mitschang et al., 2002).

The temperature distribution on the surface facing the thermal camera (opposite to the induction coil) is first extracted from thermal camera imaging. Then, the temperature distribution is measured along three lines of interest on the sample, as presented in Figure 7.3c: the center profile temperature (in green), the center width profile (in red) and the 5 mm width profile (in blue, which is parallel to the central width but 5 mm away from the center of the induction coil.

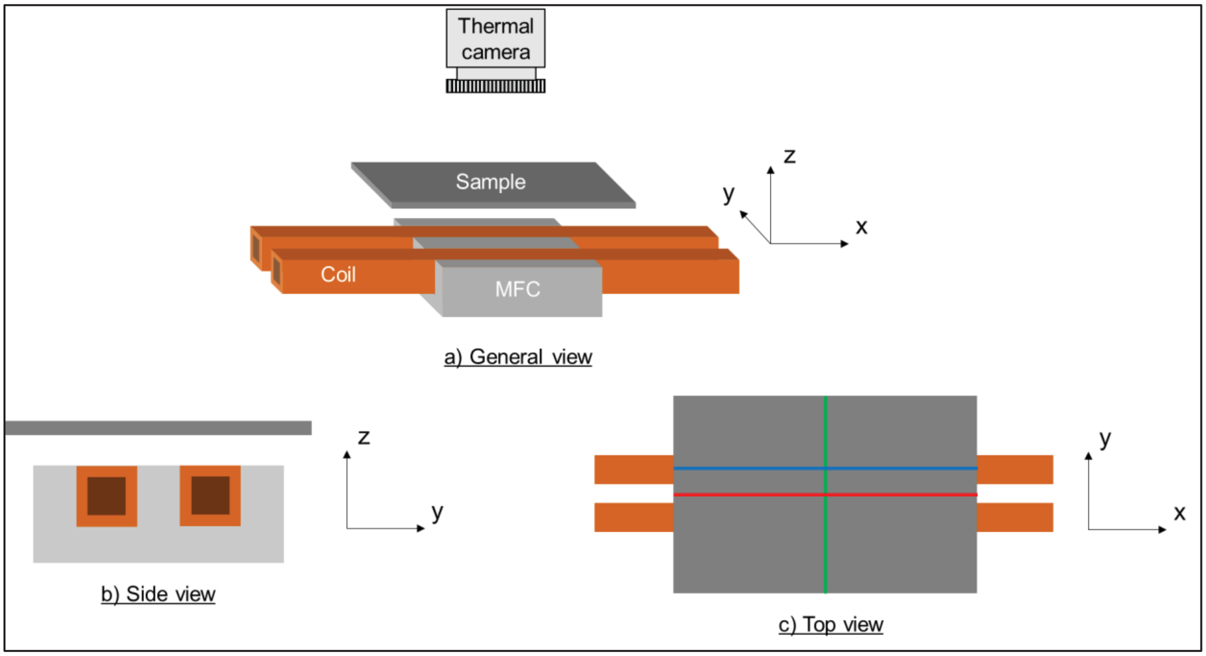

Figure 7.3 Scheme of the static induction heating setup. (a) General view of the setup, with the thermal camera located above the sample to record temperature evolution. (b) Side view showing the induction coil profile. The distance between the sample and the coil is defined as the coupling distance. (c) Top view of the setup as seen by the thermal camera, with the three lines of interest highlighted in green (center profile), red and blue (center and 5 mm width profiles)

7.3.3 Induction heating finite element model

A 3D finite element model of the induction heating process is developed using the COMSOL Multiphysics 6.1 software. The model simulates the electromagnetic field around the coil and the heat generation in the carbon fibre composite laminate located above the coil. The magnetic field amplitude is calculated first in the frequency domain and kept constant during the duration of the simulation. This reduces the calculation time compared to recalculating the magnetic field at each time step. Then, heat transfer is modelled in a subsequent time dependant step. Coupling between the two physics is done by considering the electromagnetic losses due to the induced eddy currents in the magnetic step as the heat source of the heat transfer step. Heat conduction inside the laminate and heat dissipation through radiation and convection on the laminate's boundaries are imposed using the surface-to-ambient $q_0 = \varepsilon\sigma(T_{ext}^4 - T^4)$ and the convective heat flux $q_0 = h(T_{ext} - T)$ boundary conditions, respectively. This allows to calculate the temperature evolution inside the laminate over time. The geometry of the model, reproducing the induction heating setup schematized in Figure 7.3a, is presented in Figure 7.4. A mesh composed of free tetrahedral elements is automatically generated by COMSOL Multiphysics. The PARADISO implicit direct solver is used for this simulation, and the maximum calculation time step is set at 2 s.

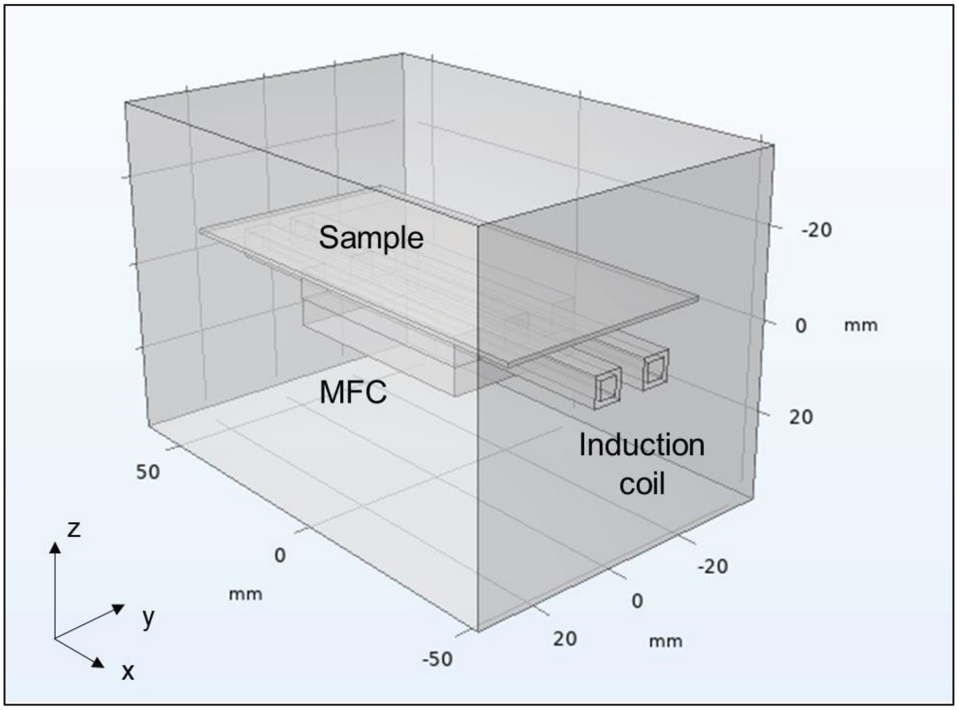

Figure 7.4 3D geometry of the static induction heating setup model in COMSOL Multiphysics

The different materials properties used in the model are reported in Table 7.2. The thermal conductivity of the CF/PEEK laminate is considered as temperature-independent (Ageorges et al., 1998a). Temperature-dependent density and specific heat capacity are modelled as reported in the literature (Holmes & Gillespie, 1993). As presented in the introduction, the homogenized in-plane electrical conductivity of the laminate is an important property to obtain reliable induction heating simulations. As the electrical conductivity of the TENAX-E HTS45 carbon fibre used in this work has not been characterized, a first induction heating measurement is employed to define the equivalent electrical conductivity of the laminate and "calibrate" the model for the tested laminate configuration. The obtained value then remains unchanged for the remaining simulations. As the $[0,90]_{2S}$ laminate is symmetric and balanced, with half the fibres in the 0° and the other half in the 90° directions, the equivalent electrical conductivity of the laminate is the same for both fibre directions in the plane. The convection coefficient is fixed at 5 W/m·K (Holmes & Gillespie, 1993) and the emissivity at 0.95 (Mitschang et al., 2002).

The potential heating of the coil and the MFC, which might affect the magnetic field generation and the laminate heating are neglected. Indeed, these contributions are minimal in the current amplitude range used in the experiments as the coil is water-cooled, which also cools down the MFC. Consequently, the temperature evolution is only calculated in the laminate samples, and not in the coil, the MFC or the surrounding air.

Table 7.2 Materials properties used in the COMSOL Multiphysics induction heating simulations

	CF/PEEK [0,90]$_{2S}$	**Copper coil**	**Magnetic field concentrator**	**Air**
Density [kg/m^3]	1600 (at 25°C) (Holmes & Gillespie, 1993) Density as f(T) is used in the model	-	-	-
Specific heat capacity [J/kg·K]	860 (at 25°C) (Holmes & Gillespie, 1993) Specific heat capacity as f(T) is used in the model	-	-	-
Thermal conductivity [W/m·K]	3.5 (in-plane) (Ageorges et al., 1998a) 0.335 (out-of-plane) (Ageorges et al., 1998a)	-	-	-
Electrical conductivity [S/m]	Defined based on experimental results	6e7 (Duhovic, L'Eplattenier, et al., 2014)	6.66e-3 (O'Shaughnessey et al., 2016)	1 (Duhovic, L'Eplattenier, et al., 2014)
Magnetic relative permeability [-]	1 (Grouve et al., 2020)	1 (Duhovic, L'Eplattenier, et al., 2014)	16 (O'Shaughnessey et al., 2016)	1 (Duhovic, L'Eplattenier, et al., 2014)
Electrical relative permittivity [-]	3.7 (Grouve et al., 2020)	1 (Duhovic, L'Eplattenier, et al., 2014)	1 (O'Shaughnessey et al., 2016)	1 (Duhovic, L'Eplattenier, et al., 2014)

7.3.4 Continuous induction welding setup

To weld CF/PEEK skins to 3D-printed honeycomb cores, pressure must be applied on the sample during heating and cooling to ensure the complete development of the welding degree. In this study, vacuum induction welding (Vac-IW) is used (Martin et al., 2024). To ensure the continuous application of pressure throughout the process, the sample is placed inside a vacuum bag. Then, the induction coil moves linearly relative to the sample at a constant speed and progressively heats up the skin and the core located close to the interface. The sample is kept under pressure after the passage of the coil for 10 min to ensure the temperature is getting below the glass transition temperature of PEI. The applied atmospheric pressure (0.1 MPa), which would be insufficient for properly welding or consolidating high performance thermoplastic composites, is here taken by the walls of the core cells. The pressure taken by the core cell walls corresponds to an approximate value of 0.5 MPa, which is in the range of adequate welding pressures for thermoplastic composites. This value is obtained by assuming that the core cell walls, which are covering around 20% of the core surface area, are supporting the totality of the applied pressure, increasing the effective pressure on the weld line to 0.5 MPa.

7.3.5 Sandwich structures characterization

Two types of characterization are conducted on the welded sandwich structures. First, the skin/core welding interface is observed by optical microscopy (Olympus GX51) to verify that a complete contact between the skin and the core was reached, and to analyze the amount of deformation at the top of the cell walls. Then, skin-core strength is measured by performing flatwise tensile (FWT) tests, following the ASTM C297 standard. A Hysol EA9696 epoxy film is used to bond the steel blocks to the sandwich samples to perform the FWT measurement. Finally, visual fracture analysis is used to assess the type of failure at the joining interface and the quality and homogeneity of the weld. If the visual analysis of a fractured sample reveals that a printing defect was present and caused an early core failure, the sample is discarded and not considered in the FWT results.

7.4 Results

7.4.1 Experiment-derived electrical conductivity

The first induction heating measurement is performed on a 5 cm by 10 cm laminate sample induction-heated with a current amplitude of 50 A. The temperature along the center profile line is extracted from the thermal camera measurements every 10 s for 90 s. Considering a conductivity of 22000 S/m allows to obtain the closest correspondence between the experimental and the simulation curves, as shown in Figure 5. This is in agreement with the expected electrical conductivity of the Tenax HTS45 fibre reported in Table 7.1. The general shape of the curve in the model matches with the experimental results, and the evolution with time also corresponds very well. Therefore, the electrical conductivity of the CF/PEEK laminates is fixed at 22000 S/m for all the other simulations.

This value for the equivalent homogeneous electrical conductivity of the laminate is 10% higher than the one presented in Table 7.1 for the same fibre. As discussed, the difference between the two values might be caused by the fact that the rule of mixture does not consider any heating mechanism at the point of contact between non-parallel fibres. This region also generates heat through contact resistance or dielectric heating, which probably explains why a larger apparent electrical conductivity is observed. The 10% error can also be attributed to uncertainties in the thermal model (magnetic field amplitude, convection coefficient, emissivity) or also to the experimental measurements conducted with the thermal camera.

The model diverges slightly from the experimental results on the edges as time and temperature increase. The model boundary conditions at the edges or the meshing in that area might be responsible for the difference. This should be addressed to obtain a more reliable model, but is satisfactory for purposes of the present study, as the general shape and evolution of the temperature profile is correctly predicted.

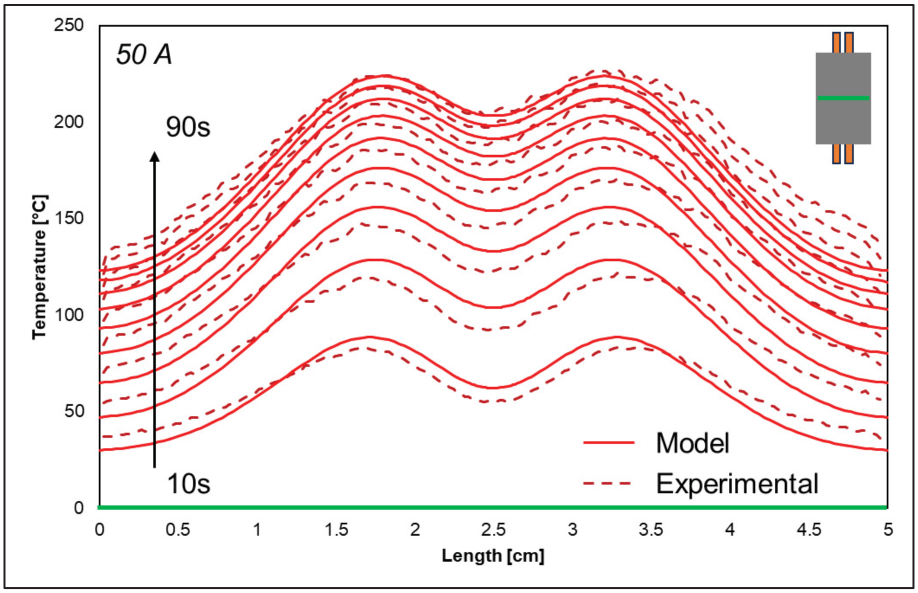

Figure 7.5 Induction heating of a 10 cm by 5 cm laminate under a 50 A current amplitude. The measured temperature along the center profile of the sample is reported every 10 seconds for 90 seconds and compared to the model's results

7.4.2 Current amplitude influence on induction heating

The experimental temperatures reached during induction heating under current values of 50 A, 63 A, 75 A and 100 A are presented in Figure 7.6 as a function of the location along the length of the CF/PEEK laminates. These current amplitudes were selected after preliminary tests which showed that the melting point of the PEEK matrix was not reached at 50 A, but that a large surface of the laminate was molten and deconsolidated at 100 A. Intermediate measurements conducted at 63 A and 75 A are then added to observe the evolution of the temperature profile under varying field amplitude and validate that the model could follow this change. The temperatures along the center profile line are extracted every 10 s during the 90 s of heating. As expected, it appears that a higher current amplitude leads to a higher temperature induced by eddy currents. The maximum recorded temperature after 90 s of heating is 225°C at 50 A, 298°C at 63 A, 362°C at 75 A and 435°C at 100 A. Both the samples heated at 75 A and 100 A reached the melting point of PEEK (343°C). Signs of deconsolidation are visible on these two samples after the heating test, as presented in Figure 7.7. As explained, it is preferable to avoid reaching the melting point of PEEK to prevent laminate deconsolidation. Thus, a current amplitude of 100 A is too high in that configuration and should be avoided. On the other hand, the welding temperature of PEI (around 270-280°C minimum) was not reached under a current of 50 A. Therefore, an electrical current in the range of 63 A to 75 A should be acceptable to perform induction welding with these CF/PEEK laminates.

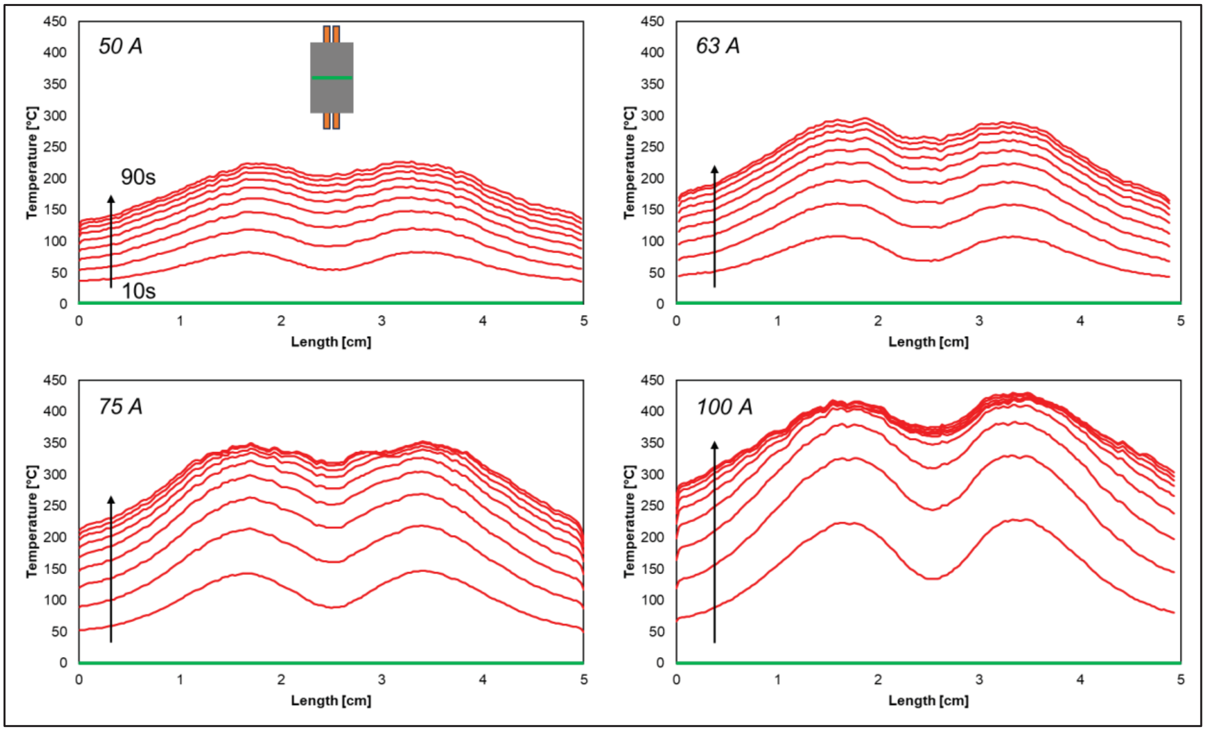

Figure 7.6 Induction heating of 10 cm by 5 cm laminates under varying current amplitudes. The measured temperature along the center profile of the sample is reported every 10 seconds for 90 seconds

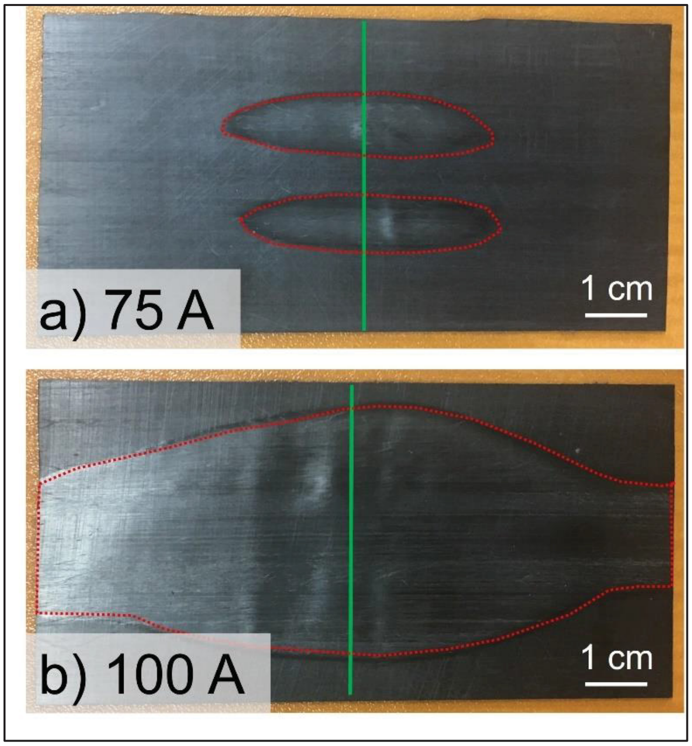

Figure 7.7 Pictures of samples heated by induction under a current of (a) 75 A and (b) 100 A after 90 s. The green line highlights the location of the temperature profile reported in Figure 7.6. The areas where the CF/PEEK laminate deconsolidated are highlighted with the red dotted lines

The experimental temperature curves are then compared with those predicted by the finite element model. Figure 7.8 shows a comparison between the simulation and the experiments after 90 s of heating under the various electrical current amplitudes. The model captures well the heating behaviour of the laminates, with some previously noted deviations close to the edges. The 75 A sample presents an asymmetrical curve, showing there might be some defects like fibre misalignment in the right side of the part. The left side of the curve on the other hand fits well with the model. Considerable disagreement is seen in Figure 8 between the model and the experiment when the laminate reaches high temperatures (e.g. 100 A curve). As shown above, the high 100 A current amplitude led to deconsolidation of the CF/PEEK laminates after 90 s, as shown in Figure 7.7. Once deconsolidation occurs, the heat generation and heat transfer are affected because the carbon fibre plies are no longer in physical contact, which reduces the eddy current generation in the laminate as well as the heat conduction in the thickness of the laminate. In that situation, the model is no longer representative of the heating mechanisms and heat transfer in the laminate.

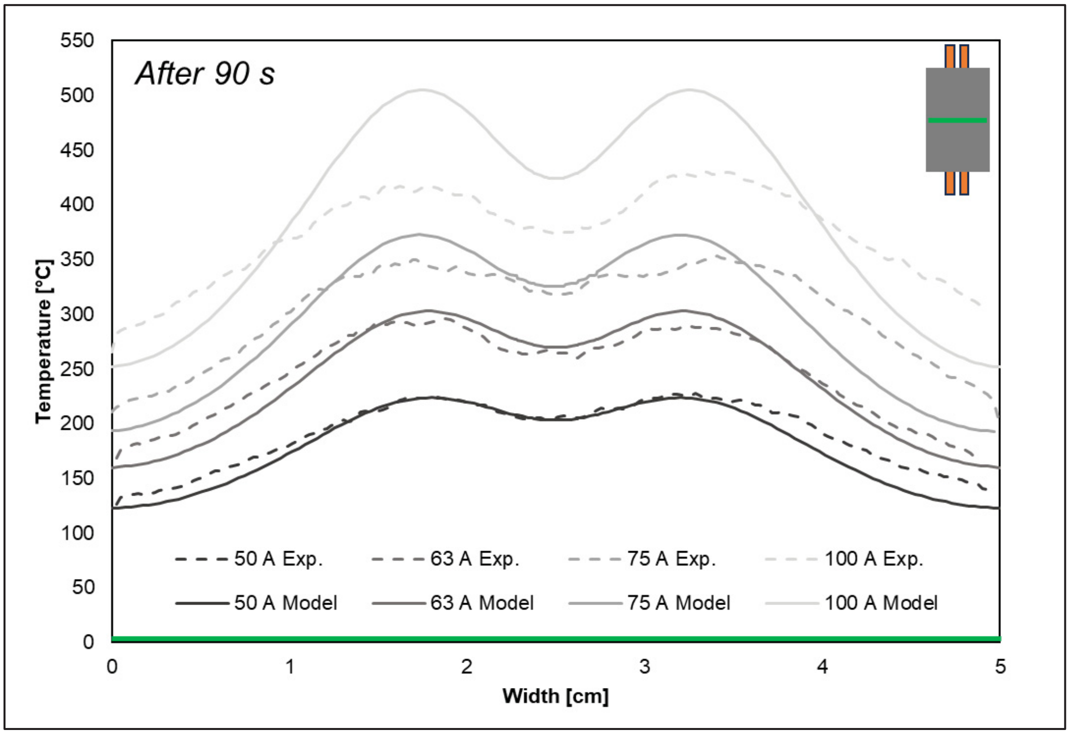

Figure 7.8 Induction heating of 10 cm x 5 cm laminates under varying current amplitudes. The temperature distribution along the center profile line is reported. Only the temperature after 90 s is shown for clarity. Experimental measurements (dashed lines) are compared to simulations (solid lines)

7.4.3 Impact of the sample width on the temperature profile

The second part of the induction heating characterization consists in observing the temperature profile along the width of the CF/PEEK laminate, for varying sample widths. Varying the width of the samples is expected to impact the edge effects. Measurements are conducted at 50 A to avoid deconsolidating the samples, thus allowing reuse.

First, the complete temperature field recorded by the thermal camera after 90 s is presented in Figure 7.9. One can notice the presence of important edge effects in the 5 cm-wide and the 6.25 cm-wide sample (areas of high temperature located close to the edges, as highlighted by the blue circles in Figure 7.9). Some edge effects are also visible for the 7.5 cm-wide sample while larger samples did not produce any visible edge effects. The reduction and elimination of edge effects is caused by the fact that the MFC remains 5 cm-wide, which means that wider samples do not have their edges close to it anymore, but rather in areas where the magnetic field amplitude is lower. The model correctly predicts the temperature distribution in the laminate samples during induction heating. It can adapt to the change of width and anticipate the elimination of the edge effects for larger samples with the heat concentrated in the center of the laminates.

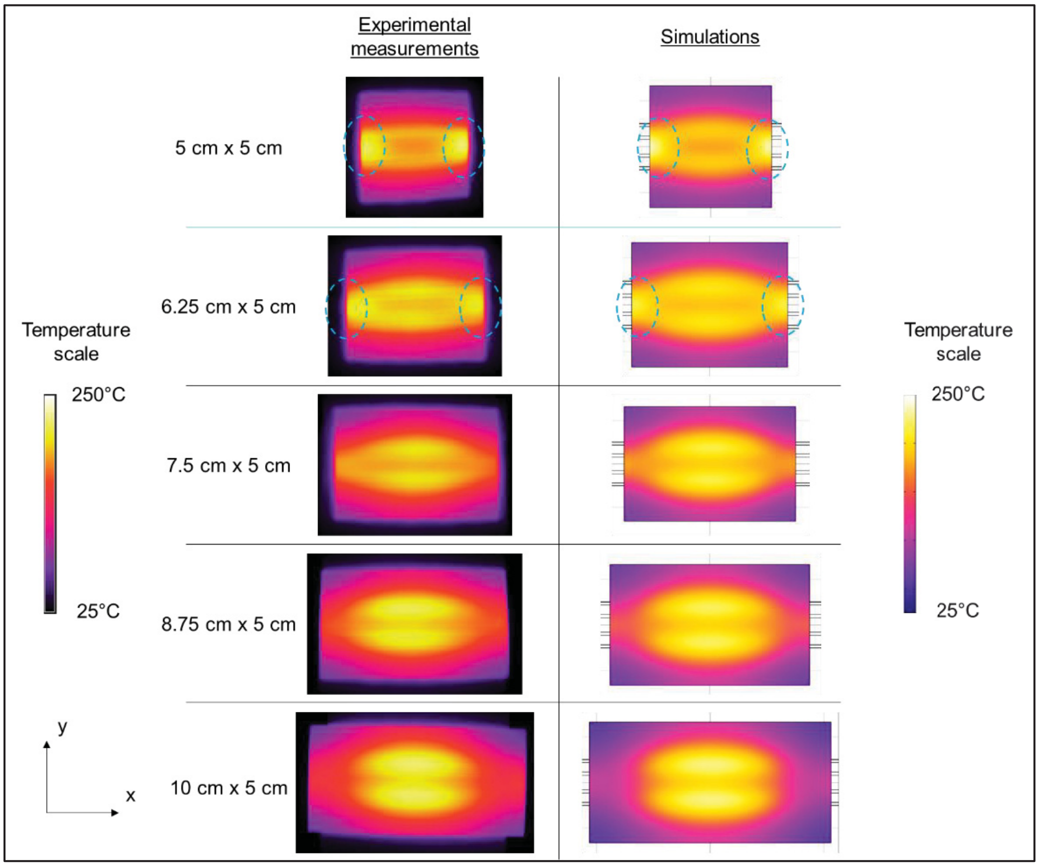

Figure 7.9 Temperature distribution on the CF/PEEK samples surface under a 50 A current for varying samples widths. Experimental results as recorded by the thermal camera are compared to simulations. Edge effects are highlighted by the blue circles. The induction coil is located behind the samples and is orientated vertically

Then, the center line profile temperature distribution (Figure 7.3c green line) is analyzed. As observed in the dashed line of Figure 7.10, it appears that the maximum temperature reached on the samples decreases as the width decreases, from 224°C for a 10 cm wide sample down to 188°C for a 5 cm wide sample. This decrease in temperature indicates that a slower welding speed or a higher current amplitude will be required to weld those narrow skins. The curves are then compared to the simulated temperature distributions (solid lines in Figure 7.10). The blue curve was used in Figure 7.5 to calibrate the model. It appears that the model can correctly predict the variation of temperature observed experimentally, which would help predict the impact of changing the laminate dimensions.

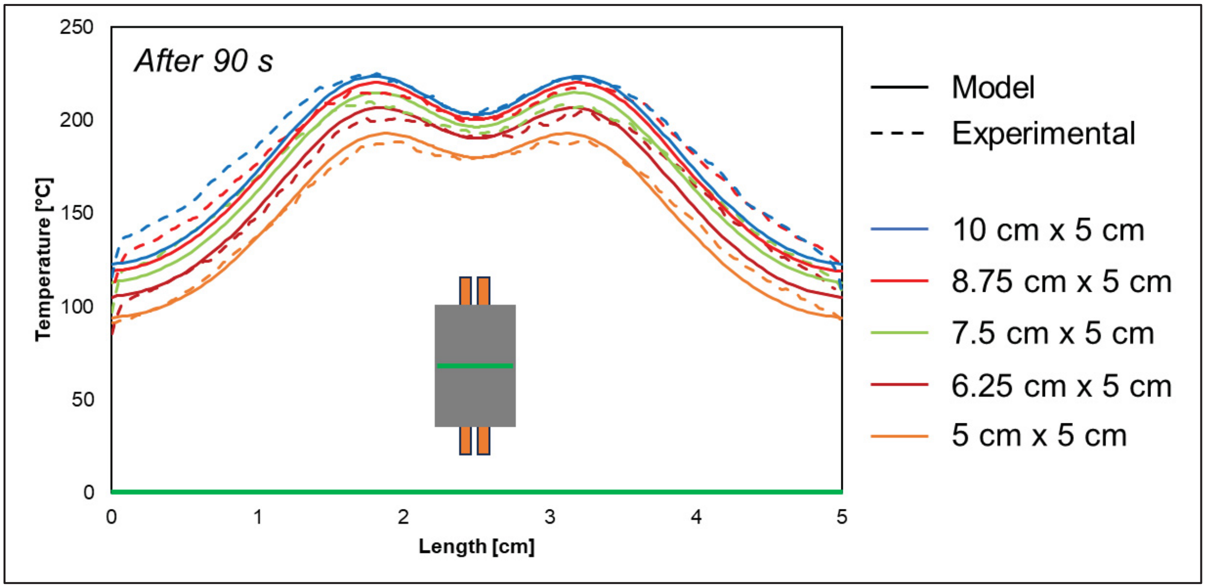

Figure 7.10 Induction heating of laminates under 50 A current amplitude for varying sample widths. The temperature distribution along the center profile is reported. Only the temperature after 90 seconds is shown for clarity. Experimental measurements (dashed lines) are compared to simulations (solid lines)

Finally, temperature is extracted for both width profile lines of interest (red and blue in Figure 7.3c) and the results are presented in Figure 7.11. The x-axis is fixed at zero for the left edge of the 5 cm-wide sample, and the wider samples are centered compared to it. This gives more clarity to compare the samples among themselves. The length that would be welded to the honeycomb core is then located between 0 and 5 mm on the x-axis. It appears that there is a significant change of curvature. As it was observed on the temperature distributions (Figure 7.9), edge effects are reduced when the width of the sample increases. The objective is to have a more homogeneous temperature distribution along the width of the sample during the induction welding process.

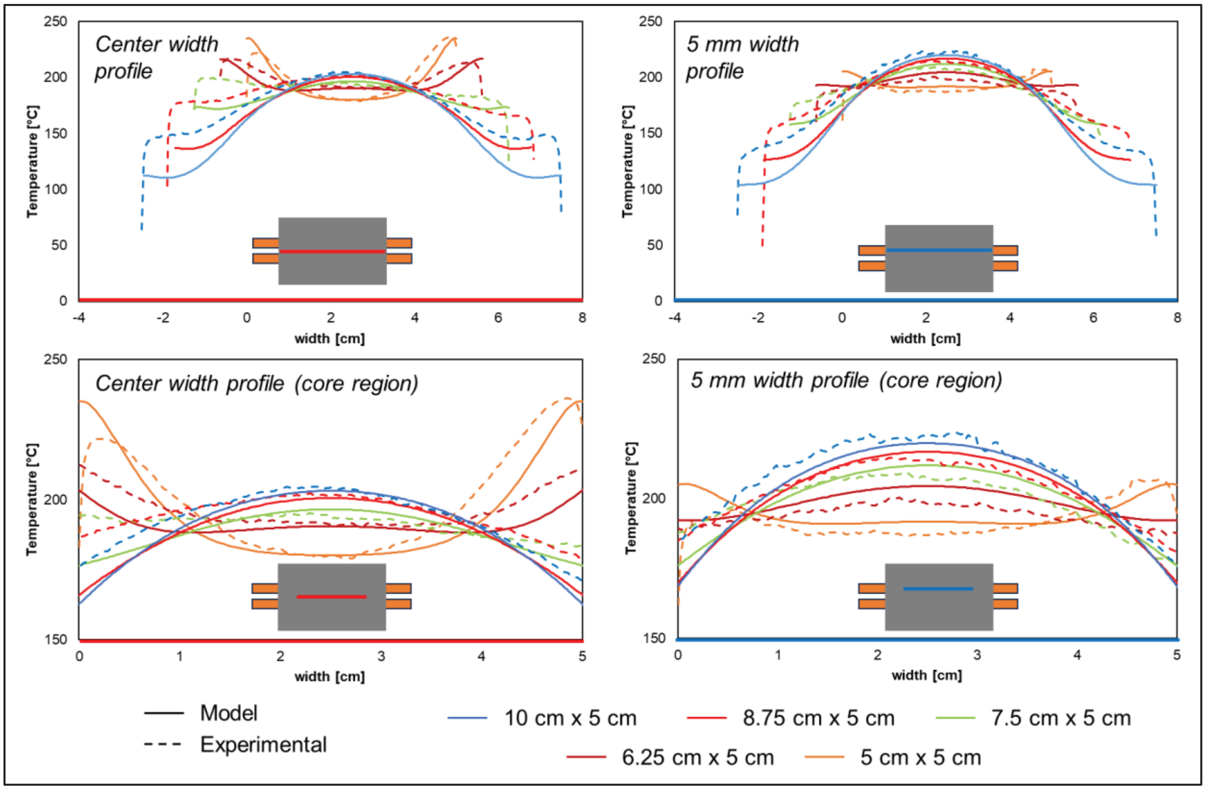

Figure 7.11 Induction heating of laminates under 50 A current amplitude for varying sample widths. The temperature distribution along both width profiles is reported. Only the temperature after 90 seconds is shown for clarity. Experimental measurements (dashed lines) are compared to simulations (solid lines)

These results confirm that the 5 cm-wide skin seems unfavorable for sandwich structures of similar width, as it would be impossible to prevent the edge effects and the related non-homogeneous degree of welding along the width. The same observation can be made for large skins (8.75 and 10 cm-wide), which lead to more heat generation in the center of the laminate, inducing a lower degree of welding close to the edges. Therefore, out of the presented curves, it seems that 6.25 cm and 7.5 cm-wide samples exhibit the most favorable heating behaviour with the most homogeneous temperature distribution along the width.

The temperature distribution along the lines of interests of the samples is also calculated with the model to verify its accuracy. The curves are compared with the presented experimental results. For the center profile as shown in Figure 7.10, the model can correctly predict the reduction of the temperature at shorter widths. The shape of the temperature profile is also correctly predicted, which further confirms the quality of the model. For the width profile, the model diverges from the experimental results when getting farther away from the center.

7.4.4 Optical microscopy on welded sandwich structures

The welding lines of the induction welded sandwich samples are first observed by optical microscopy, with a focus on the evolution of the cell wall deformation at the point of contact with the skin. This is the point where heat is generated and where welding occurs. Figure 7.12 presents the optical micrographs of the sandwich cross-section for samples welded with skins width of 5, 6.25, 7.5 and 10 cm skins. 8.75 cm-wide samples are not further evaluated as their heating profile is very similar to the 10 cm-wide ones.

With a 5 cm-wide skin, presented in Figure 7.12a, more heat was generated close to the edge as this is where the cell wall is the most deformed. This agrees with the temperature distribution observed by thermal imaging, resulting from edge effects. As expected, this sample exhibits a non-homogeneous welding profile that will lead to non-homogeneous weld. On the other hand, the opposite behaviour is observed in Figure 7.12c, welded with a 7.5 cm-wide skin and Figure 7.12d, with a 10 cm-wide skin. The use of a wider skin leads to more heat generation in the center of the sample and therefore more visible deformation in that area. It even appears on the optical microscopy images that the laminate started to deform in the center, highlighting the large heating induced in that region. Overall, the non-homogeneity of the heat generation appears clearly in the samples with extreme skin widths. It is expected that these samples will consequently exhibit a non-homogeneous degree of welding along their width. The sample welded with a 6.25 cm-wide skin (Figure 7.12b) exhibits the most homogeneous heating, as the deformation of the cell walls is similar on the four walls along the width. This also agrees with the thermal imaging results, which show that the temperature profile with that skin width was the most uniform.

Decreasing the welding speed will allow previously less heated areas to be heated up enough, letting them reach higher degree of welding. But at the same time, the other areas of the sample will certainly overheat, leading to core crushing, as it started to be observed in Figure 7.12c and d, and skin deconsolidation. Non-homogeneity of the temperature distribution cannot be compensated by adjusting the speed, which highlights the interest of correctly choosing the skin's width to provide a homogeneous temperature profile. Optical microscopy results also confirm that choosing 6.25 cm-wide skins is appropriate.

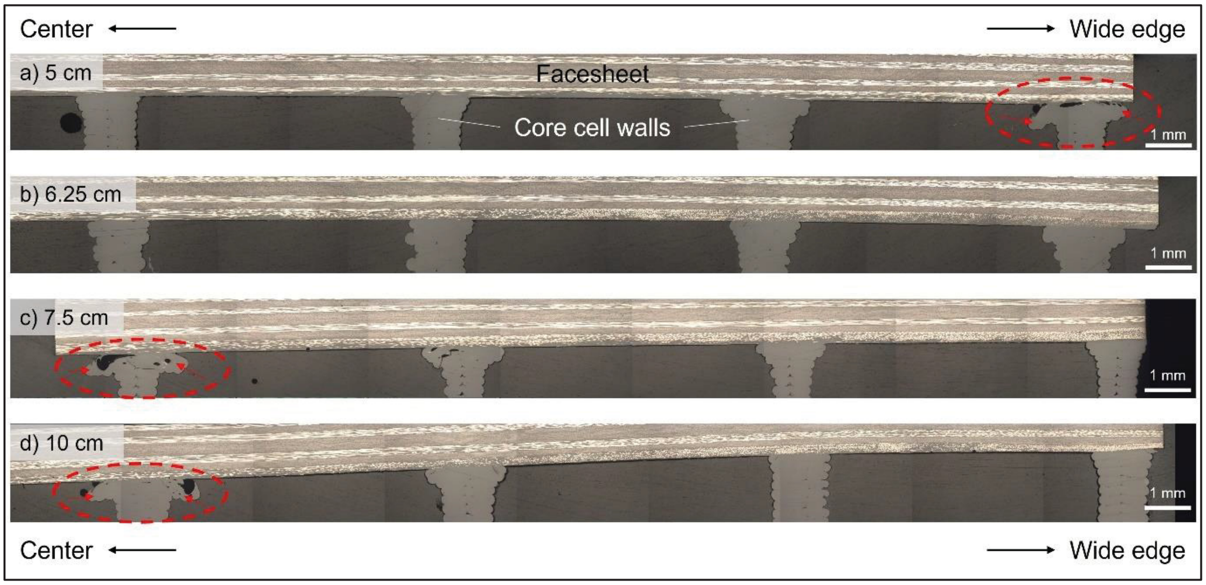

Figure 7.12 Optical microscopy images for sandwich samples welded by induction. The welding profile is shown for samples with varying skin width: (a) 5 cm, (b) 6.25 cm, (c) 7.5 cm and (d) 10 cm. The left side of the figure correspond to the center of the welded sample's cross-section, while the right side corresponds to its wide edge. The cell walls that faced overheated and crushing are highlighted by the dashed red circles. The deformed wall layers are highlighted by the red arrows

7.4.5 Skin-core strength

The skin-core strength of welded sandwich specimens is characterized by performing FWT mechanical tests. The resulting skin-core strengths of the welded samples are reported in Figure 7.13. Each data point on the graph represents one FWT test. Three samples were tested for the higher strength samples (at 0.7 mm/s for the 6.25 cm-wide skins and at 0.8 mm/s for the 7.5 cm-wide skins) to validate the repeatability of the method. The optimal welding speed is defined as the speed at which the highest skin-core strength is reached without observing core crushing on the sample. Fractured sandwich samples are then visually analyzed to observe the failure mode and the homogeneity of the degree of welding. One representative sample for each skin's width welded at optimal speed are presented in Figure 7.14.

It can first be observed in Figure 7.13 that, for a given skin's width, reducing the welding speed increases the maximum skin-core strength. This trend was expected as the laminate spends more time under the induction coil at lower speed, therefore reaching higher temperatures and maintaining them for a longer duration (Lionetto et al., 2017). Secondly, a larger optimal welding speed is obtained with the use of wider skins. This corresponds to the observation made in Figure 7.10 where it was seen that a wider skin leads to a higher temperature in the laminate.

However, the use of 10 cm wide skins also leads to non-homogeneous heating, as observed in optical microscopy images (Figure 7.12). It is also confirmed by observing the fractured samples (Figure 7.14d), where it appears that the failure mode is adhesive close to the edges with a transition to a core failure in the center, highlighting the higher degree of welding in that area. The fraction of the surface where adhesive failure occurred (highlighted by the red lines in Figure 7.14a) is evaluated at 43.5%. When the skin's width is reduced to 7.5 and 6.25 cm, the optimal welding speed becomes smaller, but the maximum strength increases, as a homogeneous heating and homogeneous degree of welding are reached at the skin/core interface. When observing fractured sandwich samples (Figure 7.14b and c), it also appears that the failure mode is mostly core failure (95.6% and 89.6% of the surface in Figure 7.14b and c, respectively), which tends to indicate that the dominant characteristic for the flatwise tensile strength is the strength of the 3D-printed core itself. The weld surpasses the resistance of the core, indicating its high quality. The experimental skin/core strength then decreases again for 5 cm-wide skins, which once again is probably caused by a non-homogeneous heating along the skin's width, although it is less visible in Figure 7.14a. The adhesive failure is reported on 18.9% of the surface on that sample. Based on the results, the 7.5 cm-wide skins welded at 0.8 mm/s and the 6.25 cm-wide skins welded at 0.7 mm/s present the best mechanical properties. The optimal choice would depend on the desired balance between the welding speed and the amount of excess skin to be trimmed after welding.

Overall, the maximum measured skin-core strengths range between 5 and 7 MPa for the six tested sandwich samples that were welded using 6.25 and 7.5 cm-wide skins. This is higher than what is reported in different articles characterizing sandwich structures with flat-wise tensile tests. Widagdo et al. (CF/epoxy skins bonded to glass fibres/phenolic resin honeycomb core with FM-300 adhesive) and Hegde et al. (CF/cyanate ester skins bonded to Kevlar/phenolic resin honeycomb core with epoxy film adhesive) reported maximum strength between 5 and 5.2 MPa (Hegde & Hojjati, 2019; Widagdo et al., 2020). Butukuri et al. (CF/epoxy skins to honeycomb core with FM-300 adhesive) reported similar strengths for Nomex cores, and higher strengths only for aluminium cores (Butukuri et al., 2012). For polymer-based sandwich structures, the presented vacuum induction welding method shows higher results than other structures assembled by adhesive bonding, with the advantages of minimal surface preparation and a shorter processing time.

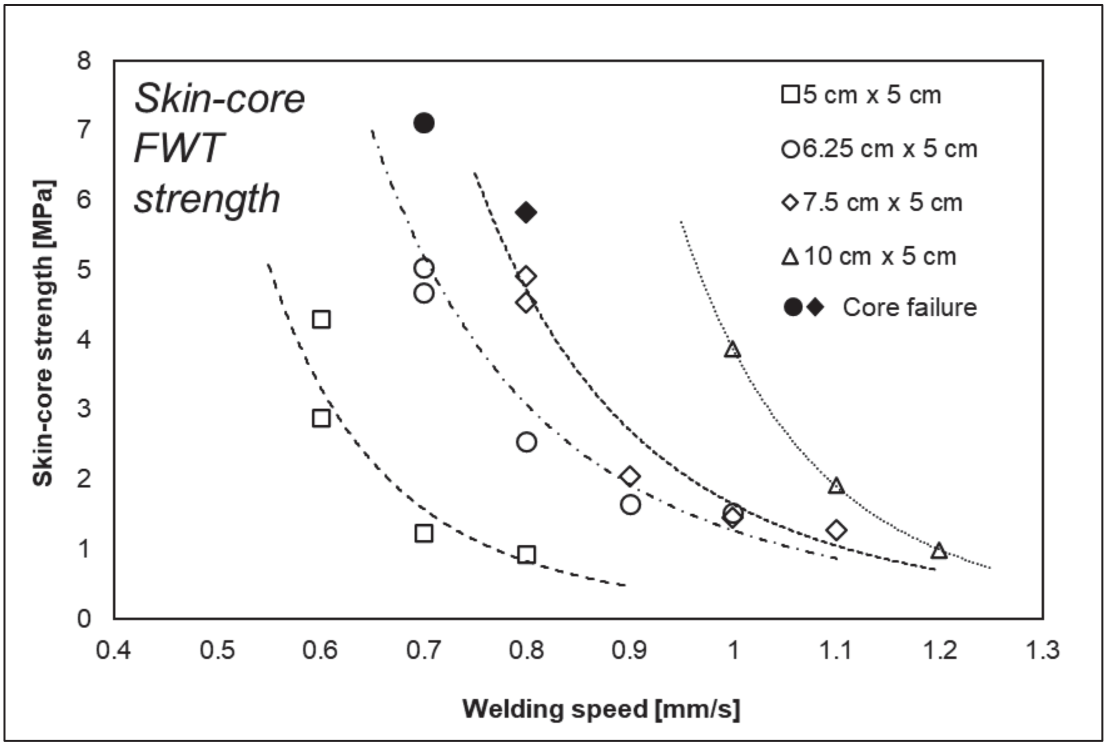

Figure 7.13 Skin-core FWT strength of induction welded sandwich structures as a function of the welding speed. Each point represents one measurement. Dashed/dotted trend lines are guides to identify more clearly each dataset. Core failure is indicated by filled black data points

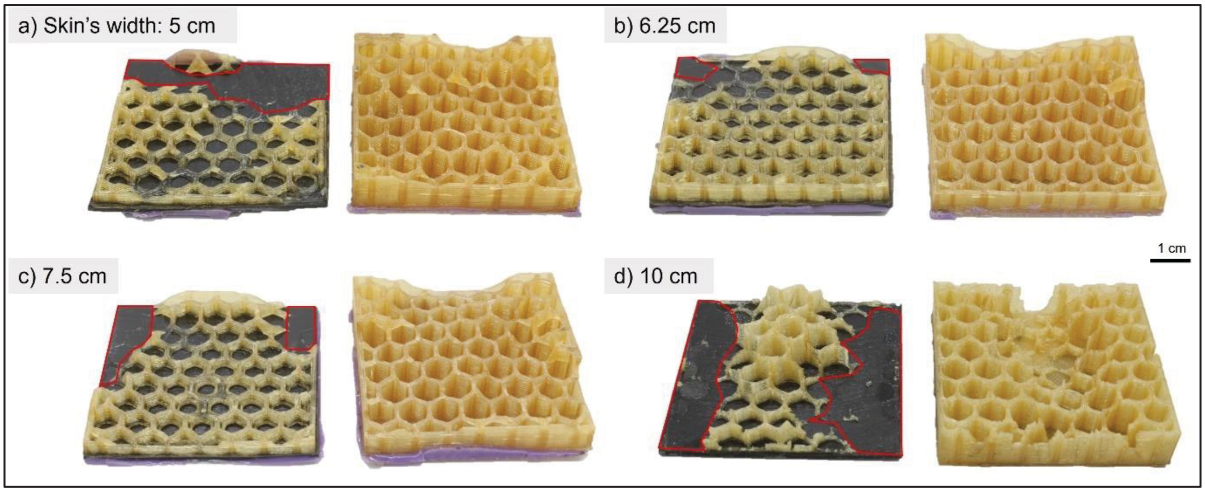

Figure 7.14 Fractured induction welded sandwich samples. The samples were welded using a skin's width of (a) 5 cm, (b) 6.25 cm, (c) 7.5 cm, (d) 10 cm. The red lines correspond to the surface areas where adhesive failure occurred

7.5 Conclusion

This paper presents a susceptor-less method to join CF/PEEK skins to honeycomb cores produced by 3D-printing. The heat generated inside the skin due to induced eddy currents allows for the weld to happen. To handle the edge effects that are typically observed in conductive materials during induction welding, it is proposed to add sacrificial length to the CF/PEEK skin in which edge effects can occur, leaving the effective surface area of the skin in contact with the core to experience homogeneous heating.

The heating behaviour of the laminate is observed by thermal imaging, validating the benefit of using extra width on the skin to limit edge effects. A 3D model on COMSOL Multiphysics is then presented to predict the temperature profile of the samples during the process, at variable sample widths and induction current values. The good agreement between the simulations and the experimental results shows that the COMSOL model can be used as a tool to predict the impact of changing the current or increasing the sample dimensions. This can help engineers minimize the number of trials necessary to characterize induction welding and better predict the welding by induction.

Finally, induction welding of sandwich samples is performed to validate the assembly of sandwich panels by induction welding. The application of the Thermabond process allows to weld by induction at a lower temperature, avoiding deconsolidation in the facesheets and reducing the risk of core crushing. Flatwise tensile tests show that higher skin-core strength can be reached with this process, compared to other reported methods. Fracture analysis of tested samples confirms the non-homogeneous heating when using too wide or too narrow skins, and its consequences on the weld quality. This shows the benefits of selecting an optimal set of dimensions for the facesheet laminate.

7.6 Acknowledgements

This work was funded by CREPEC (Research Center for High Performance Polymer and Composite Systems), NSERC (Natural Sciences and Engineering Research Council of

Canada) (grant number ALLRP 556497-20), PRIMA Québec (Pôle de Recherche et d’Innovation en Matériaux Avancés) (grant number R20-13-004), the Canadian Space Agency (CSA), Ariane Group, NanoXplore inc, Mekanik and Dyze Design.

CONCLUSION

Synthesis of the results

First, a methodology to select magnetic particles to prepare magnetic hysteresis losses susceptors has been presented. This provides engineers and researchers a tool to determine, based on a few characterization tests, which magnetic particles are most adapted to develop a hysteresis losses susceptor based on the selected thermoplastic matrix and the available induction welding setup. The importance of the Curie temperature of the magnetic particles was also highlighted, as it can provide inherent temperature-control when properly selected but can also limit the use of a material if it is too low. The presented case study on two different thermoplastic matrices (PP and PEEK) and three magnetic materials (Fe, Ni and magnetite) demonstrated the usefulness of the methodology by concluding that Ni was favorable for PP but unable to reach welding temperature of PEEK, which may therefore be used with magnetite particles. These results are valid for the presented induction welding setup.

Then, the application of the methodology determined that Ni particles were the most suitable candidate for PEI-based induction welding susceptors. Films of these susceptors showed good Ni particles distribution, minimal porosity level and density similar to the expected theoretical value, validating the manufacturing method. Induction heating of the susceptors with different Ni concentrations was measured using a thermal camera, showing that PEI/Ni samples were able to reach 300°C and more, which is inside and above the desired welding temperature window. The temperature-control feature based on the Curie temperature of Ni particles is also confirmed, removing the risk of starting to cause degradation in the material.

The induction welding of sandwich skins to 3D-printed honeycomb cores was then demonstrated. First, the induction welding setup was adapted to place the sandwich panel sample inside a vacuum bag, allowing to apply a constant and homogeneous pressure on the parts to be welded during the entirety of the process. The vacuum pressure, approximately 0.1 MPa, is usually insufficient for welding. But when using hollow sandwich cores like honeycombs, the pressure is supported by the walls of the cells, which cover only a fraction of the surface and therefore experience a higher local pressure. The presence of a PEI surface layer on the GF/PEEK skins (Thermabond process) allowed to weld them to the 3D-printed PEI honeycomb core using the developed PEI/Ni-10%vol susceptor. The influence of the welding speed on the skin/core strength was assessed, showing that going too slow could lead to overheating, while welding too fast did not provide enough heat to melt the materials at the interface. A welding speed of 0.5 mm/s was optimal for the set-up and power employed, allowing to reach skin/core strength around 5 MPa, which is comparable to what was previously reported for sandwich panels assembled by adhesive bonding.

Then, the development and manufacturing of the susceptor material in the form of a 3D-printing filament was presented. The compounding and the shaping of the filament was conducted using a single process step in an extruder. The obtained filament was characterized, showing a high porosity level and filament diameter variability, but good Ni particles distribution. Printability of the material was demonstrated, proving that it is possible to deposit the susceptor by 3D-printing in various geometries. Printed films replicating the previously tested susceptor pressed films are characterized, showing that the high porosity level still present inside the sample reduced its heating capability by around 30 °C, but was still able to reach the required welding temperatures. This difference is caused by the inconsistent filament diameter and the porosities in printed samples. Finally, susceptor was printed on top of honeycomb cores, to demonstrate the printability of the materials in complex geometries. Two susceptor width geometries are evaluated, which demonstrated that printed susceptor can be deposited in complex patterns. The weldability of the material was demonstrated by welding skins to cores using the vacuum induction welding technique. Optical microscopy observations confirmed that welding occurred, although lower welding speeds were required compared to welding with pressed films. FWT tests showed that welding correctly occurred at the interface, reaching up to 4.5 MPa for the sample welded at 0.15 mm/s with variable printed susceptor width. Fracture analysis showed core failure in that sample, highlighting the strength of the weld. Other samples exhibited cohesive failure, also indicating that a high degree of welding was reached.

Finally, the developed vacuum induction welding technique was applied to another heating mechanism to show its versatility. The use of CF/PEEK skins instead of GF/PEEK ones allows the heat to be generated directly in the skins, removing the need for a susceptor material. There, the skin is directly placed on the core and placed under vacuum to be welded. The heat distribution in the CF/PEEK skins was analyzed by thermal imaging, showing the presence of edge effects which prevented the obtention of a homogeneous temperature distribution at the joining line. The use of wider skins was proposed to avoid these edges effects. A model was developed using the COMSOL Multiphysics software to predict the temperature distribution and the presence of edge effects, giving a tool to define the optimal width of the CF/PEEK facesheets. Then, samples were welded by induction using variable widths of skins to demonstrate the impact on the skin/core strength. Samples with wide skins can be welded faster but cannot reach high strength due the non-homogeneous heat distribution at the weld line. On the other hand, the presence of edge effects on narrow skins also limited the maximum obtained strength. The optimal width was demonstrated to be between 6.25 and 7.5 mm for a 5 mm wide sandwich sample, welded at speeds of 0.7 and 0.8 mm/s, respectively. The strongest samples reached strength up to 7 MPa and exhibited failure inside the 3D-printed core, highlighting that the weld was stronger than the core structure. This is an indication that the welding process performs well and can be used to assemble high-performance thermoplastic composite sandwich panels by induction welding.

Based on the list of sub-objectives presented in 2.2, sub-objective 1 has been completed with the results presented in Chapter 3. This content has been published as a journal paper in *Advanced Engineering Materials* in 2022 (Martin et al., 2022), which has already been cited by other researchers working on induction heating (Barroeta Robles et al., 2022; Hoang et al., 2023; Mariani & Malucelli, 2023; Rak & Tucek, 2022). Sub-objective 2 is covered by Chapter 4 and 5, the latter of which was published as a journal paper in *Composites Part A* in 2024 (Martin et al., 2024). Sub-objective 3 is covered by the results presented in Chapter 6. Finally, Chapter 7 fulfils the sub-objective 4. The content of this chapter has been submitted as a journal paper to *Composites Part B* in 2024 and is currently undergoing the peer-review process.

Original contributions

The development of the material selection methodology presented in Chapter 3 is an important contribution to the field, as it provides guidelines for the selection of magnetic particles in hysteresis losses susceptors. As presented, the material of the ferromagnetic particles, their magnetic properties and their Curie temperature influence greatly the heating capabilities of the susceptor. It must be correctly adapted to the thermoplastic matrix and the available induction welding setup to produce efficient susceptors.

Then, production of PEI/Ni susceptors was demonstrated, which is a first for this material. The manufacturing process was able to produce reliable and repeatable susceptor films, showing minimal porosity level and excellent Ni particles distribution. The induction heating tests showed that the desired welding temperature can be reached, demonstrating the ability of the PEI/Ni material to be used as an induction welding susceptor.

To assemble sandwich panels by induction welding, the vacuum induction welding (Vac-IW) technique was developed and demonstrated. The application of pressure on the sample by placing the parts in a vacuum bag allows to get a constant and homogeneous pressure throughout the complete process. One of the major advantages is the absence of surface preparation on the surface to be welded. The validation of the technique was conducted through FWT tests, which showed that the welded sandwich panels exhibited equivalent to higher skin/core strength than sandwich panels assembled by adhesive bonding. This is a major forward in the production of all-thermoplastic sandwich panels by induction welding.

Then, the development of the susceptor filament is totally new, as a printable susceptor is demonstrated for the first time and validated by using it to weld sandwich panels. This gives the opportunity to deposit the susceptor only in the areas where it is needed, and therefore localize the heat generation at the points of contact. The quantity and composition of deposited material can be optimized to match the required heat on different points of the structures (layer height, susceptor concentration). This can help reduce the quantity of needed material and minimize the weight penalty on the structure.

Finally, the transfer of the Vac-IW technique to susceptor-less welding has been shown, by welding CF/PEEK skins to honeycomb cores without any susceptors. Once again, no surface preparation was required on the parts to welded. The heat distribution in the skins was correctly predicted by the proposed COMSOL model, which can be used in other cases (materials, geometries, etc.) to predict the required dimensions of the skins. The skin/core strength surpassed the printed core tensile strength, highlighting once again the promising capabilities of the method.

In the context of the PEEKbot project and lunar applications, all-thermoplastic and adhesive-free sandwich panels are very interesting and promising structures. The demonstration of the assembly by induction welding offers the opportunity to produce sandwich panels for the lunar rover which offer thermal insulation, would not be outgassing, and would experience minimal internal stresses during thermal cycling.

RECOMMANDATIONS

The material selection methodology was demonstrated by conducting a case study with three magnetic materials. It would be interesting to expand the study to more materials, including promising ones like AlNiCo, SmCo or NdFeB alloys. These hard magnetic materials exhibit very large hysteresis and could be interesting candidates for hysteresis losses susceptors.

About the susceptor films, a methodology to test and characterize the mechanical properties of susceptor must be established to quantify the impact of the metallic particles. Also, it would be interesting to develop a heating simulation model, incorporating the evolution of the physical and magnetic properties with temperature, to predict the temperature evolution of the hysteresis losses susceptor films. This could then be used to optimize the required volume fraction of magnetic particles in the susceptor. The balance must be found between the heating capabilities and the impact on the mechanical properties of the susceptor.

The proposed induction welding setup presents some limitations and would require some improvements. The first one is regarding the alignment of the induction coil with the sample. As of now, the coil alignment is not guaranteed, which can affect the heating homogeneity and the temperature distribution in the part. This will become even more problematic when scaling up the setup to weld larger sandwich panels. Linked to that, the distance between the sample and the coil must also be better measured and ensured to be conserved during the process. It has been demonstrated that even 1 mm of additional distance between the coil the welding line can significantly decrease the heat generation. To ensure good repeatability, the coupling distance must be guaranteed by some mechanisms, such as support located on both extremity of the coil. Supports like these could also help with the coil’s alignment.

The geometry of the magnetic field concentrator (MFC) and its influence on the susceptor’s heating rate can also be investigated. A wider MFC would ensure that high magnetic field amplitude is present on larger surface area. However, one must keep in mind that having a proper thermal contact with the coil (using a thermally conductive paste) is essential to ensure that the MFC is cooled down during the process. If the volume of the MFC is increased, it must be verified that the cooling system (water circulating inside the copper induction coil) is efficient enough to evacuate the heat generated inside the MFC.

Coming to the susceptor 3D-printing filament, characterization revealed a large porosity level and a variable filament diameter, two important parameters that must be improved to obtain better printed susceptor quality. The extruding parameters (temperature, screw speeds, etc.) must be adjusted to reduce the porosities inside the filament. A reliable winding system must be put in place to ensure that the filament is pulled constantly during the extrusion. By balancing the extrusion speed, extruder nozzle diameter and pulling speed, the filament diameter should exhibit less variability and match the expected diameter of 1.75 mm.

Then, optimization of the deposited layer can be conducted. Results from Chapter 6 present only two printing geometries with similar overall thickness (1 mm). Other configurations with different number of layers, variable width angle and Ni concentration should be investigated to find optimal parameters. This could also help increasing the welding speed, which is currently much lower than when welding with pressed films of susceptor.
As discussed in Chapter 6, thermal conductivity in the sandwich panel samples occurs during the induction welding process. The use of a variable welding speed (starting slow, then increasing to match the forward thermal conduction) could improve the homogeneity of the welding profile and reduce the total welding time. Modelling efforts on the continuous induction welding of sandwich panels using hysteresis losses susceptors could help define the optimal coil displacement speed.

Finally, on the CF/PEEK sandwich panels, the presented model could be extended to the continuous induction welding process, considering not only the heat generation in the laminate during a static test, but the heat transfer in the rest of the structure as the coil moves along the sandwich panel. The thermal history at the interface should be measured and compared with the model to validate its accuracy. The temperature evolution at the welding interface could also be used to predict the degree of welding based on the coupled model of intimate contact and healing. This could then be compared to FWT results, which would also help defining the optimal welding speed to obtain the most favorable thermal history, and consequently the highest skin/core strength.

The last step would be to scale-up the Vac-IW method and apply it to the assembly of larger sandwich panels. To do so, the set-up must be more robust and repeatable, with better control of coil alignment, coupling distance and vacuum pressure application.

ANNEX I

SUPPORTING INFORMATION – MATERIAL SELECTION METHODOLOGY FOR AN INDUCTION WELDING MAGNETIC SUSCEPTOR BASED ON HYSTERSIS LOSSES

Romain G. Martin[a], Christer Johansson[b], Jason R. Tavares[c] and Martine Dubé[a],

[a] CREPEC, Department of Mechanical Engineering, École de technologie supérieure, 1100 Notre-Dame West, Montreal, Quebec, Canada H3C 1K3
[b] RISE Research Institutes of Sweden, Arvid Hedvalls Backe 4, Göteborg, Sweden, SE-411-33
[c] CREPEC, Department of Chemical Engineering, Polytechnique Montréal, 2500 chemin de Polytechnique, Montréal, Québec, Canada, H3T 1J4

Paper published in *Avanced Engineering Materials*, March 2022

Modelling of the magnetic field around an induction coil is performed using FEMM4.2 software. The section of the hairpin coil (straight and single-turn coil) is simplified as a 6 x 6 mm square with a 4 x 4 mm square hole inside of it, where the cooling water is circulating. The two square sections are separated by 6.4 mm. The magnetic field concentrator is simplified as a 12.6 mm high and 32 mm wide rectangle, surrounding the coil sections. The materials are defined as following: air for the surrounding space and for the inside of the coil (water can be approximated as air in terms of magnetic response), copper for the coil section and Ferrotron 559H for the field concentrator. As this latter is not available in the software materials library, it is created following the material technical datasheet. The current inside the copper coil sections is fixed at 700 A. The current must be positive in one of the two sections and negative in the other, as the induction coil is a closed loop. The default Dirichlet boundary condition is used in the simulations.

ANNEX II

HYSTERESIS LOSSES MAGNETIC SUSCEPTOR HEATING RATE CHARACTERIZATION

Romain G. Martin[a], Martin Figueiredo[b], Christer Johansson[c], Jason R. Tavares[d] and Martine Dubé[a],

[a] CREPEC, Department of Mechanical Engineering, École de technologie supérieure, 1100 Notre-Dame West, Montreal, Quebec, Canada H3C 1K3
[b] Polytech Paris-Saclay, Orsay, France, rue Louis de Broglie, Building 620, Orsay, France, 91190
[c] RISE Research Institutes of Sweden, Arvid Hedvalls Backe 4, Göteborg, Sweden, SE-411-33
[d] CREPEC, Department of Chemical Engineering, Polytechnique Montréal, 2500 chemin de Polytechnique, Montréal, Québec, Canada, H3T 1J4

Paper published in *SAMPE Journal*, September 2023

This article was published in the SAMPE Journal in September 2023 (Martin, Figueiredo, et al., 2023a). Chapter 4 of the present document is based on some of the results presented hereafter.

II.1 Abstract

Welding techniques are emerging as a new method to join thermoplastic composite parts. They present a fast and efficient alternative to adhesives and mechanical fasteners. Induction welding is a welding technique that relies on the application of an oscillating magnetic field on the joining interface, where a material called a magnetic susceptor generates heat by interacting with the applied magnetic field. In this work, susceptors relying on magnetic hysteresis losses made of polyetherimide (PEI) and nickel (Ni) particles are investigated with varying Ni concentration. The materials are mixed using an internal mixer and pressed to form films approximately 500µm thick. To characterize the heating rates of the susceptor materials, samples are placed on an induction coil – a water-cooled copper tube in which AC current (frequency 388kHz), generates an alternating magnetic field – and the temperature

evolution is measured using a thermal camera. An increasing concentration of Ni particles results in increased heating rate and maximum temperature reached by the samples. The temperature-time experimental curves are compared with theoretical heating curves to verify if the model can be used to predict the temperature evolution at the joining interface during a welding process.

II.2 Introduction

II.2.1 Thermoplastic welding

Welding techniques are gaining popularity in the aerospace industry as alternatives to adhesive bonding and mechanical fastening to join thermoplastic composite parts. These techniques are fast, efficient, typically require less to no surface preparation and allow to obtain equivalent mechanical properties as other methods (Yousefpour et al., 2004). The working principle to weld two parts – known as adherents – is to generate heat directly at the joining interface to melt or soften thermoplastic materials on the welding line, allow polymer chain diffusion through the interface, and ultimately weld the two adherents (Wool et al., 1989; Bastien & Gillespie, 1991). Different welding techniques are available to join various geometries, the three most promising of which are ultrasonic welding, resistance welding and induction welding (Villegas et al., 2013; Yousefpour et al., 2004). In the latter, heat is generally induced at the joining interface by placing a heating element that reacts to an applied alternating magnetic field. This material is called a susceptor.

II.2.2 Types of susceptors

A susceptor can generate heat through two different mechanisms: eddy currents and hysteresis losses (Bayerl et al., 2014). In the first one, the material must be electrically conductive, allowing for the formation of induced eddy currents. These currents loops dissipate heat through Joule effect. These susceptors are therefore called electrical susceptors and are typically metallic meshes, electrically conductive films or carbon fibres (Ahmed et al., 2006; Bayerl et al., 2014; Dermanaki Farahani et al., 2018). The second mechanism relies on magnetic hysteresis of magnetic materials to heat up when subjected to an alternating magnetic field. The electromagnetic energy is absorbed by the magnetic material and released as heat, due to the magnetic hysteresis effects inside the material (Martin et al., 2021; Suwanwatana et al., 2006a; Wetzel & Fink, n.d.). These susceptors are called hysteresis losses susceptors, or magnetic susceptors. They can be made of magnetic particles distributed inside a thermoplastic polymer, typically identical to the matrix of the adherents. Metallic magnetic particles can also experience heating through eddy currents depending on the particles diameter, but this is usually negligible in micro-meter sized particles. This paper will focus on the characterization of the heating rate of these hysteresis losses susceptors. It must be noted that heat can also be induced directly into the adherents when they are made of electrically conductive materials such as carbon fibres (Rudolf et al., 2000). In that case, no external material is required at the joining interface, which grants this technique the name of susceptor-less induction welding.

II.2.3 PEI-based hysteresis losses susceptors

Herein, polyetherimide (PEI) susceptors are developed to join PEI-based composite materials. PEI is an amorphous thermoplastic (T_g = 215-217°C) which is widely used in the aerospace industry due to its high mechanical properties. A methodology published by the authors allows to select a suitable magnetic material that can be dispersed in PEI to manufacture a magnetic susceptor (Martin et al., 2022). This work showed that multiple parameters, such as the applied magnetic field amplitude, the magnetic material absorbed energy density and the frequency of the alternating field affects the heating capability of a hysteresis losses susceptor. By applying this methodology for material selection, it appears that micrometer-sized Nickel (Ni) particles are good candidates because of their high absorbed energy density and their compatible Curie temperature of 358°C. To ensure good welding properties, it is crucial to know the heating rate of the susceptor, which will allow predicting the temperature evolution at the joining line and the welding degree during the process. This paper presents a method to characterize the heating rate of PEI/Ni susceptor by applying a magnetic field on it and measuring its temperature evolution with a thermal camera.

II.3 Experimentation

II.3.1 Samples preparation

PEI ULTEM 1010 (SABIC) pellets are used as the thermoplastic matrix for the susceptors. Ni particles (Sigma-Aldrich) with an average particles size of 5µm are mixed with PEI in an internal mixer (HAAKE^{TM} Rheomix OS 1010) to ensure good dispersion and distribution of the particles. The PEI is softened at 320°C and 50rpm for 4 minutes in the mixer, then the Ni particles are added in the mixer for 4 more minutes at the same temperature and same mixing speed. The Ni volume fraction is varied at 10% and 20%. The resulting mixed material is recovered and shredded in small pellets (around 2mm of diameter). These pellets are then pressed into susceptor films for 10 minutes at 320°C in a hydraulic press. 4x2cm^2 samples are cut from the films for induction heating tests and 1x1cm^2 samples for optical microscopy observations. A Nikon Eclipse MA100N optical microscope is used to obtain images at 50x magnification for each concentration.

The density of the samples is then evaluated using the water displacement method – or Archimedes method – as described in ASTM D792 standard. Every sample is characterized, and the obtained density is compared with the theoretical value. Finally, the emissivity of the samples is determined by placing one specimen on a hot plate and measuring its temperature with thermal camera and with a thermocouple attached to its surface. The actual emissivity value is obtained when the reading from the thermal camera matches the one from the thermocouple.

II.3.2 Heating rate measurement setup

The experimental setup is made of an Ambrell EASYHEAT 10kW generator, providing alternating current into a water-cooled copper induction coil. The coil is equipped with a removable magnetic field concentrator (MFC), made of Ferrotron 559H (Fluxtrol), that increases the magnetic field amplitude in the area where the sample is located. A suspension system, made of a Kapton film in tension between two supports, is holding the sample at a fixed distance from the induction coil. This distance is fixed at 4mm. A FLIR A700 thermal camera is fixed on top of the sample to record its temperature evolution during the test. The setup is presented in Figure-A II.1. The current amplitude in the induction coil is fixed at 600A and its frequency at 388kHz. Measurements are conducted with and without the MFC on susceptor samples at 10% and 20% of Ni volume fraction.

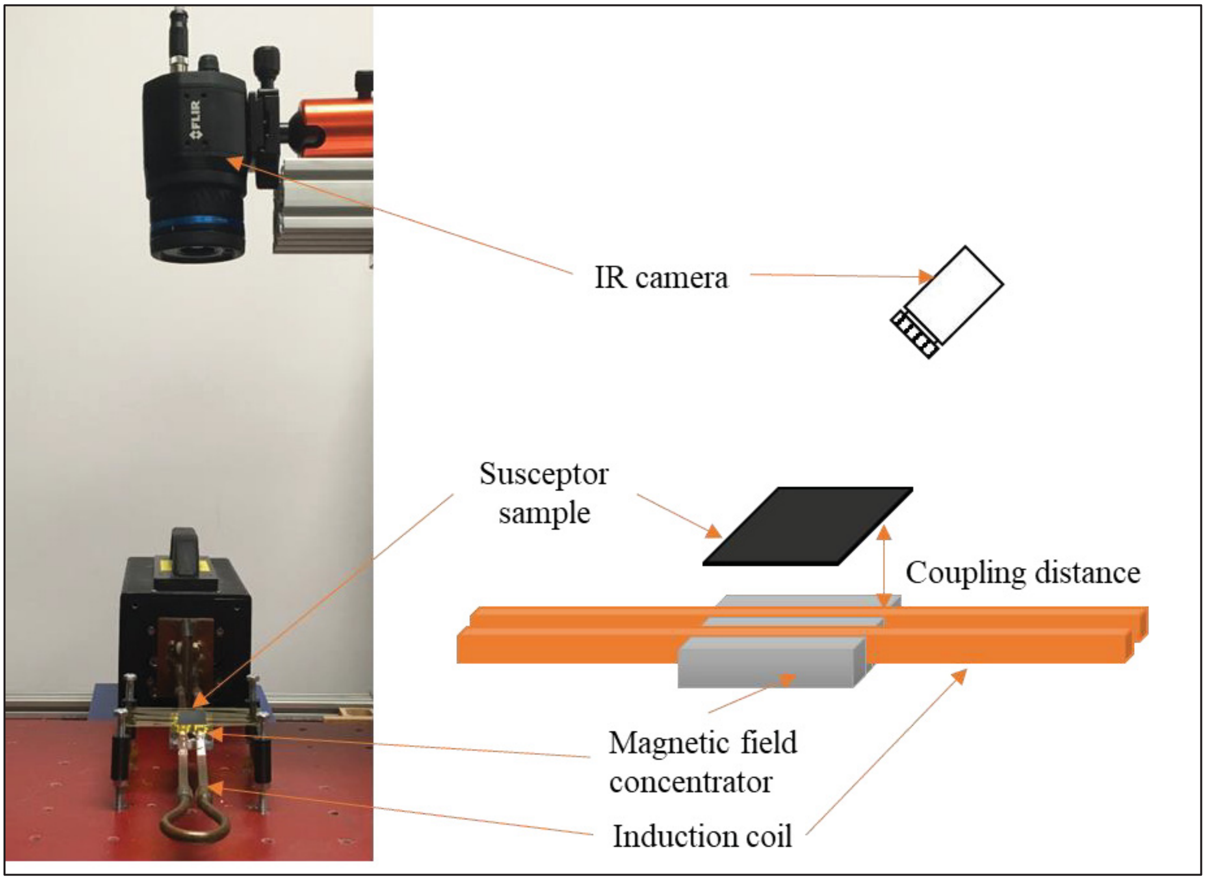

Figure-A II-1 Experimental setup picture (left) and scheme (right). The hanging support made of Kapton tape allows to control the coupling distance. It is located on top of the induction coil, here equipped with the MFC. On the top part of the picture, the thermal camera is recording the temperature evolution of the sample

II.4 Results

II.4.1 Preliminary characterization of the susceptor samples

First, the distribution of Ni particles in the PEI matrix is verified by optical microscopy to ensure the quality of the mixing procedure is satisfying. Samples are polished and observed through optical microscopy. Figure-A II.2 shows homogeneous distribution of the Ni particles (in white) in PEI (in grey). No visible porosities are observed in any of the pictures for both 10%vol and 20%vol concentration. The porosity volume fraction is therefore assumed to be zero in the susceptor films. The average density and standard deviation of each sample is reported in Table-A II.1.

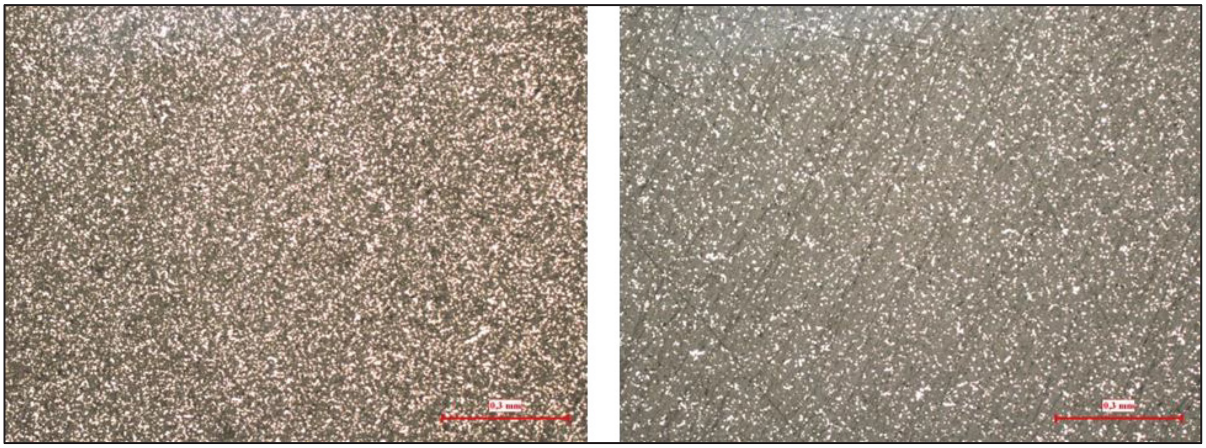

Figure-A II.2 Optical microscopy images of PEI/Ni susceptor films at Ni concentration of 20%vol (left) and 10%vol (right). The PEI matrix appears in grey, and the Ni particles appear in white. The red scale represents 300 microns.

Table-A II.1 Average experimental and theoretical density of induction heating samples for PEI/Ni at 10%vol and 20%vol. The standard deviation on the experimental average is also reported

Induction heating samples density [g/cm^3]		
Ni volume fraction	Experimental measurement	Theoretical value
20%	2.856 ± 0.068	2.796
10%	2.048 ± 0.050	2.033

As no porosities are visible in microscope pictures (Figure-A II.2) and the density is as expected (Table-A II.1), it can be concluded that the expected Ni content is obtained and that Ni particles are well distributed in the samples, highlighting the efficiency of the mixing procedure. Finally, the emissivity value for the PEI/Ni susceptor samples is determined to be 0.9, which corresponds to what has been observed for other Ni-based susceptors (Martin et al., 2022). This value will be used in the thermal camera for the induction heating rate characterization.

II.4.2 Experimental heating rate characterization

The heating rate of the susceptors is measured using the presented setup (Figure-A II.1). The induction magnetic field is turned on for 60s then turned off. The temperature evolution is measured for one more minute to observe the cooling part of the curve. The measured temperature evolution is reported in Figure-A II.3. Five measurements are conducted for each configuration. As expected, the heating rate and the maximum temperature is higher for 20%vol samples. The presence of the MFC increases the magnetic field amplitudes, leading to even higher heating rates. The samples present a good repeatability during induction heating. The initial heating rate – the slope at the beginning of the curve – is measured to be 85.7, 47.4, 22.6 and 15.3°C/s for samples at 20% - 600A, 10% - 600A, 20% - 600A no magnetic flux concentrator (MFC) and 10% - 200A no MFC, respectively. The shape of the curves – a sharp initial temperature increase which then slows down to eventually reach a plateau below Ni Curie temperature – indicates that the hysteresis losses are the dominating heating mechanism. If eddy current heating was significant, temperature would keep increasing. One can notice more variability in the measurements done at 600A without MFC. This might have been caused by unwanted external air stream in the laboratory during the test, which affected the thermal losses and therefore the temperature evolution recorded by the thermal camera. This shows that it is very important to get repeatable tests conditions to obtain reliable results.

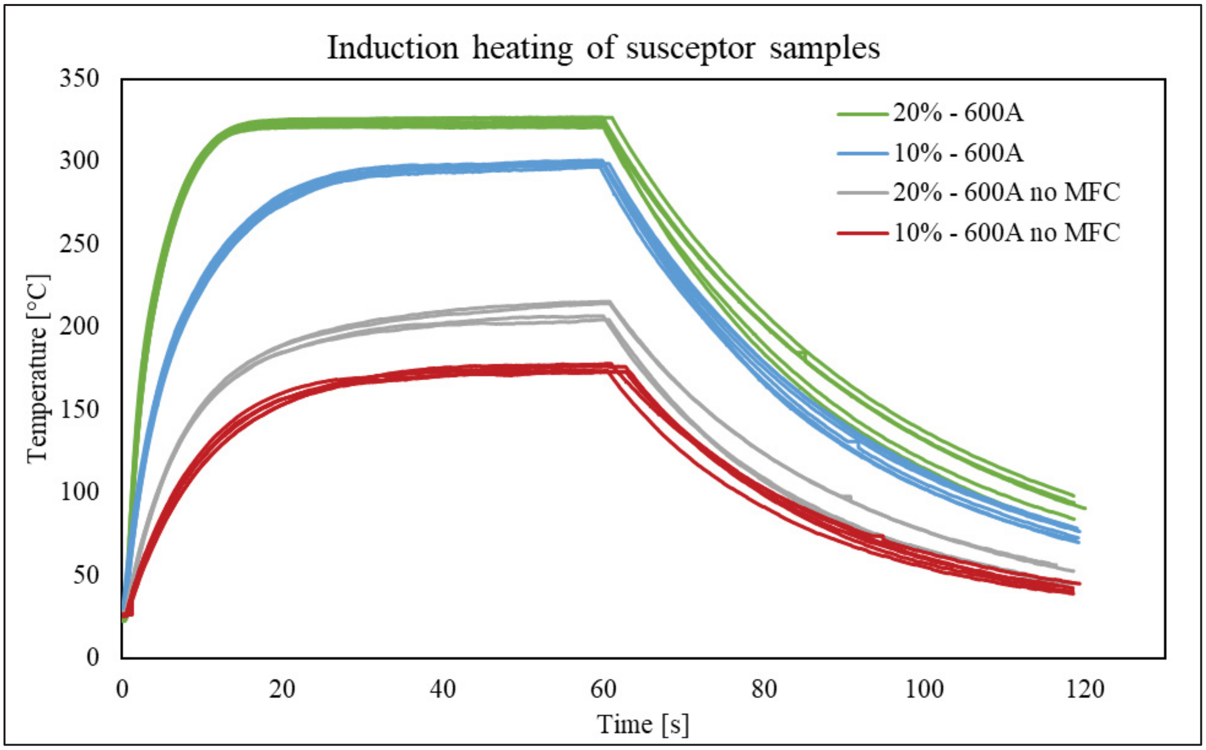

Figure-A II.3 Induction heating curves for PEI/Ni susceptors at two concentrations (10%vol and 20%vol), with and without an MFC mounted on the induction coil. The coupling distance is fixed at 5mm and the current travelling through the coil at 600A

II.4.3 Theoretical heating rate modelling

Three main mechanisms contribute to the temperature evolution of a susceptor: the heating by hysteresis losses, the heating due to the proximity of the hot MFC and the thermal losses in the environment. It is assumed that there is no eddy current heating in the Ni particles. These contributions are presented below and are added in the model aiming to predict the induction heating of a susceptor.

II.4.3.1 Isolated heating rate due to hysteresis losses

Based on Wetzel and Fink's work, the heating rate of an isolated volume of susceptor due to hysteresis losses can be predicted by using the following equation (Wetzel & Fink, n.d.):

$$\frac{dT}{dt} = fE_h \left(\rho c_p + \left(\frac{1}{v_f} - 1 \right) \tilde{\rho} \tilde{c}_p \right)^{-1} \tag{II.1}$$

A few parameters and their evolution with temperature must be characterized to predict the heating rate of the susceptor. The absorbed energy density E_h is the amount of electromagnetic energy that is absorbed by the magnetic material – here the Ni particles – and released into heat. This value depends on the applied magnetic field amplitude H_m, which must also be known. The other required parameters are the density of Ni particles ρ and PEI matrix $\tilde{\rho}$, as well as their specific heat capacity, c_p and $\tilde{c}_p$ respectively.

The magnetic permeability of the sample depends on the magnetic permeability of the two components. Based on magnetometer measurements done in a previous work, Ni particles presents a relative magnetic permeability of 7 (lower than bulk Ni due to demagnetization effects in the particles) (Martin et al., 2022). PEI is not magnetic and can therefore be assumed to have a relative magnetic permeability of 1. The relative magnetic permeability of the PEI/Ni samples can be computed using the rule of mixtures, and values of 1.6 at 10% of Ni and 2.2 at 20% of Ni are obtained.

The magnetic field amplitude H_m depends on the coil geometry, the presence or not of the MFC, the current intensity in the induction coil, the distance between the coil and the sample, or the coupling distance, and finally the sample's magnetic permeability. This can be computed using for instance COMSOL Multiphysics 5.4 software. Details about the simulation model are available in II.7. Figure-A II.4 shows the induction magnetic field amplitude norm around the coil. The field lines in the figure indicate the field direction. It is then possible to calculate the field amplitude along the susceptor width with a current of 600A and a coupling distance of 4mm, with and without MFC, shown in Figure-A II.5. It can be observed that there is decrease in magnetic field amplitude in the center of the sample. This comes from demagnetization effects in the sample when subjected to a magnetic field. As the magnetic permeability is larger at 20%Ni compared to 10%Ni, demagnetization effects are stronger, leading to a larger decrease of the magnetic field amplitude.

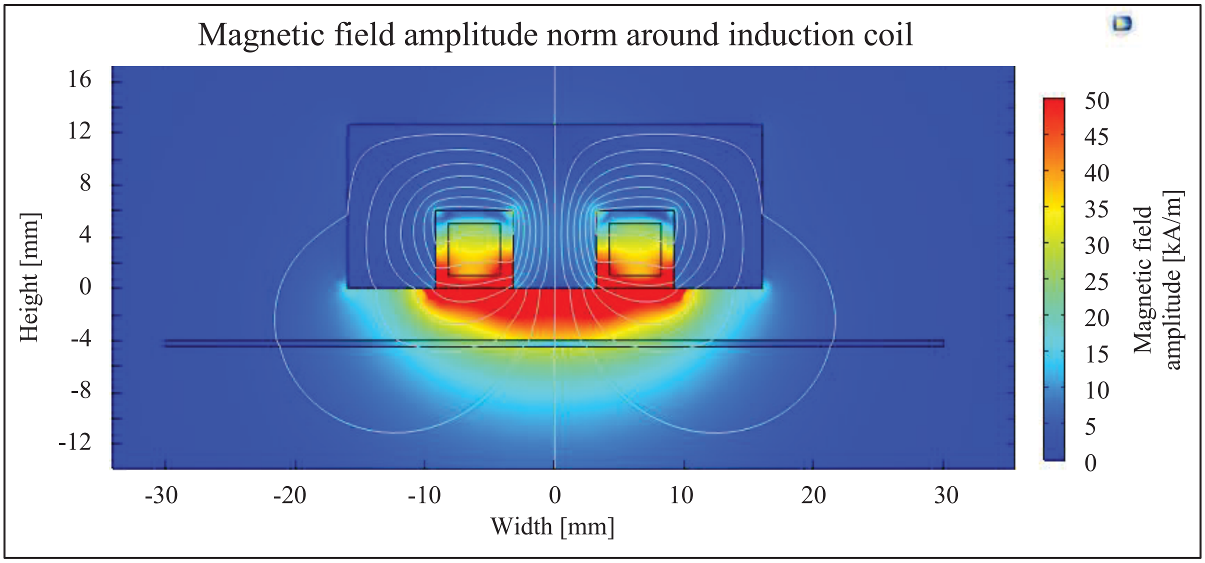

Figure-A II.4 Modelling (COMSOL Multiphysics 5.4) of the magnetic field amplitude norm around a coil equipped with an MFC at 600A with a magnetic permeability of the sample fixed at 2.2 (PEI/20%Ni)

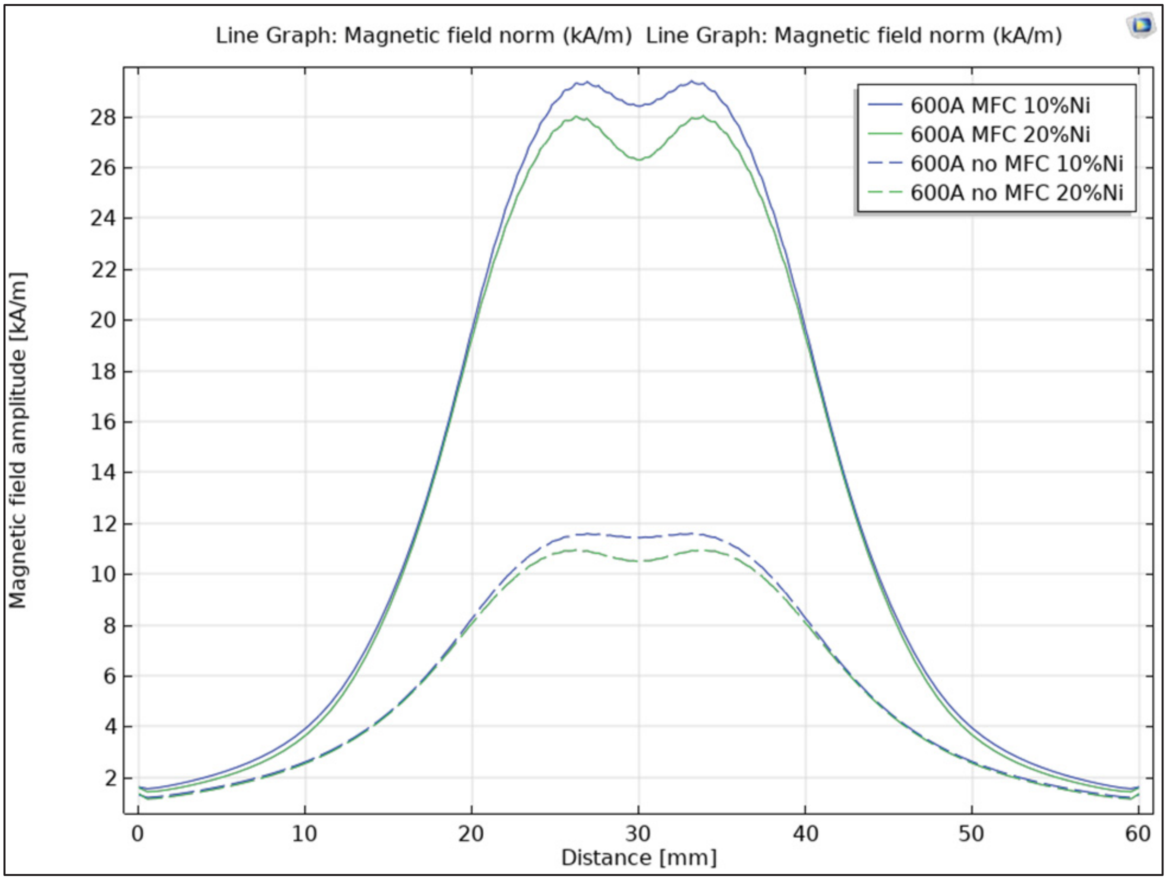

Figure-A II.5 Modelling (COMSOL Multiphysics 5.4) of the magnetic field amplitude norm along the susceptor width with a current amplitude of 600A in the induction coil (frequency 388kHz) and a coupling distance of 4mm. Solid lines shows the amplitude for a coil equipped with an MFC and dashed lines for a coil without MFC. Blue lines correspond to PEI/Ni-10%vol samples and green lines to PEI/Ni-20%vol sample

The magnetic field amplitude selected to calculate the model curves is the average between the maximum and the local minimum located in the center of the curve. This is done to obtain a more representative value along the sample width. It appears that when the coil is equipped with the MFC, the field amplitude is 29kA/m for PEI/Ni-10%vol samples and 27.5kA/m for PEI/Ni-20%vol samples. Without the MFC, it is 11.5kA/m for PEI/Ni-10%vol samples and 10.5kA/m PEI/Ni-20%vol samples. These values are used to obtain the value for E_h at room temperature (in J/m^3, with m^3 referring to the total volume of Ni particles in the sample), which can be calculated using Equation (II.2). This relation is known as the

Steinmetz law (Landgraf et al., 2008; Steinmetz, 1984) and is based on results presented in (Martin et al., 2022).

$$E_h = 4.193 \cdot 10^{-3} \cdot {H_m}^{1.2737} \tag{II.2}$$

Therefore, based on Equation (II.2), the values for E_h for Ni particles are around 2024kJ/m^3 for PEI/Ni-10%vol samples and 1892kJ/m^3 for PEI/Ni-20%vol samples with the MFC mounted on the coil and 623kJ/m^3 for PEI/Ni-10%vol samples and 555kJ/m^3 for PEI/Ni-20%vol samples without the MFC. The evolution of E_h with temperature is approximated as a linear decrease until reaching a value of 0 at the Curie temperature of Ni, which is 358°C.

The density and specific heat capacity of Ni particles and PEI matrix are taken from the literature. Ni density is considered as fixed at 8900kg/m^3. Its specific heat capacity is following the relation proposed in Suwanwatana et al. (Suwanwatana et al., 2006a):

$$c_p = 423.5 + 0.5 \cdot T \quad with\, T\, in\, [°C] \;\; for\, 25 < T < 325[°C] \tag{II.3}$$

The density of PEI (based on its specific volume) is reported in different online databases (*CAMPUSplastics | Datasheet ULTEM^{TM} Resin 1010*, n.d.; UL Prospector, 2018) and is assumed to follow:

$$\begin{aligned} \tilde{\rho} &= 1280 - 0.2 \cdot T \quad when\, T < 200[°C] \\ \tilde{\rho} &= 1380 - 0.7 \cdot T \quad when\, T > 200[°C] \end{aligned} \tag{II.4}$$

Finally, DSC results (measured with a TA DSC 2500 and presented in Figure-A II.6) indicates that the specific heat capacity of PEI is following:

$$\begin{aligned} \tilde{c}_p &= 855 + 2.3 \cdot T \quad when\, T < 217[°C] \\ \tilde{c}_p &= 1680 \quad when\, T > 217[°C] \end{aligned} \tag{II.5}$$

With these parameters, it is possible to predict the evolution of temperature of an isolated volume of susceptor, based on Equation (II.1).

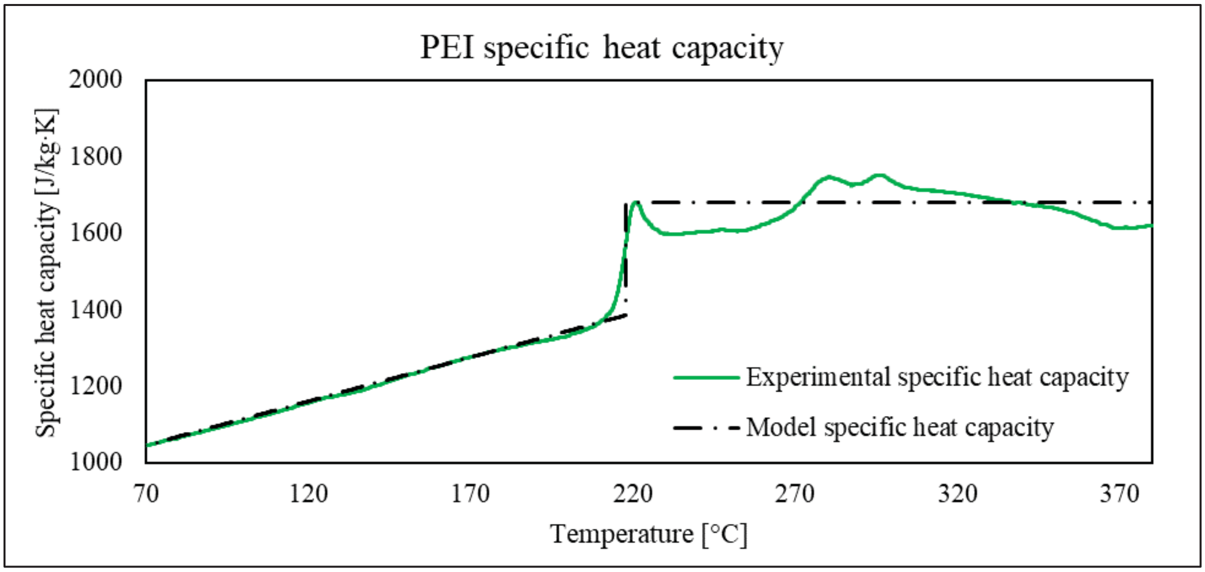

Figure-A II.6 PEI specific heat capacity measured by DSC. The experimental curve is in green and the model curve in black

II.4.3.2 Thermal losses in the environment

In the case of the presented measurements, the samples are not isolated, but suspended in the air, which implies heat losses to the environment. The cooling part of the curve (after 60s) can be used to evaluate the cooling rate of the samples, and therefore the thermal losses. From the cooling rate, the thermal losses power can be calculated using the following relation:

$$P_{thermal\ losses} = \bar{\rho} V \bar{c_p} \left. \frac{\Delta T}{\Delta t} \right|_{cooling} \tag{II.6}$$

Where $\bar{\rho}$ and $\bar{c_p}$ are the density and the specific heat of the susceptor, respectively, and V its volume. These values are calculated using the mixture rule, at the given volume fraction of Ni in the susceptor. The following assumptions are made:

- Thermal losses can be expressed as a 2nd order polynomial function of temperature
- They are the same during the heating phase and the cooling phase.

The thermal power losses for the experimental results (Figure-A II.3) calculated using Equation (II.6) are presented in Figure-A II.7. These curves are an arithmetic mean of all the thermal losses curves of a data set, and they are used in the model to predict the temperature evolution.

It appears that for a given Ni volume fraction (10%vol or 20%vol), the thermal losses curves at high and low magnetic field amplitude overlap, indicating that no matter the maximum temperature reached by the samples, the thermal losses are the same. On the other hand, there is a large difference between the thermal losses at 10% and 20% of Ni volume concentration. This could come from an inaccurate expression of the density or the specific heat evolution with temperature and it should be further investigated.

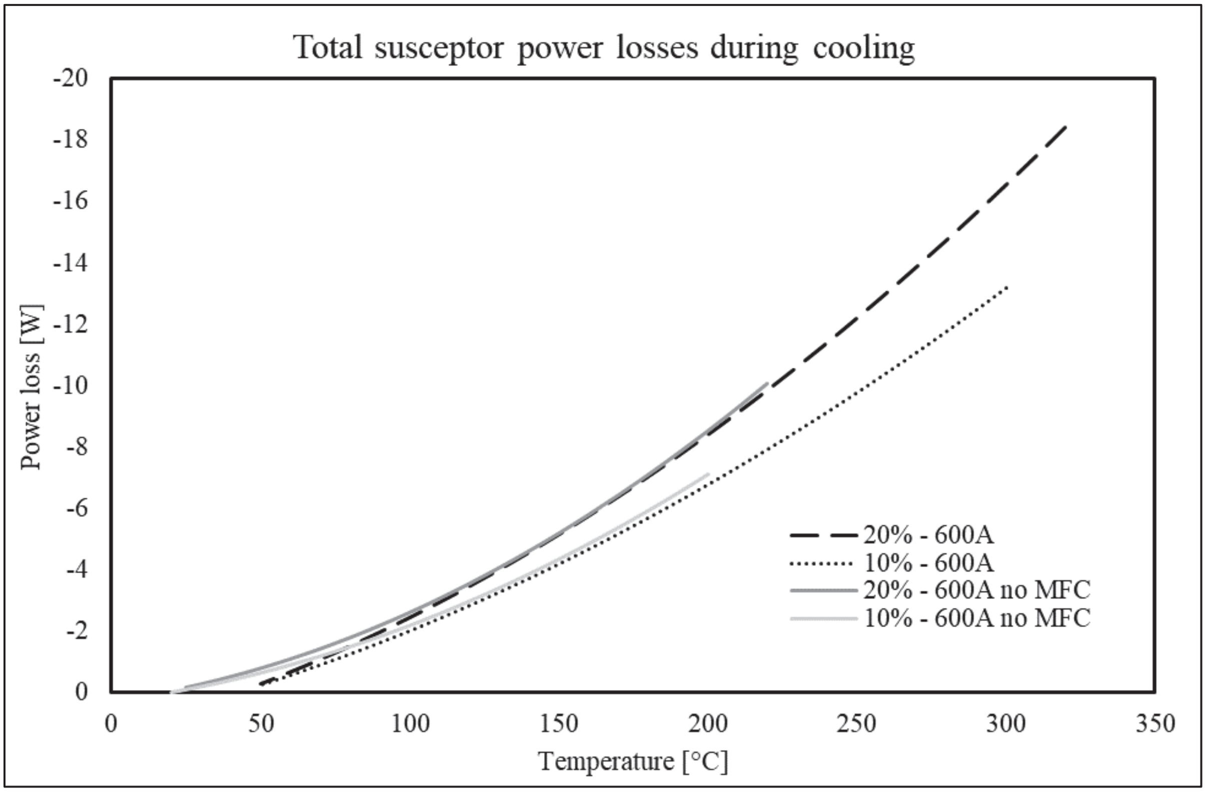

Figure-A II.7 Thermal losses of susceptor samples. Each curve is an arithmetic mean of the thermal losses of each sample from a single data set

II.4.3.3 Influence of the proximity of the MFC

When an MFC is mounted on the induction coil, it will heat up during the process, due to induced eddy currents inside of it. As the coupling distance is very small, being in the vicinity of a hot metallic part can increase the temperature of the susceptor and affect the results of the experiment. To analyse the influence of the MFC, samples of PEI with a small addition 2%vol of carbon black (CB) are prepared following the same procedure as PEI/Ni samples. The goal is to obtain an opaque PEI film that will not heat up by hysteresis losses effects, therefore only observing the gain of temperature due to the proximity of the MFC. The temperature evolution is measured using the same experimental setup and the results are presented in Figure-A II.8. It appears clearly that at 600A without MFC (solid blue line), there is no significant temperature change, highlighting the fact that no hysteresis losses nor eddy currents are induced in the sample. On the other hand, when the coil is equipped with the MFC (dashed blue line), a temperature increase is observed, indicating that power is received by the sample during the measurement. This contribution is added to the model to predict the temperature evolution of the susceptor, using the following expression for the power received from the MFC as a function of time during the 60s of heating:

$$P_{MFC} = -6.0 \cdot 10^{-4} \cdot t^2 + 5.75 \cdot 10^{-2} \cdot t + 0.31 \tag{II.7}$$

With t being the time since the beginning of the induction heating, when the MFC starts to heat up.

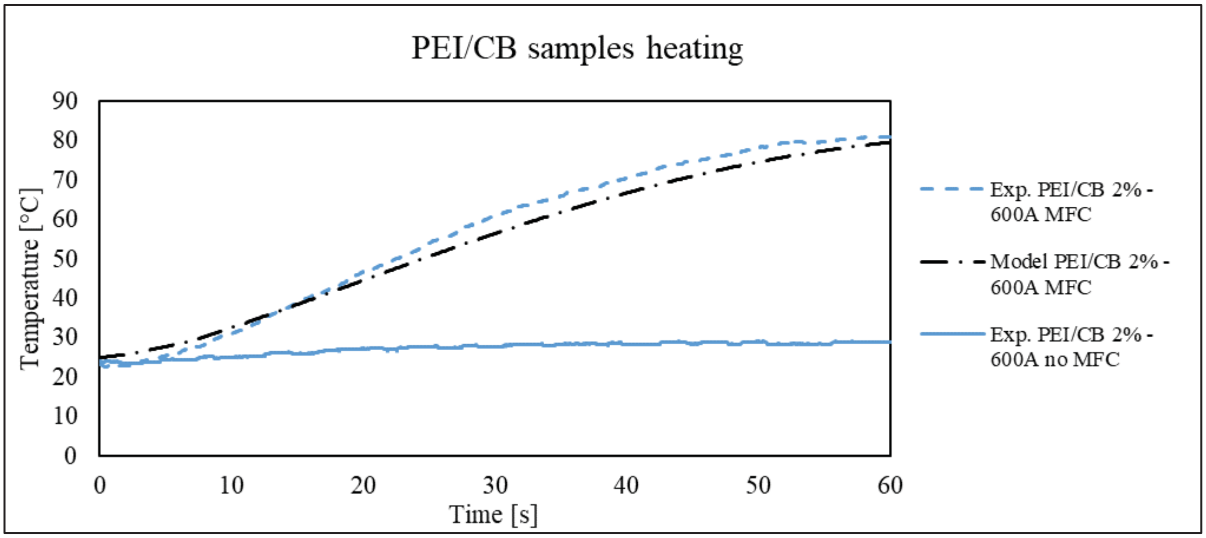

Figure-A II.8 Heating of PEI/CB samples. The model equation, based on Equation (II.7) and measured thermal losses, used in the susceptor's heating rate model is shown in black

II.4.3.4 Comparison between model and experimental results

The model allows prediction of the induction heating curve of a susceptor with a given Ni concentration, a given magnetic field amplitude, and the presence or not of an MFC.

It considers the three main contributions that were previously presented:

- Heating due to hysteresis losses in an isolated volume of magnetic susceptor,
- Heating due to the proximity of the MFC,
- Cooling due to thermal losses to the surrounding environment.

The resulting curves are presented in Figure-A II.9 alongside with the obtained experimental results. Only one representative curve of each data set is kept for clarity.

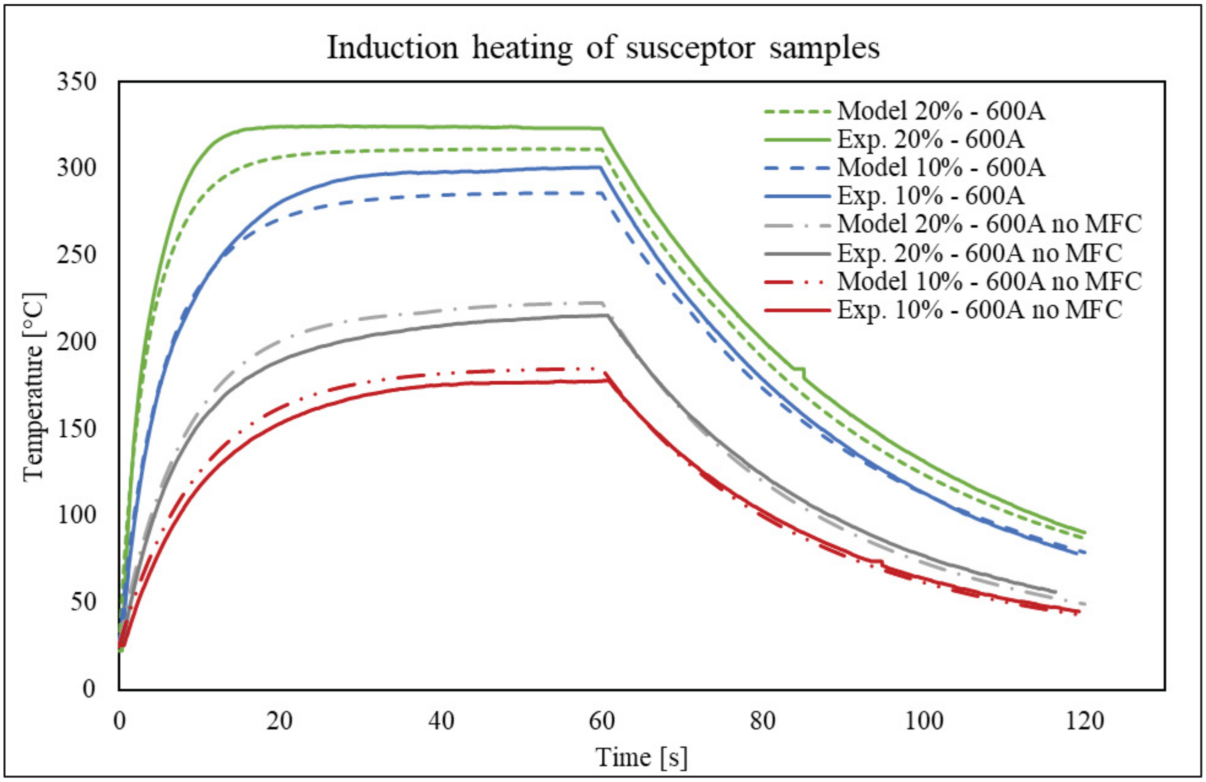

Figure-A II.9 Comparison of the model curves and the experimental results

It appears in Figure-A II.9 that the overall shape of the model curve is really close to the experimental data, assessing the validity of the modelling approach. First, it is interesting to compare the initial heating rate between experimental measurements and model values, as presented in Table-A II.2. At the very beginning of the curve, it can be considered that there are no thermal losses, because the temperature is still very close to the ambient temperature (Martin et al., 2022). The experimental results are quite close to the modelled values, showing that the model is correctly predicting the susceptor's isolated heating rate.

Table-A II.2 Predicted and average measured initial heating rates for susceptor samples. The standard deviation on the experimental averages is also reported

Initial heating rate (Predicted / Measured) [°C/s]		
Ni volume fraction	600A – MFC	600A – no MFC
20%	83.9 / 85.2 ± 6.1	24.5 / 22.6 ± 0.4
10%	49.8 / 47.4 ± 3.7	16.3 / 15.4 ± 0.9

When looking at the maximum temperature reached in the model and in the experiments (summarized in Table-A II.3), different observation can be made for curves with MFC and without MFC. At low magnetic field amplitude (600A no MFC). The model slightly overestimates the experimental results by around 5.5%. This can come from higher-than-expected thermal losses during the heating phase, due to different external conditions, as discussed earlier. The error can also come from the selected emissivity value (0.9), as a higher emissivity would result in larger measured temperature.

For both data sets measured with the MFC, the model curves slightly underestimate the experimental results. This should be further investigated to understand why we observe these differences. The average maximum experimental temperature and the modelled one are 324°C and 311°C at 20%vol, and 299°C and 286°C at 10%vol, respectively. Overall, the model curves are fitting well the data, showing around 4% of error compared to the experimental measurements. The divergence probably comes from inaccuracy in some temperature-dependant materials parameters, especially at higher temperature. That would explain why this deviation is not observed at lower magnetic field amplitude. It is also possible that the thermal losses are actually slightly lower during heating than cooling, which would go against one of the hypotheses of this model. Finally, the power received from the MFC might vary a little between the PEI/CB and PEI/Ni samples due to a different absorption of the two materials.

Table-A II.3 Experimental average and modelled maximum temperatures during induction heating experiments. The standard deviation on the experimental averages is also reported

Maximum temperature (Predicted / Measured) [°C]		
Ni volume fraction	600A – MFC	600A – no MFC
20%	311 / 324 ± 2.5	223 / 210 ± 5.5
10%	286 / 299 ± 1.2	185 / 175 ± 2.2

II.5 Conclusion

This study presents the heating rate characterization of PEI/Ni susceptors for induction welding. It highlights the quality of the mixing method, allowing to obtain well distributed Ni with a good control of the volume fraction. Then, experimental results showed good repeatability inside a data set, confirming the ability to produce reliable and repeatable susceptors. A model based on some critical parameters that must be defined beforehand was presented. Simulations of the magnetic field allowed to calculate the applied field amplitude and the corresponding absorbed energy density, then the analyze of the cooling curves of the samples gave an indication on the thermal losses. The influence of being in the vicinity of the magnetic field concentrator which gets hot during the process was also investigated and included in the model. Ultimately, the model heating curves were compared to the experimental results and show a good fit, with an error of around 5%. This paper also presented a general procedure to prepare and validate a model for hysteresis losses susceptors.

Future work should include more extensive modelling of the heating behaviour of the susceptor to consider thermal conduction inside the sample. Also, a more detailed understanding of the thermal losses is needed to obtain a better prediction of the temperature evolution of the susceptor.

II.6 Acknowledgements

The authors acknowledge financial support from CREPEC (Research Center for High Performance Polymer and Composite Systems), NSERC (Natural Sciences and Engineering Research Council of Canada) (grant number ALLRP 556497-20), PRIMA Québec (Pôle de Recherche et d’Innovation en Matériaux Avancés) (grant number R20-13-004), the Canadian Space Agency (CSA), Ariane Group, NanoXplore inc, Mëkanic and Dyze Design. They also want to thank Mr. Thomas Delavenne for designing the hanging sample support used in the experiments, Mr. Félix Leblanc for manufacturing the PEI/CB samples, and Ms. Maryam Shokrollahi for the DSC measurement.

II.7 Appendix – COMSOL Multiphysics model details

Simulations of the magnetic field around the induction coil is performed using the AC/DC module in COMSOL Multiphysics 5.4. The profile section of the induction coil and the magnetic flux concentrator (MFC) is defined as follows: the coil is made of to square section of outside dimensions 6 x 6 mm and inner dimensions 4 x 4 mm, and the flux concentrator is a large rectangle of 32 x 12.6 mm encompassing the induction coil. The materials are copper for the induction coil, with water inside of it, Ferrotron 995H for the MFC (not available in the default material library, created with a magnetic permeability of 18, as per the material datasheet) and air for the surroundings. The general outer limit is a large circle of 100mm of radius where default Dirichlet conditions are applied. A triangular default mesh is applied for the simulation. Current travelling in the coil is set at 600A in one half and -600A in the other one. This comes from the fact that a closed-loop coil is used, so the current travels in opposite direction in both sides. Figure-A II.4 presents the results for the magnetic field amplitude norm simulations. On top of the color map showing the amplitude of the magnetic field, lines indications its direction are added. Finally, a line is drawn 5mm away from the coil, where the sample is lying during heating test. This line is the reference for the results of the field amplitude presented in Figure-A II-5.

ANNEX III

POLISHING PROCEDURE

This section presents a procedure to prepare optical microscopy samples using the automatic polishing machine.

First, samples are mounted into an acrylic resin from Metlab Corp. The two parts of this resin can be found in the blue cabinet (toxic materials) for the powder and in the yellow cabinet (flammable materials) for the hardener in the A-4402 lab. It is mandatory to wear gloves and lab safety glasses to manipulate these products. The preparation of the resin must be conducted in a ventilated fumehood.

The resin powder bottle contains a blue measuring spoon, while a transparent spoon is located on the shelf next to the hardener bottle. Make sure not to mix both spoons. Mix 2 volumes of resin powder with one volume of liquid hardener to prepare the acrylic mounting resin. Typically, 30 mL of powder and 15 mL of hardener allow for the preparation of two optical microscopy samples. The working time is about 2 min so make sure that the samples are ready before mixing the resin and the hardener. Place your samples in white mounting cups, making sure that the surface to be observed is facing the bottom face of the cup. Use a plastic clip to hold the sample in place if needed. Once ready, prepare the resin and pour it on the samples. As the resin is viscous, the samples might move while pouring, so it is recommended to hold them in place using a wooden stick. Make sure to completely fill the mounting cup with resin, even for small samples. Then, wait for around 15 min for the acrylic resin to cure at room temperature. Once it is completed, remove the bottom face of the mounting cup and extract the sample, which is now ready for polishing.

The optical microscopy samples used in this work were prepared using the MOTOPOL™ 2000 automatic polisher from Buehler presented in Figure-A III.1. This machine is in A-2150. It allows to polish six samples at a time. The polishing parameters such as the speed and direction of rotation, the applied force and the polishing time can be adjusted on the top (Figure-A III.2) and bottom (Figure-A III.3) control panels.

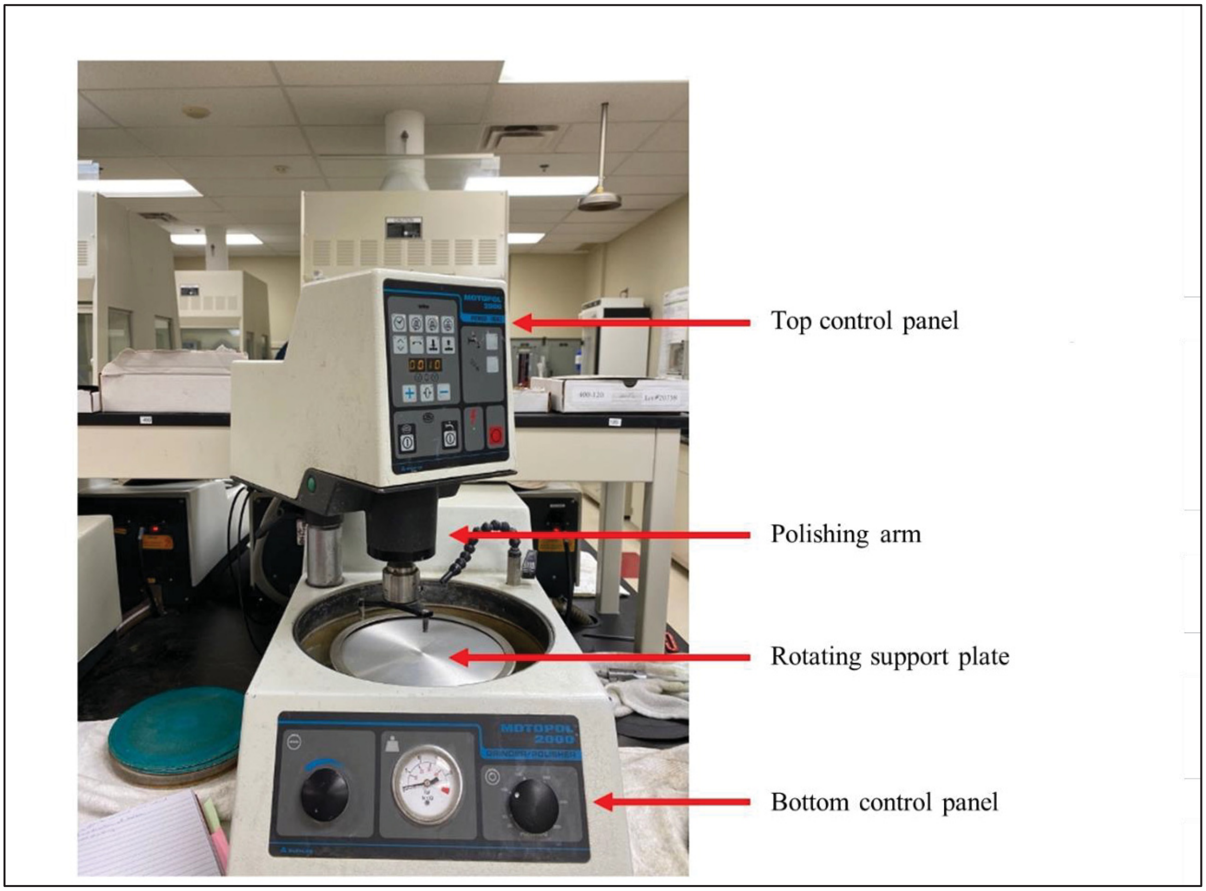

Figure-A III.1 General view of the automatic polisher. The main parts are highlighted by the red arrows

Figure-A III.2 Top control panel. In 1, the parameters of the samples support are controlled. Water flowing during the polishing cycle is activated by button 2. Time of polishing of defined in zone 3. Zone 4 allows to manually turn on and off the rotation of the bottom plate and the water. Button 5 is the emergency stop button of the machine

Figure-A III.3 Bottom control panel, where the force applied on the samples during polishing and the speed of rotation of the bottom plate can be tuned

The following parameters were used to polish the samples:

- Samples support plate rotation speed: 60 rpm
- Samples support plate rotation direction: opposite to the bottom plate
- Water activated during the polishing cycle
- Polishing time: steps of 1 min
- Applied force: around 45 lbf or 200 N
- Bottom plate rotation speed: 100 rpm

The following sequence of grinding papers and corresponding polishing time is followed, by steps of 1 min:

- 1 min with 320 paper
- 2 min with 400 paper
- 4 min with 600 paper
- 6 min with 800 paper
- 8 min with 1200 paper

After each 1 min polishing step, water is poured on the grinding paper to clean it from residues. After 2 cycles of 1 min, the grinding paper is changed for a new one, even if the same grade continues to be used. This step yielded satisfying results for the polishing of PEI and PEEK based composite materials but could be adapted if other materials are used.

After finishing the polishing sequence, the samples can be unmounted from the support plate and dried with paper, making sure not to scratch the surface. To make sure no dust is still present on the surface, kimwipes can be used to gently clean the surface prior to perform the microscope observations.

ANNEX IV

FWT SAMPLES PREPARATION

The protocol to bond FWT steel blocks to sandwich panels samples is presented in the section. To perform a FWT test on a 5 cm by 5 cm sandwich panel sample following ASTM C297 standard (ASTM C297, 2021), two steel blocks must be adhesively bonded to the sample, one on each side, to connect the sample to the testing jig mounted on the tensile test machine. The Hysol EA9696 adhesive, a modified epoxy adhesive film, is recommended to be used for this step. Loctite 415 acrylic glue was used for the tests presented in Chapter 5, but it was later replaced by the EA9696 adhesive as it provided better strength and more repeatability.

As the EA9696 adhesive must be stored in the freezer to avoid polymerization and moisture absorption, it is recommended to precut enough 5 cm by 5 cm squares of adhesive films in advance to limit the time the roll of adhesive spends outside of the freezer. One should keep in mind that two squares of adhesive films are required to prepare one sandwich samples (one per steel block).

Before adding the adhesive films, both faces of the sandwich panel sample and the surfaces of the two steels blocks that will be bonded to it must be thoroughly prepared. It is mandatory to wear gloves during the subsequent steps to make sure the samples remain clean after preparation, and to protect the skin from acetone. The first step is to clean the surfaces with acetone. If the polymer of the sample is dissolved by acetone, replace it with another solvent that does not dissolve the sample. Then, use grinding paper (grade 120 or similar) to grind the working surfaces. This has multiple effects:

- It increases the roughness of the surfaces, which improves the strength of the adhesive bond.
- It removes the remaining traces of adhesive or polymer on the steel blocks.

- It removes the passive oxidated layer on the steel blocks, which can prevent the proper bonding of the adhesive.

After this step, parts must be cleaned again with acetone to remove the dust created during grinding. The cleaning can be repeated multiple times until the surface are clean. This is very important as the presence of dust or particles at the surface will be detrimental to the good adhesion of the steel blocks.

Then, the adhesive layer can be added. It is recommended to first place the two adhesive films on the two steel blocks with the protective white film still on. Then, press one block against the other to make sure the adhesive film is flat and well tacked on each surface. Then, use a cutter to remove the excess of adhesive on the sides of the blocks. This will limit the amount of adhesive squeezing out during the curing process.

The homemade FWT alignment setup can be used to assemble the steel blocks and the sandwich sample while ensuring proper alignment of the parts. First, the bottom steel block is installed, with two out or four edge alignment tabs. The protective liner of the adhesive film can then be removed (Figure-A IV.1a). Secondly, the sample is installed on the first block (Figure-A IV.1b). The second block can then be placed on top of the sample. At that point, it is essential to make sure that the cylindrical holes in the two steel blocks are perpendicular to each other (Figure 1.23), to be able to mount the samples on the testing machine. To finish the assembly, the alignment setup is closed by adding the two other alignment tabs and secure them with the bracket (Figure-A IV.1c).

Once the alignment is completed, the sample can be placed in the oven for 90 min at 120°C for curing. To apply pressure on the sample, the cylinder weight from the internal mixer in A-4402.2 (approx. 5 kg) can be used. It is placed on top of the steel blocks inside the oven, as shown in Figure-A IV.2.

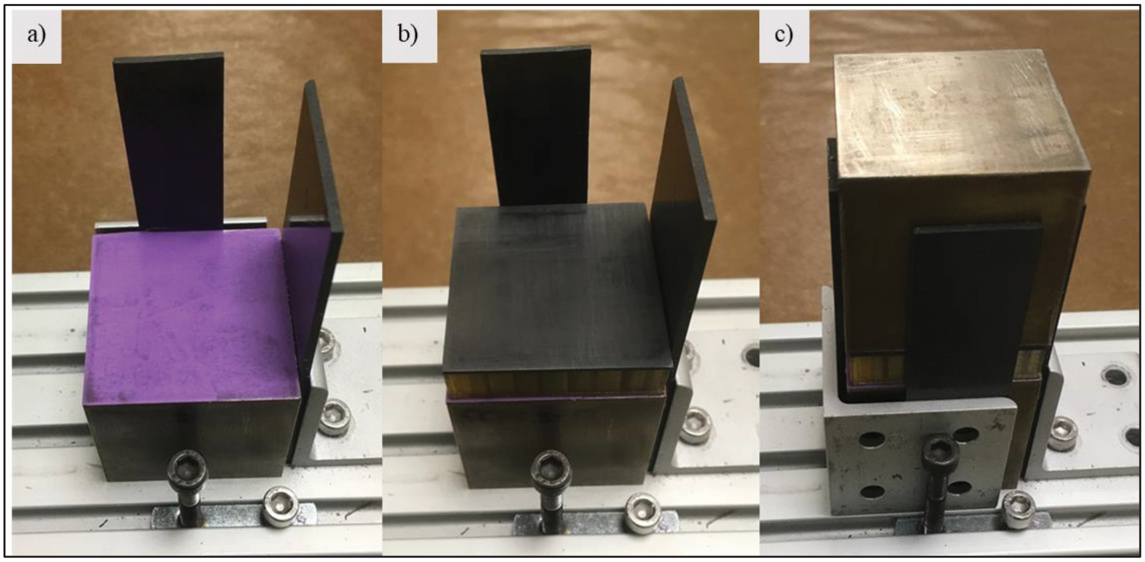

Figure-A IV.1 Sequence of assembly of the FWT samples

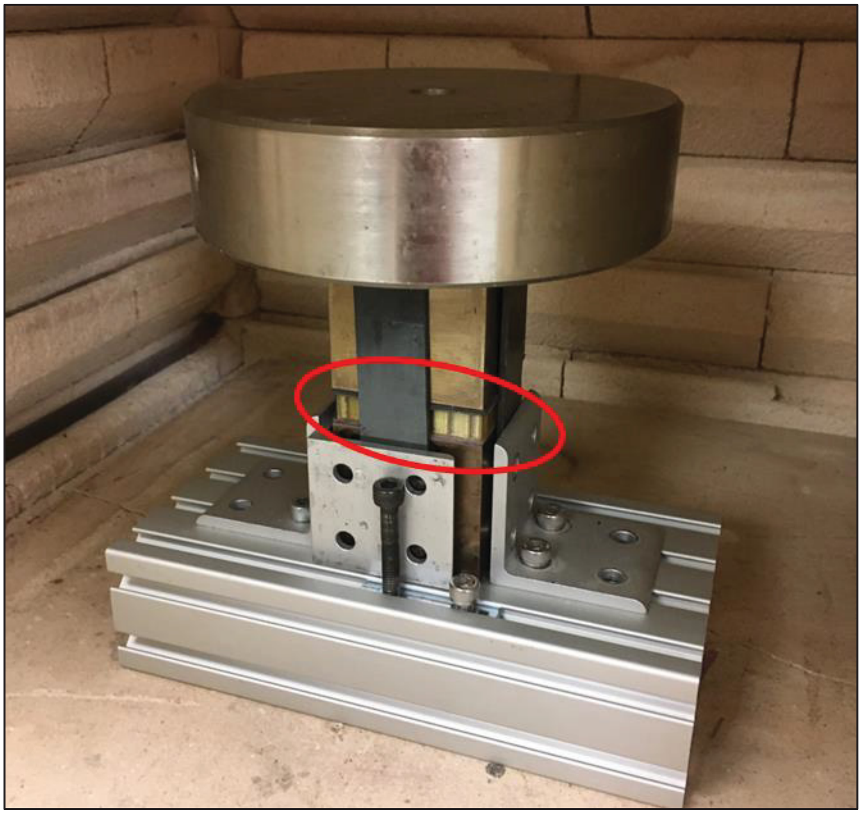

Figure-A IV.2 Alignment setup in the oven. The red circle highlights the position of the sandwich sample. The weight placed on top is used to apply pressure during curing

After curing, the parts are taken out of the oven and let for at least 45 min to cool down. Make sure to wear high temperature gloves to do it, as the parts are very hot. The sample must be left in the alignment jig with the weight on during this period, to make sure the adhesive correctly cools down. Once it cools down, remove the weight (it might still be hot!) and open the alignment jig to recover the sample. The alignment jig is ready to be used to prepare another sample.

After FWT tests, blocks must be separated for the fractured sample. The parts can be placed in the oven at 180°C for 2 h, which starts the degradation of the adhesive and allows to separate the sample and the blocks. This temperature is low enough for PEI-based material to be separated without softening, allowing the recovery of the samples. For lower temperature polymers, the sample might be lost in the process, in that case make sure it is completely removed from the steel blocks. Residues of adhesives or polymer can be removed with a razor blade to clean the steel blocks. If that is not enough, place the blocks 1-2 h in the oven at 300°C to burn the residues. The blocks should cool down to room temperature before being mounted again on a new sample.

REFERENCES

Absi, C., Alsinani, N., & Laberge Lebel, L. (2022). Carbon fiber reinforced poly(ether ether ketone) rivets for fastening composite structures. *Composite Structures*, *280*, 114877. https://doi.org/10.1016/j.compstruct.2021.114877

Ageorges, C., & Ye, L. (2002). *Fusion bonding of polymer composites: From basic mechanisms to process optimization*. Springer-Verlag.

Ageorges, C., Ye, L., & Hou, M. (2000). Experimental investigation of the resistance welding of thermoplastic-matrix composites. Part II: Optimum processing window and mechanical performance. *Composites Science and Technology*, *60*(8), 1191–1202. https://doi.org/10.1016/S0266-3538(00)00025-7

Ageorges, C., Ye, L., & Hou, M. (2001). Advances in fusion bonding techniques for joining thermoplastic matrix composites: A review. *Composites Part A: Applied Science and Manufacturing*, *32*, 839–857. https://doi.org/10.1016/S1359-835X(00)00166-4

Ageorges, C., Ye, L., Mai, Y.-W., & Hou, M. (1998a). Characteristics of resistance welding of lap shear coupons. Part I: Heat transfer. *Composites Part A: Applied Science and Manufacturing*, *29*(8), 899–909. https://doi.org/10.1016/S1359-835X(98)00022-0

Ageorges, C., Ye, L., Mai, Y.-W., & Hou, M. (1998b). Characteristics of resistance welding of lap shear coupons.: Part II. Consolidation. *Composites Part A: Applied Science and Manufacturing*, *29*(8), 911–919. https://doi.org/10.1016/S1359-835X(98)00023-2

Ahmadzadeh, M., Romero, C., & McCloy, J. (2017). Magnetic analysis of commercial hematite, magnetite, and their mixtures. *AIP Advances*, *8*(5), 056807. https://doi.org/10.1063/1.5006474

Ahmed, T. J., Stavrov, D., Bersee, H. E. N., & Beukers, A. (2006). Induction welding of thermoplastic composites—An overview. *Composites Part A: Applied Science and Manufacturing*, *37*(10), 1638–1651. https://doi.org/10.1016/j.compositesa.2005.10.009

Åkermo, M., & Aström, B. T. (2000a). Modeling compression molding of all-thermoplastic honeycomb core sandwich components. Part A: Model development. *Polymer Composites*, *21*(2), 245–256. https://doi.org/10.1002/pc.10182

Åkermo, M., & Aström, B. T. (2000b). Modeling compression molding of all-thermoplastic honeycomb core sandwich components. Part B: Model verification. *Polymer Composites*, *21*(2), 257–267. https://doi.org/10.1002/pc.10183

Alshaer, A. W., & Harland, D. J. (2021). An investigation of the strength and stiffness of weight-saving sandwich beams with CFRP face sheets and seven 3D printed cores. *Composite Structures*, *257*, 113391. https://doi.org/10.1016/j.compstruct.2020.113391

ASTM C297. (2021). *Standard Test Method for Flatwise Tensile Strength of Sandwich Constructions*.

Åström, B. T., Akermo, M., Carlsson, A., & McGarva, L. D. (1998). *All-thermoplastic sandwich concept*. 705–718.

Avenet, J., Le Corre, S., Jean-Luc, B., & Levy, A. (2021). Temperature and contact pressure effects on the adhesion development of high performance thermoplastic composites. *ESAFORM 2021*. https://doi.org/10.25518/esaform21.409

Avenet, J., Levy, A., Bailleul, J.-L., Le Corre, S., & Delmas, J. (2020). Adhesion of high performance thermoplastic composites: Development of a bench and procedure for kinetics identification. *Composites Part A: Applied Science and Manufacturing*, *138*, 106054. https://doi.org/10.1016/j.compositesa.2020.106054

Bae, D., Shin, P., Kwak, S., Moon, M., Shon, M., Oh, S., & Kim, G. (2015). Heating behavior of ferromagnetic Fe particle-embedded thermoplastic polyurethane adhesive film by induction heating. *Journal of Industrial and Engineering Chemistry*, *30*, 92–97. https://doi.org/10.1016/j.jiec.2015.05.007

Banea, M. D., & da Silva, L. F. M. (2009). Adhesively bonded joints in composite materials: An overview. *Proceedings of the Institution of Mechanical Engineers, Part L: Journal of Materials: Design and Applications*, *223*(1), 1–18. https://doi.org/10.1243/14644207JMDA219

Barazanchy, D., Pandher, J., & Van tooren, M. (2021). *The edge-effect in thermoplastic induction welding*. https://doi.org/10.2514/6.2021-1890

Barazanchy, D., Pandher, J., & Van tooren, M. (2022). The effect of induction welding coil shape on heat generation. *AIAA SCITECH 2022 Forum*. https://doi.org/10.2514/6.2022-0406

Barazanchy, D., & van Tooren, M. (2023). Heating mechanisms in induction welding of thermoplastic composites. *Journal of Thermoplastic Composite Materials*, *36*(2), 473–492. https://doi.org/10.1177/08927057211011621

Barazanchy, D., Van tooren, M., & Ali, M. (2021). Microscopic level modeling of induction welding heating mechanisms in thermoplastic composites. *Journal of Thermoplastic Composite Materials*, *36*, 089270572110466. https://doi.org/10.1177/08927057211046648

Barroeta Robles, J., Dubé, M., Hubert, P., & Yousefpour, A. (2022). Repair of thermoplastic composites: An overview. *Advanced Manufacturing: Polymer & Composites Science*, *8*(2), 68–96. https://doi.org/10.1080/20550340.2022.2057137

Barroeta Robles, J., Dubé, M., Hubert, P., & Yousefpour, A. (2023). Healing study of poly (ether-imide) and poly ether ether ketone using resin films and a parallel plate rheometer. *Composites Part A: Applied Science and Manufacturing*, *174*, 107736. https://doi.org/10.1016/j.compositesa.2023.107736

Bastien, L. J., & Gillespie, J. W. (1991). A non-isothermal healing model for strength and toughness of fusion bonded joints of amorphous thermoplastics. *Polymer Engineering & Science*, *31*(24), 1720–1730. https://doi.org/10.1002/pen.760312406

Bayerl, T., Duhovic, M., Mitschang, P., & Bhattacharyya, D. (2014). The heating of polymer composites by electromagnetic induction – A review. *Composites Part A: Applied Science and Manufacturing*, *57*, 27–40. https://doi.org/10.1016/j.compositesa.2013.10.024

Bayerl, T., Schledjewski, R., & Mitschang, P. (2012). Induction Heating of Thermoplastic Materials by Particulate Heating Promoters. *Polymers and Polymer Composites*, *20*, 333–342. https://doi.org/10.1177/096739111202000401

Becker, S., & Mitschang, P. (2022). Process Improvement of Continuous Induction Welding of Carbon Fiber-Reinforced Polymer Composites. *Journal of Materials Engineering and Performance*, *31*(9), 7049–7060. https://doi.org/10.1007/s11665-022-06842-0

Beehag, A., & Ye, L. (1996). Role of cooling pressure on interlaminar fracture properties of commingled CF/PEEK composites. *Composites Part A: Applied Science and Manufacturing*, *27*(3), 175–182. https://doi.org/10.1016/1359-835X(95)00027-Y

Bengtsson, P. (2006). *Rapid Automated Induction Lamination (RAIL) of carbon fiber weave and thermoplastic film*. http://urn.kb.se/resolve?urn=urn:nbn:se:ltu:diva-45796

Bensaid, S., Trichet, D., & Fouladgar, J. (2005). 3-D Simulation of induction heating of anisotropic composite materials. *Magnetics, IEEE Transactions On*, *41*, 1568–1571. https://doi.org/10.1109/TMAG.2005.845047

Bertotti, G. (1998). Ch. 1—Magnetic Hysteresis. In G. Bertotti (Ed.), *Hysteresis in Magnetism* (pp. 3–30). Academic Press. https://doi.org/10.1016/B978-012093270-2/50050-7

Bertotti, G. (2001). Magnetic Losses. In K. H. J. Buschow, R. W. Cahn, M. C. Flemings, B. Ilschner, E. J. Kramer, S. Mahajan, & P. Veyssière (Eds.), *Encyclopedia of Materials: Science and Technology* (pp. 4798–4804). Elsevier. https://doi.org/10.1016/B0-08-043152-6/00839-1

Beukers, A. (1992). *A new technology for sandwich plates and structures based on the use of in-situ foamable thermoplastic films*. https://www.semanticscholar.org/paper/A-new-technology-for-sandwich-plates-and-structures-Beukers/a2e1fe537fe3562068036c3b90429bbdfc34c786#related-papers

Birman, V., & Kardomateas, G. A. (2018). Review of current trends in research and applications of sandwich structures. *Composites Part B: Engineering*, *142*, 221–240. https://doi.org/10.1016/j.compositesb.2018.01.027

Brassard, D., Dubé, M., & Tavares, J. R. (2019). Resistance welding of thermoplastic composites with a nanocomposite heating element. *Composites Part B: Engineering*, *165*, 779–784. https://doi.org/10.1016/j.compositesb.2019.02.038

Brassard, D., Dubé, M., & Tavares, J. R. (2021). Modelling resistance welding of thermoplastic composites with a nanocomposite heating element. *Journal of Composite Materials*, *55*(5), 625–639. https://doi.org/10.1177/0021998320957055

Breuer, U., Ostgathe, M., & Neitzel, M. (1998). Manufacturing of all-thermoplastic sandwich systems by a one-step forming technique. *Polymer Composites*, *19*(3), 275–279. https://doi.org/10.1002/pc.10100

Brooks, R., Kulandaivel, P., & Rudd, C. (2008). *Skin Consolidation in Vacuum Moulded Thermoplastic Composite Sandwich Beams*. 627–637.

Brown, K. A., Brooks, R., Warrior, N. A., & Kulandaivel, P. P. (2007). Modelling the impact behaviour of thermoplastic composite sandwich structures. *16th International Conference on Composite Materials, ICCM-16–"A Giant Step Towards Environmental Awareness: From Green Composites to Aerospace*.

Butler, C. A., Mccullough, R. L., Pitchumani, R., & Gillespie, J. W. (1998). An Analysis of Mechanisms Governing Fusion Bonding of Thermoplastic Composites. *Journal of Thermoplastic Composite Materials*, *11*(4), 338–363. https://doi.org/10.1177/089270579801100404

Butukuri, R. R., Bheemreddy, V., Chandrashekhara, K., Berkel, T. R., & Rupel, K. (2012). Evaluation of skin-core adhesion bond of out-of-autoclave honeycomb sandwich structures. *Journal of Reinforced Plastics and Composites*, *31*, 331–339. https://doi.org/10.1177/0731684412437267

Byron Pipes, R., Hearle, J. W. S., Beaussart, A. J., Sastry, A. M., & Okine, R. K. (1991). A Constitutive Relation for the Viscous Flow of an Oriented Fiber Assembly. *Journal of Composite Materials*, *25*. https://doi.org/10.1177/002199839102500907

Cabrera, N. O., Alcock, B., & Peijs, T. (2008). Design and manufacture of all-PP sandwich panels based on co-extruded polypropylene tapes. *Composites Part B: Engineering*, *39*(7), 1183–1195. https://doi.org/10.1016/j.compositesb.2008.03.010

Callister, W. D. (1997). *Materials Science and Engineering: An Introduction*. Wiley.

Campbell, F. C. (2004a). Chapter 3—Matrix Resin Systems. In F. C. Campbell (Ed.), *Manufacturing Processes for Advanced Composites* (pp. 63–100). Elsevier Science. https://doi.org/10.1016/B978-185617415-2/50009-5

Campbell, F. C. (2004b). Chapter 8—Adhesive Bonding. In F. C. Campbell (Ed.), *Manufacturing Processes for Advanced Composites* (pp. 235–254). Elsevier Science. https://doi.org/10.1016/B978-185617415-2/50009-5

CAMPUSplastics | datasheet ULTEM^{TM} Resin 1010. (n.d.). Retrieved December 5, 2022, from https://www.campusplastics.com/campus/en/datasheet/ULTEM%E2%84%A2+Resin+1010/SABIC/658/aa087958

Canadian Space Agency. (2019, February 28). *Canada's role in Moon exploration*. Canadian Space Agency. https://www.asc-csa.gc.ca/eng/astronomy/moon-exploration/canada-role.asp

Canadian Space Agency. (2020, December 16). *Artemis program: Missions to the Moon*. Canadian Space Agency. https://www.asc-csa.gc.ca/eng/astronomy/moon-exploration/artemis-missions.asp

Carroccio, S., Puglisi, C., & Montaudo, G. (1999). Thermal degradation mechanisms of polyetherimide investigated by direct pyrolysis mass spectrometry. *Macromolecular Chemistry and Physics*, *200*(10), 2345–2355. https://doi.org/10.1002/(SICI)1521-3935(19991001)200:10<2345::AID-MACP2345>3.0.CO;2-T

Castanie, B., Bouvet, C., & Ginot, M. (2020). Review of composite sandwich structure in aeronautic applications. *Composites Part C: Open Access*, *1*, 100004. https://doi.org/10.1016/j.jcomc.2020.100004

Chikazumi, S. (2009). *Physics of Ferromagnetism*. OUP Oxford.

Coey, J. M. D. (2010). *Magnetism and Magnetic Materials*. Cambridge University Press.

Cogswell, F. N., Meakin, P. J., Smiley, A. J., Harvey, M. T., & Booth, C. (1989). Thermoplastic interlayer bonding of aromatic polymer composites. *Composites Manufacturing*, 2315–2325.

Colak, Z. S., Sonmez, F. O., & Kalenderoglu, V. (2002). Process Modeling and Optimization of Resistance Welding for Thermoplastic Composites. *Journal of Composite Materials*, *36*(6), 721–744. https://doi.org/10.1177/0021998302036006507

Cole, V. (1982). *Special Fastener Development for Composite Structure*. Flight Dynamics Laboratory, Air Force Wright Aeronautical Laboratories, Air Force Systems Command, United States Air Force.

Costa, A. P. da, Botelho, E. C., Costa, M. L., Narita, N. E., Tarpani, J. R., Costa, A. P. da, Botelho, E. C., Costa, M. L., Narita, N. E., & Tarpani, J. R. (2012). A Review of Welding Technologies for Thermoplastic Composites in Aerospace Applications. *Journal of Aerospace Technology and Management*, *4*(3), 255–265. https://doi.org/10.5028/jatm.2012.04033912

Crozier, R., & Mueller, M. (2016). *A new MATLAB and octave interface to a popular magnetics finite element code*. 1256. https://doi.org/10.1109/ICELMACH.2016.7732685

Daniel, I., & Gdoutos, E. (2010). Failure Modes of Composite Sandwich Beams. In *Major Accomplishments in Composite Materials and Sandwich Structures: An Anthology of ONR Sponsored Research* (pp. 197–227). https://doi.org/10.1007/978-90-481-3141-9_9

Dara, P., & Loos, A. (1985, September 1). *Thermoplastic matrix composite processing model*. https://www.semanticscholar.org/paper/Thermoplastic-matrix-composite-processing-model-Dara-Loos/b935691d33c125688392f6a62af3d085d3f87a86

de Gennes, P. (1971). Reptation of a Polymer Chain in Presence of Fixed Obstacles. *The Journal of Chemical Physics*, *55*, 572. https://doi.org/10.1063/1.1675789

de Wit, A. J., van Hoorn, N., Straathof, L. S., & Vankan, W. J. (2023). Numerical simulation of inductive heating in thermoplastic unidirectional cross-ply laminates. *Frontiers in Materials*, *10*. https://www.frontiersin.org/articles/10.3389/fmats.2023.1155322

Denkena, B., Schmidt, C., Schmitt, C., & Kaczemirzk, M. (2022). Experimental Investigation on the Use of a PEI Foam as Core Material for the In-Situ Production of Thermoplastic Sandwich Structures Using Laser-Based Thermoplastic Automated Fiber Placement. *Materials*, *15*(20), Article 20. https://doi.org/10.3390/ma15207141

Dermanaki Farahani, R., & Dubé, M. (2017). Novel Heating Elements for Induction Welding of Carbon Fiber/Polyphenylene Sulfide Thermoplastic Composites. *Advanced Engineering Materials*, *19*(11), e201700294. https://doi.org/10.1002/adem.201700294

Dermanaki Farahani, R., Janier, M., & Dubé, M. (2018). Conductive films of silver nanoparticles as novel susceptors for induction welding of thermoplastic composites. *Nanotechnology*, *29*. https://doi.org/10.1088/1361-6528/aaa93c

Dubé, M., Hubert, P., Yousefpour, A., & Denault, J. (2008). Current leakage prevention in resistance welding of carbon fibre reinforced thermoplastics. *Composites Science and Technology*, *68*(6), 1579–1587. https://doi.org/10.1016/j.compscitech.2007.09.008

Duchesne, O., Therriault, D., & Gosselin, F. P. (2023). *3D-printing of a geometry optimized sandwich panel for a lunar rover's frame*. International Conference on Composites Materials 2023 (ICCM23), Belfast, UK.

Duhovic, M., Hümbert, M., Mitschang, P., Maier, M., Caldichoury, I., & L'Eplattenier, P. (2014). Further advances in simulating the processing of composite materials by electromagnetic induction. *Proceedings of the 13th International LS-DYNA Users Conference*. https://lsdyna.ansys.com/wp-content/uploads/attachments/further-advances-in-simulating-the-processing-of-composite-materials-by-electromagnetic-induction.pdf

Duhovic, M., L'Eplattenier, P., Çaldichoury, I., Mitschang, P., & Maier, M. (2014). Advanced 3D finite element simulation of thermoplastic carbon fiber composite induction welding. *16th European Conference on Composite Materials, ECCM 2014*.

Dutz, S., & Hergt, R. (2013). Magnetic nanoparticle heating and heat transfer on a microscale: Basic principles, realities and physical limitations of hyperthermia for tumour therapy. *International Journal of Hyperthermia : The Official Journal of European Society for Hyperthermic Oncology, North American Hyperthermia Group*, *29*. https://doi.org/10.3109/02656736.2013.822993

Dutz, S., Hergt, R., Mürbe, J., Müller, R., Zeisberger, M., Andrä, W., Töpfer, J., & Bellemann, M. E. (2007). Hysteresis losses of magnetic nanoparticle powders in the single domain size range. *Journal of Magnetism and Magnetic Materials*, *308*(2), 305–312. https://doi.org/10.1016/j.jmmm.2006.06.005

Fink, B. K., McCullough, R. L., & Gillespie Jr., J. W. (1992). A local theory of heating in cross-ply carbon fiber thermoplastic composites by magnetic induction. *Polymer Engineering & Science*, *32*(5), 357–369. https://doi.org/10.1002/pen.760320509

Gaier, J. R., YoderVandenberg, Y., Berkebile, S., Stueben, H., & Balagadde, F. (2003). The electrical and thermal conductivity of woven pristine and intercalated graphite fiber–polymer composites. *Carbon*, *41*(12), 2187–2193. https://doi.org/10.1016/S0008-6223(03)00238-0

Gao, X., Zhang, M., Huang, Y., Sang, L., & Hou, W. (2020). Experimental and numerical investigation of thermoplastic honeycomb sandwich structures under bending loading. *Thin-Walled Structures*, *155*, 106961. https://doi.org/10.1016/j.tws.2020.106961

Goncharov, A. L., Chulkov, I. S., Kozyrev, Kh. M., Shcherbakov, A. V., & Dragunov, V. K. (2024). Determination of the Curie temperature of structural alloys by analyzing the electrical characteristics of wires. *Journal of Magnetism and Magnetic Materials*, *589*, 171560. https://doi.org/10.1016/j.jmmm.2023.171560

Goodenough, J. (2002). Summary of losses in magnetic materials. *Magnetics, IEEE Transactions On*, *38*, 3398–3408. https://doi.org/10.1109/TMAG.2002.802741

Grouve, W., Vruggink, E., Sacchetti, F., & Akkerman, R. (2020). Induction heating of UD C/PEKK cross-ply laminates. *Procedia Manufacturing*, *47*, 29–35. https://doi.org/10.1016/j.promfg.2020.04.112

Grünewald, J. (2018). *Thermoplastic composite sandwiches for structural helicopter applications*. /paper/Thermoplastic-composite-sandwiches-for-structural-Gr%C3%BCnewald/5cf0d90ba6ed17b791c35d8217cb36191b434e6d

Grünewald, J., Parlevliet, P., & Altstädt, V. (2017a). Definition of process parameters for manufacturing of thermoplastic composite sandwiches – Part A: Modelling. *Journal of Thermoplastic Composite Materials*. https://doi.org/10.1177/0892705717729013

Grünewald, J., Parlevliet, P., & Altstädt, V. (2017b). Manufacturing of thermoplastic composite sandwich structures: A review of literature. *Journal of Thermoplastic Composite Materials*, *30*(4), 437–464. https://doi.org/10.1177/0892705715604681

Grünewald, J., Parlevliet, P., & Altstädt, V. (2018). Definition of process parameters for manufacturing of thermoplastic composite sandwiches – Part B: Model verification. *Journal of Thermoplastic Composite Materials*, *31*(6), 803–819. https://doi.org/10.1177/0892705717722189

Grünewald, J., Parlevliet, P., Matschinski, A., & Altstädt, V. (2019). *Mechanical performance of CF/PEEK–PEI foam core sandwich structures*. https://doi.org/10.1177/1099636217715704

Hagenbeek, M., Bramon, J., & Villegas, I. (2018). *Controlling the edge effect using a bypass conductor for induction welding of carbon fibre thermoplastic composites*. 18th European Conference on Composite Materials (ECCM18), Athens, Grece.

Harland, D., Alshaer, A. W., & Brooks, H. (2019). An Experimental and Numerical Investigation of a Novel 3D Printed Sandwich Material for Motorsport Applications. *Procedia Manufacturing*, *36*, 11–18. https://doi.org/10.1016/j.promfg.2019.08.003

Harrison, E. P. (1904). XX. On the variation with temperature of the magnetic permeability of nickel and iron. *The London, Edinburgh, and Dublin Philosophical Magazine and Journal of Science*, *8*(44), 179–205. https://doi.org/10.1080/14786440409463188

Hegde, S. R., & Hojjati, M. (2019). Effect of core and facesheet thickness on mechanical property of composite sandwich structures subjected to thermal fatigue. *International Journal of Fatigue*, *127*, 16–24. https://doi.org/10.1016/j.ijfatigue.2019.05.031

Heimerdinger, M. W. (1994). *Repair technology for thermoplastic aircraft structures*. 79th meeting of the AGARD structures and Materials Panel on "Composite Repair of Military Aircraft Structures," Seville, Spain.

Herrmann, A. S., Zahlen, P. C., & Zuardy, I. (2005). Sandwich Structures Technology in Commercial Aviation. In O. T. Thomsen, E. Bozhevolnaya, & A. Lyckegaard (Eds.), *Sandwich Structures 7: Advancing with Sandwich Structures and Materials* (pp. 13–26). Springer Netherlands.

Hoang, V.-T., Lee, D.-S., Kweon, J.-H., Kwak, B.-S., & Nam, Y.-W. (2023). Multifunctional heating film as susceptor for induction-welded single-lap carbon fiber reinforced polyetherketoneketone thermoplastic composite joints: Thermal and mechanical behavior. *Journal of Reinforced Plastics and Composites*, 07316844231198309. https://doi.org/10.1177/07316844231198309

Hoff, N. J., & Mautner, S. E. (1998). Sandwich Construction. In *Structures Technology: Historical Perspective and Evolution*. AIAA.

Hoffman, T., Duhovic, M., Mang, P., & Mitschang, P. (2023). *Decoupled electromagnetic simulation of the induction welding process of CFRTP composites*. 23rd International Conference on Composites Materials (ICCM23), Belfast, UK.

Holmes, S. T., & Gillespie, J. W. (1993). Thermal Analysis for Resistance Welding of Large-Scale Thermoplastic Composite Joints. *Journal of Reinforced Plastics and Composites*, *12*(6), 723–736. https://doi.org/10.1177/073168449301200609

Hou, Z., Tian, X., Zhang, J., & Li, D. (2018). 3D printed continuous fibre reinforced composite corrugated structure. *Composite Structures*, *184*, 1005–1010. https://doi.org/10.1016/j.compstruct.2017.10.080

Hsiao, B. S., & Sauer, B. B. (1993). Glass transition, crystallization, and morphology relationships in miscible poly(aryl ether ketones) and poly(ether imide) blends. *Journal of Polymer Science Part B: Polymer Physics*, *31*(8), 901–915. https://doi.org/10.1002/polb.1993.090310801

Ji, X., Matsuo, S., Sottos, N. R., & Cahill, D. G. (2022). Anisotropic thermal and electrical conductivities of individual polyacrylonitrile-based carbon fibers. *Carbon*, *197*, 1–9. https://doi.org/10.1016/j.carbon.2022.06.005

Johnson, A. (2008). Novel hybrid structural core sandwich materials for aircraft applications. *Undefined*.

Kane, B., Wasselynck, G., Huu Kien, B., Trichet, D., & Berthiau, G. (2020). Focalization of Electromagnetic Power at the Interface Between Two Composites Materials for Induction Welding. *The European Physical Journal Applied Physics*, *91*. https://doi.org/10.1051/epjap/2020200022

Kim, H. J., Yarlagadda, S., Shevchenko, N. B., Fink, B. K., & Gillespie, J. W. (2003). Development of a Numerical Model to Predict In-Plane Heat Generation Patterns During Induction Processing of Carbon Fiber-Reinforced Prepreg Stacks. *Journal of Composite Materials*, *37*(16), 1461–1483. https://doi.org/10.1177/0021998303034460

Kim, Y. H., & Wool, R. P. (1983). A theory of healing at a polymer-polymer interface. *Macromolecules*, *16*(7), 1115–1120. https://doi.org/10.1021/ma00241a013

Kindinger, J. (2001). Ch. 24—Lightweight Structural Cores. In *Composites* (Vol. 21). ASM International.

Kneller, E. F., & Luborsky, F. E. (1963). Particle Size Dependence of Coercivity and Remanence of Single-Domain Particles. *Journal of Applied Physics*, *34*, 656–658. https://doi.org/10.1063/1.1729324

Kodiyalam, S., Nagendra, S., & DeStefano, J. (1996). Composite sandwich structure optimization with application to satellite components. *AIAA Journal*, *34*(3), 614–621. https://doi.org/10.2514/3.13112

Kratz, J. (2010). *Processing composite sandwich structures using out-of-autoclave technology*. McGill University.

Krishnan, K. M., Pakhomov, A. B., Bao, Y., Blomqvist, P., Chun, Y., Gonzales, M., Griffin, K., Ji, X., & Roberts, B. K. (2006). Nanomagnetism and spin electronics: Materials, microstructure and novel properties. *Journal of Materials Science*, *41*(3), 793–815. https://doi.org/10.1007/s10853-006-6564-1

Landgraf, F. J. G., Emura, M., & de Campos, M. F. (2008). On the Steinmetz hysteresis law. *Journal of Magnetism and Magnetic Materials*, *320*(20), e531–e534. https://doi.org/10.1016/j.jmmm.2008.04.011

Latsuzbaya, T., Middendorf, P., Voelkle, D., & Weber, C. (2023). *Fusion Bonding of Thermoplastic Mono-material Sandwich Structures with Honeycomb Core*. SAMPE International Conference 2023, Seattle, WA. https://doi.org/10.33599/nasampe/s.23.0335

Lee, J. S., Cha, J., Yoon, H., Lee, J.-K., & Kim, Y. K. (2015). Magnetic multi-granule nanoclusters: A model system that exhibits universal size effect of magnetic coercivity. *Scientific Reports*, *5*, 12135. https://doi.org/10.1038/srep12135

Lee, W. I., & Springer, G. S. (1987). A Model of the Manufacturing Process of Thermoplastic Matrix Composites. *Journal of Composite Materials*, *21*(11), 1017–1055. https://doi.org/10.1177/002199838702101103

Levy, A., Heider, D., Tierney, J., & Gillespie Jr, J. (2013). Inter-layer Thermal Contact Resistance Evolution with the Degree of Intimate Contact in the Processing of Thermoplastic Composite Laminates. *Journal for Composite Materials*, *48*. https://doi.org/10.1177/0021998313476318

Li, X., Zhang, T., Li, S., Liu, H., Zhao, Y., & Wang, K. (2021). The effect of cooling rate on resistance-welded CF/PEEK joints. *Journal of Materials Research and Technology*, *12*, 53–62. https://doi.org/10.1016/j.jmrt.2021.02.071

Lin, W., Miller, A. K., & Buneman, O. (1992). *Predictive capabilities of an induction heating model for complex-shape graphite fiber/polymer matrix composites*. *24*, T606–T620. 24th International SAMPE Technical Conference.

Lionetto, F., Pappadà, S., Buccoliero, G., & Maffezzoli, A. (2017). Finite element modeling of continuous induction welding of thermoplastic matrix composites. *Materials & Design*, *120*, 212–221. https://doi.org/10.1016/j.matdes.2017.02.024

Lu, C., Qi, M., Islam, S., Chen, P., Gao, S., Xu, Y., & Yang, X. (2018). Mechanical performance of 3D-printing plastic honeycomb sandwich structure. *International Journal of Precision Engineering and Manufacturing-Green Technology*, *5*(1), 47–54. https://doi.org/10.1007/s40684-018-0005-x

Ma, W., & Elkin, R. (2021). All-Thermoplastic Sandwich Composites. In *Sandwich Structural Composites* (pp. 159–184). CRC Press.

Mahdi, S., Kim, H.-J., Gama, B. A., Yarlagadda, S., & Gillespie, J. W. (2003). A Comparison of Oven-cured and Induction-cured Adhesively Bonded Composite Joints. *Journal of Composite Materials*, *37*(6), 519–542. https://doi.org/10.1177/0021998303037006776

Mantell, S. C., & Springer, G. S. (1992). Manufacturing Process Models for Thermoplastic Composites. *Journal of Composite Materials*, *26*(16), 2348–2377. https://doi.org/10.1177/002199839202601602

Mantell, S. C., Wang, Q., & Springer, G. S. (1992). Processing Thermoplastic Composites in a Press and by Tape Laying—Experimental Results. *Journal of Composite Materials*, *26*(16), 2378–2401. https://doi.org/10.1177/002199839202601603

Mariani, A., & Malucelli, G. (2023). Insights into Induction Heating Processes for Polymeric Materials: An Overview of the Mechanisms and Current Applications. *Energies*, *16*(11), Article 11. https://doi.org/10.3390/en16114535

Martin, R. G., Figueiredo, M., Johansson, C., Tavares, J. R., & Dubé, M. (2023a). Characterization of Magnetic Susceptor Heating Rate Due to Hysteresis Losses in Thermoplastic Welding. *SAMPE Journal*, *59*(5), 19–27.

Martin, R. G., Figueiredo, M., Johansson, C., Tavares, J. R., & Dubé, M. (2023b). Hysteresis Losses Magnetic Susceptor Heating Rate Characterization. *SAMPE Conference Proceedings. Seattle, WA, April 17 -20, 2023. Society for the Advancement of Material and Process Engineering – North America.*, 1112–1127.

Martin, R. G., Johansson, C., Tavares, J. R., & Dubé, M. (2021). *Heating rate prediction for induction welding magnetic susceptors*. 11–23.

Martin, R. G., Johansson, C., Tavares, J. R., & Dubé, M. (2022). Material Selection Methodology for an Induction Welding Magnetic Susceptor Based on Hysteresis Losses. *Advanced Engineering Materials*, *24*(3). https://doi.org/10.1002/adem.202100877

Martin, R. G., Johansson, C., Tavares, J. R., & Dubé, M. (2023). *Thermal Characterization of Thermoplastic Composite Adherends for Induction Welding using Insulating Interlayers*. 13th Canada-Japan Workshop on Composites (CJWC13), Québec City, QC.

Martin, R. G., Johansson, C., Tavares, J. R., & Dubé, M. (2024). Manufacturing of thermoplastic composite sandwich panels using induction welding under vacuum. *Composites Part A: Applied Science and Manufacturing*, *182*, 108211. https://doi.org/10.1016/j.compositesa.2024.108211

McGaffigan, T. H. (1994). *Temperature auto-regulating, self-heating recoverable articles* (United States Patent US5319173A). https://patents.google.com/patent/US5319173/en

Meakin, P. J., Cogswell, F. N., Halbritter, A. J., Smiley, A. J., & Staniland, P. A. (1991). Thermoplastic interlayer bonding of aromatic polymer composites—Methods for using semi-crystallized polymers. *Composites Manufacturing*, *2*(2), 86–91. https://doi.org/10.1016/0956-7143(91)90184-I

Milone, A. F., Ortalli, I., & Soardo, G. P. (1982). Curie temperature of Ni−Fe alloys in the region (24÷35)% Ni from Mössbauer experiments. *Il Nuovo Cimento D*, *1*(1), 18–20. https://doi.org/10.1007/BF02450180

Mitschang, P., Rudolf, R., & Neitzel, M. (2002). Continuous Induction Welding Process, Modelling and Realisation. *Journal of Thermoplastic Composite Materials*, *15*, 127–153. https://doi.org/10.1177/0892705702015002451

Mørup, S., Hansen, M., & Frandsen, C. (2011). Magnetic Nanoparticles. In *Comprehensive Nanoscience and Technology* (Vol. 1, pp. 433–487). https://doi.org/10.1016/B978-0-12-374396-1.00036-2

Moser, L. (2012). Experimental Analysis and Modeling of Susceptorless Induction Welding of High-Performance Thermoplastic Polymer Composites. *Undefined*. /paper/Experimental-Analysis-and-Modeling-of-Susceptorless-Moser/f24c3df7520ba247dce7fc9adc0906f6dcd84086

Muhlethaler, J., Biela, J., Kolar, J. W., & Ecklebe, A. (2012). Core Losses Under the DC Bias Condition Based on Steinmetz Parameters. *IEEE Transactions on Power Electronics*, *27*(2), 953–963. https://doi.org/10.1109/TPEL.2011.2160971

Nagel, J. R. (n.d.). *Induced Eddy Currents in Simple Conductive Geometries Due to a Time-Varying Magnetic Field*. 8.

Nettles, A. T. (2006). *Measuring Core/Facesheet Bond Toughness in Honeycomb Sandwich Structures*. 68.

Neumeyer, T., Knoechel, J. F., Mühlbacher, M., Kroeger, T., Altstädt, V., & Schreier, P. (2017). *Thermoplastic Sandwich Structures—Processing Approaches Towards Automotive Serial Production*. 21st International Conference on Composite Materials, Xi’an.

O’Shaughnessey, P. G., Dubé, M., & Villegas, I. F. (2016). Modeling and experimental investigation of induction welding of thermoplastic composites and comparison with other welding processes: *Journal of Composite Materials*. https://doi.org/10.1177/0021998315614991

Özen, İ., Çava, K., Gedikli, H., Alver, Ü., & Aslan, M. (2020). Low-energy impact response of composite sandwich panels with thermoplastic honeycomb and reentrant cores. *Thin-Walled Structures*, *156*, 106989. https://doi.org/10.1016/j.tws.2020.106989

Pappadà, S., Rametta, R., Passaro, A., Lanzilotto, L., & Maffezzoli, A. (2010). Processing, mechanical properties, and interfacial bonding of a thermoplastic core-foam/composite-skin sandwich panel. *Advances in Polymer Technology*, *29*(3), 137–145. https://doi.org/10.1002/adv.20186

Pappadà, S., Rametta, R., Passaro, A., Lanzilotto, L., Maffezzoli, A., & Cetma, C. (n.d.). *Effect of the manufacturing process and skin-core adhesion efficiency on the mechanical properties of a thermoplastic sandwich*. 10.

Pappadà, S., Salomi, A., Montanaro, J., Passaro, A., Caruso, A., & Maffezzoli, A. (2015). Fabrication of a thermoplastic matrix composite stiffened panel by induction welding. *Aerospace Science and Technology*, *43*, 314–320. https://doi.org/10.1016/j.ast.2015.03.013

Park, G., Oh, K., Kong, C., & Park, H. (2014). Investigation on Adhesion Properties of Sandwich Composite Structures Considering on Surface Treatments. *International Journal of Aerospace System Engineering*, *1*(1), 16–20. https://doi.org/10.20910/IJASE.2014.1.1.016

Pegoretti, A. (2021). Towards sustainable structural composites: A review on the recycling of continuous-fiber-reinforced thermoplastics. *Advanced Industrial and Engineering Polymer Research*, *4*(2), 105–115. https://doi.org/10.1016/j.aiepr.2021.03.001

Pflug, J., Verpoest, I., Bratfisch, P., & Vandepitte, D. (2001). *Thermoplastic Folded Honeycomb Cores—Cost Efficient Production of All Thermoplastic Sandwich Panels*.

Pitchumani, R., Ranganathan, S., Don, R. C., Gillespie, J. W., & Lamontia, M. A. (1996). Analysis of transport phenomena governing interfacial bonding and void dynamics during thermoplastic tow-placement. *International Journal of Heat and Mass Transfer*, *39*(9), 1883–1897. https://doi.org/10.1016/0017-9310(95)00271-5

Pollard, D., Ward, C., Herrmann, G., & Etches, J. (2017). The manufacture of honeycomb cores using Fused Deposition Modeling. *Advanced Manufacturing: Polymer & Composites Science*, *3*(1), 21–31. https://doi.org/10.1080/20550340.2017.1306337

PRIMA Québec. (2020). Vision Rover Lunaire PEEKbot: Conception et fabrication avancée d'un rover lunaire à base de composites thermoplastiques. *PRIMA Québec*. https://www.prima.ca/project/vision-rover-lunaire-peekbot-conception-et-fabrication-avancee-dun-rover-lunaire-a-base-de-composites-thermoplastiques/

Rak, J., & Tucek, J. (2022). Solving magnetic induction heating problem with multidimensional Fredholm integral equation methods: Alternative approach for optimization and evaluation of the process performance. *AIP Advances*, *12*(10), 105110. https://doi.org/10.1063/5.0100480

Renault, B. (2023). *Suscepteurs ferro-magnétiques pour le soudage par induction de composites thermoplastiques en utilisant la chauffe par hystérésis* [Projet de Maitrise]. École de technologie supérieure (ÉTS).

Rozant, O., Bourban, P.-E., & Månson, J.-A. E. (2001). Manufacturing of three dimensional sandwich parts by direct thermoforming. *Composites Part A: Applied Science and Manufacturing*, *32*(11), 1593–1601. https://doi.org/10.1016/S1359-835X(00)00184-6

Rudolf, R., Mitschang, P., & Neitzel, M. (2000). Induction heating of continuous carbon-fibre-reinforced thermoplastics. *Composites Part A-Applied Science and Manufacturing*, *31*, 1191–1202. https://doi.org/10.1016/S1359-835X(00)00094-4

SABIC. (2021). *ULTEM Resin 1010 Technical data sheet*.

Sanders, P. (1987). Electromagnetic welding: An advance in thermoplastics assembly. *Materials & Design*, *8*(1), 41–45. https://doi.org/10.1016/0261-3069(87)90059-8

Seneviratnae, W., Tomblin, J., Teoh, J. J. C., Saathoff, B. J., & Smith, N. A. (2021). *Induction Heating Analysis Validation of CF/PEKK laminates with Magnetic Flux Controller*. SAMPE neXus 2021, Virtual event.

Shi, H., Villegas, I. F., & Bersee, H. E. (2017). Analysis of void formation in thermoplastic composites during resistance welding. *Journal of Thermoplastic Composite Materials*, *30*(12), 1654–1674. https://doi.org/10.1177/0892705716662514

Shokrollahi, H. (2017). A review of the magnetic properties, synthesis methods and applications of maghemite. *Journal of Magnetism and Magnetic Materials*, *426*, 74–81. https://doi.org/10.1016/j.jmmm.2016.11.033

Silverman, E. M., & Griese, R. A. (1989). Joining methods for graphite/PEEK thermoplastic composites. *SAMPE Journal*, *25*(5), 34–38.

Skawinski, O., Binetruy, C., Krawczak, P., Grando, J., & Bonneau, E. (2004). All-Thermoplastic Composite Sandwich Panels – Part I: Manufacturing and Improvement of Surface Quality. *Journal of Sandwich Structures & Materials*, *6*(5), 399–421. https://doi.org/10.1177/1099636204040094

Slayton, R., & Spinardi, G. (2016). Radical innovation in scaling up: Boeing's Dreamliner and the challenge of socio-technical transitions. *Technovation*, *47*, 47–58. https://doi.org/10.1016/j.technovation.2015.08.004

Smiley, A., Halbritter, A., Cogswell, F., & Meakin, P. J. (1991). Dual Polymer Bonding of Thermoplastic Composite Structures. *Polymer Engineering & Science*, *31*(7), 526–532. https://doi.org/10.1002/PEN.760310709

Sonmez, F., & Hahn, H. (1997). Analysis of the On-Line Consolidation Process in Thermoplastic Composite Tape Placement. *Journal of Thermoplastic Composite Materials*, *10*, 543–572. https://doi.org/10.1177/089270579701000604

Spaldin, N. (2003). *Magnetic Materials Fundamentals* (Cambridge University Press).

Steinmetz, Chas. P. (1984). On the law of hysteresis. *Proceedings of the IEEE*, *72*(2), 197–221. Proceedings of the IEEE. https://doi.org/10.1109/PROC.1984.12842

Stokes, V. (2003). Experiments on the Induction Welding of Thermoplastics. *Polymer Engineering & Science*, *43*, 1523–1541. https://doi.org/10.1002/pen.10129

Stokes, V. K. (1989). *Joining methods for plastics and plastic composites: An overview*. https://doi.org/10.1002/pen.760291903

Sugiyama, K., Matsuzaki, R., Ueda, M., Todoroki, A., & Hirano, Y. (2018). 3D printing of composite sandwich structures using continuous carbon fiber and fiber tension. *Composites Part A: Applied Science and Manufacturing*, *113*, 114–121. https://doi.org/10.1016/j.compositesa.2018.07.029

Suwanwatana, W., Yarlagadda, S., & Gillespie, J. W. (2006a). Hysteresis heating-based induction bonding of thermoplastic composites. *Composites Science and Technology*, *66*(11), 1713–1723. https://doi.org/10.1016/j.compscitech.2005.11.009

Suwanwatana, W., Yarlagadda, S., & Gillespie, J. W. (2006b). Influence of particle size on hysteresis heating behavior of nickel particulate polymer films. *Composites Science and Technology*, *66*(15), 2825–2836. https://doi.org/10.1016/j.compscitech.2006.02.033

Teijin Carbon America, Inc. (2019). *TENAX® Continuous Filament Yarn Product Data Sheet*.

Teijin Carbon America, Inc. (2020). *Tenax®-E TPUD PEEK-2-34-HTS45 P12 12K-UD-145 Product Data Sheet*.

Testo SE & Co. (2017). *Thermography Pocket Guide*. https://static-int.testo.com/media/1d/b7/21fc65abbea1/Pocket-Guide-Thermography-EN.pdf

The hardness of metals: A visual representation of the Mohs scale for mettalic elements and alloys. (n.d.). Alan's factory Outlet. Retrieved May 5, 2021, from https://www.sccboe.org/cms/lib/AL50000450/Centricity/Domain/779/the-hardness-of-metals-a-visual-representation-of-the-mohs-scale.pdf

Toray Composites Materials America, Inc. (2018a). *T300 Standard Modulus Carbon Fiber*.

Toray Composites Materials America, Inc. (2018b). *T700S Standard Modulus Carbon Fiber*.

Toray Composites Materials America, Inc. (2024). *T1000G Intermediate Modulus Carbon Fiber*.

Townsend, S., Adams, R., Robinson, M., Hanna, B., & Theobald, P. (2020). 3D printed origami honeycombs with tailored out-of-plane energy absorption behavior. *Materials & Design*, *195*, 108930. https://doi.org/10.1016/j.matdes.2020.108930

Trende, A., Åström, B. T., Wöginger, A., Mayer, C., & Neitzel, M. (1999). Modelling of heat transfer in thermoplastic composites manufacturing: Double-belt press lamination. *Composites Part A: Applied Science and Manufacturing*, *30*(8), 935–943. https://doi.org/10.1016/S1359-835X(99)00016-0

Troughton, M. J. (Ed.). (2009a). Ch. 11—Induction Welding. In *Handbook of Plastics Joining (Second Edition)* (pp. 113–120). William Andrew Publishing. https://doi.org/10.1016/B978-0-8155-1581-4.50013-5

Troughton, M. J. (Ed.). (2009b). Chapter 18—Mechanical Fastening. In *Handbook of Plastics Joining (Second Edition)* (pp. 175–201). William Andrew Publishing. https://doi.org/10.1016/B978-0-8155-1581-4.50020-2

Tsiangou, E., Teixeira de Freitas, S., Fernandez Villegas, I., & Benedictus, R. (2019). Investigation on energy director-less ultrasonic welding of polyetherimide (PEI)- to epoxy-based composites. *Composites Part B: Engineering*, *173*, 107014. https://doi.org/10.1016/j.compositesb.2019.107014

Tumanski, S. (2011). Ch. 3—Magnetic Materials. In *Handbook of Magnetic Measurements*. Routledge Handbooks Online. https://doi.org/10.1201/b10979-4

UL Prospector. (2018). *ULTEM^{TM} Resin 1000—Americas* (p. 18). https://www.protolabs.com/media/1014801/ultem-1000-im.pdf

Van den Berg, S., Luckabauer, M., Wijskamp, S., & Akkerman, R. (2023). Determination of the anisotropic electrical conductivity of carbon fabric reinforced composites by the six-probe method. *Journal of Thermoplastic Composite Materials*, *36*(11), 4257–4283. https://doi.org/10.1177/08927057231154546

Van Ingen, J. W., Buitenhuis, A., Wijngaarden, M., & Simmons, F. (2010, May 19). *Development of the Gulfstream G650 induction welded thermoplastic elevators and rudder*.

Vieille, B., Casado, V. M., & Bouvet, C. (2012). *Comparative study on the impact behavior and damage tolerance of woven carbon fiber reinforced thermoplastic– and thermosetting– composites*. 1–8. https://oatao.univ-toulouse.fr/6792/

Villegas, I. F., Moser, L., Yousefpour, A., Mitschang, P., & Bersee, H. E. (2013). Process and performance evaluation of ultrasonic, induction and resistance welding of advanced thermoplastic composites. *Journal of Thermoplastic Composite Materials*, *26*(8), 1007–1024. https://doi.org/10.1177/0892705712456031

Vinum, M. G., Almind, M. R., Engbæk, J. S., Vendelbo, S. B., Hansen, M. F., Frandsen, C., Bendix, J., & Mortensen, P. M. (2018). Dual-Function Cobalt–Nickel Nanoparticles Tailored for High-Temperature Induction-Heated Steam Methane Reforming. *Angewandte Chemie International Edition*, *57*(33), 10569–10573. https://doi.org/10.1002/anie.201804832

Vodicka, R. (1996). *Thermoplastics for Airframe Applications A Review of the Properties and Repair Methods for Thermoplastic Composites*.

Wahyuningsih, S., Ramelan, A., & Kristiawan, Y. (2019). Transformation of Magnetite (Fe3O4) and Maghemite (γ–Fe2O3) to α–Fe2O3 from Magnetic Phase of Glagah Iron Sand. *Journal of Engineering Science*, *15*, 11–21. https://doi.org/10.21315/jes2019.15.2

Walter, N. A., & Scialdone, J. J. (1997). *Outgassing Data for Selecting Spacecraft Materials* [Numeric Database].

Wei, Q., Gilder, S., & Maier, B. (2014). Pressure dependence on the remanent magnetization of Fe-Ni alloys and Ni metal. *Physical Review B*, *90*. https://doi.org/10.1103/PhysRevB.90.144425

Weidmann, F., Ziegmann, G., & Wieser, J. (2023). A review of mode I dominant interfacial fracture toughness test methods of skin-core bonding for thermoplastic composite sandwich structures. *Journal of Thermoplastic Composite Materials*, *36*(6), 2643–2673. https://doi.org/10.1177/08927057221083493

Westrum, E. F., & Grønvold, F. (1969). Magnetite (Fe3O4) Heat capacity and thermodynamic properties from 5 to 350 K, low-temperature transition. *The Journal of Chemical Thermodynamics*, *1*(6), 543–557. https://doi.org/10.1016/0021-9614(69)90015-9

Wetzel, E. D., & Fink, B. K. (n.d.). *Feasibility of Magnetic Particle Films for Curie Temperature-Controlled Processing of Composite Materials*. 83.

Wetzel, E. D., & Fink, B. K. (2001). *Adherend Thermal Effects During Bonding with Inductively Heated Films*. https://doi.org/10.21236/ada389305

Widagdo, D., Kuswoyo, A., Nurpratama, T. O., & Hadi, B. K. (2020). Experimental flatwise tensile strength dataset of carbon fibre reinforced plastic sandwich panels with different core material preparations. *Data in Brief*, *28*, 105055. https://doi.org/10.1016/j.dib.2019.105055

Williams, J.-P., Paige, D. A., Greenhagen, B. T., & Sefton-Nash, E. (2017). The global surface temperatures of the Moon as measured by the Diviner Lunar Radiometer Experiment. *Icarus*, *283*, 300–325. https://doi.org/10.1016/j.icarus.2016.08.012

Williamson, J. R. (1991). Advanced materials for space structures. *Acta Astronautica*, *24*, 197–202. https://doi.org/10.1016/0094-5765(91)90167-4

Wilson, G. (1992). 13—Slurry Pumps. In V. S. Lobanoff & R. R. Ross (Eds.), *Centrifugal Pumps (Second Edition)* (pp. 226–245). Gulf Professional Publishing. https://doi.org/10.1016/B978-0-08-050085-0.50016-3

Wingfield, J. R. J. (1993). Treatment of composite surfaces for adhesive bonding. *International Journal of Adhesion and Adhesives*, *13*(3), 151–156. https://doi.org/10.1016/0143-7496(93)90036-9

Wise, R., & Worrall, C. (2014). Novel Induction Heating to Join Carbon Fibre Composites. *SEICO 14: 35th International Technical Conference & Forum "Low Cost Composite Processing, from Aerospace OOA to Automotive Thermoplastic*.

Wool, R. P., Yuan, B.-L., & McGarel, O. J. (1989). Welding of polymer interfaces. *Polymer Engineering & Science*, *29*(19), 1340–1367. https://doi.org/10.1002/pen.760291906

Worrall, C., & Wise, R. (2014). Novel Induction Heating Technique for Joining of Carbon Fibre Composites. *ECCM16 - 16th European Conference on Composite Materials*.

Xiao, X., Hoa, S., & Street, K. (1994). Repair of thermoplastic resin composites by fusion bonding. *ASTM Special Technical Publication*, 30–44.

Xinyu, F., Yubin, L., Juan, L., Chun, Y., & Ke, L. (2009). Modeling of Heat Conduction in Thermoplastic Honeycomb Core/Face Sheet Fusion Bonding. *Chinese Journal of Aeronautics*, *22*(6), 685–690. https://doi.org/10.1016/S1000-9361(08)60159-4

Yang, F., & Pitchumani, R. (2001). A fractal Cantor set based description of interlaminar contact evolution during thermoplastic composites processing. *Journal of Materials Science*, *36*(19), 4661–4671. https://doi.org/10.1023/A:1017950215945

Yang, F., & Pitchumani, R. (2002). Healing of Thermoplastic Polymers at an Interface under Nonisothermal Conditions. *Macromolecules*, *35*(8), 3213–3224. https://doi.org/10.1021/ma010858o

Yarlagadda, S., Fink, B. K., & J. W. Gillespie, J. (2016). Resistive Susceptor Design for Uniform Heating during Induction Bonding of Composites. *Journal of Thermoplastic Composite Materials*. https://doi.org/10.1177/089270579801100403

Yarlagadda, S., Kim, H. J., Gillespie, J. W., Shevchenko, N. B., & Fink, B. K. (2002). A Study on the Induction Heating of Conductive Fiber Reinforced Composites. *Journal of Composite Materials*, *36*(4), 401–421. https://doi.org/10.1177/0021998302036004171

Yixiong, F., Qiu, H., Gao, Y., Zheng, H., & Tan, J. (2020). Creative design for sandwich structures: A review. *International Journal of Advanced Robotic Systems*, *17*, 172988142092132. https://doi.org/10.1177/1729881420921327

Yousefpour, A., Hojjati, M., & Immarigeon, J.-P. (2004). Fusion Bonding/Welding of Thermoplastic Composites. *Journal of Thermoplastic Composite Materials*, *17*(4), 303–341. https://doi.org/10.1177/0892705704045187

Zenkert, D. (1997). *The handbook of sandwich construction*. Engineering Materials Advisory Services Ltd. (EMAS).